

NASA CR-72695
R-8039

LITHIUM-FLUORINE-HYDROGEN
PROPELLANT INVESTIGATION

by

H. A. Arbit, S. D. Clapp, and C. K. Nagai

Rocketdyne
A Division of North American Rockwell Corporation

prepared for

NATIONAL AERONAUTICS AND SPACE ADMINISTRATION

NASA Lewis Research Center
Contract NAS3-11230
Stephen M. Cohen, Project Manager



N70-27965

FACILITY FORM 602

(ACCESSION NUMBER)
241
(PAGES)
CR-72695
(NASA CR OR TX OR AD NUMBER)

(TITLE)
I
(CODE)
27
(CATEGORY)

NASA CR-72695
R-8039

FINAL REPORT

LITHIUM-FLUORINE-HYDROGEN PROPELLANT INVESTIGATION

by

H. A. Arbit, S. D. Clapp, and C. K. Nagai

ROCKETDYNE
A Division of North American Rockwell Corporation
Canoga Park, California 91304

Prepared for

NATIONAL AERONAUTICS AND SPACE ADMINISTRATION

May 1970

Contract NAS3-11230

NASA Lewis Research Center
Cleveland, Ohio
Stephen M. Cohen, Project Manager
Liquid Rocket Technology Branch

PRECEDING PAGE BLANK NOT FILMED.

FOREWORD

The work described herein was carried out by the Research Division of Rocketdyne, a division of North American Rockwell Corporation, from June 1968 to October 1969. Mr. S. M. Cohen, Lewis Research Center, was NASA Project Manager. Mr. T. A. Coultas was Rocketdyne Program Manager, and Mr. S. D. Clapp, who was responsible for technical guidance of the program, functioned as Project Manager. Mr. H. A. Arbit was Principal Investigator.

This final report was prepared in compliance with Paragraph D, Exhibit B, Modification No. 3, of NASA Contract NAS3-11230 entitled, "Lithium-Fluorine-Hydrogen Propellant Investigation". This report incorporates the interim report originally issued as Rocketdyne document R-7809, April 1969.

Important contributions to the conduct of the program and to the preparation of report material were made by the following Rocketdyne personnel:

L. W. Carlson, G. A. Hosack, R. F. Kuhn, Jr., and K. W. Tate.

ABSTRACT

Results are reported of a three-part program which continued the investigation of the Li/F₂/H₂ tripropellant combination begun in a previous study (NASA CR-72325). Objectives of the program were: (1) to investigate the feasibility of a simplified injection method, (2) to measure thrust chamber heat flux, and (3) to determine specific impulse efficiency at simulated altitude conditions. Nominal test conditions were: P_c = 750 psia (5.17 x 10⁶ N/m²), F₂/Li mixture ratio = 2.74, H₂ = 20 to 35 percent. Experimental firings gave the following results: (1) a simplified injection method involving the use of a fuel-rich LF₂/GH₂ gas generator is feasible, with corrected c* efficiency of approximately 98 percent at nominal test conditions, (2) Li/F₂/H₂ heat flux is approximately 10 B/in.²/sec (16 x 10⁶ W/m²) in the combustion chamber and 10.7 B/in.²/sec (27 x 10⁶ W/m²) at the throat at nominal test conditions, and (3) measured Li/F₂/H₂ specific impulse efficiency with a 60:1 expansion ratio nozzle is 95 percent at nominal test conditions, corresponding to a calculated vacuum specific impulse of 509 lbf/lbm/sec (4991 N/kg/sec) deliverable by a regeneratively cooled engine. No lithium system operational problems were encountered.

CONTENTS

Foreword	iii
Abstract	v
Summary	1
Introduction	5
Task I: Injection Configuration Investigation	6
Task II: Injector Performance and Heat Flux Determination	7
Task III: Altitude Performance Tests	7
Design of Thrust Chamber Components	9
Fuel-Rich Gas Generator	10
Lithium Injector	15
Water-Cooled Combustion Chamber	21
Water-Cooled Nozzle	26
Nozzle Skirt	28
Experimental Facilities and Procedures	33
Propellant Systems	33
Instrumentation and Data Recording	36
Calibration Procedures	40
Test Procedures	42
Experimental Firings	45
Introduction	45
Task I Firings Using Oxidizer-Rich Gas Generator	46
Task I Firings Using Fuel-Rich Gas Generator	48
Task II Experimental Firings	54
Task III Experimental Firings	56
Results and Discussion	59
Tripropellant Injection Methods	59
Thrust Chamber Heat Transfer	64
Altitude Performance	72
Concluding Remarks	77
References	79
<u>Appendix A</u>	
Performance Calculation Methods	153
<u>Appendix B</u>	
Measurement Error Analysis	163

<u>Appendix C</u>	
Thrust Calibration and Measurement Procedures	175
<u>Appendix D</u>	
Heat Transfer Measurement and Data Reduction Procedures	181
<u>Appendix E</u>	
Cold-Flow Studies of Single-Element Lithium Injector	193
<u>Appendix F</u>	
Effect of Particle Size on Li/F ₂ /H ₂ Performance	203
<u>Appendix G</u>	
Design and Installation of Exhaust Diffuser	215
<u>Appendix H</u>	
Specific Impulse Efficiencies of Task II Test Firings	225
<u>Appendix I</u>	
Nomenclature	227
<u>Appendix J</u>	
Distribution List	233

TABLES

1. Lithium Injection Tube Orifice Tips Used in Run No. 69-9 . . .	83
2. Test Data Summary, Oxidizer-Rich Gas Generator Firings . . .	84
3. Test Data Summary, Fuel-Rich Gas Generator Firings	85
4. Test Data Summary, Characteristic Velocity Efficiency, Oxidizer-Rich Gas Generator Injection Method	86
5. Test Data Summary, Characteristic Velocity Efficiency, Fuel-Rich Gas Generator Injection Method	87
6. Summary of Heat Transfer Data	88
7. Data Summary, Altitude Performance Tests	91

ILLUSTRATIONS

1. Schematics of Li/F ₂ /H ₂ Thrust Chambers	92
2. Test Matrix of Percent Hydrogen and F ₂ /Li Mixture Ratio for the Li/F ₂ /H ₂ Experimental Firings	93
3. Gas Generator Propellant Flowrates Corresponding to Indicated Tripropellant Test Conditions of Percent Hydrogen and F ₂ /Li Mixture Ratio	94
4. Gas Generator F ₂ /H ₂ Mixture Ratio and Chamber Temperature Corresponding to Indicated Tripropellant Test Conditions of Percent Hydrogen and F ₂ /Li Mixture Ratio	95
5. Schematic of Doublet/Showerhead LF ₂ /GH ₂ Injection Element, Mod I Injector	96
6. Face Pattern of Doublet/Showerhead LF ₂ /GH ₂ Injector, Mod I	97
7. Gas Generator Injector Face Temperatures for Copper and Nickel at Design Conditions as Functions of Firing Duration	98
8. Schematic of Unlike-Doublet LF ₂ /GH ₂ Injector, Mod II	99
9. Penetration of LF ₂ Streams into GH ₂ Jets in the Mod II LF ₂ /GH ₂ Injector at Operating Conditions Corresponding to Indicated Tripropellant Test Conditions	100
10. Face Pattern of Unlike-Doublet LF ₂ /GH ₂ Injector, Mod II	101
11. Temperature of the Outer Surface of a Graphite Liner in the Gas Generator Chamber, as Function of Firing Duration, for the Indicated Thickness of Graphite	102
12. Assembled Gas Generator Chamber, Showing Graphite Liner and Porous Carbon Washer	103
13. Chamber Pressures and Lithium Flowrates Corresponding to Indicated Tripropellant Test Conditions of Percent Hydrogen and F ₂ /Li Mixture Ratio	104
14. Gas Injection Mach Number, Lithium Droplet Volume Mean Diameter, and Penetration of Gas Jet by Lithium Stream at Indicated Tripropellant Test Conditions of Percent Hydrogen and F ₂ /Li Mixture Ratio	105
15. Schematic of Biplanar Lithium/Gas Injection Element for Mod I, II, and III Lithium Injectors	106

16.	Face Pattern of Lithium Injector, Mod I and II	107
17.	Schematic of Thrust Chamber Assembly Used in the Task I Firings With the Fuel-Rich Gas Generator Injection Method and the Mod I Lithium Injector	108
18.	Lithium Injector Modifications, Mod I, II, and III	109
19.	Gambill's Heat Transfer Correlation for Forced-Convection Subcooled Boiling Applied to Water at 100 F (311 K) in a 0.125-Inch (3.18-mm) Diameter Channel	110
20.	Components of the 4-Inch (10.16-cm), High Heat Flux, Water- Cooled, Combustion Chamber Section	111
21.	Assembled 4-Inch (10.16-cm), High Heat Flux, Water-Cooled, Combustion Chamber Section	112
22.	Shell and Liner of 9-Inch (22.86-cm), Low Heat Flux, Water- Cooled, Combustion Chamber Section	113
23.	Water-Cooled Nozzle; Side View Showing Coolant Inlet and Outlet Tubes	114
24.	Water-Cooled Nozzle; View From Upstream End, Looking Towards Throat	115
25.	Thermal Response of Uncooled Graphite Nozzle. Li/F ₂ /H ₂ at P _c = 750 psia (5.17 x 10 ⁶ N/m ²), F ₂ /Li MR = 2.25, H ₂ = 35 Percent. Axial Conduction Neglected	116
26.	Thermal Response of Uncooled Copper Nozzle. Li/F ₂ /H ₂ at P _c = 750 psia (5.17 x 10 ⁶ N/m ²), F ₂ /Li MR = 2.25, H ₂ = 35 Percent. Axial Conduction Neglected	117
27.	Schematic Flow Diagram of Liquid Lithium System	118
28.	Photograph of Lithium System on Test Stand, With Engine in Place	119
29.	Schematic Flow Diagram of Fluorine System	120
30.	Schematic Flow Diagram of Hydrogen System	121
31.	Schematic of Basic Instrumentation for the Li/F ₂ /H ₂ Tripropellant Firings	122
32.	Programmed Firing Sequence, Showing Timing of Propellant and Lithium Purge Gas Flows	123
33.	Chamber Configurations Employed With the Oxidizer-Rich Gas Generator Tripropellant Injection Method	124

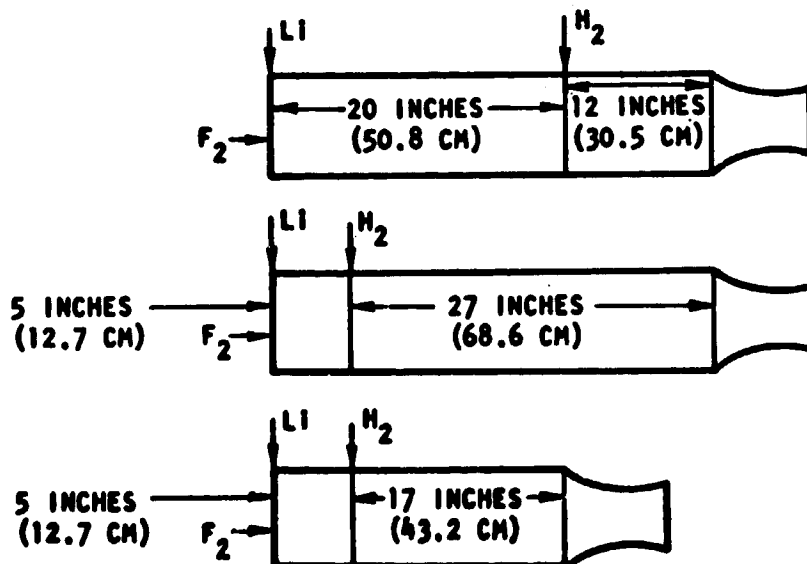
34.	Gas Generator Mounted on Test Stand	125
35.	Schematic of Test Hardware Used for the Task II Firings	126
36.	Typical Posttest Appearance of Convergent Portion of Water-Cooled Nozzle, Showing Deposited Wall Coating	127
37.	Schematic of Test Hardware Used in the Task III Altitude Simulation Firings	128
38.	Photograph of Test Stand, Showing Engine and Diffuser in Place for Altitude Simulation Firing	129
39.	Corrected Characteristic Velocity Efficiency (Based on Chamber Pressure) of $\text{Li}/\text{F}_2/\text{H}_2$ With Oxidizer-Rich Gas Generator Injection Method, as Function of Percent Hydrogen	130
40.	Corrected Characteristic Velocity Efficiency (Based on Chamber Pressure) of $\text{Li}/\text{F}_2/\text{H}_2$ With Oxidizer-Rich Gas Generator Injection Method, as Function of Length of Li/F_2 Combustion Chamber, at Indicated Nominal Test Conditions	131
41.	Corrected Characteristic Velocity Efficiency (Based on Chamber Pressure) of $\text{Li}/\text{F}_2/\text{H}_2$, With Fuel-Rich Gas Generator Injection Method, as Function of F_2/Li Mixture Ratio and Chamber Length at Indicated Percentages of Hydrogen	132
42.	Typical Combustion Chamber Heat Fluxes Obtained in a $\text{Li}/\text{F}_2/\text{H}_2$ Test Firing, Showing Measured Values in Each Step, Estimated Heat Flux From Graphite Chamber Liner, and Net Radial Heat Flux. Faired Lines Used for Illustration	133
43.	Experimental Heat Flux Data for Indicated Pretest Gas Generator Firing	134
44.	Experimental Heat Flux Data for Indicated $\text{Li}/\text{F}_2/\text{H}_2$ Firing	135
45.	Experimental Heat Flux Data for Indicated $\text{Li}/\text{F}_2/\text{H}_2$ Firing	136
46.	Experimental Heat Flux Data for Indicated $\text{Li}/\text{F}_2/\text{H}_2$ Firing	137
47.	Experimental Heat Flux Data for Indicated Posttest Gas Generator Firing	138
48.	Measured Heat Fluxes During $\text{Li}/\text{F}_2/\text{H}_2$ Gas Generator Portions of the Indicated Tripropellant Test Firings	139
49.	Heat Flux Profiles for Pretest Gas Generator Firing and for Step 1 of $\text{Li}/\text{F}_2/\text{H}_2$ Firing, Run No. 69-7	140

50.	Thrust Chamber Heat Flux During Pretest LF_2/GH_2 Firing and Three Steps of $\text{Li}/\text{F}_2/\text{H}_2$ Firing (Run No. 69-7)	141
51.	Combustion Chamber and Nozzle Throat Heat Flux for $\text{Li}/\text{F}_2/\text{H}_2$, as Functions of F_2/Li Mixture Ratio, at Indicated Percentages of Hydrogen	142
52.	Experimental Heat Transfer Coefficients, Pretest LF_2/GH_2 Gas Generator Firing (Run No. 69-7), Compared With Values Calculated From Bartz Simplified Equation	143
53.	Experimental Heat Transfer Coefficients, $\text{Li}/\text{F}_2/\text{H}_2$ Tests at Indicated Percentages of Hydrogen (Run No. 69-7), Compared With Values Calculated From Bartz Simplified Equation	144
54.	Comparison of Thrust Measurements Obtained Directly From Load Cell, $(F_{\text{vac}})_{\text{LC}}$, and by Integration of Nozzle Pressures, $(F_{\text{vac}})_{\text{PN}}$, in the Altitude Simulation Firings	145
55.	Measured, Uncorrected, Vacuum Specific Impulse and Specific Impulse Efficiency Obtained in the $\text{Li}/\text{F}_2/\text{H}_2$ Altitude Simulation Firings, $\epsilon = 60$	146
56.	Comparison of Measured and Theoretical Nozzle Pressures for Typical $\text{Li}/\text{F}_2/\text{H}_2$ Altitude Simulation Test	147
57.	Comparison of Measured and Theoretical Nozzle Pressures for Typical LF_2/GH_2 Gas Generator Portion of Tripropellant Firing	148
58.	Weight Percent of Condensed Material (Liquid LiF) in Combustion Chamber.	149
59.	Weight Percent of Condensed Material in Divergent Nozzle	150
60.	Vacuum Specific Impulse Deliverable by Li (533 K)/ LF_2 (85 K)/ LH_2 (20 K) Engine ($\epsilon = 60$) Cooled Regeneratively With Liquid Hydrogen, Based on Test Data, at Indicated Chamber Pressures and F_2/Li Mixture Ratios, as Function of Percent Hydrogen	151

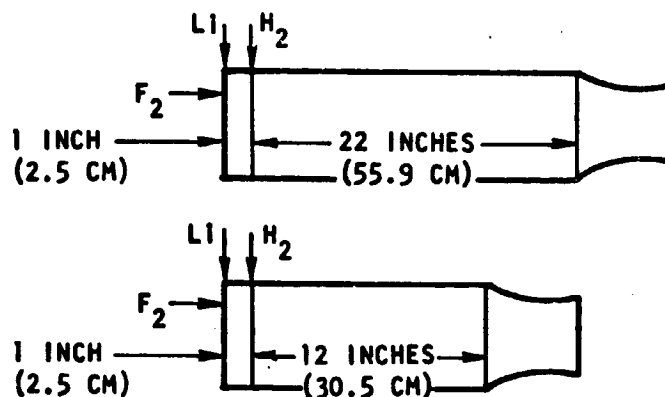
SUMMARY

Realization of the high specific impulse theoretically available from the lithium-fluorine-hydrogen tripropellant combination depends first upon the achievement of complete lithium combustion and second upon the attainment of efficient nozzle expansion of the combustion products. A study of the fundamental feasibility of the $\text{Li}/\text{F}_2/\text{H}_2$ combination was begun in a preceding investigation (NASA CR-72325), in which an injection method designed to optimize lithium combustion conditions was developed. The present program continued and extended the previous work, in the areas of injection method simplification, thrust chamber heat transfer characterization, and specific impulse determination with a 60:1 expansion ratio nozzle at simulated altitude conditions.

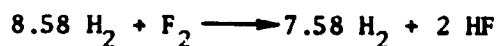
A high degree of lithium atomization is a critical requirement for high c^* efficiency with the $\text{Li}/\text{F}_2/\text{H}_2$ tripropellant combination. Gas-augmented atomization is the most practical and efficient means of obtaining the small lithium droplets which are required. In the original injection concept, vitiated fluorine gas produced in a highly oxidizer-rich LF_2/GH_2 gas generator is used for this purpose. The bulk of the hydrogen is added after completion of the fluorine-lithium reaction. Approximately 100-percent c^* efficiency was obtained in the previous study with this injection method, in the thrust chamber configurations sketched below:



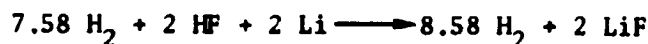
Study of this injection method was continued in the present program, with the hydrogen injector moved to 1 inch (2.54 cm) from the lithium injector. This approximates the injection of all propellants at the same axial location. The following two configurations were employed, both of which gave approximately 98-percent c^* efficiency:



The investigation of Li/F₂/H₂ combustion efficiency was continued in the present program with a study of a simplified injection method which eliminates the disadvantages of the original thrust chamber concept (need for two hydrogen injectors and material problems associated with hot fluorine in the gas generator and extremely high Li/F₂ combustion gas temperature). In the simplified injection method, a fuel-rich gas generator is used in which all of the hydrogen is reacted with the fluorine. At nominal conditions (F₂/Li mixture ratio = 2.74, H₂ = 25 percent), the molar proportions are as follows:



The resulting mixture of HF and H₂ is then injected into the main combustion chamber, where it atomizes and reacts with the liquid lithium:



This procedure also approximates the injection of all three propellants at the same axial location, but under the most adverse conditions, namely, that the fluorine reacts preferentially with the hydrogen and the lithium

then reacts with the resulting HF. This reduces combustion chamber temperature from 9800 R (5440 K) to about 4400 R (2440 K). The injection method using the fuel-rich gas generator also gave approximately 98-percent c^* efficiency, with chamber lengths as low as 7 inches (17.8 cm).

Nominal test parameters in this program were as follows:

1. Chamber Pressure: 750 psia ($5.17 \times 10^6 \text{ N/m}^2$)
2. Thrust: 2000 lbf (8896 N)
3. F_2/Li Mixture Ratio: 2.25 to 3.25 (stoichiometric is 2.74)
4. Hydrogen Proportion: 20 to 35 percent of total propellant flowrate.

Heat transfer characteristics of the $\text{Li}/F_2/H_2$ tripropellant combination were determined. These could be divided into two regimes, one representing the combustion chamber and entrance region of the convergent nozzle and the other representing the remaining expansion section of the nozzle. The two zones were characterized by qualitative differences in the amount of condensed material deposited on the walls. In the combustion chamber and nozzle entrance, the amount of condensate was substantial, while in the rest of the nozzle it was negligibly small. The condensation and deposition processes have two opposing effects on heat transfer in the water-cooled combustion chamber. The first is an enhancement, resulting from the heat of condensation, and the other is a reduction, caused by the insulating effect of the deposited coating. The net effect is a function of firing duration. In the present tests, the enhancement effect was somewhat greater than the insulating effect. Measured heat fluxes in the combustion chamber and upstream portion of the convergent nozzle were higher than the levels predicted by the Bartz simplified equation. At near-nominal test conditions ($P_c = 700 \text{ psia}$, $4.83 \times 10^6 \text{ N/m}^2$; F_2/Li mixture ratio = 2.96; $H_2 = 25$ percent), chamber heat flux was 9.9 B/in.²/sec ($16 \times 10^6 \text{ W/m}^2$), which is about 2.5 times the Bartz prediction; a significant portion of this enhancement, however, is attributable to the high contraction ratio (11.5) employed. In the transonic and supersonic

regions of the nozzle, where condensation effects were minimal, measured heat flux values were somewhat less than the Bartz predictions. At the same test conditions, throat heat flux was $16.7 \text{ B/in.}^2/\text{sec}$ ($27 \times 10^6 \text{ W/m}^2$), or about 2/3 the Bartz value. Measured heat flux levels were inversely proportional to the percentage of hydrogen in the tripropellant combination.

The simulated altitude tests were carried out with a 60:1 expansion ratio conical nozzle, using an exhaust diffuser to obtain full nozzle flow. Measured, uncorrected, specific impulse efficiency at nominal Li/F₂/H₂ test conditions varied from approximately 92 percent at the 20-percent hydrogen level to 95 percent at 25- to 35-percent hydrogen. This corresponds to delivered, uncorrected, vacuum specific impulse of 486, 506, and 510 lbf/lbm/sec (4766, 4962, and 5001 N/kg/sec) at nominal 20-, 25-, and 35-percent hydrogen, respectively, measured with liquid lithium-liquid fluorine-gaseous hydrogen. Conversion of the measured specific impulse efficiencies to values of vacuum specific impulse actually deliverable by a thrust chamber with the geometry tested but cooled regeneratively with liquid hydrogen gave maximum deliverable vacuum specific impulse of approximately 509 lbf/lbm/sec (4991 N/kg/sec) at near-nominal test conditions (25-percent hydrogen). The high expansion efficiency, as well as combustion efficiency, attainable with the Li/F₂/H₂ tripropellant combination has thus been demonstrated.

No lithium system operational problems whatever were encountered in the course of this program.

INTRODUCTION

The performance potential of the lithium-fluorine-hydrogen tripropellant combination is among the highest available from chemical propellants. Typically, theoretical vacuum specific impulse is 540 lbf/lbm/sec (5295 N/kg/sec) at chamber pressure of 750 psia (5.17×10^6 N/m²) and expansion ratio of 60. This is substantially higher than that available from any known bipropellant combination. A comprehensive analytical and experimental investigation to determine whether this theoretical potential can be achieved in a practical thrust chamber was begun in an earlier program (Ref. 1). The present study, which is a continuation and extension of the previous work, constitutes a progression of effort in furthering the technology base of the lithium-fluorine-hydrogen tripropellant system.

The primary purpose of the earlier investigation was to determine the basic feasibility of the Li/F₂/H₂ tripropellant combination; that is, to establish whether the three propellants could be injected and reacted so that thermodynamic equilibrium would be approached in a combustion chamber of reasonable size. Because the gas phase reactions of fluorine with hydrogen, fluorine with lithium, and lithium with hydrogen fluoride are more rapid by several orders of magnitude than the physical process of vaporization, the critical factor in attainment of the desired equilibria is the degree to which the lithium is initially atomized. Hence, particular attention was given to the establishment of criteria for liquid metal atomization and to the development of a thrust chamber concept which would not only produce very small lithium droplets but would also permit the lithium to react under the most favorable conditions. The resulting system gave nearly 100-percent c* efficiency, thus demonstrating the fundamental feasibility of the Li/F₂/H₂ tripropellant combination.

With basic performance and operational feasibilities established in the initial study, the present investigation was directed to the acquisition of technology pertinent to the eventual design of a practical engine configuration. The areas considered of immediate importance were the

simplification of the tripropellant injection technique, the determination of thrust chamber heat transfer characteristics, and the assessment of deliverable specific impulse under simulated altitude conditions. Consequently, this program was divided into the following three tasks:

Task I: Injector Configuration Investigation

Task II: Injector Performance and Heat Flux Determination

Task III: Altitude Performance Tests

TASK I: INJECTION CONFIGURATION INVESTIGATION

To optimize the conditions for complete lithium combustion, the thrust chamber concept developed in the previous study (Ref. 1) consisted of a two-stage combustion system. In the first stage, the lithium-fluorine reaction takes place and in the second, the hydrogen is added and mixed with the Li/F_2 combustion products. The hot, gaseous fluorine required for atomizing and burning the liquid lithium is produced in an oxidizer-rich gas generator in which the liquid fluorine is reacted with a very small fraction of the hydrogen.

Although this system produces essentially complete tripropellant combustion, it has several practical disadvantages. These include material requirements for containment of both the hot, gaseous fluorine in the gas generator and the 9800 R (5440 K) Li/F_2 reaction products in the combustion chamber as well as the need for two hydrogen injectors (one each for the gas generator and the mixing chamber). These disadvantages can be eliminated by use of a fuel-rich gas generator in which all of the hydrogen, instead of just a small fraction of it, is reacted with the fluorine. This yields a mixture of HF and H_2 to atomize and react with the lithium, at the relatively low temperature of about 4400 R (2440 K). This approach also eliminates the need for a separate mixing chamber in which the bulk of the hydrogen is added.

The primary objective of Task I of the present program was to carry out the analyses and designs required for this system simplification and to determine the combustion characteristics of a system using a fuel-rich gas generator by experimental firings. The task was initiated with a continuation of the experimental characterization of the oxidizer-rich gas generator injection concept. This involved determination of the effect on c^* efficiency of decreasing the length of the Li/F_2 combustion chamber to 1 inch (2.54 cm). Use of the short Li/F_2 chamber approximated the injection of all three propellants at the same axial position and thus provided information for effecting the desired injection method simplification.

TASK II: INJECTOR PERFORMANCE AND HEAT FLUX DETERMINATION

Knowledge of the heat transfer characteristics of the $\text{Li}/\text{F}_2/\text{H}_2$ combination is an essential prerequisite for the design of practical tripropellant thrust chambers. The primary objective of this task was to experimentally determine thrust chamber heat flux by conducting a series of test firings employing temperature-instrumented, water-cooled hardware. Design of suitable water-cooled thrust chamber components was an essential portion of the task. The injection method using the fuel-rich gas generator was employed in the Task II firings. A secondary, concomitant objective was the continued confirmation of injector performance by measurement of c^* efficiency.

TASK III: ALTITUDE PERFORMANCE TESTS

High overall engine performance requires both efficient propellant combustion (c^* efficiency) and efficient expansion of the combustion products (C_F efficiency). The primary objective of Task III was to determine the overall performance characteristics of the $\text{Li}/\text{F}_2/\text{H}_2$ tripropellant system under simulated altitude conditions. The large expansion ratio required for these tests was obtained by attaching a 60:1 area ratio nozzle extension to the water-cooled thrust chamber used in the Task II firings. A self-starting exhaust diffuser was joined to the nozzle to permit it to

flow full. In addition to furnishing specific impulse performance data, the altitude simulation firings also provided further c^* efficiency and heat flux data. Measurements of the specific impulse obtained with a full-flowing, 60:1 expansion ratio nozzle permitted reasonable estimates to be made of the vacuum specific impulse actually deliverable by a $\text{Li}/\text{F}_2/\text{H}_2$ engine of the type tested and cooled regeneratively with liquid hydrogen.

All three tasks of the program were successfully completed. In addition to the test data obtained from the experimental $\text{Li}/\text{F}_2/\text{H}_2$ tripropellant firings, this investigation also provided valuable additional experience in the operation of a liquid lithium system for rocket engine testing. Prior to the start of the present program, some modifications were made to the original lithium system on the basis of the experience gained in the previous investigation (Ref. 1). In the present test series, there were no lithium system incidents whatever nor were there any test aborts or failures resulting from malfunction of any lithium system component.

DESIGN OF THRUST CHAMBER COMPONENTS

The designs of the thrust chamber components developed in this program and the analyses on which the designs were based are presented in this section. The components retained from the earlier Li/F₂/H₂ study (oxidizer-rich gas generator, lithium injector, and uncooled, graphite-lined, chamber and nozzle sections) have been previously described in detail (Ref. 1).

The thrust chamber concept incorporating the injection method developed in the previous Li/F₂/H₂ study (Ref. 1) includes an oxidizer-rich gas generator. The simplified concept studied in the present program uses a fuel-rich gas generator. Both are shown schematically in Fig. 1. The significant differences between the two injection schemes are as follows:

1. In the oxidizer-rich gas generator injection method, the F₂/H₂ mixture ratio in the gas generator is about 500 and the product gas, which atomizes and reacts with the liquid lithium, is essentially fluorine at about 1000 R (550 K).
2. In the simplified injection method using the fuel-rich gas generator, the F₂/H₂ mixture ratio in the gas generator is in the range 1.3 to 3.0 and the product is a mixture of HF and H₂ at about 3500 R (1950 K).

Because of these differences, use of the simplified injection method necessitated design of a fuel-rich gas generator (LF₂/GH₂ injector and combustion chamber) and a lithium injector. The other new thrust chamber components in the present investigation included water-cooled chamber and nozzle sections for measurement of heat flux profiles and a 60:1 area ratio nozzle for determination of altitude performance.

FUEL-RICH GAS GENERATOR

Design Requirements

Nominal chamber pressure was 500 psia ($3.45 \times 10^6 \text{ N/m}^2$) in the previous study (Ref. 1) and 750 psia ($5.17 \times 10^6 \text{ N/m}^2$) in the present investigation. Nominal sea level thrust (2000 lbf, 8896 N) remained unchanged. The desired range of test parameters was covered by a nine-point matrix of hydrogen percentage and F_2/Li mixture ratio, as shown in Fig. 2. The design point (F_2/Li mixture ratio = 2.74, H_2 = 25 percent) is indicated at the center of the matrix. A single nominal F_2/Li mixture ratio was used in Task I, while the entire nine-point range was covered in Tasks II and III.

Design requirements for the fuel-rich gas generator were predicated on the use of the same "three-in-one" testing technique employed in the earlier study (Ref. 1), wherein three discrete hydrogen flowrates at nearly constant F_2/Li mixture ratio are programmed during the course of a single firing. Each tripropellant test included approximately 9 to 12 seconds of gas generator operation. However, to provide the capability for longer-duration firings, the gas generator components were designed for approximately 20 seconds of operation.

The required ranges of fluorine and hydrogen flowrates corresponding to the planned variations in percent hydrogen and F_2/Li mixture ratio are shown in Fig. 3. The range of nominal fluorine flowrate is 1.89 to 2.68 lb/sec (0.86 to 1.21 kg/sec) and that of nominal hydrogen flowrate is 0.81 to 1.63 lb/sec (0.37 to 0.74 kg/sec). The corresponding ranges of F_2/H_2 mixture ratio (1.28 to 3.01) and theoretical combustion temperature in the gas generator (2520 to 4630 R, 1400 to 2570 K) are shown in Fig. 4.

LF₂/GH₂ Injector, Mod I

The substantial hydrogen flowrates in the fuel-rich gas generator permitted consideration of injection patterns which are known to give high combustion efficiency with the LF₂/GH₂ combination. These include designs in which the fluorine atomization is accomplished by gas augmentation or by self-impingement. Examples of the former are a triplet element, in which two LF₂ streams impinge within a central, showerhead GH₂ jet, or a gas/liquid unlike-doublet element, in which a single LF₂ stream is directed into a GH₂ jet. The latter is exemplified by a doublet/showerhead element, consisting of a self-impinging LF₂ doublet and two showerhead GH₂ jets enveloping the spray which it produces. Both types have been studied in a number of experimental investigations (e.g., Ref. 2) and requisite design criteria are well established.

Primary requirements for the LF₂/GH₂ injector include adequate fluorine atomization, uniformity of propellant distribution, suitable injection pressure drops, and design simplicity. These requirements are fulfilled by a doublet/showerhead element, which has been found to give approximately 98-percent c* efficiency with LF₂/GH₂ in a comparatively small chamber (L* = 30 inches, 76.2 cm, Ref. 2). Because the characteristic length of the gas generator chamber was about 86 inches (218 cm), fluorine combustion was expected to be essentially complete. An estimate of the degree of fluorine atomization obtained with the doublet/showerhead element sketched in Fig. 5 was made from the following correlation, which was developed from the original Ingebo equation (Ref. 3) on the basis of experimental results (Ref. 4):

$$D_{30} = \frac{25,400}{2.64 (\bar{v}_L/\bar{D}_L)^{1/2} + 0.97 C |\bar{v}_G - \bar{v}_L|} \quad (1)^*$$

*Nomenclature is given in Appendix I.

The factor C corrects for the differences in physical properties between the heptane-air combination and environmental pressure used in the original study (Ref. 3) and the fluorine-hydrogen combustion conditions in the gas generator. Calculated volume mean fluorine droplet size was approximately 80 microns, indicating satisfactory atomization. This design also permitted the use of reasonable hydrogen injection velocity (Mach number ≈ 0.4) and pressure drop (150 psi, 1.03×10^6 N/m²) at the design point; corresponding values for the fluorine were 115 ft/sec (35 m/sec) and 250 psi (1.72×10^6 N/m²). The injection pattern, consisting of 25 such elements within the 5-inch (12.7-cm) chamber diameter, is shown in Fig. 6.

Candidate injector materials were nickel, copper, stainless steel, and aluminum, all of which have been successfully used with liquid fluorine. The selection was based on heat transfer considerations. Gas generator injector face temperatures were calculated as functions of firing duration from the Bartz equation (Ref. 5), assuming the heat transfer coefficients at the injector face to be the same as those at the chamber wall. The injectors were considered to be uncooled metal masses undergoing transient heating. Results for copper and nickel, which are the better materials, are shown in Fig. 7. Both metals reach their maximum usable temperatures in about 14 seconds. Copper was selected as the material of construction because of greater ease of machining and more rapid establishment of prerun chill conditions. No special protection was used for the injector face, because the cooling provided by the flowing propellants would give an ample safety margin even for a 20-second firing.

Fluorine was supplied to the injector through a stainless-steel dome which had passages drilled through it for chilling with liquid nitrogen. The customary procedure of cooling an LF₂ injector by prerun flow of LN₂ through the orifices could not be used in the tripropellant firings because this would also have chilled the lithium injection tubes, which were heated by hot helium as a preconditioning procedure for subsequent lithium injection. Hydrogen was supplied through two inlets brazed to the injector body which fed a ring manifold within it.

LF₂/GH₂ Injector, Mod II

The first use of the Mod I LF₂/GH₂ injector was in a checkout test of the fuel-rich gas generator. In this firing, some burning of the central portion of the injector, behind the face, occurred, probably because of contamination or hydrogen leakage into the fluorine manifold. To avoid delaying the program schedule by the time required to fabricate a duplicate replacement injector, a simplified design was developed (Mod II) which was not only much less complex than Mod I (requiring less than one-third the fabrication time) but which also eliminated the need for a separate fluorine dome.

The Mod II design employed gas-augmented atomization. It incorporated four unlike-doublet elements, each consisting of a showerhead hydrogen jet into which a single liquid fluorine stream was injected (Fig. 8). All four fluorine orifices were fed from a single inlet at the center; each of the four hydrogen orifices was supplied through a separate individual port. This basic injection pattern was used in the lithium injector of the earlier study (Ref. 1). Total fluorine and hydrogen orifice areas were the same as in the Mod I design, so that injection velocities and pressure drops were unchanged.

Estimates of the degree of fluorine atomization and uniformity of propellant distribution were obtained, respectively, by calculating the volume mean diameter of the fluorine droplets after gas/liquid interaction and the extent to which the liquid stream penetrated the gas jet. The following correlations, developed in Ref. 1, were used for this purpose:

$$D_{30} = \phi \left[\frac{136 \mu_L \sigma_L^{3/2} D_L^{1/2}}{\rho_L^{1/2} \rho_G^2 (\Delta V)^4} \right]^{1/3} \quad (2)$$

$$x_p = 2.5 D_L \frac{V_L \cos \theta}{V_G} \left[\frac{\rho_L}{\rho_G} \right]^{1/2} \quad (3)$$

The estimated volume mean droplet size of the fluorine in this design was considerably less than that for the Mod I injector over the entire test matrix, so that the degree of atomization was considered quite adequate. Penetration of the hydrogen jets, shown in Fig. 9, varied as the test matrix was traversed because of the large changes in hydrogen flow-rate. At the midpoint of the matrix, the degree of penetration was about 80 percent; the values at the matrix extremes were approximately 45 and 108 percent. These variations did not affect gas generator combustion efficiency to any substantial extent because the extremely fine degree of fluorine atomization ensured very rapid fluorine vaporization and reaction. The indicated, slight "over-penetration" of the hydrogen jets at the lowest hydrogen flowrates with the higher F_2/Li mixture ratios was more apparent than real, because the calculations did not include an allowance for the normal expansion of the gas jet after injection.

The Mod II LF_2/GH_2 injector was also fabricated from copper. Liquid nitrogen passages cross-drilled through the injector body permitted effective prerun chilling. A photograph of the injector face is shown in Fig. 10. This injector was successfully used for the duration of the experimental program (total firing time approximately 175 seconds).

Combustion Chamber

Because of its strength at high temperatures, compatibility with fluorinated materials, and ease of machining, graphite was the material of choice for the uncooled combustion chamber of the fuel-rich gas generator. Calculations were made of the temperatures at the outer surfaces of graphite cylinders of varying thickness as functions of time, under typical gas generator operating conditions, by the method of Ref. 6. The results, shown in Fig. 11, indicated that a 1-inch (2.54 cm) graphite liner in a stainless-steel shell would be adequate for the present application. A layer of insulating material between the graphite and the steel provided further assurance of nonexcessive steel temperatures.

With the LF_2/GH_2 injector used in the oxidizer-rich gas generator (Ref. 1), which operated at a mixture ratio of 500, only nine 0.0135-inch (0.343-mm) showerhead GH_2 jets were injected into a dense, radially directed, LF_2 spray. This resulted in initially nonuniform combustion gas. Consequently, one or two mixing plates were incorporated into the combustion chamber to improve the uniformity of the product gas at the chamber exit. The injectors designed for the fuel-rich gas generator, however, provided a much greater degree of initial cross-sectional uniformity, so that mechanical mixing was not required.

The gas generator combustion chamber was 10 inches (25.4 cm) long, with an internal diameter of 5 inches (12.7 cm). It consisted of an ATJ graphite liner within a stainless-steel shell. The shell length was extended sufficiently beyond the graphite liner to permit inclusion of the lithium injector (described below) at the chamber exit. A 0.125-inch (3.18-mm) asbestos mat, saturated with epoxy resin, was wrapped around the graphite liner prior to insertion into the shell, to anchor the liner, act as insulator, and absorb radial expansion. Longitudinal expansion was absorbed by a 0.25-inch (0.64-cm) porous carbon washer at the chamber inlet. A photograph of the fuel-rich gas generator combustion chamber, with the graphite liner and carbon washer in place, is shown in Fig. 12.

There was only minor erosion of the graphite liner during each firing and several tests could usually be made with the same one, although, in some cases, small longitudinal cracks were present in the graphite liner following a test. However, after introduction of the Mod II lithium injector (see below), the liner was replaced after each test, along with the lithium injector to which it was integrally bonded.

LITHIUM INJECTOR

Design Requirements

The essential requirements for efficient lithium combustion are high degrees of liquid lithium atomization and uniformity of propellant distribution.

These factors are discussed in detail in Ref. 1 with regard to the Li/F₂ reaction. They are equally valid for the Li/(HF + H₂) reaction which characterizes the fuel-rich gas generator injection concept. It was expected that smaller lithium droplet sizes might be required for Li/(HF + H₂) than for Li/F₂ to achieve comparable combustion efficiency, for two reasons. First, the reaction temperature of Li/(HF + H₂) is 3700 to 5000 R (2050 to 2780 K), depending on the proportion of hydrogen, compared to about 9800 R (5440 K) for the Li/F₂ reaction; this would decrease the lithium vaporization rate. Second, the presence of diluent hydrogen in the Li/(HF + H₂) reaction mixture adversely affects the rate of diffusion of HF to the flame zone around a lithium droplet.

Efficient lithium combustion can be obtained only when the droplets burn by the so-called "small drop" mechanism (Ref. 1), by which the LiF first forms a porous layer around the lithium droplet through which the HF diffuses inwards and the product H₂ diffuses outwards as the reaction proceeds. When the droplet temperature reaches the melting point of LiF (2060 R, 1140 K), the latter melts and the reaction continues by HF diffusion through the thin liquid layer. As the droplet temperature increases and as it is accelerated in the combustion gas stream, the LiF evaporates. Finally, when the droplet temperature reaches the boiling point of lithium (about 4600 R, 2550 K, at combustion chamber pressure), rapid, vaporization rate-controlled combustion begins. This may be considered as the lithium "ignition point".

Heat balance calculations were made for a lithium droplet burning at its surface in a fixed-composition mixture of HF and H₂ prior to lithium vaporization. The results indicated that for any size droplet being heated by the Li/HF reaction, a constant fraction of the droplet mass must be converted to LiF to heat the droplet to a given temperature (such as the lithium boiling point). Hence, the nominal thickness of the LiF layer around a lithium droplet when it reaches the lithium boiling point (excluding any LiF which may have evaporated) is directly proportional to the droplet diameter. Lithium droplet ignition, or initiation of

vaporization rate-limited combustion, in a mixture of HF and H₂ requires about half the LiF layer thickness as in an F₂ atmosphere. Consequently, the required lithium droplet size for the (HF + H₂) reaction was expected to be on the order of half of that for the F₂ reaction. This atomization criterion was used in the lithium injector design.

The volume mean lithium droplet diameters calculated from Eq. 2 for the oxidizer-rich gas generator injection concept were about 10 to 11 microns. Hence, the design objective for the size of the lithium droplets required for the fuel-rich gas generator concept was about 5 to 6 microns.

The degree of distribution uniformity resulting from the interaction of a single liquid stream with a single gas jet is a function of the extent to which the liquid penetrates the jet. Theoretically, the penetration distance should be equal to the jet diameter at the point of intersection. Practically, cold-flow tests have indicated that maximum distribution uniformity is obtained when the penetration distance calculated from Eq. 3 is approximately 80 percent of the gas orifice diameter.

Injector Design

For design purposes, propellant flowrates over the test matrix (Fig. 2) were based on two restraints:

1. Use of an existing nozzle, fabricated in the previous study (Ref. 1), for the Task I experimental firings (throat diameter = 1.475 inch, 3.747 cm).
2. Maximum lithium system pressurization level of 1000 psi (6.89×10^6 N/m²).

Nominal chamber pressure and lithium flowrate variations are shown in Fig. 13, corresponding to the fluorine and hydrogen flowrates in Fig. 3. Design point chamber pressure was 690 psia (4.76×10^6 N/m²); the range over the test matrix was 615 to 765 psia (4.24×10^6 to 5.27×10^6 N/m²).

Lithium flowrate at the design point was 0.86 lb/sec (0.39 kg/sec), with a range of 0.70 to 0.98 lb/sec (0.32 to 0.44 kg/sec).

The desired degrees of lithium atomization and gas jet penetration cannot be simultaneously obtained by use of a simple doublet pattern for the lithium injector, as in the oxidizer-rich gas generator method (Ref. 1), because of the large quantities of gas which must be accommodated in the fuel-rich gas generator design. For this reason, a biplanar injection scheme was employed, wherein a single lithium stream was injected into a single showerhead gas jet, followed by the impingement of four additional gas jets into the reacting central stream downstream of the lithium/gas impingement point. The central gas jet was sized to give the proper lithium droplet volume mean diameter and gas jet penetration, on the conservative assumption that the auxiliary gas jets would not contribute to lithium atomization. Gas injection Mach number was about 0.5 over the entire range of test parameters, volume mean lithium droplet diameter was about 5 to 6 microns, and penetration of the central gas jet by the lithium stream was 76 to 87 percent. These three parameters remain essentially constant over the test matrix, as shown in Fig. 14. This desirable result reflects the self-adjustment of the fluorine and lithium flowrates to changing hydrogen flowrate during a firing at constant F_2/Li mixture ratio.

Lithium Injector, Mod I

The basic lithium injector design consisted of an eight-element pattern in a graphite core, with lithium delivered through stainless-steel tubes from an external manifold. Four outer gas jets were added to the previously used gas/liquid doublet (Ref. 1) to form the injector pattern (Fig. 15 and 16). The injector shell was integral with that of the gas generator chamber, with the lithium injector core positioned against the graphite chamber liner. The advantages of this method of assembly over the use of a completely separate lithium injector unit were the elimination of one sealed interface in the system and substantially lower cost of fabrication.

As in the original lithium injector, liquid lithium was injected through stainless-steel tubes, one to each element, from an external ring manifold. However, instead of welding the tubes to the shell, as before, swaged connectors were used. This allowed the graphite injector core and the lithium inlet tubes to be changed without difficulty.

A schematic of the thrust chamber assembly with the fuel-rich gas generator is shown in Fig. 17.

Lithium Injector, Mod II

The drilled passages for the lithium tubes in the Mod I injector entered the graphite core at the interface between the injector body and the graphite liner of the gas generator chamber. This injector was used in the first three firings employing the fuel-rich gas generator. In each of these tests, there was some local gas leakage between the gas generator chamber liner and the lithium injector core, with the gas then flowing around the lithium tubes into the main combustion chamber. This resulted in minor erosion of the gas generator shell where it contacted the hot gas. To eliminate this leakage, the lithium injector thickness was increased from 1.52 inch (3.86 cm) to 3.00 inch (7.62 cm). This had the effect of moving the lithium tube passages away from the interface between the injector and the graphite liner (Fig. 18). In addition, the method of assembly was improved by first bonding the liner to the injector with epoxy resin, then wrapping the entire unit with asbestos cloth saturated with epoxy resin prior to insertion into the shell.

In firings made with the Mod II injector, erosion of the steel shell around the lithium inlet tubes was completely eliminated, indicating that moving the tube passages away from the liner-injector interface had solved the leakage problem.

Lithium Injector, Mod III

Tests with both the Mod I and Mod II injectors resulted in some erosion of the graphite face around the injection elements, accompanied by the burning away of most of the length of the lithium inlet tube orifices. To reduce this erosion, the distance between the injector face and the point of impingement of the lithium stream with the central gas jet was increased from 0.237 inch (0.60 cm) to 0.562 inch (1.43 cm) by recessing the injector face 0.325 inch (0.83 cm) as indicated in Fig. 18. With this model, localized graphite face erosion around the injection elements was substantially reduced from that experienced with Mod I and Mod II injectors. Correspondingly, less of the orifice tips of the lithium injection tubes was burned away.

Lithium Injector, Mod IV

To determine the effect on combustion efficiency of increasing the size of the lithium droplets, the gas injection area of the lithium injector was doubled, thus decreasing the gas injection Mach number from 0.5 to 0.25. The central gas orifice was sized to retain the same degree of penetration by the liquid stream (~80 percent) as in the preceding injectors. The resulting gas orifice sizes were 0.221 inch (5.61 mm) at the center and 0.323 inch (8.20 mm) for the four outer orifice (Fig. 15). The estimated volume mean lithium droplet diameter resulting from the reduction of gas injection velocity was approximately 15 microns, or about three times that originally obtained.

Lithium Injection Tube Modifications

The lithium injection tube design used in all the firings except the last two was the same as in the earlier study (Ref. 1), except for orifice size. It consisted of a 3/16 by 0.020 inch (4.76 by 0.51 mm) tube to which an orifice tip 0.43 inches (1.09 cm) long with a contoured orifice 0.0625 inch (1.59 mm) in diameter was welded. Both tube and orifice tip

were type 321 stainless steel. Although the recessed face of the Mod III injector resulted in less erosion of the orifice tips than in the non-recessed models, a significant amount of erosion remained. Posttest orifice lengths ranged from 0.0 to 0.3 inch (0.0 to 7.6 mm). This was accompanied by minor erosion of the graphite injector body between the lithium tube orifice and the central gas orifice of each injection element. To investigate possible methods of minimizing the erosion of the lithium injection tube orifice tips, a number of variations of orifice material and length were made in the next-to-last firing (Run No. 69-9). The results are summarized in Table 1. It was found that while stainless steel and nickel orifices were substantially eroded, a tantalum orifice was not visibly affected. Consequently, tantalum orifice tips were used on all eight lithium injection tubes in Run No. 69-10, which was the final test firing. None of these tips was discernibly eroded. The demonstrated durability of tantalum in this application will be of significance in future designs of lithium injectors and combustion chambers.

WATER-COOLED COMBUSTION CHAMBER

Design Requirements

The water-cooled combustion chamber was designed prior to the completion of the Task I test firings which determined the feasibility of the fuel-rich gas generator injection concept. It was therefore not known which injection method would be used for the heat flux determinations. Consequently, a basic design requirement for the water-cooled chamber was compatibility with either the oxidizer- or fuel-rich gas generator injection concept. Other requirements were provisions for measurement of axial and circumferential heat flux profiles and capability for 30 seconds of steady-state firing duration. The design approach taken was to estimate the cooling requirements for each of the injection methods and to specify a segmented chamber, to provide for the various possible heat flux regimes by the use of only two types of chamber segments.

Chamber Heat Flux

Three heat transfer regimes identified with the oxidizer- and fuel-rich gas generator injection methods were defined for the water-cooled chamber. These were:

1. The Li/F₂ combustion chamber associated with the oxidizer-rich gas generator injection scheme.
2. The first 4 inches of the combustion chamber associated with the fuel-rich gas generator injection scheme.
3. The mixing chamber following hydrogen injection in the oxidizer-rich gas generator injection scheme or the main portion of the combustion chamber in the fuel-rich gas generator injection scheme.

Heat transfer coefficients and heat fluxes were estimated for each of these zones. It was found that in any one of the three zones only minor variations in heat flux would be expected over the planned parametric variations in test conditions, because of the mutually compensating effects of changes in mass flowrate, pressure, and temperature. Consequently, each of the zones could be characterized by a single value of expected heat flux.

For Zone 1, in which radiation is the dominant mode of heat transfer, heat flux was calculated in Ref. 1 as approximately 26 B/in.²/sec (42.5 x 10⁶ W/m²); indirect experimental evidence indicated a value of about 29 B/in.²/sec (47.4 x 10⁶ W/m²). For design purposes, maximum Zone 1 heat flux was taken as 40 B/in.²/sec (65.4 x 10⁶ W/m²).

Heat flux levels in Zones 2 and 3 were calculated from both the Bartz (Ref. 5) and Dittus-Boelter (Ref. 7) equations. The Bartz equation, although originally developed for nozzle heat transfer calculations, is extensively employed for estimation of combustion chamber heat flux:

$$h = \frac{0.026}{D_t^{0.2}} \left[\frac{\mu^{0.2} C_p}{Pr^{0.6}} \right] \left[\frac{P_c g_c}{c^*} \right]^{0.8} \left[\frac{D_t}{r_c} \right]^{0.1} \left[\frac{A_t}{A} \right]^{0.9} \sigma_B \quad (4)$$

The Dittus-Boelter equation is the most widely used, steady-state, convective turbulent flow heat transfer correlation:

$$\text{Nu} = 0.023 \text{Re}^{0.8} \text{Pr}^{0.4} \quad (5)$$

Because this equation is applicable only to fully developed momentum and thermal boundary layers, corrections must be applied for heat transfer augmentation in the intake region, where the boundary layers are not fully developed. For Zone 2, which will be located at the chamber entrance, a conservative correction factor of four was used, based on the data of Ref. 8.

For Zone 2, heat flux calculated from the Bartz equation was about 7 B/in.²/sec ($11.4 \times 10^6 \text{ W/m}^2$), while that calculated from the Dittus-Boelter equation was about 9 B/in.²/sec ($14.7 \times 10^6 \text{ W/m}^2$). Allowing a factor of two for the customary uncertainties in these heat transfer estimates and for the minor contribution resulting from radiation, this would permit an additional "safety factor" of about two for the maximum design heat flux of 40 B/in.²/sec ($65.4 \times 10^6 \text{ W/m}^2$) used for Zone 1. A chamber segment designed to accommodate heat flux of this magnitude would therefore be adequate for both Zones 1 and 2.

An approximate measurement of the heat flux in Zone 3 at nominal 500-psia ($3.45 \times 10^6 \text{ N/m}^2$) chamber pressure (Ref. 1) indicated a value of about 2 B/in.²/sec ($3.3 \times 10^6 \text{ W/m}^2$), which is in fairly good agreement with the Bartz and Dittus-Boelter estimates. On this basis, and with the customary allowances, design heat flux for Zone 3 was taken as 10 B/in.²/sec ($16.3 \times 10^6 \text{ W/m}^2$). The safety margins included in the design calculations were considered sufficient to compensate for possible enhancement of heat flux caused by condensation of Li and LiF on the walls of the cooled combustion chamber.

Chamber Design

To calculate the coolant passage sizes and coolant velocity requirements for the water-cooled combustion chamber segments, the Gambill correlation for forced convection subcooled boiling (Ref. 9) was used. This correlation gives burnout heat flux as a function of coolant inlet temperature, velocity, and degree of subcooling:

$$\left[\frac{Q}{A}\right]_{\max} = \frac{\pi}{24} \lambda \rho_V \left[\frac{\sigma_L g g_c (\rho_L - \rho_V)}{(\rho_V)^2} \right]^{1/4} \left[1 + \left(\frac{\rho_L}{\rho_V} \right)^{0.923} \frac{C_L (T_s - T_b)}{25 \lambda} \right] + 0.005 \frac{k_L}{D} (Re)^{0.95} (Pr)^{0.4} (T_w - T_b) \quad (6)$$

Coolant heat of vaporization, liquid and vapor density, and saturation temperature are determined at the static pressure in the flow channel; surface tension is evaluated at the saturation temperature; specific heat, conductivity, viscosity, and Prandtl number are evaluated at the liquid bulk temperature. Wall temperature was assumed to be 30 F (17 K) above saturation temperature. Equation 6 is a superposition in which the first term represents the boiling contribution to burnout heat flux in the absence of forced convection and the second term represents the forced convection contribution in the absence of boiling.

To make the calculations, a computer program was written in which the input variables were coolant passage diameter, coolant velocity, and degree of subcooling; the output was the burnout heat flux, with the boiling and forced convection components separately listed. A series of calculations was made with water as coolant and with parametric variations of passage diameter, velocity, and degree of subcooling. Typical results are shown in Fig. 19, for the case of water at 100 F (311 K) in a 0.125-inch (3.18-mm) passage. Maximum allowable heat flux (i.e., cooling capability) increases significantly (30 to 60 percent) with increasing inlet bulk temperature (70 to 160 F, 294 to 344 K) at constant water velocity and degree of subcooling. This arises primarily because of the increased

forced convection contribution, due to the inverse variation of liquid viscosity with temperature. Consequently, the maximum heat flux which can be accommodated by water may be significantly raised by increasing the inlet bulk temperature over the ranges of temperature (70 to 160 F, 294 to 344 K) and pressure (200 to 1000 psi, 1.38×10^6 to 6.89×10^6 N/m²) considered. The calculations also indicated that coolant velocity is the most significant factor in establishing total heat flux capability while coolant passage dimension is not a major parameter. The subcooled boiling contribution is limited to 3 to 5 B/in.²/sec (4.9×10^6 to 8.2×10^6 W/m²) in the ranges investigated. The convective contribution is of this order of magnitude only at the lowest coolant velocity considered (40 ft/sec, 12.2 m/sec) and is generally substantially greater.

Burnout heat flux levels could be used for estimation of the coolant requirements because of the ample safety margins included in the calculation of design heat flux values. Accommodation to actual heat flux in the test firings was made by suitable adjustments of water velocity through the coolant passages.

Two water-cooled combustion chamber segments were designed: a 4-inch (10.16-cm) section for Zone 1 or 2 and a 9-inch (22.86-cm) section for Zone 3. The 4-inch (10.16-cm), high heat flux section consisted essentially of a copper liner within a stainless-steel shell. The coolant passages, ninety 0.12 by 0.08 inch (3.0 by 1.9 mm) axial slots, were machined around the outer circumference of the liner and filled with wax; a layer of copper was then plated over the outer surface and the filler material was removed. Stainless-steel inlet and outlet rings were brazed to the liner and its machining was then completed. The stainless-steel shell was welded to two manifold rings which provided thermopile ports and water inlet and outlet tubes. Four thermopiles each were located on the inlet and outlet sides. Each pair was placed at a particular point on the chamber circumference relative to the orientation of the lithium injector elements; one at the center of an element, one midway between neighboring elements, and two at intermediate points. Further, each pair of thermopiles was inserted into a single coolant passage, to

permit definition of the circumferential heat flux profile over the segment length. The copper liner was press-fit into the shell, with a stainless-steel filler block between the two to provide structural support in the region which was machined out to permit proper brazing of the liner components. A seal plate was provided for the water manifold O-ring seals. The components of the high heat flux chamber segment are shown in Fig. 20 and the assembled unit is shown in Fig. 21.

The 9-inch (22.86-cm), low heat flux section also consisted of a copper liner within a steel shell. Its design, however, was simpler than that of the high heat flux segment. The cooling passages consisted of 16 axial slots (0.750 by 0.113 inches, 19.1 by 2.9 mm) machined around the periphery of the copper liner. The shell was a 1015-steel spool to which flanges containing the water manifolds and inlet and outlet tubes were welded. The casing was cadmium-plated to prevent rusting. The relatively low heat load allowed the use of mild steel in place of stainless for the shell. The liner was press-fit into the casing, with O-ring seals at each water manifold. A photograph of the liner and shell is shown in Fig. 22.

Although the low heat flux chamber section was fabricated, it was not used in any of the Li/F₂/H₂ tests, because the first firings of Task II showed that heat flux levels in a water-cooled chamber section were significantly higher than the design value of the low heat flux segment. Consequently, only the 4-inch (10.16-cm), high heat flux section was used in the test firings of Tasks II and III.

WATER-COOLED NOZZLE

Configuration

The water-cooled nozzle section configuration was patterned after the un-cooled nozzles used in the previous study (Ref. 1) and in Task I of the present program. The 15-degree conical contour was retained, as well as the 15-degree angle of convergence, 1.475-inch (3.75-cm) throat diameter,

and 4.0-inch (10.16-cm) throat radius of curvature. The exit diameter (2.56 inch 6.47 cm) corresponded to an expansion ratio of three. This expansion ratio was established by the initial area ratio of the uncooled nozzle skirt which was to be attached to the cooled nozzle segment, as discussed below.

Cooling Requirements

Heat flux at the throat was estimated from the Bartz equation (Ref. 5) as about 25 B/in.²/sec (40.9×10^6 W/m²) at the maximum hydrogen flowrate. For design purposes, a value of 35 B/in.²/sec (57.2×10^6 W/m²) was used. The Gambill correlation (Eq. 6) indicated that water velocity of about 140 ft/sec (42.7 m/sec) would be required for forced convection subcooled boiling under these conditions. With gas side wall temperature of 900 F (750 K) and coolant side wall temperature about 30 F (17 K) higher than water saturation temperature, coolant water bulk temperature rise would be about 20 F (11 K).

Design

The basic design of the water-cooled nozzle section consisted of a copper core with circumferential coolant passages machined around its outer surface, over which a layer of nickel was plated. The circumferential coolant passages permitted measurement of axial, but not circumferential, heat flux variations. It was decided to forego the latter because (1) circumferential variations of heat flux in the nozzle are generally small, frequently within the limits of error of the measurements, (2) use of circumferential coolant passages permitted the critical heat flux measurements to be made, which are those at a number of axial points, particularly in the throat region, and (3) substantial design, fabrication, and operational complexities would have been introduced by inclusion of circumferential heat flux measurement capability in the nozzle region.

The copper core of the water-cooled nozzle section had 42 coolant passages (0.155 by 0.074 inch, 3.94 by 1.88 mm) machined around its periphery.

Exterior walls were formed on this matrix by filling the grooves with rigid, non-metallic material, then plating the outside of the unit with nickel to a nominal finished thickness of 0.22 inch (5.6 mm). Following completion of this electroforming process, the filler was removed. Coolant entries and exits were provided by milling two slots into each passage and spotfacing the slots in groups. Water inlet and outlet tubes were welded at the spotfaces. Flanges were provided at each end of the water-cooled nozzle segment for joining it to the water-cooled chamber and to the nozzle skirt. A photograph of the segment is shown in Fig. 23; the entrance flange and interior contour are shown in Fig. 24.

NOZZLE SKIRT

The uncooled nozzle skirt, extending to area ratio 60, was designed for attachment to the water-cooled nozzle section. The design required determination of the initial area ratio (i.e., the exit area ratio of the water-cooled segment) and of the contour.

Determination of Initial Expansion Ratio

The initial expansion ratio depended upon the wall material and the test conditions. The thermal response of the inner surface of an uncooled nozzle was estimated for copper and graphite by use of standard transient temperature charts (Ref. 10), with heat transfer coefficients calculated from the Bartz equation (Ref. 5). Test conditions were those at maximum heat flux ($P_c = 750$ psia, 5.17×10^6 N/m², $H_2 = 35$ percent); variables were wall thickness and firing duration. Two models were assumed for these calculations: a flat plate and a cylindrical shell. The former is the more conservative (i.e., it predicts higher wall temperatures for a given set of test conditions). Results of these estimates are summarized in Fig. 25 (graphite) and Fig. 26 (copper), which show inner surface temperatures as functions of nozzle expansion ratio, at various combinations of firing time and wall thickness. Typical differences between the flat plate and cylindrical shell models are also illustrated.

For design purposes, the test duration for the uncooled nozzle skirt was taken as that of the altitude simulation firings (6 seconds). Assuming maximum operating temperatures of graphite and copper to be 3200 F (2030 K) and 1500 F (1100 K), respectively, it is apparent from Fig. 25 and Fig. 26 that copper imposes a slightly lower limit on firing time than graphite. On the basis of these calculations, an initial expansion ratio of three was selected for the nozzle skirt.

Determination of Nozzle Contour

An optimized nozzle contour for two-phase flow is one in which the thrust coefficient is maximized on the basis of nozzle aerodynamics, chemical kinetics, condensation and agglomeration rates, and drag losses, including the effects of wall friction and of particle thermal and velocity lags. At present, it is not possible to design directly an optimum nozzle contour by simultaneous inclusion of all these factors in the analysis, together with appropriate coupling effects. A number of approximate treatments have been described (for example, Ref. 11 through 16). These are not only idealized, but necessarily introduce additional uncertainties by requiring estimates to be made of imperfectly known fundamental input data (particle sizes or size distributions, particle drag and heat transfer coefficients, chemical reaction rates, etc.). Typical results of calculations made by these methods indicate that impulse losses resulting from particle lag increase with particle diameter, that particles of less than about 2 microns diameter generally follow gas velocity and temperature quite closely, that most of the nonrecoverable losses associated with two-phase flow are incurred in the high-acceleration transonic region, and that the difference between the particle lag losses in a conventional nozzle and in an optimized contour is small (Ref. 17 and 18). Hence, contouring a nozzle to improve gas-particle flow performance can result in only very modest gains, so that design and fabrication of a complex contour are usually not warranted.

A nozzle contour optimized for two-phase flow would be unique to a specific application, because the optimization is critically dependent upon the

weight fraction and size distribution of the particles in the mixture as well as on the gas properties. Moreover, none of the available analyses accounts for interphase mass transfer during the expansion process. This assumption of no interphase mass transfer would be valid if there were no significant increase in particle weight fraction between the chamber and the nozzle exit, or, to a lesser extent, if all the condensation occurred well downstream of the sonic region and the particle sizes were small. For the Li/F₂/H₂ tripropellant combination, the weight percent of condensed material in the combustion products varies widely with percent hydrogen and F₂/Li mixture ratio over the test matrix (Ref. 1). In addition, most of the condensation occurs in the nozzle, accompanied by solidification of liquid LiF at high percentages of hydrogen and by the appearance of unreacted liquid lithium at F₂/Li mixture ratios below stoichiometric. Because of these variations in the two-phase flow conditions, and particularly because of the variations in the weight percent of condensed material at the throat (which changes from 0 to about 50-percent over the test matrix), a nozzle contour optimized for mid-matrix flow conditions would exhibit significant departures from optimum at the matrix extremes.

Under these conditions, and with present knowledge of the expansion characteristics of the Li/F₂/H₂ combustion products, a simple conical nozzle, for which the aerodynamic properties are well known and which does not require elaborate design and fabrication, was the contour of choice. Another consideration favoring this selection was the fact that a 15-degree cone had been used for the initial expansion section immediately downstream of the nozzle throat in the preceding study (Ref. 1) and in Task I of the present program. The high values of both c^* and I_s obtained with these conical low-area ratio nozzles, even at the highest particle-loading conditions, indicated that for this propellant combination the losses caused by particle velocity and thermal lags are probably quite small. For these reasons, a 15-degree conical contour was used.

The nozzle skirt was divided into two sections at area ratio 10, primarily to permit redundant nozzle pressure measurements to be made in the sea-level firings which would increase the reliability of the thrust data in

the altitude simulation tests. The section from area ratio 3 to area ratio 10 was attached to the water-cooled nozzle in the Task II sea-level tests to determine the thrust contribution of this nozzle segment. This permitted normalization of the corresponding data in the altitude simulation tests (Appendix C).

Thermal Analysis

The nozzle skirt consisted of a thick-walled copper section extending from area ratio 3 to area ratio 10 and a mild-steel section from area ratio 10 to area ratio 60.

A two-dimensional thermal analysis was carried out on the nozzle skirt, using a boundary layer solution for estimating local heat transfer coefficients. The heat transfer coefficients provided by this solution were then programmed into a 244-node thermal network for computer solution. Ten regions were developed to simulate the actual assembly of nozzle sections, junctions, and flanges. With good contact of mating surfaces, the maximum gas side wall temperature after 6 seconds of operation at 750 psia ($5.17 \times 10^6 \text{ N/m}^2$) chamber pressure was estimated as 1220 F (930 K). This maximum would occur at the steel flange slightly downstream of the area ratio 10 attach point. Maximum gas side temperature on the copper wall section would be about 1080 F (850 K) at a point slightly downstream of the junction at area ratio 3. If there were poor contact between the water-cooled nozzle segment and the uncooled copper section, the location of the maximum wall temperature would shift to this junction and would reach about 1230 F (940 K). Maximum back side wall temperature after a 6-second firing at 750 psia ($5.17 \times 10^6 \text{ N/m}^2$) chamber pressure would be approximately 140 F (330 K) and 720 F (650 K) on the copper and steel nozzle sections, respectively. With wall temperatures of 1000 F (810 K), calculated heat flux values at area ratios of 3, 10, and 60 were approximately 7, 2, and 0.3 B/in.²/sec (11.4×10^6 , 3.3×10^6 , and $0.5 \times 10^6 \text{ W/m}^2$), respectively.

These data indicated that the uncooled copper skirt would be satisfactory for attachment to the water-cooled nozzle in the sea-level firings as well as in the altitude simulation tests.

Fabrication

The nozzle skirt segment from area ratio 3 to area ratio 10 was machined from an OFHC copper billet. The segment from area ratio 10 to area ratio 60 was made from a 0.37-inch (9.4-mm) 1020-steel sheet, which was rolled, welded, and machined to size. An entrance flange was provided for joining to the copper skirt segment. The exit flange was welded to the nozzle body at about area ratio 35 instead of at the nozzle exit, primarily because of the off-the-shelf availability of the proper size stainless-steel bellows which joined the nozzle to the diffuser.

EXPERIMENTAL FACILITIES AND PROCEDURES

The experimental firings of this program were carried out in the Propulsion Research Area of the Santa Susana Field Laboratory, on the test stand used in the previous study (Ref. 1).

PROPELLANT SYSTEMS

Lithium

The liquid lithium facility designed, installed, and operated in the earlier program (Ref. 1) was modified prior to the start of the present test series to simplify its operation and to eliminate several minor problems. The major components of the modified system, which is shown schematically in Fig. 27, are described below.

Tank. The original lithium tank was a 48-inch (122-cm) length of 6-inch (15.2-cm), schedule 80, 304 stainless-steel pipe with welded, ring-sealed, flanged ends, mounted on a portable skid. This was replaced by a tank consisting of a 72-inch (183-cm) length of the same pipe, with a flanged end at the top and a hemispherical cap at the bottom. The tank, ASME coded for 1300 psi at 600 F (8.95×10^6 N/m² at 590 K), was mounted vertically on permanent supports anchored to the test pit roof. The increased tank capacity permitted a larger number of firings to be made between fillings.

Valves. The type of lithium main valve* previously used (Ref. 1) was retained. This was a special, 1-inch (2.54-cm), bellows-sealed, stainless-steel globe valve with integral valve seat, rated at 1000 psi at 500 F (6.89×10^6 N/m² at 530 K). Other system valves were conventional Annin globe valves.

Flow Line. The length of the 1-inch (2.54-cm) delivery line (schedule 10, welded joint, 304 stainless-steel pipe) between the lithium tank

*Manufactured by Wm. Powell Co., Cincinnati, Ohio 45214

and the main valve was decreased from about 18 feet (5.49 m) in the earlier system to about 6 feet (1.83 m). The in-line, stainless-steel, screen filter (0.018-inch, 0.46-mm, mesh) previously used was retained in the flow line downstream of the purge line connection point.

Burst Diaphragm. A stainless-steel burst diaphragm, rated at 300 psi at 600 F (2.07×10^6 N/m² at 590 K) and replaceable after each firing, was installed downstream of the main valve. This allowed the valve to be exercised and checked immediately before each test, prior to tank pressurization. In the event of valve leakage, the diaphragm would also have prevented inadvertent entrainment and potential solidification of liquid lithium during pretest flow of helium purge gas.

Flowmeter. The magnetic flowmeter (MSA Model FM-4) previously used was retained. It consists essentially of a 1-inch (2.54-cm), schedule 10, 304 stainless-steel pipe mounted within a permanent, 890-gauss magnet. Flow of lithium through the line generates a d-c voltage whose magnitude is directly proportional to the flowrate.

Purge Gas System. The helium purge gas heater consisted of a 48-inch (122-cm) length of 2-inch (5.08-cm), schedule 40, stainless-steel pipe filled with 0.25-inch-diameter (6.35-mm) steel balls. When initially heated to 800 F (700 K), it supplied helium at 500 F (530 K) minimum for at least 20 seconds at nominal flowrates. A turbine flowmeter between the heater and the purge gas valve was used as a flow indicator. Two stainless-steel ball check valves with Inconel tension springs were positioned between the purge gas heater and the lithium delivery line.

Helium Purification System. To avoid introduction of significant amounts of impurities (such as water, air, or particulate matter) into the lithium system with the pressurant gas, a dryer (artificial Zeolite molecular sieve), a de-oxygenator (copper turnings at 500 F, 530 K) and a 10-micron filter were included in the helium supply line.

Heating System. The lithium system was heated by external electrical resistance heaters. Radiant-type heaters were used for the tank (Lindberg "Hevi-Duty," Model 40731) and for the purge gas heater (Lindberg Model 50352). The lithium flow lines and the purge gas line were heated by tubular heaters (Calrod Model 5D12G2). The main valve was placed in a container filled with copper shot in which cartridge heaters (Calrod Model 7C846A101) were imbedded.

For control purposes, the heater electrical supply was divided into three 110-volt and three 220-volt sources, the former for the tank heaters and the latter for the rest of the system. The power from each source was independently varied by means of manually controlled transformers. Automatic temperature controls were used for the magnetic flowmeter (Foxboro "Rotax" controller) and the lithium main valve (Wheelco Controller).

The lithium tank and the purge gas heater were insulated with 1 inch (2.54 cm) of high-temperature insulation (Technit "Thermoshield") covered by 1 inch (2.54 cm) of fiberglass. The lithium and purge gas flow lines were insulated with 2 inches (5.08 cm) of fiberglass. All insulation was over-wrapped with heavy aluminum foil. A photograph of the lithium system is shown in Fig. 28.

Lithium Tank Loading and System Heating. Lithium was purchased in the form of 2.7-pound (1.22-kg) cylindrical ingots packed in individual cans in an inert atmosphere. The cans were opened and the tank was loaded under an argon blanket. A small amount of metallic sodium (0.5 percent) was added with the lithium to ensure line wetting, which is essential for proper operation of the magnetic flowmeter.

System heating (lithium tank and lines to ~550 F, 560 K, purge gas heater to ~800 F, 700 K) required about 3 hours, starting at ambient temperature.

Fluorine

A schematic diagram of the fluorine system, which was rated at 3000 psi (2.07×10^7 N/m²), is shown in Fig. 29. Fluorine gas, supplied from a

bank of eight, 330-pound (150-kg) capacity, high-pressure cylinders was liquified in an LN₂-jacketed condenser and stored in a jacketed, 15-gallon ($5.68 \times 10^{-2} \text{ m}^3$) run tank. The piping arrangement was such that the line to the main fluorine valve was filled before fluorine flow to the tank began, to eliminate gas pockets in the line. The delivery line between the tank and injector (including valves and flowmeters) was also LN₂-jacketed.

Hydrogen

Gaseous hydrogen was supplied to the test stand from a 450-pound (204-kg) capacity, 3000-psi ($2.07 \times 10^7 \text{ N/m}^2$) reservoir through a delivery system incorporating appropriate regulators, valves, filters, and gages. The test stand hydrogen system, shown schematically in Fig. 30, consisted of two branches. One branch (shown on right side of figure) was used only in the first two tripropellant firings, to supply the oxidizer-rich gas generator employed with the original injection scheme (Ref. 1). The main branch was used in all the firings. It included three venturi meters and valves in parallel. By successive operation of these valves at a given upstream pressure setting, several discrete hydrogen flowrates could be programmed during the course of a single firing. This capability for making multipoint tests was of substantial value in the experimental program.

INSTRUMENTATION AND DATA RECORDING

The basic test instrumentation used in both the sea-level and altitude simulation firings is shown schematically in Fig. 31, which illustrates the simplified injection method employing the fuel-rich gas generator. Additionally, in the first two Li/F₂/H₂ firings, which used the oxidizer-rich gas generator, the branch hydrogen line (Fig. 30) included pressure and temperature measurements at the sonic venturi, as in the main hydrogen line. The instrumentation required for the heat flux measurements and for the determination of nozzle pressure profiles in the altitude simulation

tests, which is not shown in Fig. 31, is discussed below. Conventional instrumentation was used in the auxiliary systems (purge, pressurization, and cooling).

Thrust

The thrust chamber mount was supported on flexures which allowed free movement parallel to the engine axis, restrained in the thrust direction by a Baldwin-Lima-Hamilton double-bridge load cell (Model U-283). To avoid nonaxial thrust vectors, the chamber was supported by a flexible steel cable near its center of gravity. Tension in the cable was adjusted to eliminate cantilever action on the load cell.

Pressure

Pressure measurements were made with bonded strain gage transducers. For pressures above atmospheric, Taber "Teledyne" Series 206 were used; for those below atmospheric, Data Sensor Type 015-A were employed. Chamber pressures were determined both in the gas generator and in the main combustor. At each axial location, three or four circumferential pressure taps were manifolded together, and the manifold pressure was measured. The other pressure measurements shown in Fig. 31 were made with close-coupled transducers at each location. Pressures in the nozzle skirt were measured with close-coupled transducers at area ratios 3.7, 5.2, 7.0, 9.0, 11.4, 15.0, 20.0, 30.0, 40.0, 50.0, and 58.5.

Flowrate

Hydrogen. Hydrogen flowrates were measured with sonic venturi meters (Flow-Dyne Model Series V-16).

Fluorine. Two turbine flowmeters in series (Fischer-Porter Model RF-1-50) were used to measure volumetric fluorine flowrates.

Lithium. An MSA magnetic flowmeter was used to measure lithium flow-rates, as described previously in the discussion of the lithium propellant system.

Temperature

Fluorine. Liquid fluorine temperature was measured with two, shielded, platinum resistance bulbs (Rosemount Model 176) immersed in the liquid stream, one upstream of the first flowmeter and the other downstream of the second.

Hydrogen. Temperatures in the venturi plena were measured with iron-constantan thermocouples.

Lithium. Temperatures at various points of the lithium system were monitored by means of externally welded thermocouples. In addition, a sheathed chromel/alumel thermocouple was immersed in the liquid lithium immediately upstream of the injection manifold to measure lithium injection temperatures.

Heat Flux Measurement Instrumentation

Water-Cooled Thrust Chamber Components. The calorimetric heat flux determinations in the water-cooled combustion chamber and nozzle segments (Appendix D) required measurements of water flowrates and temperatures. Flowrates were measured with turbine flowmeters. Temperatures were measured with specially made thermopiles in the combustion chamber and with conventional differential thermocouples in the nozzle. The thermopiles were used in the combustion chamber because inlet and outlet water temperatures were measured separately in four of the small coolant passages, in each of which the water flowrate and the temperature rise were fairly small. The thermopile consisted of four chromel-alumel elements (5-mil wire) embedded in epoxy resin within an Inconel sheath. In the nozzle segment, water temperature differentials across each passage were much larger, so that single-element thermocouples could be used.

Copper Nozzle Section. Heat flux in the copper nozzle segment (extending from area ratio 3 to area ratio 10) was measured by means of specially designed and fabricated transducers. Details of their design and calibration are given in Appendix D.

Steel Nozzle Skirt. Temperatures along the outer wall of the steel nozzle segment (extending from area ratio 10 to area ratio 60) were measured with iron/constantan thermocouples welded along its length.

Data Recording

Pressure, temperature, and flow measurements were recorded on tape during each firing by means of a Beckman Model 210 Data Acquisition and Recording System. This system acquires analog data from the transducers, which it converts to digital form in binary-coded decimal format. The latter are recorded on tape for computer processing.

The Beckman Data Acquisition Unit sequentially samples the input channels at a rate of 5625 samples per second. Programmed computer output consists of tables of time versus parameter values (in engineering units), printed out as either the instantaneous values at approximately 10-millisecond intervals during the firing or as average values over prespecified time slices, together with calibration factors, prerun and postrun zero readings, and related data. The same computed results are also machine plotted and displayed as CRT outputs on appropriately scaled and labeled grids.

Primary data recording for these firings was on the Beckman 210 system. In addition, the following auxiliary recording systems were employed:

1. An 8-channel Brush Mark 200 recorder was used in conjunction with the Beckman unit to establish time intervals for data reduction and quick-look information at the most important parameters.

2. A CEC, 36-channel, direct-reading oscillograph was used as backup for the Beckman 210 system, as indicator of possible oscillatory combustion, and for precise recording of firing-event timing.
3. Direct-inking graphic recorders were used to set prerun propellant supply pressures, for monitoring fluorine system chill-down and lithium system heating, to provide quick-look information, and as secondary backup to the Beckman and oscillograph systems.

CALIBRATION PROCEDURES

Transducer calibrations were used not only to obtain appropriate factors for test data reduction, but also to develop statistical histories of each transducer so that estimates of short- and long-term deviations could be made and probable error bands calculated (Appendix B). The calibration methods used for the various types of transducers are described below.

Thrust

The thrust-measuring load cell was calibrated in-place. A permanently mounted, manually operated, hydraulic force cell was used to deflect the load cell exactly as did the engine, through a yoke-tension rod system. Known loads were applied to the force cell through a Morehouse compression-type, temperature-compensated, proving ring calibrated by the National Bureau of Standards.

In measuring rocket engine static thrust, care must be taken to apply properly the input-output factors determined under calibration conditions to the load cell readings obtained during test firings. Seemingly minor differences, such as in the temperatures and pressurization levels of the propellant inlet lines or in diffuser pressures (in altitude simulation firings), may have significant effects on measured thrust. Consequently, the thrust calibration and measurement procedures used in this program are described in detail in Appendix C.

Pressure

Pressure transducers were calibrated end-to-end by mounting them on stand manifolds in which pressures were read with high-precision Heise Bourdon-tube gages. The latter were calibrated periodically on Ruska dead-weight testers with weights traceable to NBS standards.

Flowrate

Fluorine. Calibrations of the turbine flowmeters to obtain volume flowrates as functions of rotational speeds were made with water. Transfer of the cycles-per-gallon factors to liquid fluorine usage requires application of corrections to allow for the differences in temperature and viscosity between water and LF_2 . The temperature correction (70 to -310 F, 295 to 83 K), which is a function of meter material and not of meter size, has been estimated as 1.005 (Ref. 19) and 1.009 (Ref. 20); average 1.007. The viscosity correction, which is a boundary layer phenomenon and therefore depends on flowmeter size, was estimated as 0.992 (1 inch, 2.54 cm, Ref. 19), so that the net correction applicable to the water calibration factors was 1.007×0.992 , or 0.999. This was within the readability limits of meter output and was therefore considered negligible. Hence, volumetric flow factors determined with ambient-temperature water were used for liquid fluorine without correction.

Hydrogen. The sonic venturi meters were calibrated with hydrogen by the manufacturer.* Mass flowrate was determined from the following equation:

$$w_{GH_2} = K \sqrt{\frac{P}{T}} \quad (7)$$

The calibrations established curves which gave values of K as functions of hydrogen pressure and temperature at the venturi inlet. The flow coefficient curves were calculated from the standard ASME equations (Ref. 21).

*Flow-Dyne Engineering, Inc., 3701 W. Vickery St., Fort Worth, Texas 76107

Lithium. The magnetic flowmeter was calibrated for lithium by the manufacturer* to establish the variation of the flowrate factor (gpm/mv output) with temperature. A Leeds & Northrup Type K potentiometer was used to calibrate the amplification-recording circuits.

Temperature

Resistance Thermometers. Resistance of the platinum thermometers used in the LF_2 line was converted to millivolt output by a triple-bridge system. This was calibrated by substituting a decade resistance box for the sensor, and setting it at various resistances corresponding to a temperature-resistance calibration supplied by the manufacturer** for each instrument. These precision platinum resistance sensors have no significant calibration drift. They were checked upon receipt by immersion in liquid nitrogen and liquid oxygen; temperature readings were correct within the limits of readability.

Thermocouples and Thermopiles. Thermocouples and thermopiles were used on the basis of standard NBS millivolt/temperature tables.

TEST PROCEDURES

Immediately before each firing, the lithium main valve was cycled, the system downstream of the fluorine main valve was passivated, and prerun transducer zero readings were obtained. In tests employing water-cooled thrust chamber components, both prerun and postrun zeros were obtained with water flowing at test level flowrates.

Test sequencing was controlled by automatic electronic timers. Typical programming for the first few tests using the fuel-rich gas generator injection scheme is indicated in Fig. 32. The purpose of the preliminary

*MSA Research Corp., Evans City, Pennsylvania

**Rosemount Engineering Co., 4900 West 78th Street, Minneapolis 24, Minnesota

flow of hot helium purge gas was to displace the air in the lithium system downstream of the burst diaphragm (Fig. 27) and to heat the lithium injection tubes. Duration of this purge gas flow was increased from the 5 seconds shown in Fig. 32 to 18 seconds in later firings because the shorter duration flow did not always heat all the tubes sufficiently. Gas generator operation (with one hydrogen valve open) was begun 3 seconds before the start of lithium flow. Lithium flow duration was 5.1 to 6.0 seconds. During this time, the other two hydrogen valves were successively opened, to give three discrete hydrogen flowrates during the lithium flow, each 1.7 to 2.0 seconds in duration. Gas generator operation was continued for 1.0 to 2.0 seconds after cessation of lithium flow, to react with lithium remaining in the delivery line and brought in by the helium purge. A relay system over-ride ensured that the lithium purge gas valve did not close until the lithium main valve was fully open, and that it opened as soon as the lithium main valve began to close.

EXPERIMENTAL FIRINGS

INTRODUCTION

For descriptive purposes, the experimental firings carried out in this investigation are divided into three series, corresponding to the three tasks into which the program was divided. The types and numbers of tests conducted in each of these tasks were as follows:

TASK I: Injection Configuration Investigation

1. Tripropellant firings using the oxidizer-rich gas generator injection method.
 - a. Preliminary tests to check functioning of fluorine/hydrogen and lithium systems (four gas generator firings).
 - b. Tests using original thrust chamber, with hydrogen injection at 1 inch (2.54 cm) downstream of lithium injector (two Li/F₂/H₂ firings).
2. Tripropellant firings using the fuel-rich gas generator injection method.
 - a. Tests of fuel-rich gas generator (four gas generator firings).
 - b. Tests using fuel-rich gas generator and new lithium injector in combination with the original tripropellant combustion chamber and nozzle (six Li/F₂/H₂ firings).

TASK II: Injector Performance and Heat Flux Determination

1. Tests using fuel-rich gas generator injection method, with water-cooled thrust chamber components (three Li/F₂/H₂ firings).

TASK III: Altitude Performance Tests

1. Tests with 60:1 area ratio nozzle (four Li/F₂/H₂ firings).

Details of the individual test firings are given below.

TASK I FIRINGS USING OXIDIZER-RICH GAS GENERATOR

Preliminary Tests

The experimental portion of the present program was begun with two series of preliminary tests. These were carried out to check the functioning of the fluorine/hydrogen and lithium systems prior to initiation of the tripropellant firings. The fluorine and hydrogen systems were tested by means of a series of firings of the original, oxidizer-rich, gas generator, and the lithium system by a series of flow tests to atmosphere.

Gas Generator Tests. The fluorine and hydrogen injectors and the 10-inch (25.4-cm), two-segment, gas generator used in the previous lithium-fluorine-hydrogen study (Ref. 1) were employed for these tests. In both chamber segments, nickel liners and mixing plates had been installed near the close of the earlier program (replacing the original graphite).

Target parameters for the gas generator tests were those corresponding to tripropellant firings at nominal 500 psia ($3.45 \times 10^6 \text{ N/m}^2$) chamber pressure. These conditions were achieved by use of an exit plate containing seven orifices ($D = 0.213 \text{ inch, } 5.41 \text{ mm}$) at the outlet of the gas generator chamber.

Four firings were carried out. Test data are summarized in Table 2. Essentially complete combustion was obtained in the gas generator, as in the previous study (Ref. 1). No significant problems were encountered in these tests, and the fluorine and hydrogen systems were considered satisfactory for subsequent tripropellant firings.

Liquid Lithium Flow Tests. Following completion of the lithium system modifications, a series of flow tests was conducted to check operating procedures and the functional suitability of the various system components. For these tests, lithium flow was directed to atmosphere, with heat-up procedures, tank pressurization levels, and flowrates the same as those planned for the tripropellant firings.

System heat-up was smooth, and functioning of the lithium main valve was consistent and rapid (30-millisecond opening and closing times). Three flows were made, with tank pressures of 800 to 850 psi (5.52×10^6 to 5.86×10^6 N/m²), lithium flowrates of 0.8 to 0.9 lb/sec (0.36 to 0.41 kg/sec), and durations of 1 to 3 seconds. No operational problems were encountered. These tests showed the lithium system to be functioning satisfactorily.

Tripropellant Tests

The original oxidizer-rich gas generator, lithium injector, and graphite-lined chamber sections and nozzle ($\epsilon = 2$) were employed in this series of firings, to conclude the previous investigation of the effect on c^* efficiency of variations in chamber length and in point of hydrogen addition. In the earlier Li/F₂/H₂ experimental firings (Ref. 1), the hydrogen was injected first at 20 inches (50.8 cm), then at 5 inches (12.7 cm) downstream of the lithium injector, in an overall chamber length of 32 inches (81.3 cm). While retaining the 5 inch (12.7 cm) F₂/Li combustion chamber length, the mixing length was then reduced to 17 inches (43.2 cm). These variations are shown in Fig. 33. In the present program, the hydrogen injection station was moved to 1 inch (2.54 cm) from the lithium injector, with mixing chamber lengths downstream of the hydrogen injector of 12 and 22 inches (30.5 and 55.9 cm, Fig. 33). Positioning of the hydrogen injector at only 1 inch (2.54 cm) from the F₂/Li injector essentially simulates injection of the three propellants at the same axial station. The hydrogen and lithium injectors were separated by a 1-inch (2.54-cm) spacer to avoid disruption of the lithium atomization

process by the radial hydrogen jets. Note that the "fluorine" injected into the F_2/Li chamber is actually the gas generator product obtained by reacting liquid fluorine with a very small amount of hydrogen at nominal mixture ratio of 500.

In each of the tripropellant firings carried out in the present study, as in those of the previous investigation, three test conditions were targeted by sequencing three discrete hydrogen flowrates during the test.

Run No. 68-2. This was the first tripropellant test of the present program. The gas generator and lithium injector were assembled as described in Ref. 1. A 1-inch (2.54-cm), graphite-lined, copper spacer was placed between the lithium and hydrogen injectors, and a 10-inch (25.4-cm) chamber was used downstream of the 2-inch (5.08-cm) hydrogen injector, giving a total mixing chamber length of 12 inches (30.5-cm). The firing proceeded through the sequenced functions as programmed.

Run No. 68-3. Test hardware for this firing was the same as that used in Run No. 68-2, except that the mixing chamber length was increased from 12 inches (30.5 cm) to 22 inches (55.9 cm), Fig. 33. Run No. 68-3 also proceeded as sequenced.

Following the test, the orifice tips of two of the lithium delivery tubes were found to be eroded away and the graphite core of the injector was cracked in the region of these tubes. This was apparently the result of fluorine/lithium reaction at or within the core, which also resulted in some burning of the gas generator exit flange and the lithium and hydrogen injector shells. The loss of the tube orifices was indicated by a sudden increase in lithium flowrate near the end of Step No. 2 of the firing.

TASK I FIRINGS USING FUEL-RICH GAS GENERATOR

Tests of Fuel-Rich Gas Generator

Prior to the use of the fuel-rich gas generator in the tripropellant firings, a series of tests was carried out to determine its combustion and operating

characteristics. For these tests, the lithium injector, which is located at the exit of the gas generator chamber (Fig. 17), was replaced by a graphite block into which four orifices ($D = 0.594$ inch, 1.51 cm) were drilled to permit attainment of desired chamber pressures. A stainless-steel retainer plate was attached to the chamber exit flange. The unlike-doublet LF_2/GH_2 injector (Mod II, Fig. 8) was used in the gas generator tests, as well as in all the subsequent tripropellant firings. The assembled and mounted gas generator is shown in Fig. 34.

The fuel-rich gas generator test series consisted of four firings. In the first three, single hydrogen flowrates were used, representing the extremes and the center point of hydrogen flow in the proposed tripropellant test matrix (Fig. 2). In the fourth test, three discrete hydrogen flowrates were programmed, as in a typical $Li/F_2/H_2$ firing. No operational difficulties were encountered in these tests and the gas generator functioned as planned. The copper LF_2/GH_2 injector exhibited no discernible erosion at the conclusion of the firings. Test data are summarized in Table 3.

Uncorrected c^* efficiency of the gas generator over its expected operating range was substantially constant at 97 percent. These tests demonstrated the suitability of the fuel-rich gas generator for the tripropellant firings. The high c^* efficiency obtained substantiates the design criteria used for the LF_2/GH_2 injector.

Tests of Fuel-Rich Gas Generator Injection Method

The feasibility of the simplified $Li/F_2/H_2$ injection scheme was determined by test firings in which the fuel-rich gas generator and the new lithium injector were used in combination with the graphite-lined combustion chamber and nozzle employed in the previous program (Ref. 1). Test parameters were the same as in the earlier tripropellant firings, except that nominal chamber pressure was increased from 500 psia (3.45×10^6 N/m²) to 750 psia (5.17×10^6 N/m²) by decreasing the throat diameter from 1.74 inches (4.42 cm) to 1.48 inches (3.75 cm). The expansion ratio was unchanged ($\epsilon = 2$).

Primary test variables in these firings were chamber length and percent hydrogen; nominal F_2/Li mixture ratio was 2.74. Again, three discrete hydrogen flowrates were programmed in each firing, with the sequencing shown in Fig. 32.

Run No. 68-9. Combustion chamber length (lithium injector face to start of nozzle convergence) was 30 inches (76.2 cm). The firing proceeded normally until 1.2 seconds into the second hydrogen flow step. At this point, the fluorine purge line failed between the check valve and the main fluorine valve, and the test was manually cut.

Posttest hardware inspection showed that the graphite around seven of the eight elements in the lithium injector face was irregularly eroded, with accompanying loss of most of the length of the orifice tips of the lithium injection tubes. This erosion was attributed to Li-HF reaction too near to the injector face. Data were obtained for the first two hydrogen flowrate levels.

Run No. 68-10. For this test, the combustion chamber length was reduced to 15 inches (38.1 cm). The firing proceeded smoothly to programmed completion. Posttest examination of the lithium injector again showed graphite surface erosion, as in the previous test, around five of the elements. Three elements were found to be unchanged because the lithium tubes leading to them were blocked with solid lithium, indicating that they were insufficiently heated prior to the start of lithium flow. The tubes were preheated by purge gas (helium at 1000 F, 810 K) flowing through them. At this temperature, maximum allowable pressure in the purge gas heater was 500 psia ($3.45 \times 10^6 \text{ N/m}^2$). Pressure in the main combustion chamber during gas generator operation was about 510 psia ($3.52 \times 10^6 \text{ N/m}^2$), so that positive purge gas flow was uncertain during this time. It was assumed that tube temperatures attained during the initial purge gas flow would be sustained by the high-temperature gas generator product gas. However, for three of the tubes, this was not the case. Since all the tubes had remained open in the preceding test, this was apparently a marginal situation.

Run No. 68-11. Because of the low lithium flowrate in Run No. 68-10, the test was repeated without changing the combustion chamber length. To maintain the flow of hot helium through the lithium delivery tubes during gas generator operation, purge gas heater temperature was reduced from 1000 F (810 K) to 800 F (700 K) to permit pressure increase in the heater from 500 psia ($3.45 \times 10^6 \text{ N/m}^2$) to 750 psia ($5.17 \times 10^6 \text{ N/m}^2$) (heater pressure was limited by stress considerations, which depend on temperature).

The firing proceeded as programmed. The data showed, however, that lithium flow did not begin until 1.3 seconds after the lithium valve opened. The reason for this was delayed bursting of the diaphragm in the lithium line (Fig. 27) because of an inadvertent installation error. Good data were obtained in Steps No. 2 and 3 of the firing. Following the test, the graphite around some of the lithium injector elements was eroded, as in the previous firings. There was also some erosion of the steel shell, apparently the result of leakage between the gas generator graphite chamber liner and the lithium injector.

Run No. 69-1. To eliminate the leakage from the gas generator chamber to the main combustion chamber through the lithium tube passages, the thickness of the lithium injector was increased from 1.52 inches (3.86 cm) to 3.00 inches (7.62 cm). This had the effect of moving the lithium tube passages away from the interface between the injector and the graphite liner of the gas generator chamber (Fig. 18).

Chamber length for this firing was 7 inches (17.8 cm). The firing proceeded as programmed. Posttest examination of the hardware showed no erosion at all of the back or sides of the lithium injector or of the steel shell around it, indicating that moving the tube passages away from the liner-injector interface had solved the leakage problem. Some localized erosion of the graphite at the injector face around the injection elements was observed, as in the previous tests, with accompanying partial loss of the lithium tube orifice tips.

This firing completed the planned study of the effect of combustion chamber length on the c^* efficiency obtained with the fuel-rich gas generator injection method.

Run No. 69-2. In the firings with the Mod I and Mod II lithium injectors (Fig. 18), significant erosion of the graphite surface around the injection elements was generally observed. The purpose of this test was to assess the possible benefit of increasing the distance between the injector face and the point of impingement of the lithium stream with the central gas jet. This was accomplished by recessing the injector face 0.325 inch (0.826 cm), which increased the effective impingement distance from 0.237 inch (0.602 cm) to 0.562 inch (1.43 cm), as shown in Fig. 18. Chamber length was 15 inches (38.1 cm). The firing proceeded as programmed (Fig. 32).

Again, no sign of leakage between the gas generator and main combustion chamber could be detected on posttest hardware examination. Localized graphite injector face erosion around the injection elements was substantially reduced from that of the previous tests. Correspondingly, less of the orifice tips of the lithium injection tubes was burned away. This reduced erosion represented a significant improvement over the nonrecessed injector configuration.

Run No. 69-3. The primary purpose of this test was to determine the effect on c^* efficiency of reduction in gas injection velocity from Mach 0.5 to Mach 0.25. This was accomplished by use of the Mod IV lithium injector, in which the gas injection area was twice that of the earlier injectors, with the penetration of the central gas jet by the lithium stream remaining unchanged.

All of the previous firings with the fuel-rich gas generator and lithium injector produced noticeable erosion of the graphite liner in the combustion chamber at about 1.5 to 4 inches (3.8 to 10.2 cm) downstream of the injector face in a scalloped pattern, with the eroded areas in line with

the injector elements. This indicated that the erosion was probably caused by misdirection of some raw lithium against the hot chamber wall. Although this was of no particular concern in the tests with graphite-lined chambers, it could be detrimental in the water-cooled, copper-lined chambers which were to be used in subsequent tasks.

A short series of cold-flow experiments was carried out prior to Run No. 69-3 to determine the nature of the liquid and gas distributions produced by the lithium/gas injection element. Details of these tests are given in Appendix E. The results indicated that unreacted lithium would indeed contact the chamber wall in the region of the observed erosion. Because of these observations, a second objective of Run No. 69-3 was to obtain an indication of possible thermal/chemical interaction of hot lithium with a copper-wall combustion chamber. This was carried out by replacing the graphite liner of the 5-inch (12.7-cm) chamber segment with copper. A 2-inch (5.08-cm) graphite-lined chamber section was placed between the copper-lined segment and the graphite-lined nozzle, for a total chamber length of 7 inches (17.8 cm).

The test firing proceeded as programmed. Posttest hardware examination showed substantial erosion of the copper liner, in the same scalloped pattern as observed with graphite, about 1.5 to 4 inches (3.8 to 10.2 cm) from the lithium injector. The maximum depth of the eroded regions (about 0.5 inch, 1.3 cm) was greater than that observed with graphite (about 0.2 inch, 0.5 cm). Copper weight loss during the test was about 3.5 pounds (1.59 kg), compared to total graphite weight loss in a similar firing of about 0.2 pounds (0.09 kg). Because the eroding copper added significant mass to the combustion products and, in addition, affected the combustion processes, data from this test are questionable, except possibly at the initial portion of the first step, when the erosion was just beginning.

TASK II EXPERIMENTAL FIRINGS

The simplified injection method using the fuel-rich gas generator was employed in all of the Li/F₂/H₂ firings of Tasks II and III. A schematic of the Task II test hardware is shown in Fig. 35. The graphite-lined chamber section was used immediately downstream of the lithium injector because of the apparent incompatibility of the injector with copper chamber walls shown in Run No. 69-3. Heat flux data were obtained in the 4-inch (10.2-cm) downstream section of the 9-inch (22.9-cm) combustion chamber and in the nozzle section (to $\epsilon = 3$). The uncooled nozzle extension (from $\epsilon = 3$ to $\epsilon = 10$) was used so that measured pressures in this region would be available for subsequent comparison of Task II and Task III data. The area ratio 10 nozzle flowed full in the sea-level tests.

Test Firings

Run No. 69-4. The first test with the water-cooled hardware proceeded smoothly through the three programmed steps (Fig. 32). No cooling system problems were encountered. Posttest hardware condition was excellent. Neither of the water-cooled thrust chamber sections was visibly affected by the firing.

Run No. 69-5. This firing also proceeded as programmed. Posttest, there was a slight degree of erosion of the copper liner at the upstream end of the water-cooled combustion chamber segment, where it contacted the graphite liner of the uncooled chamber section.

Run No. 69-6. The third test in this series also ran smoothly to programmed completion. Posttest hardware condition was excellent, except for a slight increase in the erosion at the inlet end of the water-cooled chamber segment.

Chamber Coating

Following each of the test firings in this series, a deposit of grayish solid material was present on the walls of the water-cooled chamber and

nozzle sections. In the water-cooled chamber and at the nozzle entrance, where the coating consisted of a mixture of LiF and Li, the thickness of the deposit was 0.08 to 0.12 inch (2.0 to 3.0 mm). The thickness of the deposit decreased in the convergent portion of the nozzle, reached about 0.002 to 0.005 inch (0.05 to 0.13 mm) immediately upstream of the throat, and remained at this value to the nozzle exit. The very thin coating at the throat and in the divergent nozzle consisted essentially of LiF. Coating thickness on the graphite liner of the uncooled chamber, by comparison, was generally in the range 0.005 to 0.010 inch (0.13 to 0.25 mm). The substantially smaller quantity of deposited material on the uncooled graphite chamber wall compared with that on the wall of the water-cooled chamber is associated primarily with the higher temperature of the former. This resulted in less condensation on the graphite wall from the combustion gases. Figure 36 is a posttest photograph of the converging portion of the water-cooled nozzle segment, showing the deposited coating; a portion of the coating has been removed to show its thickness.

The solid deposited on the walls of the water-cooled chamber plugged the chamber pressure ports in two of the three firings in the Task II series. In those two tests, chamber pressure was estimated from pressure measurements in the gas generator and near the lithium injector. Subsequently, in the Task III firings, a helium purge was maintained through the chamber pressure taps. This purge was interrupted for 200-millisecond intervals in each of the steps of the firing to permit data slices to be taken.

Lithium System Helium Purge

Following each of the Task II firings, one to three of the eight lithium injection tubes were found to be plugged with solid lithium. Apparently the reduction in helium purge gas temperature from 1000 F (810 K) to 800 F (700 K) prior to Run No. 68-11 again resulted in a marginal tube heating situation. A series of purge gas flow tests was therefore carried out to obtain data for possible increase in the duration of the hot helium purge prior to lithium flow. The tests showed that the preliminary purge

gas flow through the lithium injection tubes could be extended to about 20 seconds before the gas temperature fell below 600 F (590 K). This was done in the subsequent Task III firings and no further lithium injection tube blockage was encountered.

TASK III EXPERIMENTAL FIRINGS

Four altitude simulation tests were carried out with the 60:1 area ratio skirt attached to the 10:1 area ratio nozzle extension used in the Task II firings. The nozzle was joined to a self-starting diffuser through a stainless-steel bellows. Details of the diffuser design and mounting are given in Appendix G. A schematic of the test hardware used in the altitude simulation firings is shown in Fig. 37, and a photograph of the test stand showing the diffuser in place is shown in Fig. 38.

Test Firings

Run No. 69-7. Each altitude simulation firing was programmed as follows: 17.5 seconds of lithium purge gas flow, 3.5 seconds of gas generator operation, 6.0 seconds of Li/F₂/H₂ firing (consisting of three 2.0-second steps at different hydrogen flowrates), and, finally, 2.8 seconds of gas generator operation. This test proceeded smoothly to scheduled completion. No difficulty was encountered in the operation of the diffuser. Posttest hardware condition was excellent, with the exception of the inlet region of the water-cooled chamber section. The erosion of the copper liner in this area, which had begun in the Task II firings, continued in this test.

Run No. 69-8. Test hardware for this firing was the same as in the preceding test, and it proceeded to programmed completion. Posttest hardware examination showed that the upstream end of the copper liner in the water-cooled chamber section had been eroded down to one of the axial water passages. Test data indicated that water from this passage had flowed into the chamber during all three steps of the tripropellant firing. Consequently, performance data from this test were not usable.

Run No. 69-9. Test hardware for this firing was the same as in the first two altitude simulation tests, except that a 9-inch (22.9-cm), graphite-lined, uncooled chamber section was used in place of the previously employed combination of a 5-inch (12.7-cm) graphite-lined segment and a 4-inch (10.2-cm) water-cooled section, pending repair of the latter. The firing proceeded smoothly to scheduled completion. Posttest hardware examination showed that the copper liner of the water-cooled nozzle section had been eroded down to the first circumferential water passage at its upstream end. Test data indicated that water from this passage had flowed into the chamber only during the third step of the firing, so that valid performance data were obtained in the first two steps.

Run No. 69-10. Both the water-cooled combustion chamber segment and nozzle section were repaired prior to this final test and the water passages of each were pressure-checked at 1100 psi (7.6×10^6 N/m²) to confirm their physical integrity. In both cases, the repair consisted of re-forming the inlet portion of the copper liner and re-sealing the cooling passages in this region. The test proceeded smoothly until the end of the scheduled lithium flow, at which time the upstream water exit tube of the cooled nozzle burst and the test was terminated. It was found that the copper liner in the upstream portion of the convergent nozzle was completely eroded away. This permitted flow of hot combustion products through the water exit tube and its consequent burnout. There was no apparent damage to the water-cooled combustion chamber section, aside from very slight erosion at its inlet. Test data showed that water flow into the thrust chamber from the eroded nozzle coolant passage began at the start of lithium flow, hence no usable performance data were obtained in this firing.

Chamber Erosion

The observed erosion of both the water-cooled chamber and nozzle sections occurred at their upstream ends, where they were in contact with the hot graphite liner of the uncooled chamber segment. Because of its higher cooling capability, erosion of the water-cooled chamber section was much slower than that of the nozzle section. In both cases, it appears that heat flowing from the graphite liner probably overloaded the cooling capacity at the entrance region of the adjacent water-cooled segment.

RESULTS AND DISCUSSION

The experimental results obtained in this program are presented and discussed in the following three categories:

1. Tripropellant injection methods
2. Thrust chamber heat transfer
3. Altitude performance

The test firings of Task I contributed to the first of these categories, those of Task II contributed to the first and second categories, and those of Task III contributed to all three categories.

TRIPROPELLANT INJECTION METHODS

Oxidizer-Rich Gas Generator

Test data obtained in the two firings using the oxidizer-rich gas generator injection method are summarized in Table 4. The hydrogen injection station was 1 inch (2.54 cm) from the lithium injector and combustion chamber lengths of 12 inch (30.5 cm) and 22 inches (55.9 cm) were employed (Fig. 33). Applicable corrections were made to measured chamber pressure and thrust, as described in Appendix A; total corrections are listed in Table 4. Although, in these tests, c^* efficiencies based on chamber pressure were slightly higher than those based on thrust, the differences were within the limits of experimental error (Appendix B), confirming the previous indication (Ref. 1) that the C_F efficiency of the low expansion ratio nozzle ($\epsilon = 2$) was close to 100 percent. Again, as in the earlier study, c^* efficiencies obtained at hydrogen flowrates less than about 20 percent of total propellant flow were lower than those at hydrogen proportions greater than 20 percent. Reduced c^* efficiency at the lower hydrogen flowrates was attributed to incomplete penetration of the radial hydrogen jets into the combustion gas stream.

All c^* efficiency data obtained with the oxidizer-rich gas generator injection method, both in the earlier study and in the present investigation, are presented in Fig. 39. The primary variable is percentage of hydrogen. Nominal chamber pressure is 500 psia ($3.45 \times 10^6 \text{ N/m}^2$) and nominal F_2/Li mixture ratio is 2.74. The experimental deviations from these values do not significantly affect combustion efficiency (Ref. 1). Data at hydrogen proportions below 20 percent reflect inadequate uniformity of hydrogen distribution in the combustion mixture and will therefore not be further considered in subsequent analyses. At hydrogen flowrates greater than 20 percent, the experimental results were consistent and characteristically predictable.

Figure 40 shows c^* efficiency as a function of the length of the Li/F_2 combustion chamber at 25- to 35-percent hydrogen levels. With Li/F_2 combustion chamber lengths of 5 inches (12.7 cm) or longer, c^* efficiency was approximately 99 to 100 percent; decrease in length to 1 inch (2.54 cm) lowered c^* efficiency to approximately 98 percent. This very slight change is an indication of the efficiency of the gas-augmented atomization process in producing small lithium droplets. Variations in the length of the mixing chamber downstream of the hydrogen injector from 12 inches (30.5 cm) to 27 inches (68.6 cm) had no apparent effect on c^* efficiency, regardless of the length of the Li/F_2 combustion chamber (Fig. 39). This indicates that hydrogen mixing and heating is completed within the shorter length.

The high degree of lithium atomization produced by the oxidizer-rich gas generator injection method is confirmed by the results of the present tests. Injection of the hydrogen at 1 inch (2.54 cm) from the Li/F_2 injection station closely resembles the situation which would occur if the hydrogen were introduced through the Li/F_2 injector itself. That is, although the lithium is still atomized by the gaseous fluorine, the presence of the hydrogen in the injection region reduces the rate of diffusion of the fluorine to the lithium droplets. It also results in reaction of lithium with HF as well as with F_2 , and, most important, significantly reduces the temperature in the combustion region. For these reasons,

injection of hydrogen at 1 inch (2.54 cm) downstream of the lithium injector provides more severe conditions for lithium combustion than does addition at 5 inches (12.7 cm) or beyond. The fact that c^* efficiency is only slightly reduced by addition of the hydrogen within the Li/F_2 combustion zone shows that the degree of lithium atomization is high enough so that combustion of the lithium droplets is nearly complete. These results indicated that $\text{Li}/\text{F}_2/\text{H}_2$ c^* efficiency would probably remain high if a fuel-rich gas generator were employed to furnish a mixture of HF and H_2 as the atomizing/reactant gas, provided that the lithium droplets resulting from the atomization process were sufficiently small. Such a gas generator was therefore employed in the simplified injection method. With the same requirement for small lithium droplets, the test results indicate that c^* efficiencies of about 98 percent would be expected if all three propellants were injected at the same axial location.

Fuel-Rich Gas Generator

Nineteen test data points were obtained for the determination of c^* efficiency with the fuel-rich gas generator injection method. Of these, 13 were from Task I and 3 each were from Tasks II and III. Data are summarized in Table 5. Characteristic velocity efficiencies obtained in the other data-producing tests (six in Task II and two in Task III) were not included in this determination because the chamber pressure taps near the start of nozzle convergence were plugged by condensed solids. Chamber pressures in these cases were estimated from pressures measured in the gas generator or close to the lithium injector, and therefore were not sufficiently reliable for use in the c^* correlations.

Corrected c^* efficiencies were calculated by the methods given in Appendix A. Characteristic velocity efficiencies based on chamber pressure were obtained for all the tests. For the Task I tests, in which the expansion ratio was 2, c^* efficiencies based on thrust were also calculated, because the thrust coefficient of this short nozzle had been shown in the previous work to be close to theoretical, within the range of experimental test conditions.

The effect of chamber pressure variations on c^* efficiency in these tests was not significant; with the exception of two tests, chamber pressures were 680 ± 50 psia ($4.69 \times 10^6 \pm 0.3 \times 10^6$ N/m²).

The decrease in c^* efficiency at the higher percentages of hydrogen may be ascribed primarily to the corresponding decreases in combustion temperature. The lower temperature decreases both the vaporization rate of the lithium and the rate of diffusion of HF to the lithium droplet surface. Achievement of complete lithium combustion requires that the lithium drops burn by the "small droplet" mechanism, characterized by vapor phase reaction in a detached combustion zone (Ref. 1). After the initial surface reaction, the droplet is heated and vaporized by energy feedback from the Li/HF flame front. Because the proportion of this thermal energy which reaches the lithium droplet surface decreases as the bulk gas temperature decreases, the vaporization rate of the lithium would be correspondingly lowered. At nominal conditions ($P_c = 750$ psia, 5.17×10^6 N/m², and F_2/Li mixture ratio = 2.74), bulk gas temperature decreases from about 4500 F (2750 K) at 20-percent hydrogen to about 3400 F (2140 K) at 35-percent hydrogen (Ref. 1), and the lithium vaporization rate decreases accordingly. The lower bulk gas temperature at the high hydrogen percentage also decreases the diffusion coefficient of HF in H_2 , which is roughly proportional to the 3/2 power of the absolute temperature (Ref. 22). This corresponds to a decrease of about 45 percent in this factor between the 20- and 35-percent hydrogen levels. The effect of high percentages of hydrogen on c^* efficiency was substantially lessened at the highest F_2/Li mixture ratio (Fig. 41). Bulk gas temperature, however, varies only slightly with F_2/Li mixture ratio at the 35-percent hydrogen level (Ref. 1). Consequently, the effect of the lowered gas temperature in this case is apparently offset by the mass action effect of the large excess of HF.

The experimental results clearly demonstrate the feasibility of the fuel-rich gas generator injection method. Together with the test results obtained with the oxidizer-rich gas generator injection scheme, they indicate that the expected level of c^* efficiency if all three propellants were injected at the same axial position would be about 98 percent. The data obtained with both injection methods also confirm the conclusion previously reached

on the basis of the kinetics of the reactions involved (Ref. 1), namely, that the final combustion chamber composition is the same whether the lithium reacts with the fluorine, with the HF (formed by F_2/H_2 reaction), or with both.

Although the data from the final test firing of Task I (Run No. 69-3) are not reliable because of substantial mass addition arising from erosion of the copper chamber liner, the c^* efficiency observed at the start of the first step of the firing, when the erosion was presumably just beginning, may be used for an indication of the effect of decreased gas injection velocity on combustion efficiency. On this basis, c^* efficiency remained unchanged, at about 98 percent, when the gas injection velocity was decreased from Mach 0.5 to Mach 0.25. The fact that apparently no significant loss in c^* efficiency resulted from the indicated tripling of the volume mean lithium droplet diameter showed that the estimated sizes (approximately 5 microns and 15 microns) were probably of the right order of magnitude, based on combustion model calculations (Ref. 1). Substantially smaller sizes were not likely to be formed under the injection conditions, while the formation of substantially larger sizes would be reflected in a change in c^* efficiency.

THRUST CHAMBER HEAT TRANSFER

Experimental Results

Heat flux measurements were made in the test firings of Tasks II and III by the methods described in Appendix D. Chamber heat flux was determined at four circumferential locations over the 4-inch (10.16-cm) water-cooled segment immediately upstream of the nozzle (Fig. 35). Measurements in the nozzle were made at a number of axial positions, from the start of convergence to the exit.

Usable heat transfer data were obtained in five firings (three in Task II and two in Task III), at a total of 14 test conditions. The data* are

*All heat flux data were taken during the final 0.4 second of each step of the firing.

summarized in Table 6, which includes both measured heat flux and computed gas side heat transfer coefficients. The tabulated chamber heat flux values are the averages of the four circumferential measurements, as discussed below. Nozzle heat flux measurement locations are designated by the respective area ratios. In three of the firings, chamber pressure measurements were marginally reliable, because of plugging of the pressure taps by condensed solids. These pressure data are enclosed in parentheses. However, the tabulated pressures are well within the error limits required for heat transfer correlations.

The heat fluxes measured in the tripropellant firings were influenced by three important factors. These were: (1) condensation and deposition of LiF and Li on the walls of the water-cooled combustion chamber segment and in the upstream portion of the water-cooled nozzle section, (2) the insulating effect of the thermal barrier presented by this coating, and (3) axial heat flux to the water-cooled combustion chamber segment from the graphite liner of the chamber section adjoining it (Fig. 35). The first two factors are inherent in Li/F₂/H₂ combustion in a cooled-wall chamber and will therefore be considered in the subsequent discussion of Li/F₂/H₂ heat flux. The third factor, however, is unrelated to Li/F₂/H₂ combustion and resulted only from the experimental use of an uncooled, graphite-lined, combustion chamber section between the lithium injector and the water-cooled segment. Because the temperatures of the graphite liner were much greater than those of the adjoining copper liner in the water-cooled segment, heat flow from the graphite to the water in the coolant passages caused an increase in measured combustion chamber heat flux. The effect of this extraneous heat source is clearly shown in Run No. 69-9, in which the water-cooled cylindrical chamber section was not used and a graphite-lined combustion chamber was joined directly to the water-cooled nozzle. Measured heat flux in the first nozzle passage (Table 6) was nearly double that observed at similar test conditions when the nozzle was joined to the water-cooled segment.

An estimate of the axial heat flux from the graphite liner to the water-cooled combustion chamber section was made on the basis of the apparent

rise in heat flux in this section during the initial F_2/H_2 gas generator operation which preceded the $Li/F_2/H_2$ firing in each test. This rise was ascribed to the gradually increasing temperature of the graphite liner during the gas generator firing. The heat flux from this source is shown as a function of firing time in Fig. 42, which also indicates the effect of this extraneous heat source by showing combustion chamber heat flux during a typical test both as measured and after subtraction of the heat flow from the graphite. (Faired lines are used for this illustration.) The net values, representing radial heat flow from the combustion products, will be taken as the experimental combustion chamber heat fluxes in subsequent discussions.

Plots of measured heat flux against axial location in the thrust chamber for each of the five steps of a typical test firing (Run No. 69-7) are presented in Fig. 43 through 47. Bar plots are used, to show the axial distances covered by each measurement. The measurements made at the entrance to the convergent nozzle are not included in these plots because a slight misalignment between the chamber and nozzle disturbed the local boundary layer and resulted in erratic and unrepresentative heat flux values in the first nozzle coolant passage.

In the pretest and posttest gas generator operation (Fig. 43 and 47, respectively) and in the $Li/F_2/H_2$ firings at nominal 20- and 25-percent hydrogen (Fig. 44 and 45, respectively), nozzle heat flux increased in the convergent section to a maximum immediately upstream of the throat, then fell rapidly in the divergent section. However, at the nominal 35-percent hydrogen level (Fig. 46), heat flux at the throat decreased sharply from the values in the convergent nozzle, then rose immediately downstream of the throat before decreasing again at larger area ratios. These throat heat flux characteristics were observed in all tests at the 35-percent hydrogen level except one (Run No. 69-6, Step 3), in which the heat flux followed the conventional pattern, as at 20-25 percent hydrogen, with a maximum immediately upstream of the geometric throat.

Heat flux measurements in the 4-inch (10.2-cm) combustion chamber segment were made at four circumferential locations. The axial cooling passages at which the respective measurements were made were positioned as follows: in line with the center of an injection element (i.e., in line with a lithium orifice), midway between two injection elements (22.5 degrees from a lithium orifice), 7 degrees from a lithium orifice, and 15 degrees from a lithium orifice. In all tests, the maximum combustion chamber heat flux occurred at the station directly in line with a lithium orifice and the minimum was at the station 15 degrees from a lithium orifice. Variations of the maximum and minimum from the mean (approximately 10 to 12 percent) were not large enough to be of practical significance, so that the average value in each step was considered to be the measured combustion chamber heat flux.

The reproducibility of the experimental heat flux measurements is indicated by a comparison of the data obtained during the gas generator operating portions of separate firings. Test conditions prior to the start of lithium flow were essentially constant in all firings, at the following nominal values: $P_c = 555$ psia (3.83×10^6 N/m²), F_2/H_2 mixture ratio = 3.20, and $\dot{w}_T = 3.75$ lb/sec (1.70 kg/sec). Gas generator heat flux measurements from the various firings, plotted in Fig. 48, are in good agreement and show that the heat flux data were satisfactorily reproducible.

Discussion

Heat Flux Profiles. The heat flux profile, as used herein, is a plot of the ratio of the measured heat flux at a given axial location to that at the geometric throat against thrust chamber length. Any essential differences between the heat flux characteristics of Li/F₂/H₂ and those of a typical high-energy bipropellant combination such as F₂/H₂ would be disclosed by a comparison of the respective heat flux profiles obtained in the same test hardware, because the effects of varying chamber pressure and temperature are normalized out by this procedure. This comparison is shown for a typical test (Run No. 69-7) in Fig. 49, in which

are plotted the heat flux profiles during the pretest F_2/H_2 gas generator firing and the first step of the $Li/F_2/H_2$ test (nominal 20-percent hydrogen). The heat flux profile during the second $Li/F_2/H_2$ step (nominal 25-percent hydrogen) is very similar to that at the first, but in the third step (nominal 35-percent hydrogen) the profile is completely different, because of the extremely low heat flux at the throat. The profiles are shown to an expansion ratio of 4, because beyond this point they are all alike and the ordinate values fall below 0.1

At the 20- and 25-percent hydrogen levels in the $Li/F_2/H_2$ tripropellant combination, the $Li/F_2/H_2$ and F_2/H_2 heat flux profiles are essentially identical at the throat region and in the divergent portion of the nozzle. In the combustion chamber and at the start of nozzle convergence, the $Li/F_2/H_2$ heat flux levels are substantially higher than those of F_2/H_2 . This is the region in which significant deposition of solids on the chamber walls was observed. An estimate of the heat flux due to wall condensation was made by assuming that the coating (approximately 80:20 Li/F by weight) was deposited from the gas phase at a uniform rate over the duration of the lithium flow, to the measured final thickness (0.12 inch, 3.0 mm). Lithium fluoride was assumed to condense to the solid phase and lithium to the liquid, because its melting point is less than the wall temperature. The estimated heat flux caused by condensation on the chamber wall is approximately 5 B/in.²/sec (8×10^6 W/m²), which nearly accounts for the observed heat flux increase at the start of lithium combustion (Fig. 42).

Besides serving as a source of heat flowing into the chamber wall, the deposited coating also constitutes a thermal barrier which eventually decreases the heat flux from the combustion gases to the water-cooled chamber segment. This is similar to the decrease resulting from the deposition of carbon on the walls of hydrocarbon-burning chambers (Ref. 23). The effect of this barrier is seen in the decreasing actual heat flux during each step of the $Li/F_2/H_2$ firing as the coating builds up, and in the significantly lower combustion chamber heat flux in the posttest gas generator firing compared to the pretest value (Fig. 42).

Effect of Hydrogen Proportion on Heat Flux. A significant qualitative difference exists in the nature of the Li/F₂/H₂ combustion products at the 20- to 25-percent hydrogen level compared to the 35-percent level. At 20- to 25-percent hydrogen, condensation in the bulk flow does not begin until downstream of the throat, so that only gas-phase flow occurs in the combustion chamber, convergent nozzle, and throat region. At 35-percent hydrogen, however, a substantial portion of the product LiF is condensed in the combustion chamber, so that two-phase flow exists throughout the engine (Fig. 58 and 59). This difference will be further described in the discussion of altitude performance.

Thrust chamber heat fluxes measured at the two hydrogen levels (20 to 25 percent and 35 percent) are also qualitatively different, particularly in the region of the throat. This is shown in Fig. 50 by data from a typical test (Run No. 69-7) in which measured heat fluxes in the pretest F₂/H₂ firing and in all three Li/F₂/H₂ steps are plotted. All values have been normalized to the chamber pressure of Step 2 (700 psia, 4.83×10^6 N/m²). The curves for the F₂/H₂ firing and for the Li/F₂/H₂ steps at nominal 20- and 25-percent hydrogen are similar and follow the customary increase in the convergent nozzle to a maximum at the sonic point immediately upstream of the geometric throat, while the heat flux in the third Li/F₂/H₂ step, at nominal 35-percent hydrogen, shows a minimum at the throat region. The anomalous behavior at the highest hydrogen level may be caused by the existence of two-phase flow in the transonic region, or the large excess of hydrogen may affect the heat flux in that region because of local relaminarization of the boundary layer.

Effect of F₂/Li Mixture Ratio on Heat Flux. Heat flux in the combustion chamber and the maximum heat flux values in the throat region (at a point slightly upstream of the geometric throat) are plotted as functions of F₂/Li mixture ratio in Fig. 51. In the combustion chamber, heat flux varies inversely with F₂/Li mixture ratio at each of the three levels of hydrogen percentage, whereas, at the throat, heat flux at the 20- and 25-percent hydrogen levels varies directly with F₂/Li mixture ratio. At 35-percent hydrogen, heat flux at the throat is much lower than it is at

the lower hydrogen levels with F_2/Li mixture ratios below 3.8, but at F_2/Li mixture ratio of 4.16, the heat flux is comparable to those at lower hydrogen percentages.

Heat Transfer Correlations. A convenient and widely used method of estimating nozzle heat flux is by means of a turbulent pipe-flow correlation such as that of Bartz (Ref. 5). Although this correlation (Eq. 4) is applicable only to the nozzle, it is frequently extended by assuming that combustion chamber heat flux is equal to that calculated at the entrance to the convergent nozzle. Because reliable prediction of heat flux in a rocket engine combustion chamber is not yet possible, this extension is useful for making comparisons between different propellant combinations and operating conditions.

A recent comparison of experimental heat transfer coefficients obtained from a wide variety of propellant combinations and nozzle geometries with those calculated from the Bartz equation showed that, in general, the predicted coefficients are significantly larger than the experimentally determined values (Ref. 24). The lower experimental coefficients are attributed to the effects of the pressure gradient and flow acceleration on the velocity and thermal gradients in the nozzle boundary layer. If the contraction ratio is such that a well-developed boundary layer is present in the combustion chamber immediately upstream of the nozzle, and if this zone is sufficiently removed from the injection and primary combustion zones, the heat transfer coefficient in this region of the combustion chamber is frequently in good agreement with the Bartz prediction. However, if the contraction ratio is high, the accompanying low gas velocity near the nozzle entrance, inadequate boundary layer development, and substantial recirculation result in increased combustion chamber heat flux. Such high heat flux (relative to Bartz equation predictions) is generally observed in high contraction ratio combustion chambers with various propellants (Ref. 25) and, in particular, with F_2/H_2 (Ref. 26).

The experimental heat transfer coefficients obtained in a typical pretest F_2/H_2 gas generator firing (Run No. 69-7) are compared with those calculated

from the Bartz equation in Fig. 52. As would be expected in the large contraction ratio thrust chamber employed ($\epsilon_c = 11.5$), the experimental heat transfer coefficient in the combustion chamber is substantially greater than the Bartz prediction. Beyond the nozzle entrance region, the calculated values become equal to, then greater than, the experimental. At the throat, the difference is approximately 25 percent. The F_2/H_2 data provide a base for comparison of the $Li/F_2/H_2$ heat transfer coefficients with the corresponding Bartz values. These are shown in Fig. 53 for the 20- and 25-percent hydrogen steps of Run No. 69-7. The 35-percent hydrogen data are not included because the "abnormally" low throat heat flux in this case is directly inconsistent with turbulent pipe flow predictions.

Except for the high heat flux coefficients in the combustion chamber and in the upstream portion of the convergent nozzle caused by condensation and deposition of the wall coating, the curves for $Li/F_2/H_2$ are very similar to those of F_2/H_2 . Although the Bartz values of the heat transfer coefficient at the 25-percent hydrogen level are slightly larger than those at 20-percent hydrogen, the experimental values at 25 percent are lower than at 20 percent. This is characteristic of the tripropellant combination, because an increase in hydrogen percentage was always accompanied by an abrupt drop in measured heat flux throughout the thrust chamber. The wall coating downstream of a point about midway between the start of nozzle convergence and the throat consisted of an extremely thin, porous, layer of fluffy LiF which apparently had little effect on the heat transfer characteristics.

The combustion chamber heat transfer coefficients in the F_2/H_2 firings were approximately 2.3 times the Bartz values (Fig. 52), reflecting, at least in part, the high contraction ratio of the test hardware. For the $Li/F_2/H_2$ firings, the corresponding ratios of measured-to-predicted combustion chamber heat transfer coefficients were 4.7, 2.5, and 1.7 at 20-, 25-, and 35-percent hydrogen, respectively. The high contraction ratio effect remained, together with the decreasing effect of condensation on the wall and increasing effect of the condensed phase thermal barrier. At the nozzle throat, the experimental heat transfer coefficients were less than the Bartz predictions. The measured-to-predicted

ratios were 0.8 and 0.6 for $\text{Li}/\text{F}_2/\text{H}_2$ at 20- and 25-percent hydrogen, respectively.

ALTITUDE PERFORMANCE

Experimental Results

Altitude performance data for the $\text{Li}/\text{F}_2/\text{H}_2$ tripropellant combination were obtained with a 60:1 area ratio nozzle which was joined to a self-starting exhaust diffuser (Appendix G). Four firings were carried out in this series, each consisting of three discrete steps. However, in two of the firings and in the final step of a third, no usable performance data were obtained because of erosion of the water-cooled chamber or nozzle liner, which permitted water flow into the thrust chamber. Experimental results of the five tests in which good data were obtained are summarized in Table 7. The helium purge through the chamber pressure taps which was used to prevent their blockage by condensed solids did not function in Run No. 69-9. Chamber pressures in the two tests of this firing were derived from pressure measurements in the gas generator and are therefore enclosed in parentheses. Although the uncertainty in these chamber pressure values (maximum error is about 3 percent) did not permit reliable determinations of c^* to be made, the specific impulse efficiencies were not affected because of the very small variation of specific impulse with chamber pressure (0.008 sec/psia, 1.1×10^{-5} N/kg/sec per N/m^2). Any possible resulting error in the theoretical specific impulse upon which the I_s efficiency is based would be insignificant.

The performance parameters listed in Table 7 were calculated by the methods described in Appendix A. Thrust values were obtained in two ways, one based on load cell measurements and the other on nozzle pressure profiles (Appendix C), with good agreement between the two methods (Fig. 54). The corresponding vacuum specific impulse efficiencies were averaged to obtain the measured, uncorrected, values at each test condition. These are plotted in Fig. 55. The I_s efficiencies at both F_2/Li mixture ratios (2.5 and 3.0) fall on the same curve, which ranges from approximately 92 percent at the

20-percent hydrogen level to approximately 95 percent at 35-percent hydrogen. Maximum measured, uncorrected, vacuum specific impulse was 510 lbf/lbm/sec (5001 N/kg/sec) at F_2/Li mixture ratio of 3.0 and nominal 35-percent hydrogen; at 25-percent hydrogen, the measured, uncorrected, vacuum specific impulse was 506 lbf/lbm/sec (4962 N/kg/sec) and at 20-percent hydrogen, it was 486 lbf/lbm/sec (4766 N/kg/sec).

In all of the altitude simulation firings, full flow was established in the 60:1 area ratio nozzle as soon as lithium combustion began. This is shown by comparison of the measured and theoretical nozzle pressure profiles, as illustrated in Fig. 56 for a typical test. During the pretest and posttest F_2/H_2 gas generator operation without lithium, however, the flow separated near the nozzle exit (Fig. 57) because of the lower chamber pressures under these conditions.

Discussion

I_s Efficiency and Two-Phase Flow. Performance losses resulting from two-phase flow arise mainly from particle/gas thermal and velocity lags. Because these lags develop near the throat and remain nearly constant thereafter, the presence or absence of a condensed phase in the transonic region determines whether two-phase flow losses might be significant. Further, the magnitude of the lags is essentially determined by the size of the particles entering the nozzle (Ref. 12). Two-phase flow losses are relatively low if the particles are initially small (typically, 1 micron or less in diameter) and do not grow significantly during the expansion process. Any condensation which occurs downstream of the transonic region generally has only a minor effect on performance (Ref. 17).

The weight percent of condensed material in the $Li/F_2/H_2$ combustion products varies widely over the experimental ranges of hydrogen proportion and F_2/Li mixture ratio (Fig. 58 and 59). Near the stoichiometric mixture ratio, the weight of condensed material in the combustion chamber and at the throat increases from zero (at 25-percent hydrogen, or less) to 30 to 40 percent (at 35-percent hydrogen). It would therefore be expected

that the substantial quantities of condensed material present in the critical transonic region at the 35-percent hydrogen level would be accompanied by two-phase flow losses not apparent at the 20- to 25-percent hydrogen levels. However, measured specific impulse efficiency remained constant as the proportion of hydrogen in the tripropellant combination was raised from 25 to 35 percent (Fig. 55). It therefore appears that the lower heat flux loss accompanying the increase in hydrogen percentage was essentially compensated by the higher two-phase performance loss. For hydrogen proportions between 20 and 25 percent, two-phase flow in the throat region is not a significant performance factor; hence, the higher heat loss observed at the lower hydrogen flowrate is reflected in decreased specific impulse efficiency (Fig. 55), with no compensating effects due to two-phase flow.

As a result of incomplete combustion and/or operation at substoichiometric F_2/Li mixture ratio levels, some unreacted lithium may enter the nozzle. Theoretical performance calculations showed that, in the present tests, conditions were such that no lithium condensation would occur either in the chamber or in the nozzle. However, at low F_2/Li mixture ratios (e.g., 2.25) and high hydrogen percentages (e.g., 35 percent), lithium condensation would begin immediately downstream of the throat, and, under these conditions, both the Li and the LiF particles might affect performance.

Analytical calculations of performance losses involving two-phase flow (Ref. 11 to 19) are critically dependent upon the mass median particle size of the condensed phase. Because theoretical predictions of particle sizes are not yet possible and reliable experimental particle size measurements are extremely difficult to make, such analytical performance calculations are most productively used in reverse, that is, to estimate particle sizes from measured performance efficiencies. Computations of this type were carried out for the $Li/F_2/H_2$ tests (Appendix F). Indicated condensed phase mass median particle diameters were on the order of 0.5 to 1.0 micron, reflecting the apparent comparatively low lag losses which were observed (Ref. 13).

Deliverable Specific Impulse. The performance factor of primary practical interest derived from the altitude simulation firings is the vacuum specific impulse actually deliverable by a thrust chamber of the type tested but cooled regeneratively by liquid hydrogen. Recent Li/F₂/H₂ engine system studies (Ref. 27) have indicated that regenerative cooling with liquid hydrogen would be used in all feasible pump-turbine power cycles appropriate to this tripropellant combination. For each test condition, therefore, the experimentally measured, uncorrected, specific impulse efficiency was used to calculate the deliverable vacuum specific impulse by the procedure described in Appendix A. The results are shown in Fig. 60. Of the five test conditions, the highest vacuum specific impulse (509 lbf/lbm/sec, 4991 N/kg/sec) would occur at 25-percent hydrogen and 2.96 F₂/Li mixture ratio. This high value reflects the correspondingly high level of measured specific impulse efficiency. The lower deliverable specific impulse at F₂/Li mixture ratio of 2.5 corresponds to lower theoretical values.

The experimental results may also be extrapolated to the case of a regeneratively cooled LLi/LF₂/LH₂ engine at the following conditions: P_c = 1000 psia (6.89 x 10⁶ N/m²), F₂/Li mixture ratio = 2.74, H₂ = 25 percent, bell nozzle with ε = 100. Assuming an 0.8-power variation of heat flux with chamber pressure and the same specific impulse efficiency as experimentally measured (94.7 percent), estimated deliverable vacuum specific impulse under the given conditions is 523 lbf/lbm/sec (5129 N/kg/sec).

CONCLUDING REMARKS

This report presents the results of a three-part program in which the study of the Li/F₂/H₂ tripropellant combination begun in an earlier investigation (reported in NASA CR-72325) was continued and extended. The three parts of the present program were concerned with propellant injection methods, thrust chamber heat flux, and simulated altitude performance with a 60:1 area ratio nozzle.

It was found that with an oxidizer-rich gas generator, injection of the hydrogen at 1 inch (2.54 cm) from the lithium injector gave corrected c* efficiencies of approximately 98 percent. The same c* efficiencies were also obtained with a fuel-rich gas generator. These results indicate that this level of c* efficiency would be expected if all three propellants were injected at the same axial location. They also make available alternate methods of tripropellant injection for consideration in engine designs.

Measured Li/F₂/H₂ heat flux levels in the thrust chamber nozzle were somewhat below those predicted by the Bartz simplified equation. In the combustion chamber and at the entrance region of the convergent nozzle, the heat transfer characteristics were complicated by the presence of a layer of condensed material deposited on the walls. This coating had two opposing effects on heat flux: an increase, due to the heat of condensation, and a reduction, due to the thermal barrier formed after deposition.

The high contraction ratio of the experimental hardware increased combustion chamber heat flux in two ways, first, by the generally observed enhancement resulting from high contraction ratio and second, by the increase in chamber wall coating resulting from the low gas velocity in this region. Both these effects are expected to be reduced in thrust chambers with more conventional contraction ratios. In any event, the heat flux measurements showed that regenerative cooling would be quite feasible for a Li/F₂/H₂ engine.

The altitude simulation tests with the 60:1 area ratio nozzle showed conclusively that the high theoretical performance of the Li/F₂/H₂ tripropellant combination can be approached in experimental firings. Actual, uncorrected specific impulse efficiencies of approximately 95-percent were measured at nominal test conditions ($P_c = 700$ psia, 4.83×10^6 N/m², F₂/Li MR = 3.0, H₂ = 25 percent). This corresponds to a vacuum specific impulse of about 510 to 520 lbf/lbm/sec (4991 to 5100 N/kg/sec) deliverable by an engine regeneratively cooled with liquid hydrogen, depending upon the actual design. The experimental results confirm the earlier indications, obtained in the c* efficiency measurements, that the presence of two-phase flow has only minor effects on Li/F₂/H₂ performance. At hydrogen levels of 25 percent or less, condensation in the bulk flow begins downstream of the throat and hence has little effect on performance; at 35-percent hydrogen, where a condensed phase is present throughout the thrust chamber, indicated particles sizes are small enough so that two-phase flow losses remain low.

The present program has advanced the technology of the Li/F₂/H₂ tripropellant combination by experimental demonstration of a simplified injection method, by determination of thrust chamber heat flux, and by demonstration of the high specific impulse efficiencies (i.e., low expansion losses) attainable with a 60:1 expansion ratio nozzle. Consideration can now be given to the application of this technology to practical Li/F₂/H₂ thrust chamber design concepts.

REFERENCES

1. Arbit, H. A., R. A. Dickerson, S. D. Clapp, and C. K. Nagai, Lithium-Fluorine-Hydrogen Propellant Study, NASA CR-72325, Contract NAS3-7954, Prepared for National Aeronautics and Space Administration by Rocketdyne, a division of North American Rockwell Corporation, Canoga Park, California, February 1968.
2. Arbit, H. A., and S. D. Clapp, Fluorine-Hydrogen Performance Evaluation, Phase I, Part I: Analysis, Design, and Demonstration of High-Performance Injectors for the Liquid Fluorine-Gaseous Hydrogen Propellant Combination, NASA CR-54978, Contract NASw-1229, Prepared for National Aeronautics and Space Administration by Rocketdyne, a division of North American Aviation, Inc., Canoga Park, California, July 1966.
3. Ingebo, R. D., Drop-Size Distributions for Impinging-Jet Breakup in Air-streams Simulating the Velocity Conditions in Rocket Combustors, NACA TN-4222, March 1958.
4. Falk, A. Y., S. D. Clapp, and C. K. Nagai, Space Storable Propellant Performance Study, NASA CR-72487, Contract NAS3-11199, Prepared for National Aeronautics and Space Administration by Rocketdyne, a division of North American Rockwell Corporation, Canoga Park, California, November 1968.
5. Bartz, D. R., "A Simple Equation for Rapid Estimation of Rocket Nozzle Convective Heat Transfer Coefficients," Jet Propulsion, Vol. 27, January 1957, pp. 49-51.
6. Hatch, J. E., et al., Graphical Presentation of Difference Solutions for Transient Radial Heat Conduction in Hollow Cylinders with Heat Transfer at the Inner Radius and Finite Slabs with Heat Transfer at One Boundary, NASA TR R-56, 1960.
7. Eckert, E. R. G., and R. M. Drake, Jr., Heat and Mass Transfer, 2nd Edition, McGraw-Hill, New York, 1959, p. 211.
8. Carlson, L. W. and J. D. Seader, A Study of the Heat Transfer Characteristics of Hot Gas Ignition, Final Report, AFRPL-TR-65-158, Contract AF04 (611)-9884, Rocketdyne, a division of North American Aviation, Inc. Canoga Park, California, June 1965.

9. Gambill, W. R., "Generalized Prediction of Burnout Heat Flux for Flowing, Subcooled, Wetting Liquids," Chemical Engineering Progress Symposium Series, Vol. 59, No. 41, pp. 71-87, 1963.
10. Schneider, P. J., Temperature Response Charts, John Wiley & Sons, Inc., New York, N. Y., 1963.
11. Marble, F. E., "Nozzle Contours for Minimum Particle Lag Loss," AIAA Journal, Vol. 1, No. 12, pp. 2793-2801 (December 1963).
12. Kliegel, J. R., and G. R. Nickerson, Flow of Gas-Particle Mixtures in Axially Symmetric Nozzles, Report No. TM-7106-0023-MJ000, Space Technology Laboratories (1963).
13. Bailey, W. S. et al., "Gas-Particle Flow in Axisymmetric Nozzle," ARS Journal, Vol. 31, No. 6, pp. 793-798 (June 1961).
14. Quan, V., Analytical Predictions of Delivered Specific Impulse, Final Report, No. 02874-6008-R000, Prepared by TRW Systems for NASA, Manned Spacecraft Center, Contract NAS9-4358, 29 September 1967.
15. Rannie, W. D., "Perturbation Analysis of One-Dimensional Heterogeneous Flow in Rocket Nozzles," Detonation and Two-Phase Flow, S. S. Penner and F. A. Williams, Editors, Academic Press, New York, 1962, pp. 117-144.
16. Kliegel, J. R., "Gas-Particle Nozzle Flows," Ninth Symposium (International) on Combustion, Academic Press, New York, 1963, pp. 811-826.
17. Høglund, R. F., "Recent Advances in Gas-Particle Nozzle Flows," ARS Journal, Vol. 32, No. 5, pp. 662-671 (May 1962).
18. Marble, F. E., "The Role of Approximate Analytical Results in the Study of Two-Phase Flow in Nozzles (U)," Proceedings of the Air Force Rocket Propulsion Laboratory Two-Phase Flow Conference, AFRPL-TR-67-223, Vol. II, pp. 407-426, Air Force Rocket Propulsion Laboratory, Edwards, California, 15-16 March 1967, CONFIDENTIAL.
19. Grey, J., "Calibration of Turbine Flowmeters for Cryogenic Operations," ARS Journal, Vol. 30, pp. 192-193, February 1960.
20. Bulletin for Model 10C1510 and 10C1511 Turbine Flowmeters, Division 1, Fischer & Porter Company, Warminster, Pennsylvania, Publication No. 14815.

21. A.S.M.E. Research Committee on Fluid Meters, Fluid Meters - Their Theory and Application, Fifth Edition, American Society of Mechanical Engineers, New York, N. Y., 1959.
22. Reid, R. C. and T. K. Sherwood, The Properties of Gases and Liquids, Second Edition, McGraw-Hill Book Co., New York, N. Y., 1966.
23. Sellers, J. P., Jr., "Effect of Carbon Deposition on Heat Transfer in a LOX/RP-1 Thrust Chamber," Amer. Rocket Society Journal, Vol. 31, No. 5, 662-663 (1961).
24. von Glahn, U. H., "Correlation of Gas-Side Heat Transfer for Axisymmetric Rocket Engine Nozzles," NASA TM-X-1748, February 1969.
25. Bartz, D. R., "Turbulent Boundary-Layer Heat Transfer from Rapidly Accelerating Flow of Rocket Combustion Gases and of Heated Air," Advances in Heat Transfer, J. P. Hartnett and T. F. Irvine, Jr., Editors, Vol. 2, Academic Press, New York, N. Y., 1965, pp. 1-108.
26. Bott, J. P. and D. A. Nelson, LF₂/GH₂ Toroidal Engine Performance and Heat Transfer Study, RR-66-2, Rocketdyne, a division of North American Aviation, Inc., Canoga Park, California, March 1966.
27. Huntsinger, J. P., Tripropellant Engine System Study, Final Report, R-7877, Contract NASw-1838, Prepared for National Aeronautics and Space Administration by Rocketdyne, a division of North American Rockwell Corporation, Canoga Park, California, June 1969.

TABLE 1

LITHIUM INJECTION TUBE ORIFICE TIPS
USED IN RUN NO. 69-9

Injection Tube No.	Orifice Tip Material	Pretest Length		Posttest Length	
		in.	cm	in.	cm
1	321 SS	0.43	1.09	0.20	0.51
2	Ni 270	0.43	1.09	0.16	0.41
3	321 SS	0.67	1.70	0.35	0.89
4	Ni 270	0.67	1.70	0.25	0.64
5	Tantalum	0.43	1.09	0.43	1.09
6	321 SS	0.43	1.09 (with 0.015 in., 0.4 mm, gap around tip)	0.16	0.41
7	321 SS	0.43	1.09 (with Ni sleeve around tip)	0.20	0.51
8	321 SS	0.43	1.09 (with "Saureisen" around tip)	0.20	0.51

TABLE 2

TEST DATA SUMMARY,
OXIDIZER-RICH GAS GENERATOR FIRINGS

Run No.	Duration, seconds	\dot{w}_{LF_2}		F_2/H_2 MR	P_c		c^*		η_{c^*} (uncorrected), percent
		lb/sec	kg/sec		psia	N/m^2	ft/sec	m/sec	
68-1	2.1	2.60	1.18	520	565	3.90×10^6	1735	529	99
68-2	3.0	2.53	1.15	506	558	3.85×10^6	1730	527	98
68-3	3.0	2.36	1.07	472	538	3.71×10^6	1815	553	99
68-4	3.6	2.34	1.06	468	536	3.70×10^6	1825	556	99

TABLE 3

TEST DATA SUMMARY,
FUEL-RICH GAS GENERATOR FIRINGS

Run No.	Duration, seconds	\dot{w}_{LF_2}		\dot{w}_{GH_2}		\dot{w}_T		F_2/H_2 MR	P_c		c^* (uncorrected), ft/sec	η_{c^*} (uncorrected), percent
		lb/sec	kg/sec	lb/sec	kg/sec	lb/sec	kg/sec		psia	N/m^2		
68-5	2.0	2.32	1.05	1.22	0.55	3.54	1.60	1.90	834	5.75×10^6	8386	100.5
68-6	2.5	2.37	1.08	0.81	0.37	3.18	1.45	2.94	742	5.12×10^6	8314	96.8
68-7	2.0	2.44	1.11	1.66	0.75	4.10	1.86	1.47	913	6.29×10^6	7941	97.7
68-8												
A	2.0	2.56	1.16	0.88	0.40	3.44	1.56	2.93	790	5.45×10^6	8243	96.0
B	2.0	2.47	1.12	1.22	0.55	3.69	1.67	2.03	823	5.67×10^6	8070	96.3
C	2.0	2.33	1.06	1.65	0.75	3.98	1.81	1.41	856	5.90×10^6	7853	97.0

TABLE 4
 TEST DATA SUMMARY, CHARACTERISTIC VELOCITY EFFICIENCY,
 OXIDIZER-RICH GAS GENERATOR INJECTION METHOD
 F₂/Li Combustion Chamber Length = 1.0 inch (2.54 cm)

Run No.	68-2			68-3		
Combustion Chamber Length, in. cm	12 30.5			22 55.9		
	1	2	3	1	2	3
\dot{w}_{F_2} , lb/sec	2.48	2.37	2.26	2.68	2.61	2.45
kg/sec	1.13	1.07	1.02	1.22	1.18	1.11
\dot{w}_{Li} , lb/sec	1.21	1.03	0.93	0.94	0.80	0.97
kg/sec	0.55	0.47	0.42	0.43	0.36	0.44
\dot{w}_{GH_2} (main), lb/sec	0.82	1.14	1.54	0.83	1.15	1.56
kg/sec	0.37	0.52	0.70	0.38	0.52	0.71
\dot{w}_{GH_2} (GG), lb/sec	0.005	0.005	0.005	0.005	0.005	0.005
kg/sec	0.002	0.002	0.002	0.002	0.002	0.002
\dot{w}_T , lb/sec	4.52	4.54	4.73	4.46	4.57	4.98
kg/sec	2.05	2.06	2.15	2.02	2.07	2.26
H ₂ , percent	18.3	25.2	32.6	18.8	25.4	31.4
F ₂ /Li Mixture Ratio	2.05	2.30	2.43	2.86	3.25	2.53
P _c , psia	457	487	524	424	467	516
10 ⁶ N/m ²	3.15	3.36	3.61	2.92	3.22	3.56
F (sea level), lbf	1468	1594	1729	1426	1584	1767
N	6530	7090	7691	6343	7046	7860
c* (measured), ft/sec	7835	8354	8720	7778	8441	8643
m/sec	2388	2546	2658	2371	2573	2634
f _{TOTAL} (1)	1.009	1.008	1.007	1.013	1.010	1.010
θ _{TOTAL} (2)	1.035	1.032	1.032	1.040	1.037	1.035
[η _{c*}] _{P_c} (corrected), percent	96.8	98.3	98.2	92.4	97.4	97.6
[η _{c*}] _F (corrected), percent	94.9	96.8	96.8	90.7	95.1	95.1

(1) Total correction applicable to measured characteristic velocity.

(2) Total correction applicable to measured thrust.

TABLE 5
TEST DATA SUMMARY
CHARACTERISTIC VELOCITY EFFICIENCY, FUEL-RICH

Task No.	I								
Run No.	68-9		68-10			68-11		69-1	
Chamber Length, in.	30		15			15		7	
cm	76.2		38.1			38.1		17.8	
Step No.	1	2	1	2	3	2	3	1	2
\dot{w}_{LF_2} , lb/sec	2.52	2.35	2.58	2.40	2.23	2.41	2.32	2.53	2.36
kg/sec	1.14	1.07	1.17	1.09	1.01	1.09	1.05	1.15	1.07
\dot{w}_{Li} , lb/sec	1.05	0.97	0.45	0.49	0.45	1.05	0.91	1.11	1.04
kg/sec	0.48	0.44	0.21	0.22	0.21	0.48	0.42	0.50	0.47
\dot{w}_{GH_2} , lb/sec	0.88	1.22	0.89	1.23	1.66	1.25	1.69	0.92	1.28
kg/sec	0.40	0.55	0.40	0.56	0.75	0.57	0.76	0.42	0.58
\dot{w}_T , lb/sec	4.45	4.54	3.92	4.12	4.34	4.71	4.92	4.56	4.68
kg/sec	2.02	2.06	1.78	1.87	1.97	2.14	2.23	2.07	2.12
H ₂ , percent	19.7	26.8	22.6	29.8	38.2	26.5	34.3	20.1	27.3
F ₂ /Li Mixture Ratio	2.39	2.42	5.73	4.86	4.93	2.29	2.53	2.28	2.27
P _c , psia	639	677	574	628	666	698	734	630	663
10 ⁶ N/m ²	4.41	4.67	3.96	4.33	4.59	4.81	5.06	4.34	4.57
F (sea level), lbf	1495	1585	1363	1477	1559	1674	1771	1562	1659
N	6650	7050	6063	6570	6935	7446	7878	6948	7380
c* (measured), ft/sec	7988	8341	8255	8603	8653	8479	8576	8061	8329
m/sec	2435	2542	2516	2622	2637	2584	2614	2457	2539
f _{TOTAL} ⁽¹⁾	1.024	1.017	1.017	1.013	1.008	1.008	1.006	1.003	1.005
θ _{TOTAL} ⁽²⁾	1.064	1.052	1.043	1.040	1.036	1.033	1.030	1.029	1.030
[η _{c*}] _{P_c} (corrected), percent	96.8	96.9	97.0	98.5	97.4	98.4	95.2	96.2	96.2
[η _{c*}] _F (corrected), percent	96.1	95.1	95.6	95.8	94.8	95.9	92.9	95.6	95.4

(1) Total correction applicable to measured characteristic velocity

(2) Total correction applicable to measured thrust

EOLDOUT FRAME |

SUMMARY

LE-RICH GAS GENERATOR INJECTION METHOD

					II			III		
69-1		69-2			69-5			69-7		
7		15			9			9		
17.8		38.1			22.9			22.9		
2	3	1	2	3	1	2	3	1	2	3
2.36	2.19	2.74	2.57	2.43	2.72	2.58	2.33	2.66	2.52	2.29
1.07	1.00	1.24	1.17	1.10	1.23	1.17	1.06	1.20	1.14	1.04
1.04	1.00	0.98	0.91	0.82	0.94	0.85	0.75	0.90	0.85	0.74
0.47	0.45	0.44	0.41	0.37	0.42	0.39	0.34	0.41	0.39	0.33
1.28	1.73	0.94	1.26	1.72	0.90	1.12	1.56	0.90	1.12	1.56
0.58	0.78	0.43	0.57	0.78	0.41	0.51	0.71	0.41	0.51	0.71
4.68	4.92	4.66	4.74	4.97	4.56	4.55	4.64	4.46	4.49	4.59
2.12	2.23	2.11	2.15	2.26	2.07	2.07	2.10	2.02	2.04	2.08
27.3	35.1	20.2	26.6	34.6	19.8	24.6	33.7	20.3	24.9	34.1
2.27	2.20	2.79	2.84	2.95	2.91	3.02	3.10	2.97	2.96	3.10
663	682	640	679	704	680	696	730	669	700	757
4.57	4.70	4.41	4.68	4.85	4.69	4.80	5.03	4.61	4.83	5.22
1659	1729	1653	1761	1847						
7380	7691	7353	7833	8216						
8329	8199	8213	8596	8534	8190	8390	8635	8190	8419	8814
2539	2499	2503	2620	2601	2496	2557	2632	2496	2566	2687
1.005	1.003	1.009	1.006	1.007	1.034	1.029	1.014	1.035	1.029	1.018
1.030	1.026	1.030	1.032	1.030						
96.2	92.5	96.2	98.0	94.1	97.5	97.7	96.3	97.5	98.1	98.6
95.4	92.5	96.6	98.4	95.2						

OUT FRAME 2

TABLE 6
SUMMARY OF HEAT TRANSFER DATA

A. Test Parameters														
Task No.	II									III				
Run No.	69-4			69-5			69-6			69-7			69-9	
Step No.	1	2	3	1	2	3	1	2	3	1	2	3	1	2
P_c , psia	(664)	(674)	(739)	680	696	730	(624)	(654)	(715)	669	700	757	(695)	(725)
$10^6 N/m^2$	(4.58)	(4.65)	(5.10)	4.69	4.80	5.03	(4.30)	(4.51)	(4.93)	4.61	4.83	5.22	(4.79)	(5.00)
\dot{w}_T , lb/sec	4.34	4.40	4.52	4.56	4.55	4.64	4.11	4.18	4.41	4.46	4.49	4.59	4.62	4.63
kg/sec	1.97	1.99	2.05	2.07	2.07	2.10	1.86	1.89	2.00	2.02	2.04	2.08	2.10	2.10
H_2 , percent	20.5	25.2	34.1	19.8	24.6	33.7	21.8	26.7	35.2	20.3	24.9	34.1	18.9	23.5
F_2/Li MR	3.84	3.77	3.72	2.91	3.02	3.10	4.70	4.71	4.16	2.97	2.96	3.10	2.45	2.47

B. Area Ratio Variation With Axial Distance					
Distance From Injector Face		Contraction Ratio	Distance From Injector Face		Expansion Ratio
in.	cm		in.	cm	
Combustion Chamber		11.5	16.8	42.7	1.1
9.6	24.4	10.3	17.2	43.7	1.4
10.2	25.9	8.8	17.7	45.0	1.8
12.0	30.5	5.3	18.3	46.5	2.5
14.3	36.3	2.2	19.6	49.8	4.0
15.0	38.1	1.6	24.7	62.7	15.0
15.4	39.1	1.2	26.4	67.1	20.0
15.9	40.4	1.03	27.8	70.6	25.0
16.3	41.4	1.0	29.2	74.2	30.0
			30.2	76.7	35.0
			31.5	80.0	40.0
			33.4	84.8	50.0
			34.8	88.4	57.0

TABLE 6
(Continued)

C. Measured Heat Flux															
Run No.		69-4			69-5			69-6			69-7			69-9	
Step No.		1	2	3	1	2	3	1	2	3	1	2	3	1	2
A/A _t	Q/A														
11.5 (Chamber)	B/in. ² /sec	13.2	11.3	9.8	16.8	14.0	12.1	12.7	11.2	10.8	15.3	12.9	11.2		
	10 ⁶ W/m ²	21.6	18.5	16.0	27.5	22.9	19.8	20.8	18.3	17.6	25.0	21.1	18.3		
10.3	B/in. ² /sec	14.1	14.1	13.9	17.9	15.2	7.7	14.5	12.5	14.0	17.7	15.3	14.9	27.0	25.4
	10 ⁶ W/m ²	23.0	23.0	22.7	29.2	24.8	12.6	23.7	20.4	22.9	28.9	25.0	24.3	44.1	41.5
8.8	B/in. ² /sec				12.3	10.7	4.6	10.3	9.3	9.4	11.8	10.2	8.8	13.4	11.1
	10 ⁶ W/m ²				20.1	17.5	7.5	16.8	15.2	15.4	19.3	16.7	14.4	21.9	18.1
5.3	B/in. ² /sec	13.7	14.7	11.4	13.4	11.6	8.8	10.2	8.8	8.3	13.6	11.6	8.6	15.7	12.6
	10 ⁶ W/m ²	22.4	24.0	18.6	21.9	19.0	14.4	16.7	14.4	13.6	22.2	19.0	14.1	25.7	20.6
2.2	B/in. ² /sec	16.2	13.7	9.0	16.5	13.4	9.7	13.8	11.7	9.7	16.2	14.0	9.6	17.6	14.2
	10 ⁶ W/m ²	26.5	22.4	14.7	27.0	21.9	15.8	22.5	19.1	15.8	26.5	22.9	15.7	28.8	23.2
1.6	B/in. ² /sec	17.1	14.7	9.0	15.8	13.8	9.8	15.7	14.0	11.2	16.2	14.1	9.7	15.0	13.0
	10 ⁶ W/m ²	27.9	24.0	14.7	25.8	22.5	16.0	25.7	22.9	18.3	26.5	23.0	15.8	24.5	21.2
1.2	B/in. ² /sec	20.1	18.4	9.5	18.1	16.2	10.7	19.3	18.9	16.8	18.4	16.7	10.5	17.8	15.1
	10 ⁶ W/m ²	32.8	30.1	15.5	29.6	26.5	17.5	31.5	30.9	27.5	30.1	27.3	17.1	29.1	24.7
1.03	B/in. ² /sec	20.0	19.0	6.9	17.6	17.8	7.7	20.3	19.8	19.2	17.5	16.5	7.5	16.7	13.0
	10 ⁶ W/m ²	32.7	31.0	11.3	28.8	29.1	12.6	33.2	32.3	31.4	28.6	27.0	12.2	27.2	21.2
1.00	B/in. ² /sec	18.3	17.8	5.0	15.7	17.1	5.0	19.1	18.9	17.9	16.3	15.4	4.7	14.9	10.8
	10 ⁶ W/m ²	29.9	29.1	8.2	25.6	27.9	8.2	31.2	30.9	29.2	26.6	25.2	7.7	24.3	17.6
1.1	B/in. ² /sec	18.1	17.8	4.8	15.8	17.0	4.7	17.7	17.4	16.9	16.0	15.7	4.0	14.3	9.3
	10 ⁶ W/m ²	29.6	29.1	7.8	25.8	27.8	7.7	28.9	28.4	27.6	26.1	25.6	6.5	23.4	15.2
1.4	B/in. ² /sec	14.2	13.8	9.1	13.9	13.6	10.5	12.8	13.0	12.5	13.6	13.2	5.8	12.3	7.2
	10 ⁶ W/m ²	23.2	22.5	14.9	22.7	22.2	17.1	20.9	21.2	20.4	22.2	21.6	9.5	20.1	11.8
1.8	B/in. ² /sec	10.2	10.2	11.6	9.9	9.7	12.5	9.8	10.1	9.5	10.2	9.9	11.7	9.9	5.9
	10 ⁶ W/m ²	16.7	16.7	19.0	16.2	15.8	20.4	16.0	16.5	15.5	16.7	16.2	19.1	16.2	9.6
2.5	B/in. ² /sec	8.9	9.6	8.5											
	10 ⁶ W/m ²	14.5	15.7	13.9											
4.0	B/in. ² /sec										1.7	1.6	1.2	2.5	2.7
	10 ⁶ W/m ²										2.8	2.6	2.0	4.1	4.4
15.0	B/in. ² /sec										0.5	0.8	0.6	0.6	0.9
	10 ⁶ W/m ²										0.8	1.3	1.0	1.0	1.5
20.0	B/in. ² /sec										0.5	0.6	0.5	0.5	0.7
	10 ⁶ W/m ²										0.8	1.0	0.8	0.8	1.1
25.0	B/in. ² /sec										0.5	0.5	0.4	0.6	0.5
	10 ⁶ W/m ²										0.8	0.8	0.7	1.0	0.8
30.0	B/in. ² /sec										0.4	0.4	0.4	0.5	0.5
	10 ⁶ W/m ²										0.7	0.7	0.7	0.8	0.8
35.0	B/in. ² /sec										0.4	0.4	0.4	0.4	0.5
	10 ⁶ W/m ²										0.7	0.7	0.7	0.7	0.8
40.0	B/in. ² /sec										0.3	0.3	0.3	0.4	0.4
	10 ⁶ W/m ²										0.5	0.5	0.5	0.7	0.7
50.0	B/in. ² /sec										0.3	0.3	0.3	0.3	0.3
	10 ⁶ W/m ²										0.5	0.5	0.5	0.5	0.5
57.0	B/in. ² /sec										0.2	0.2	0.2	0.3	0.3
	10 ⁶ W/m ²										0.3	0.3	0.3	0.5	0.5

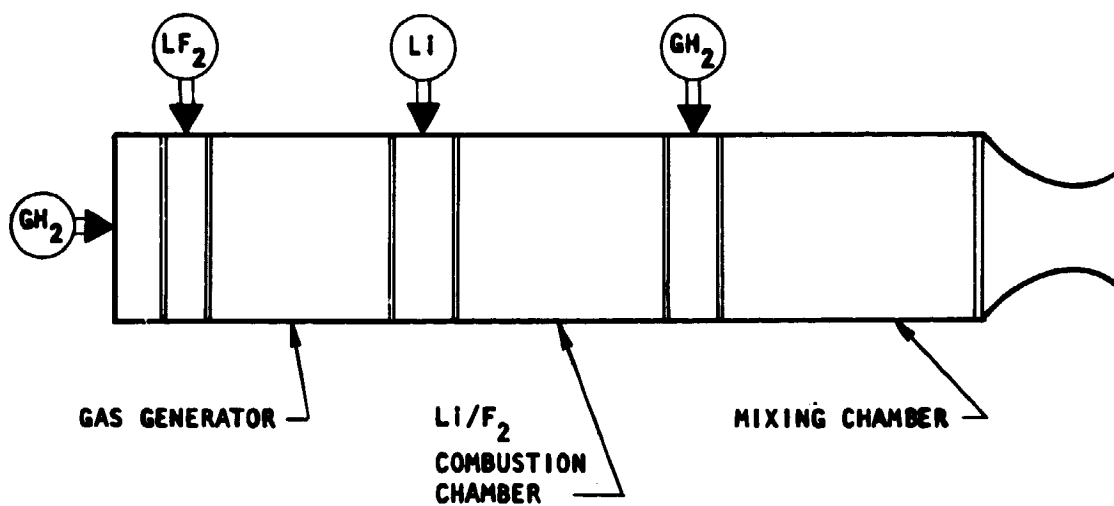
TABLE 6
(Concluded)

D. Heat Transfer Coefficients															
Run No.		69-4			69-5			69-6			69-7			69-9	
Step No.		1	2	3	1	2	3	1	2	3	1	2	3	1	2
A/A _t	h _g														
11.5 (Chamber)	10 ⁻³ B/in. ² /sec/R	4.03	3.62	4.14	5.12	4.69	5.18	3.72	3.66	4.28	4.52	3.25	4.61		
	10 ³ W/m ² /K	11.9	10.7	12.2	15.1	13.8	15.2	10.9	10.8	12.6	13.3	9.6	13.6		
10.3	10 ⁻³ B/in. ² /sec/R	3.98	4.24	5.41	4.98	4.59	2.80	3.91	3.75	5.05	4.83	3.59	5.54	7.63	7.70
	10 ³ W/m ² /K	11.7	12.5	15.9	14.7	13.5	8.24	11.5	11.0	14.9	14.2	10.6	16.3	22.4	22.7
8.8	10 ⁻³ B/in. ² /sec/R				3.36	3.17	1.64	2.76	2.74	3.33	3.17	2.37	3.16	3.59	3.15
	10 ³ W/m ² /K				9.89	9.32	4.82	8.12	8.06	9.80	9.32	6.97	9.30	10.6	9.27
5.3	10 ⁻³ B/in. ² /sec/R	3.92	4.56	4.43	3.77	3.56	3.29	2.77	2.64	2.96	3.76	2.76	3.16	4.32	3.64
	10 ³ W/m ² /K	11.5	13.4	13.0	11.1	10.5	9.68	8.15	7.77	8.71	11.1	8.12	9.30	12.7	10.7
2.2	10 ⁻³ B/in. ² /sec/R	4.56	4.04	3.29	4.60	4.04	3.56	3.74	3.49	3.38	4.41	3.29	3.43	4.75	4.08
	10 ³ W/m ² /K	13.4	11.9	9.68	13.5	11.9	10.5	11.0	10.3	9.94	13.0	9.68	10.1	14.0	12.0
1.6	10 ⁻³ B/in. ² /sec/R	4.88	4.40	3.32	4.40	4.18	3.61	4.31	4.26	3.97	4.44	3.35	3.51	4.02	3.72
	10 ³ W/m ² /K	14.4	12.9	9.77	12.9	12.3	10.6	12.7	12.5	11.7	13.1	9.90	10.3	11.8	10.9
1.2	10 ⁻³ B/in. ² /sec/R	5.89	5.69	3.53	5.15	5.02	3.99	5.48	6.01	6.32	5.13	4.01	3.82	4.83	4.37
	10 ³ W/m ² /K	17.3	16.7	10.4	15.2	14.8	11.7	16.1	17.7	18.6	15.1	11.8	11.2	14.2	12.9
1.03	10 ⁻³ B/in. ² /sec/R	5.70	5.74	2.48	4.90	5.45	2.75	5.67	6.21	7.20	4.76	3.90	2.63	4.44	3.67
	10 ³ W/m ² /K	16.8	16.9	7.30	14.4	16.0	8.10	16.7	18.3	21.2	14.0	11.5	7.74	13.1	10.8
1.00	10 ⁻³ B/in. ² /sec/R	5.40	5.59	1.79	4.47	5.44	1.78	5.53	6.15	6.95	4.57	3.74	1.65	4.03	3.06
	10 ³ W/m ² /K	15.9	16.4	5.27	13.2	16.0	5.24	16.3	18.1	20.4	13.4	11.0	4.85	11.9	9.00
1.1	10 ⁻³ B/in. ² /sec/R	5.18	5.41	1.72	4.40	5.26	1.68	4.93	5.43	6.29	4.37	3.75	1.40	3.82	2.61
	10 ³ W/m ² /K	15.2	15.9	5.06	12.9	15.5	4.94	14.5	16.0	18.5	12.9	11.0	4.12	11.2	7.68
1.4	10 ⁻³ B/in. ² /sec/R	4.10	4.25	3.46	3.95	4.28	4.00	3.59	4.06	4.67	3.77	3.20	2.08	3.32	2.02
	10 ³ W/m ² /K	12.1	12.5	10.2	11.6	12.6	11.8	10.6	11.9	13.7	11.1	9.41	6.12	9.77	5.94
1.8	10 ⁻³ B/in. ² /sec/R	2.84	3.01	4.45	2.71	2.93	4.81	2.66	3.07	3.40	2.75	2.35	4.40	2.61	1.65
	10 ³ W/m ² /K	8.36	8.85	13.1	7.97	8.62	14.2	7.83	9.03	10.0	8.09	6.91	12.9	7.68	4.85
2.5	10 ⁻³ B/in. ² /sec/R	2.49	2.87	3.22											
	10 ³ W/m ² /K	7.33	8.44	9.47											
4.0	10 ⁻³ B/in. ² /sec/R										0.43	0.45	0.47	0.75	0.88
	10 ³ W/m ² /K										1.27	1.32	1.38	2.21	2.59
15.0	10 ⁻³ B/in. ² /sec/R										0.13	0.23	0.24	0.17	0.28
	10 ³ W/m ² /K										0.38	0.68	0.71	0.50	0.82
20.0	10 ⁻³ B/in. ² /sec/R										0.12	0.19	0.20	0.15	0.23
	10 ³ W/m ² /K										0.35	0.56	0.59	0.44	0.68
25.0	10 ⁻³ B/in. ² /sec/R										0.12	0.13	0.17	0.16	0.16
	10 ³ W/m ² /K										0.35	0.38	0.50	0.47	0.47
30.0	10 ⁻³ B/in. ² /sec/R										0.10	0.12	0.16	0.13	0.15
	10 ³ W/m ² /K										0.29	0.35	0.47	0.38	0.44
35.0	10 ⁻³ B/in. ² /sec/R										0.09	0.10	0.14	0.12	0.13
	10 ³ W/m ² /K										0.26	0.29	0.41	0.35	0.38
40.0	10 ⁻³ B/in. ² /sec/R										0.08	0.10	0.12	0.10	0.12
	10 ³ W/m ² /K										0.24	0.29	0.35	0.29	0.35
50.0	10 ⁻³ B/in. ² /sec/R										0.06	0.08	0.10	0.09	0.10
	10 ³ W/m ² /K										0.18	0.24	0.29	0.26	0.29
57.0	10 ⁻³ B/in. ² /sec/R										0.06	0.07	0.09	0.07	0.09
	10 ³ W/m ² /K										0.18	0.21	0.26	0.21	0.26

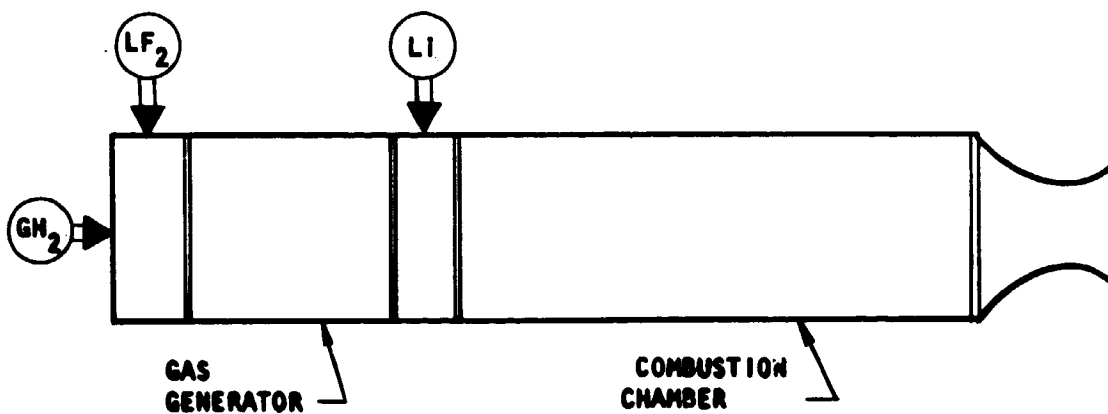
TABLE 7
 DATA SUMMARY, ALTITUDE PERFORMANCE TESTS
 Chamber Length = 9 in. (22.9 cm); $\epsilon = 60$

Run No.	69-7			69-9	
	1	2	3	1	2
\dot{w}_{LF_2} , lb/sec kg/sec	2.66 1.20	2.52 1.14	2.29 1.04	2.66 1.21	2.52 1.14
\dot{w}_{Li} , lb/sec kg/sec	0.90 0.41	0.85 0.39	0.74 0.33	1.09 0.49	1.02 0.46
\dot{w}_{GH_2} , lb/sec kg/sec	0.90 0.41	1.12 0.51	1.56 0.71	0.87 0.40	1.09 0.49
\dot{w}_{T} , lb/sec kg/sec	4.46 2.02	4.49 2.04	4.59 2.08	4.62 2.10	4.63 2.10
H ₂ , percent	20.3	24.9	34.1	18.9	23.5
F ₂ /Li, MR	2.97	2.96	3.10	2.45	2.47
P _c , psia 10 ⁶ N/m ²	669 4.61	700 4.83	757 5.22	(695) (4.79)	(725) (5.00)
F _{vac} [*] , lbf N	2201 9790	2287 10,173	2353 10,467	2157 9595	2228 9911
F _{vac} ^{**} , lbf N	2135 9497	2265 10,075	2326 10,347	2182 9706	2270 10,097
[I _{s,vac}] [*] _{meas} , lbf/lbm/sec N/kg/sec	493 4839	509 4995	513 5027	467 4579	481 4719
[I _{s,vac}] ^{**} _{meas} , lbf/lbm/sec N/kg/sec	479 4694	504 4947	507 4969	472 4632	490 4808
[I _{s,vac}] ^{***} _{meas} , lbf/lbm/sec N/kg/sec	486 4766	506 4962	510 5001	470 4609	486 4766
η_{I_s} (avg), percent	92.8	94.7	94.7	91.2	92.2
Temperature of H ₂ Coolant at Injector, R K	994 524	648 360	378 210	820 456	513 285
[I _{s,vac}] _{theo} , lbf/lbm/sec N/kg/sec	532.1 5218	537.5 5271	531.6 5213	519.9 5098	526.4 5162
[I _{s,vac}] _{del} , lbf/lbm/sec N/kg/sec	494 4844	509 4991	503 4933	474 4648	485 4756

*Uncorrected, based on direct load cell measurement (Appendix C)
 **Uncorrected, based on nozzle pressure measurements (Appendix C)
 ***Average, uncorrected, measured value



A. With Oxidizer-Rich Gas Generator



B. With Fuel-Rich Gas Generator

Figure 1. Schematics of Li/F₂/H₂ Thrust Chambers

		PERCENT HYDROGEN		
		20	25	35
F ₂ /LI MIXTURE RATIO	2.25	B	B	B
	2.74	A B	A* B	A B
	3.25	B	B	B

* DESIGN POINT

A: NOMINAL TEST POINTS, TASK I

B: NOMINAL TEST POINTS, TASKS II AND III

Figure 2. Test Matrix of Percent Hydrogen and F₂/Li Mixture Ratio for the Li/F₂/H₂ Experimental Firings

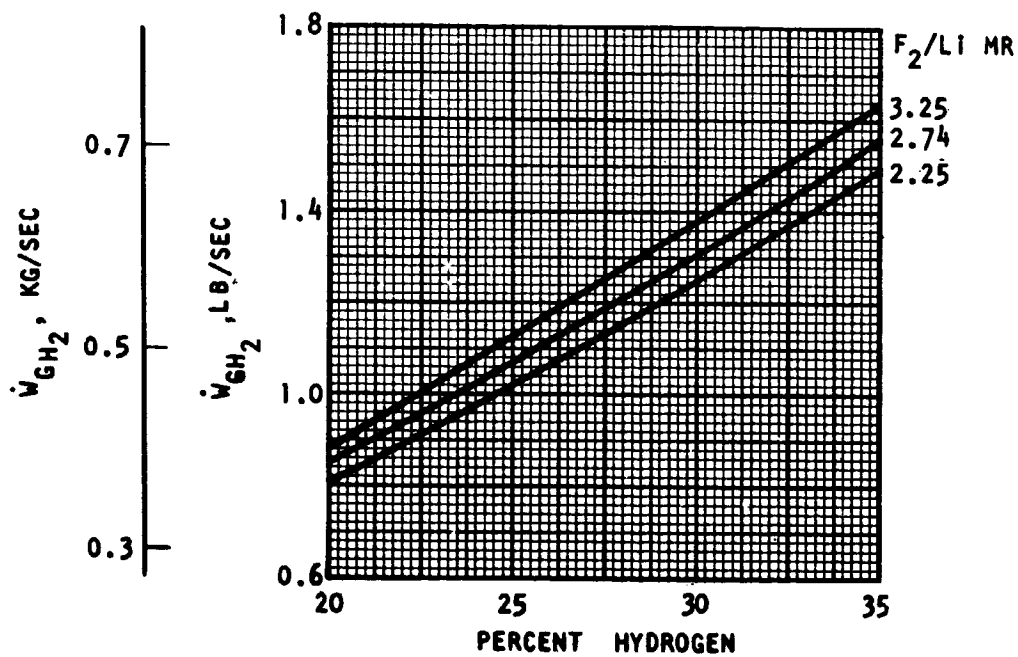
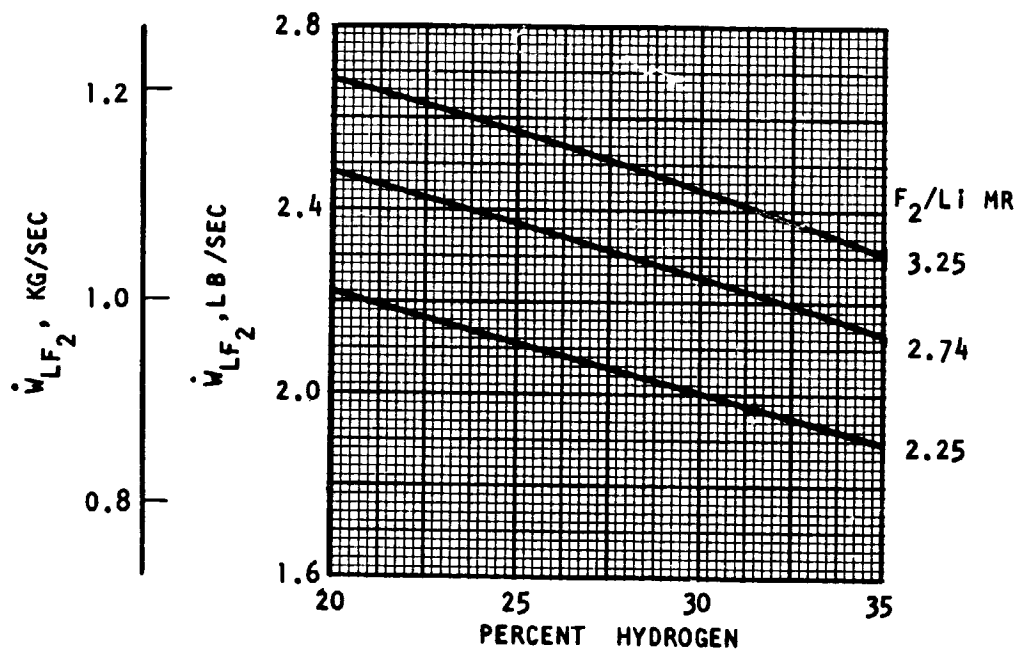


Figure 3. Gas Generator Propellant Flowrates Corresponding to Indicated Tripropellant Test Conditions of Percent Hydrogen and F_2/Li Mixture Ratio

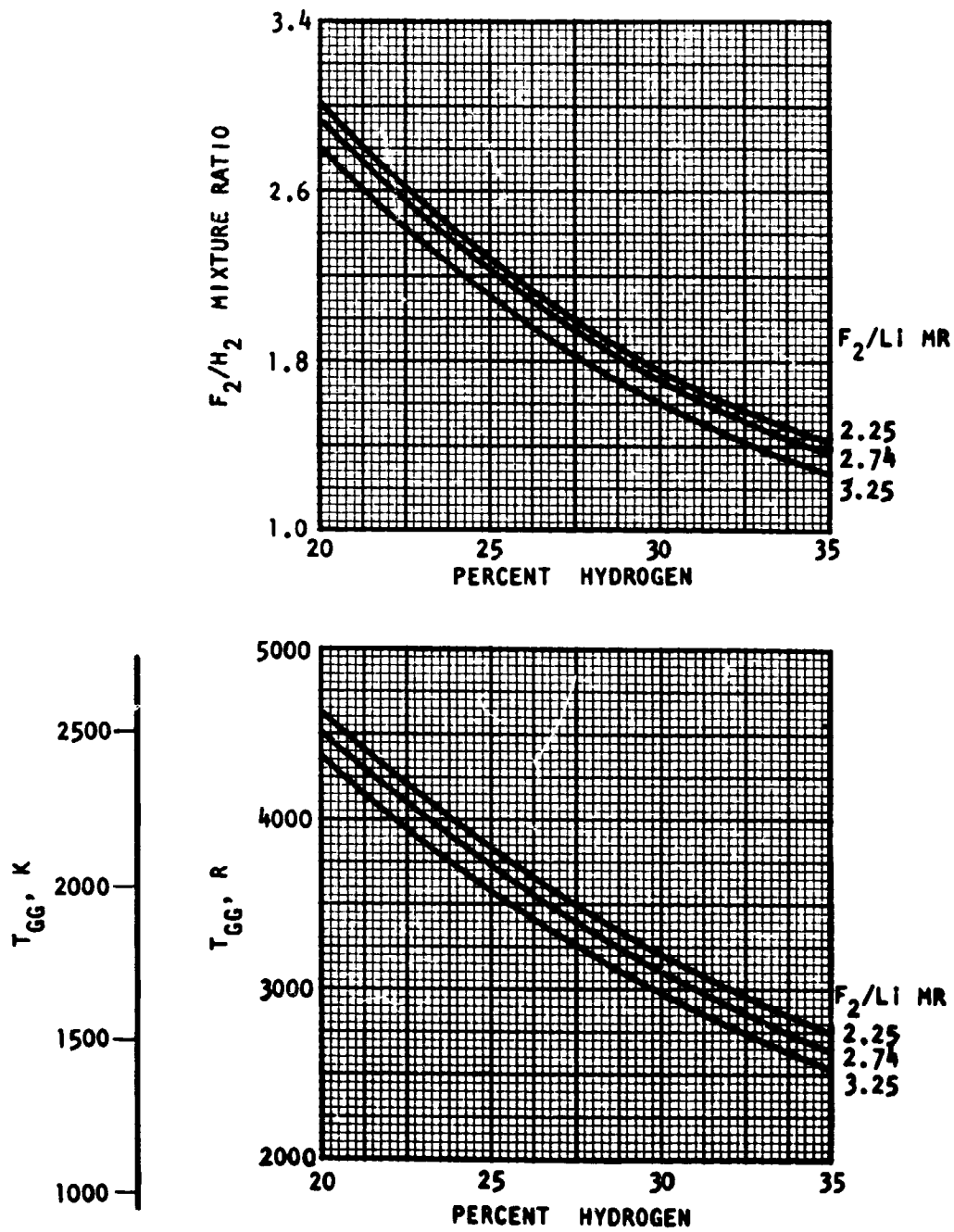


Figure 4. Gas Generator F₂/H₂ Mixture Ratio and Chamber Temperature Corresponding to Indicated Tripropellant Test Conditions of Percent Hydrogen and F₂/Li Mixture Ratio

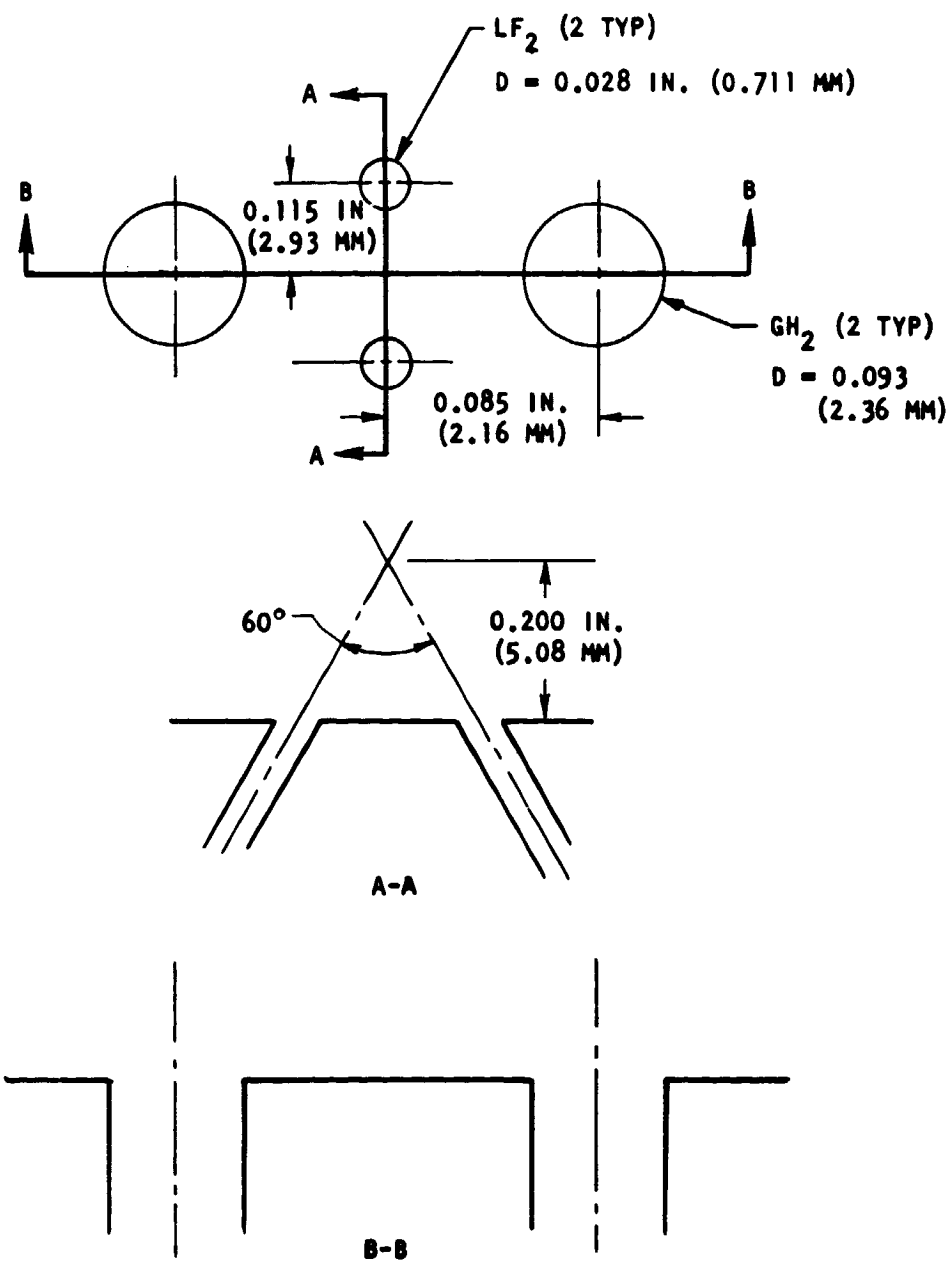


Figure 5. Schematic of Doublet/Showerhead LF_2/GH_2 Injection Element, Mod I Injector



5AJ33-11/14/68-S1B

Figure 6. Face Pattern of Doublet/Showerhead $\text{L}\text{F}_2/\text{G}\text{H}_2$ Injector, Mod I

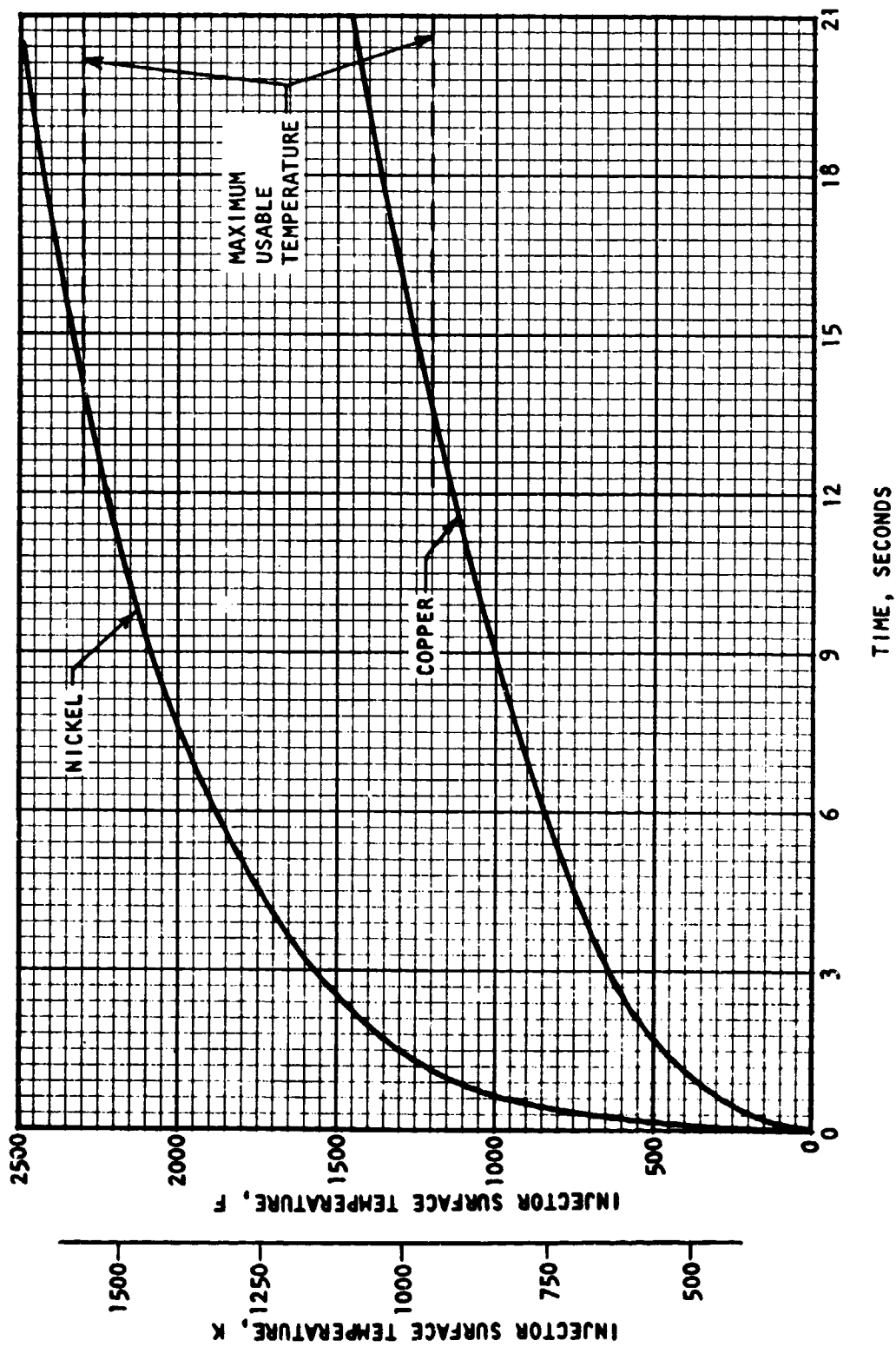


Figure 7. Gas Generator Injector Face Temperatures for Copper and Nickel at Design Conditions as Functions of Firing Duration (No Cooling Effects Included)

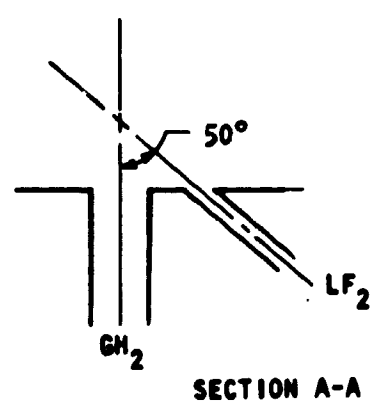
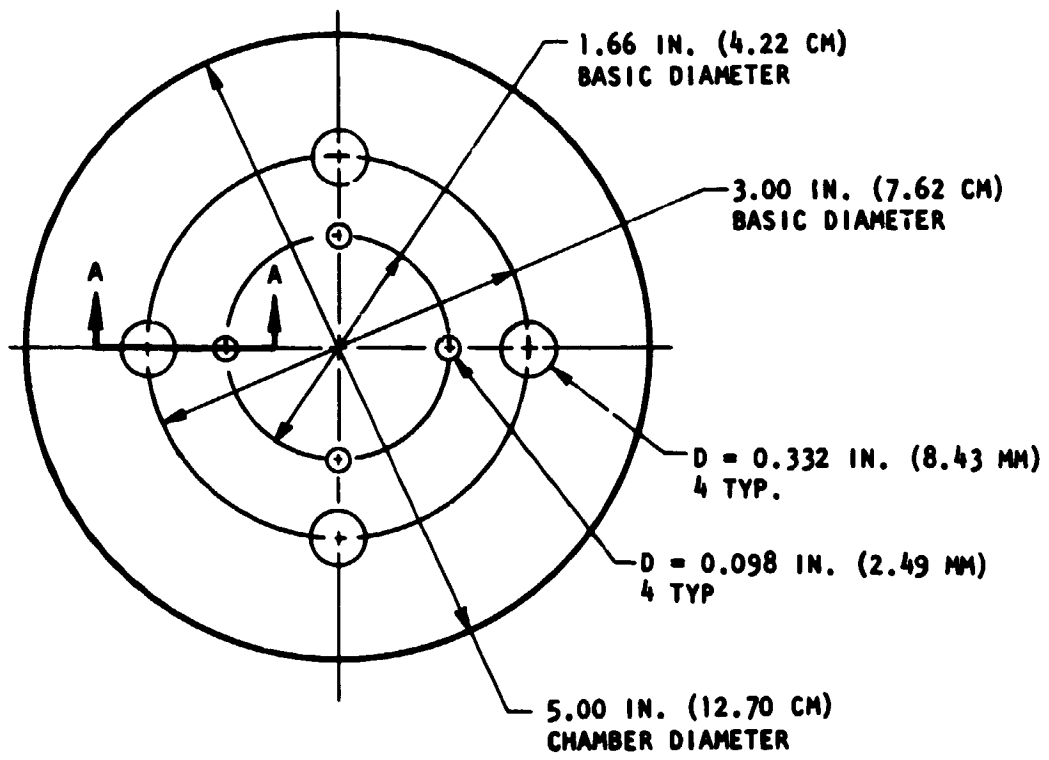
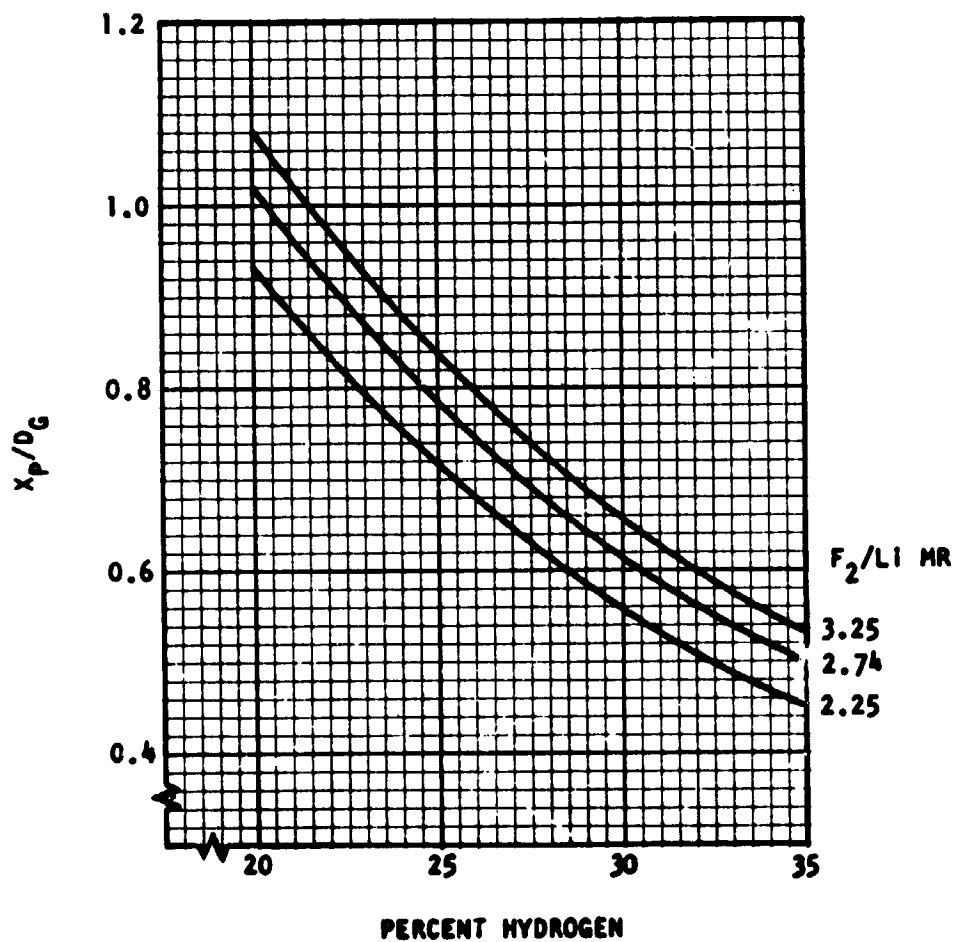


Figure 8. Schematic of Unlike-Doublet LF₂/GH₂ Injector, Mod II



X_p - Penetration of LF_2 into GH_2 , in. (cm)

D_G - Diameter of GH_2 orifice, in. (cm)

Figure 9. Penetration of LF_2 Streams into GH_2 Jets in the Mod II LF_2/GH_2 Injector at Operating Conditions Corresponding to Indicated Tripropellant Test Conditions



5AJ46-12/4/68-S1A

Figure 10. Face Pattern of Unlike-Doublet LF_2/GH_2 Injector, Mod II

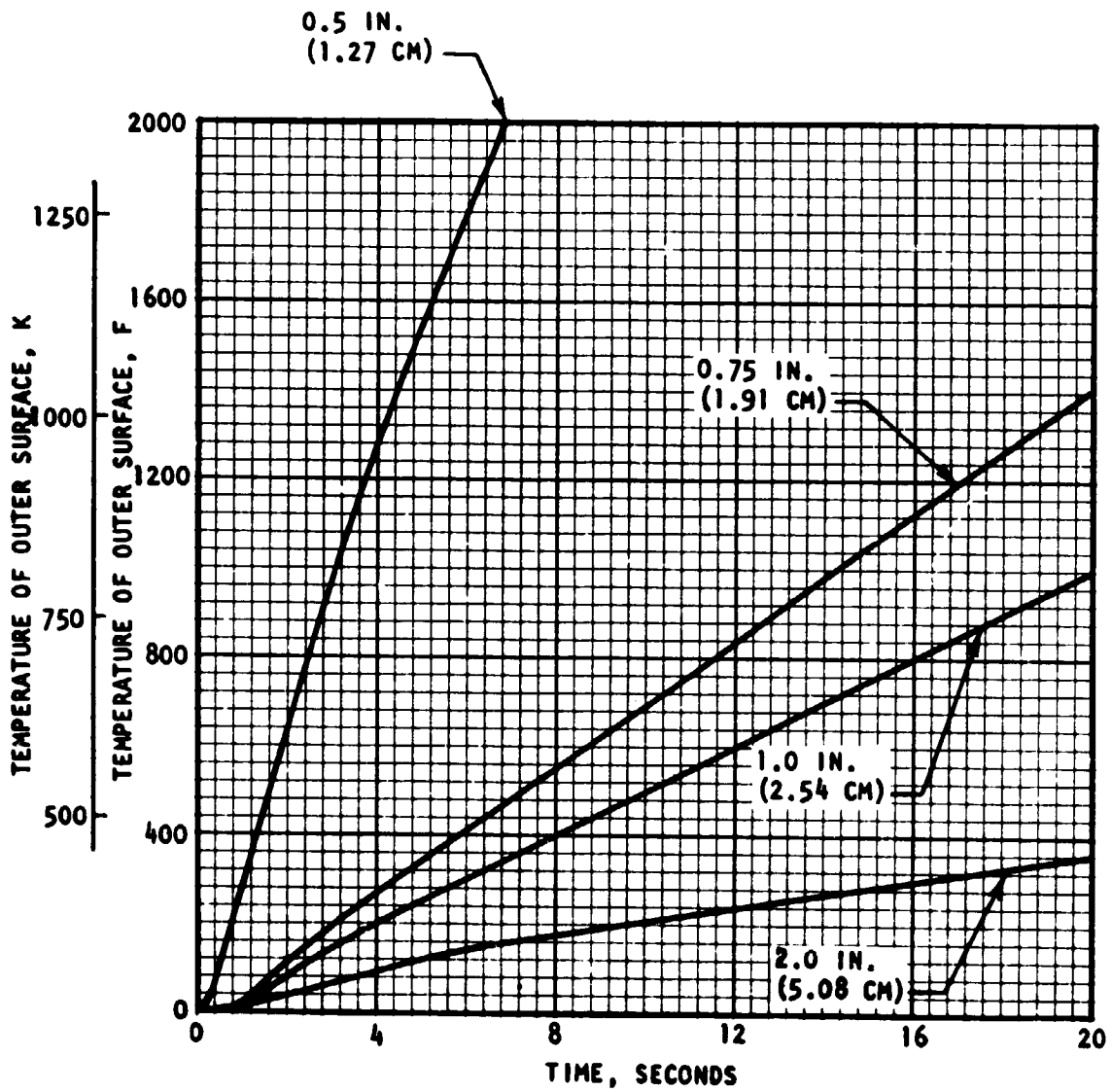
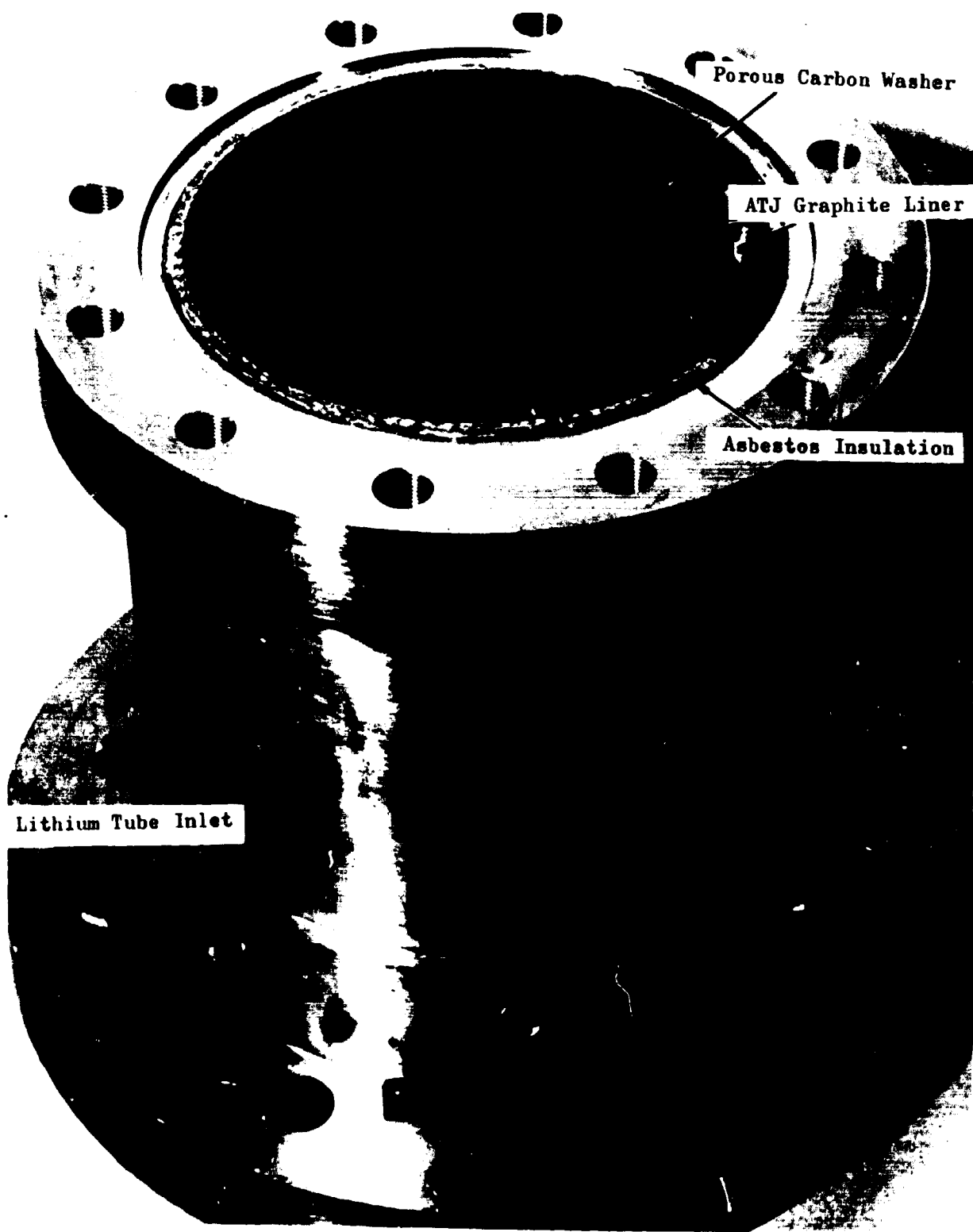


Figure 11. Temperature of the Outer Surface of a Graphite Liner in the Gas Generator Chamber, as Function of Firing Duration, for the Indicated Thickness of Graphite



5AJ33-11/14/68-S1E

Figure 12. Assembled Gas Generator Chamber, Showing Graphite Liner and Porous Carbon Washer

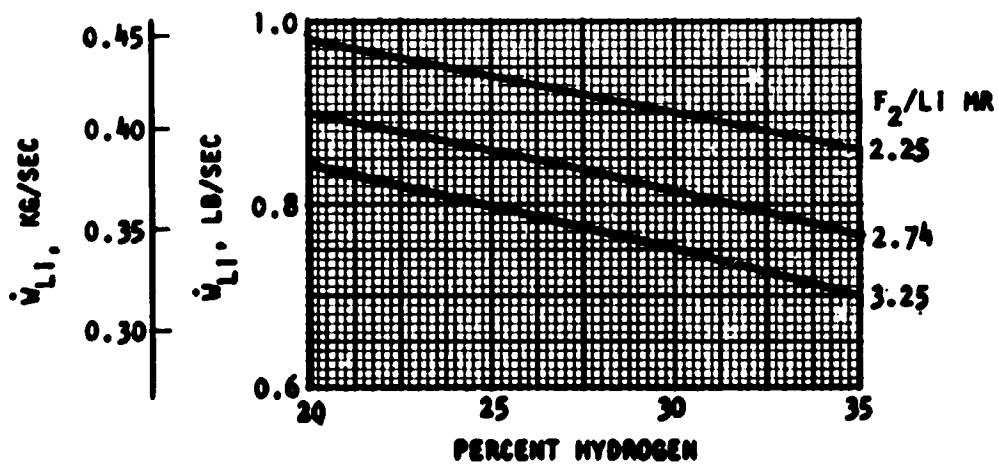
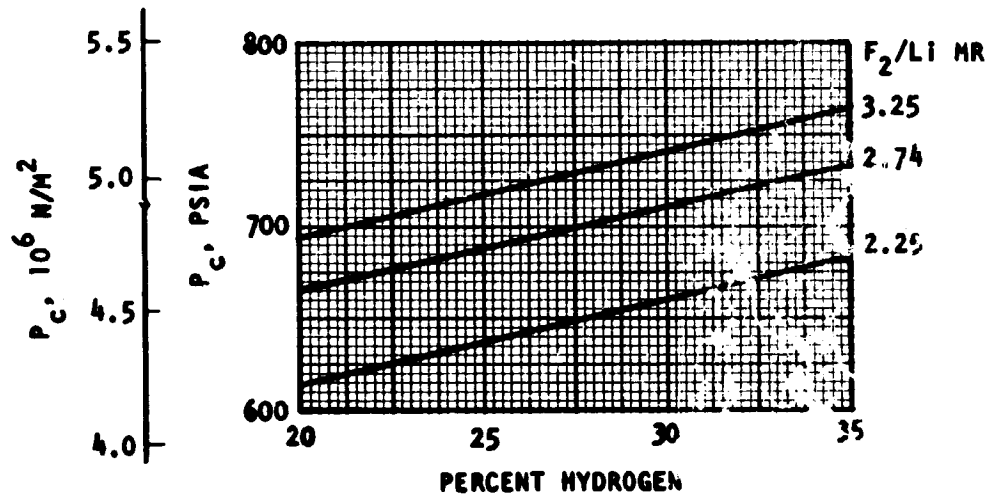


Figure 13. Chamber Pressures and Lithium Flowrates Corresponding to Indicated Tripropellant Test Conditions of Percent Hydrogen and F_2/Li Mixture Ratio

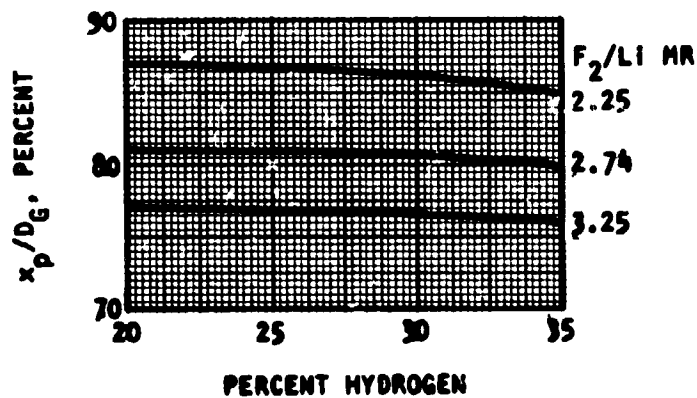
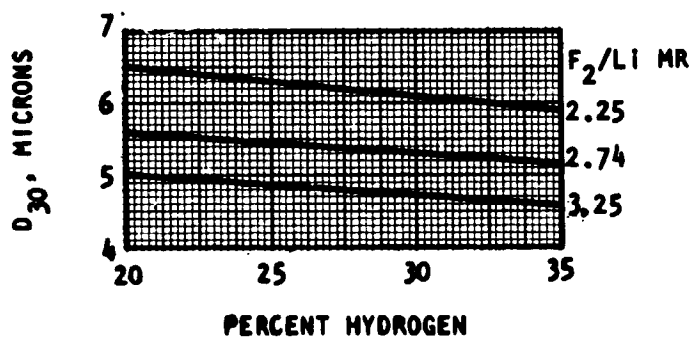
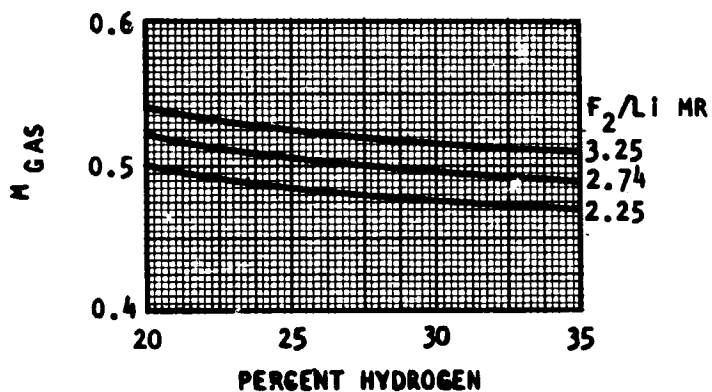


Figure 14. Gas Injection Mach Number, Lithium Droplet Volume Mean Diameter, and Penetration of Gas Jet by Lithium Stream at Indicated Tripropellant Test Conditions of Percent Hydrogen and F_2/Li Mixture Ratio

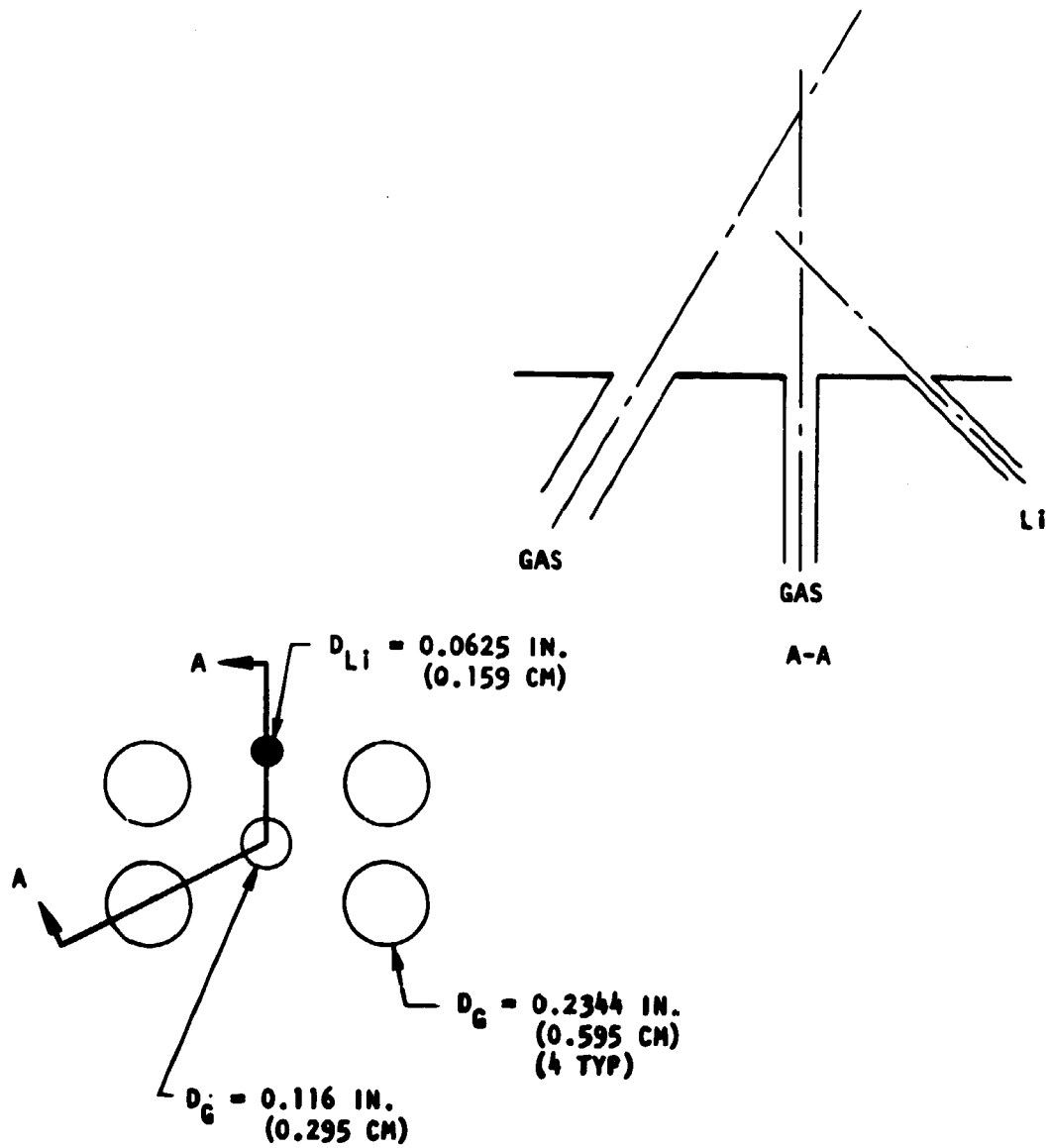
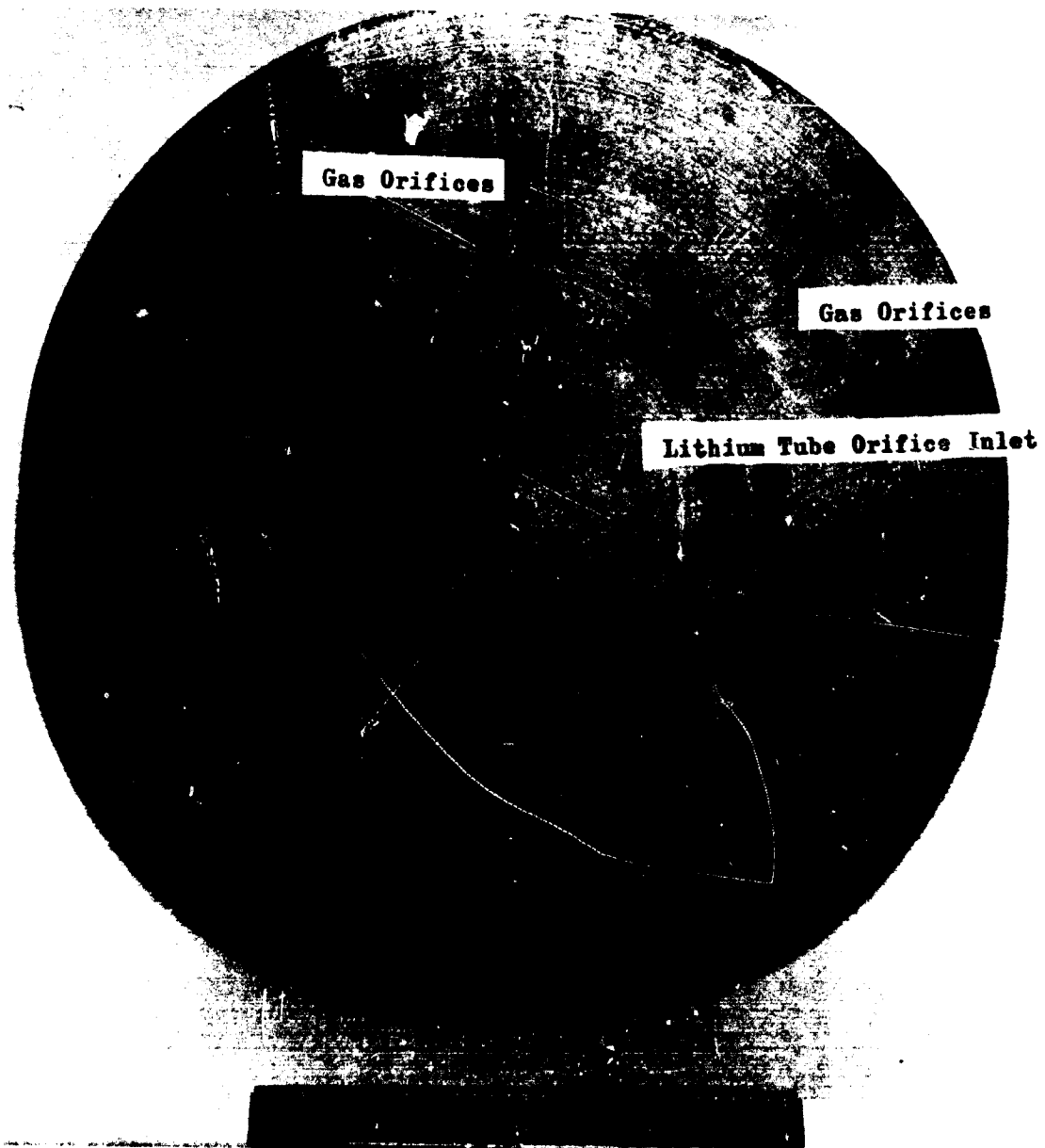


Figure 15. Schematic of Biplanar Lithium/Gas Injection Element for Mod I, II, and III Lithium Injectors



5AA34-12/16/68-S1B

Figure 16. Face Pattern of Lithium Injector, Mod I and II

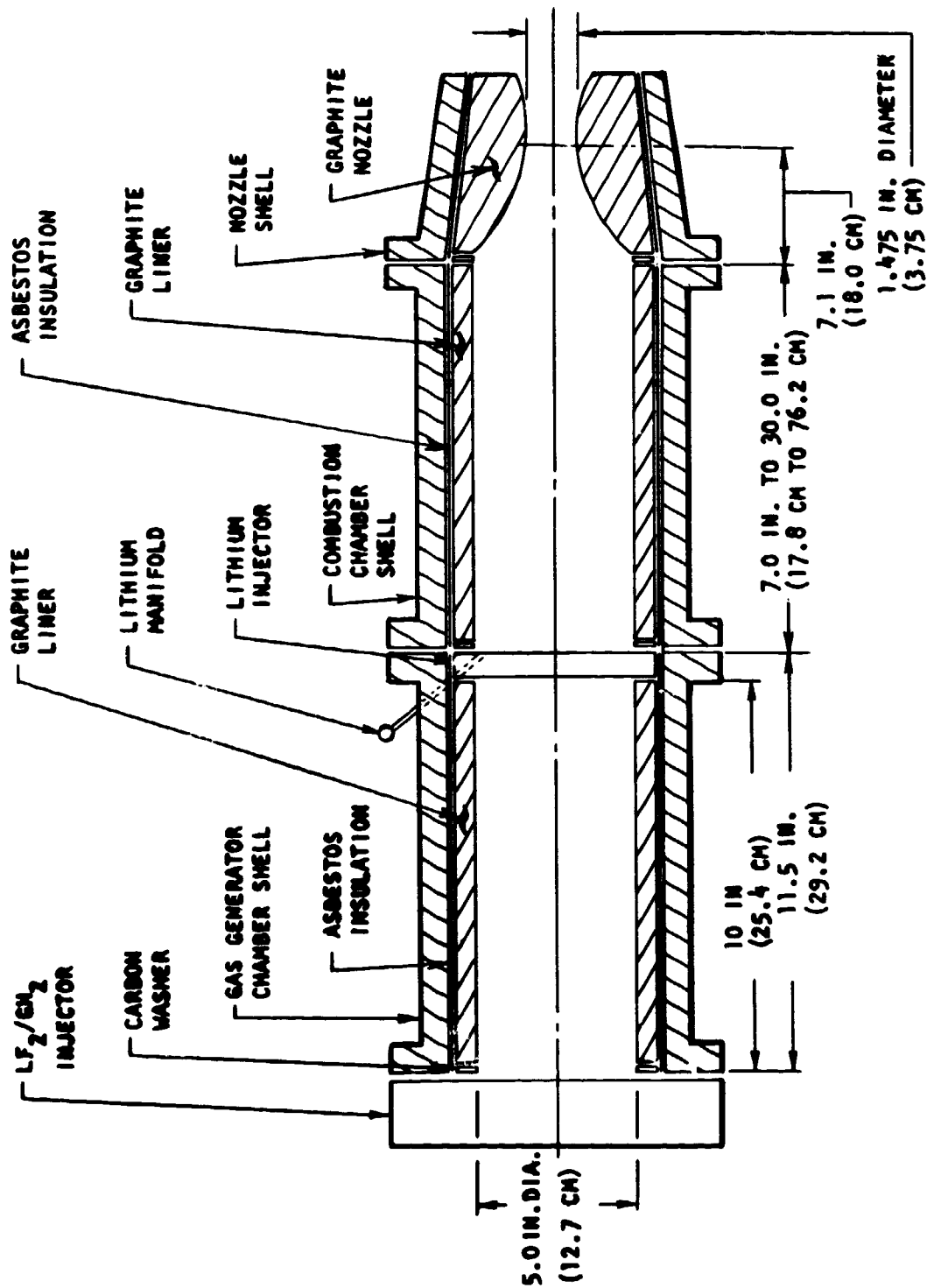


Figure 17. Schematic of Thrust Chamber Assembly Used in the Task I Firings With the Fuel-Rich Gas Generator Injection Method and the Mod I Lithium Injector

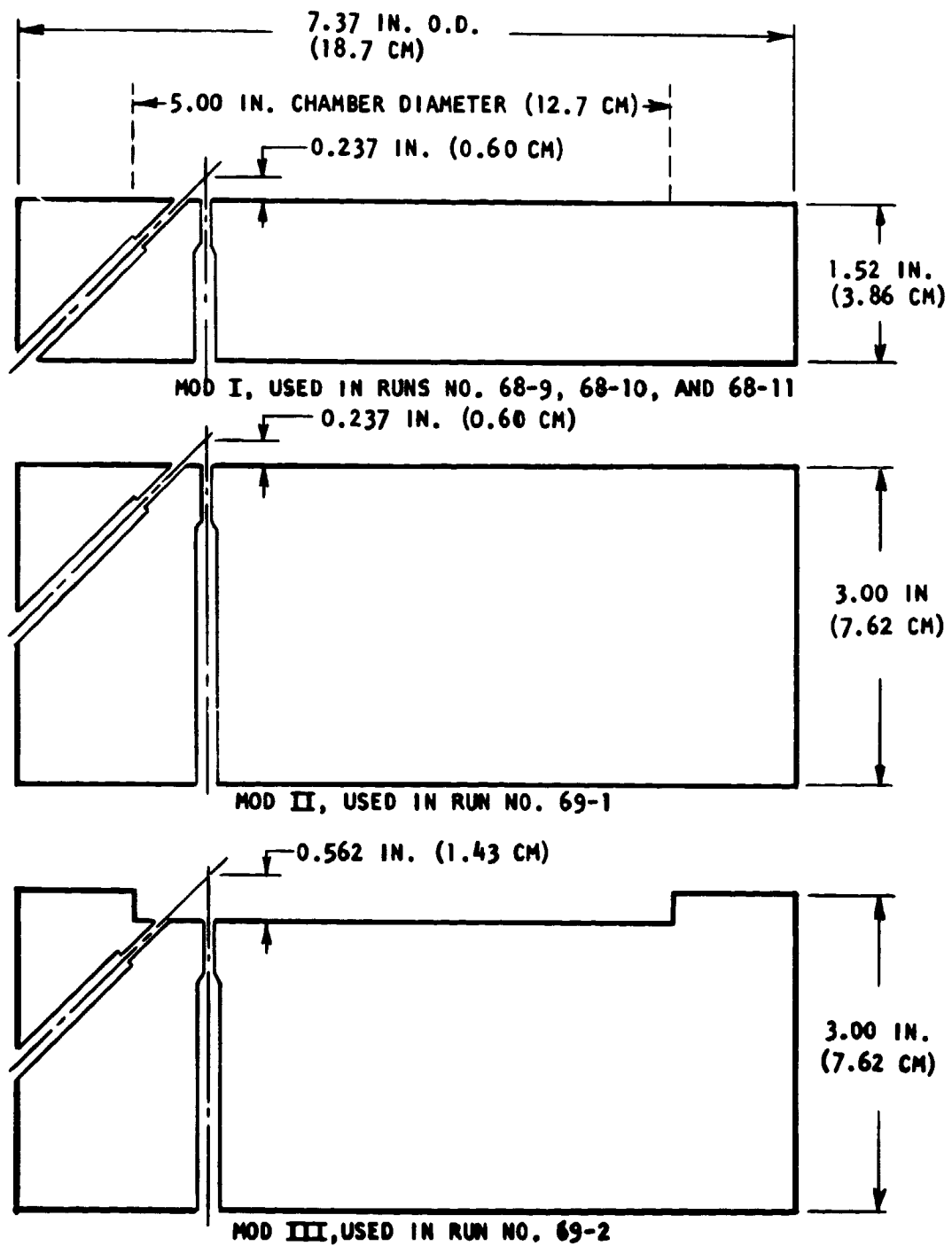


Figure 18. Lithium Injector Modifications, Mod I, II, and III

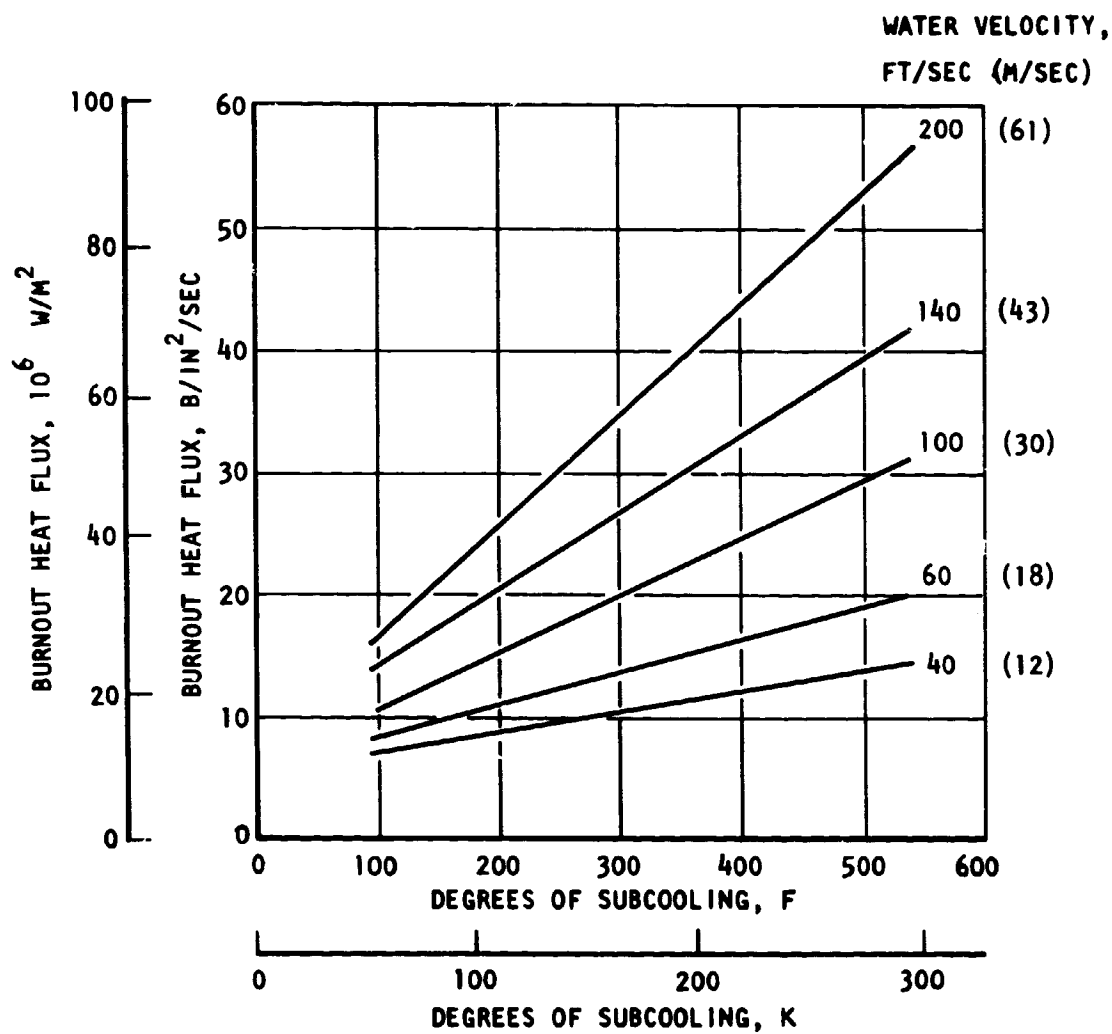


Figure 19. Gambill's Heat Transfer Correlation for Forced-Convection Subcooled Boiling Applied to Water at 100 F (311 K) in a 0.125-Inch (3.18-mm) Diameter Channel

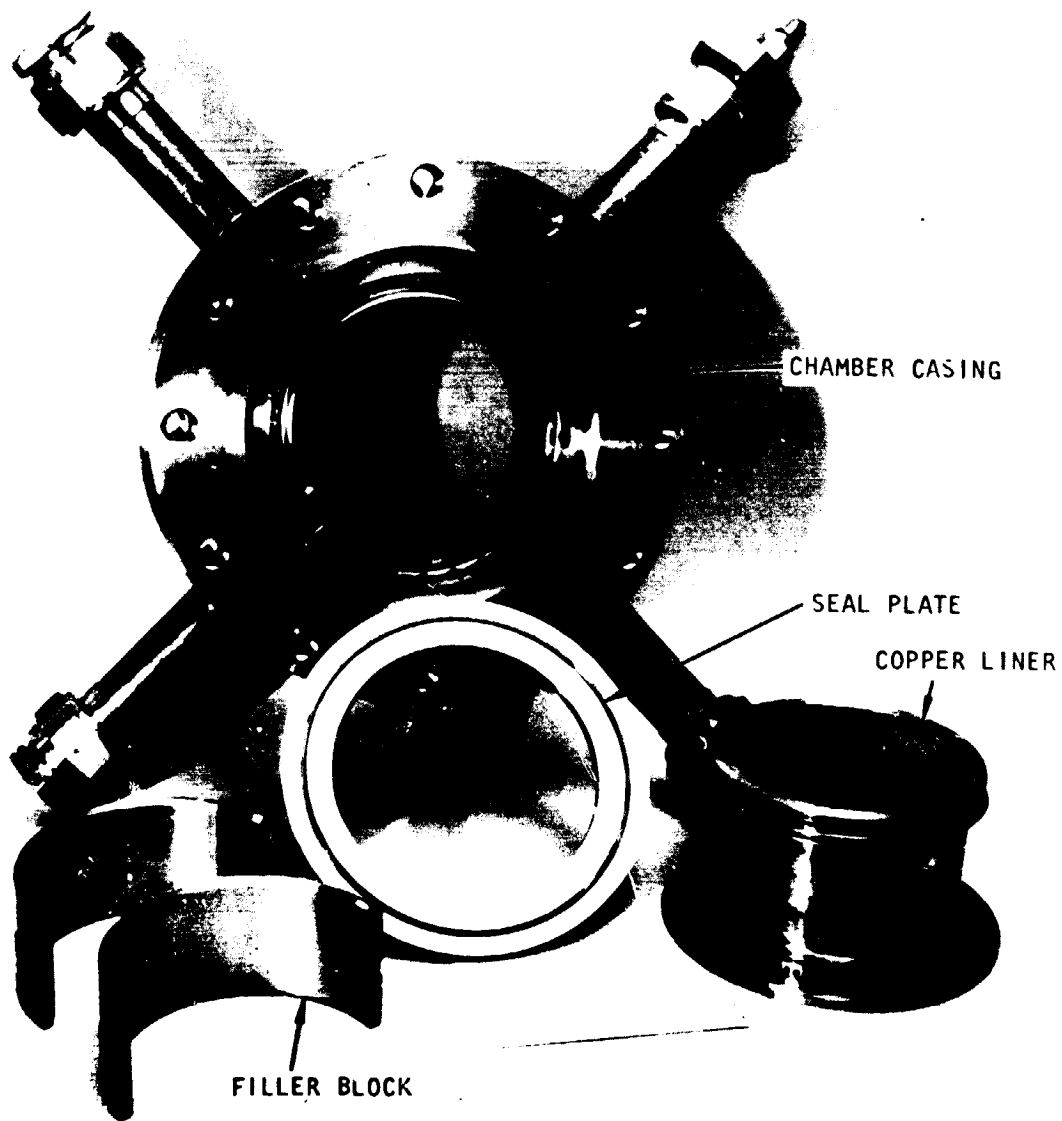


Figure 20. Components of the 4-Inch (10.16-cm), High Heat Flux, Water-Cooled, Combustion Chamber Section

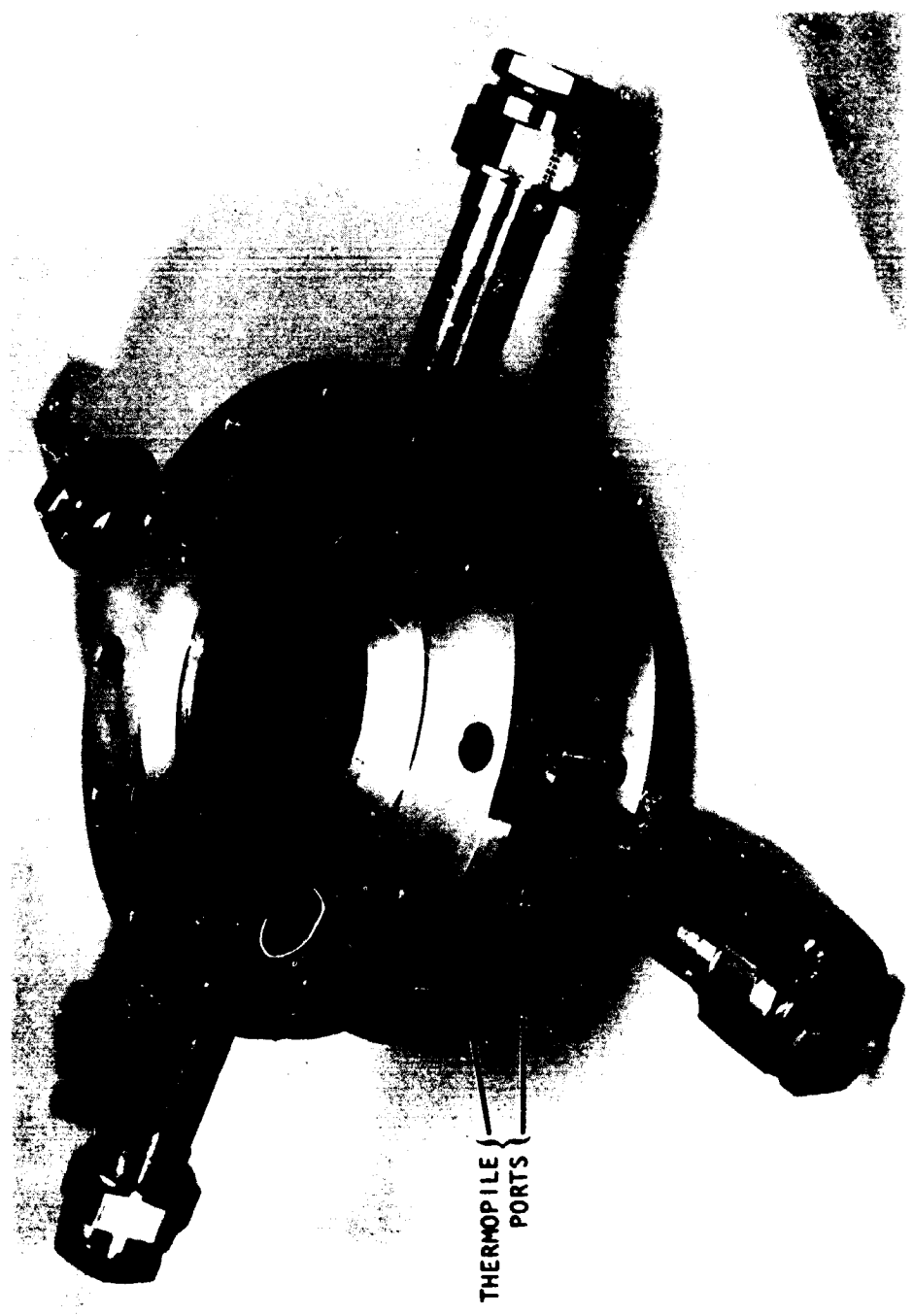


Figure 21. Assembled 4-Inch (10.16-cm), High Heat Flux, Water-Cooled, Combustion Chamber Section

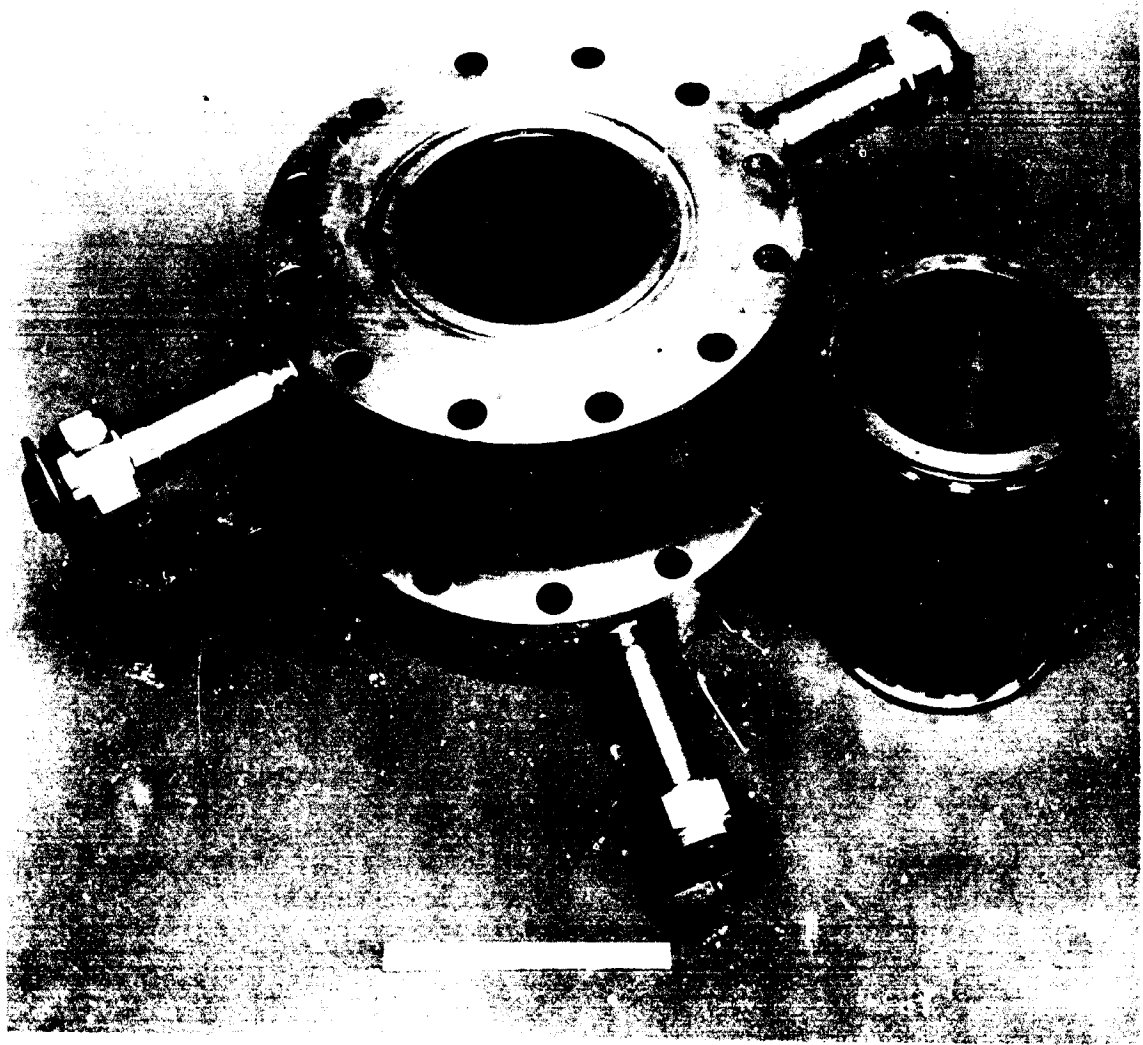


Figure 22. Shell and Liner of 9-Inch (22.86-cm), Low Heat Flux, Water-Cooled, Combustion Chamber Section

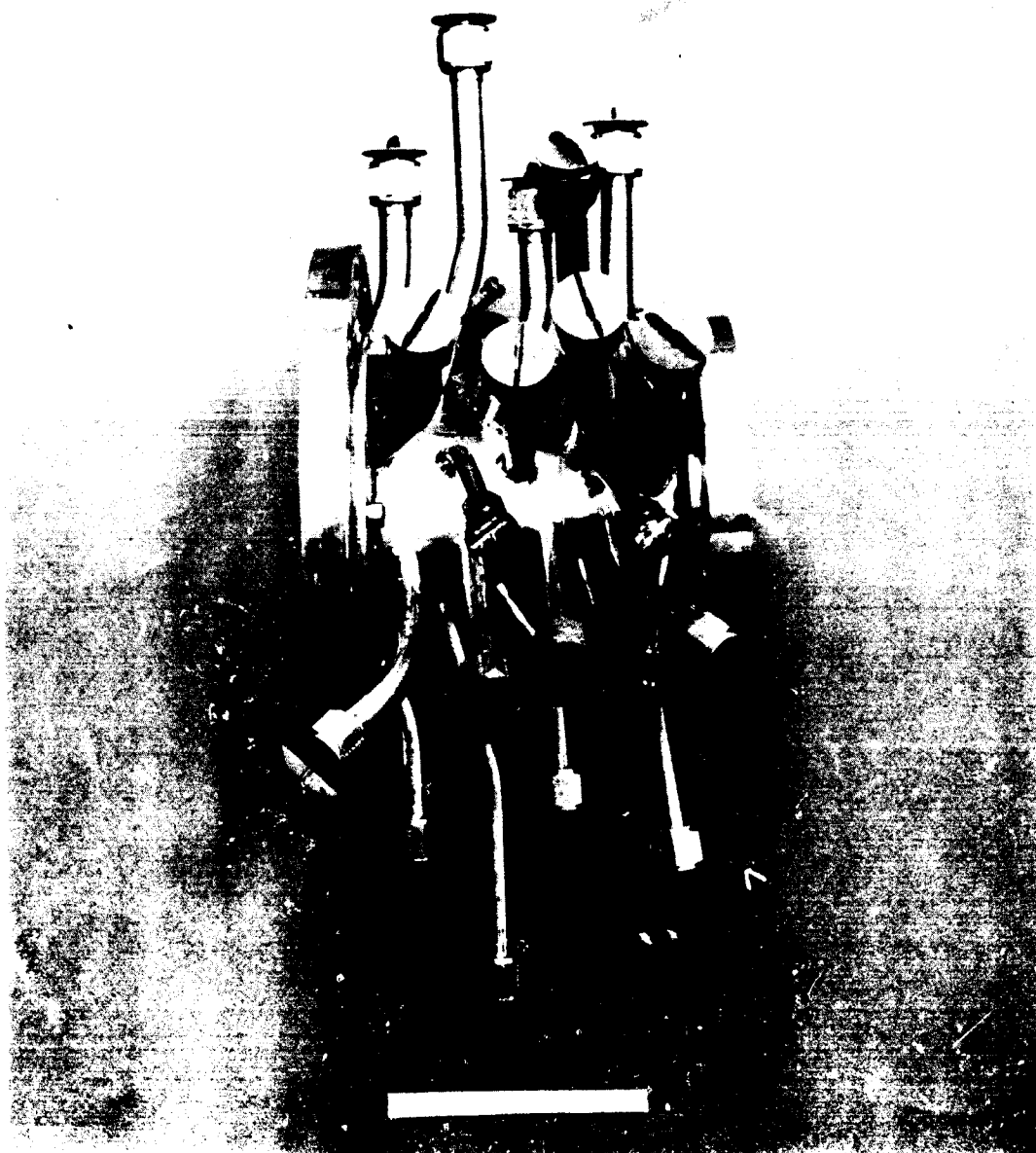


Figure 23. Water-Cooled Nozzle; Side View Showing Coolant Inlet and Outlet Tubes

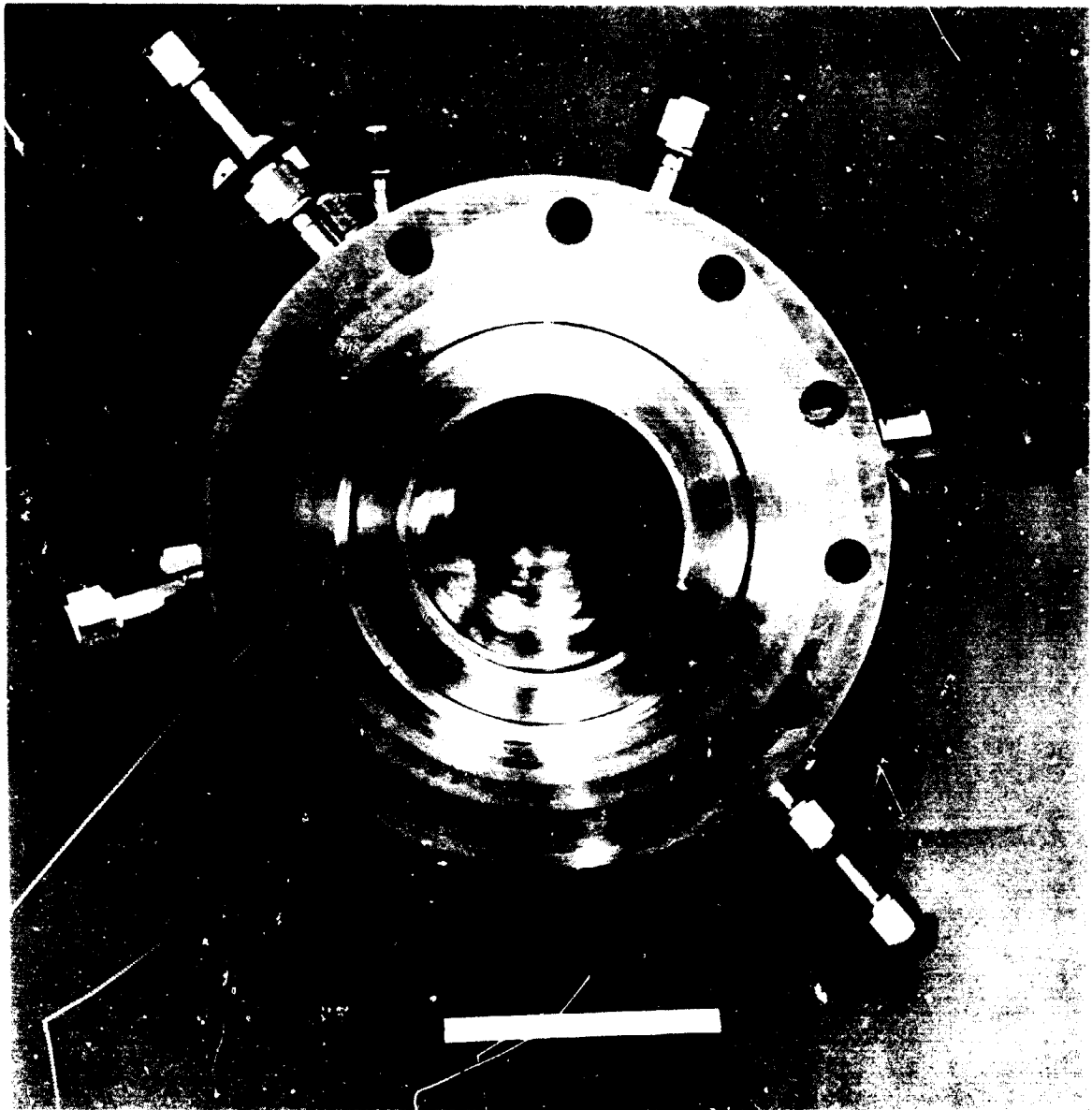


Figure 24. Water-Cooled Nozzle; View From Upstream End,
Looking Towards Throat

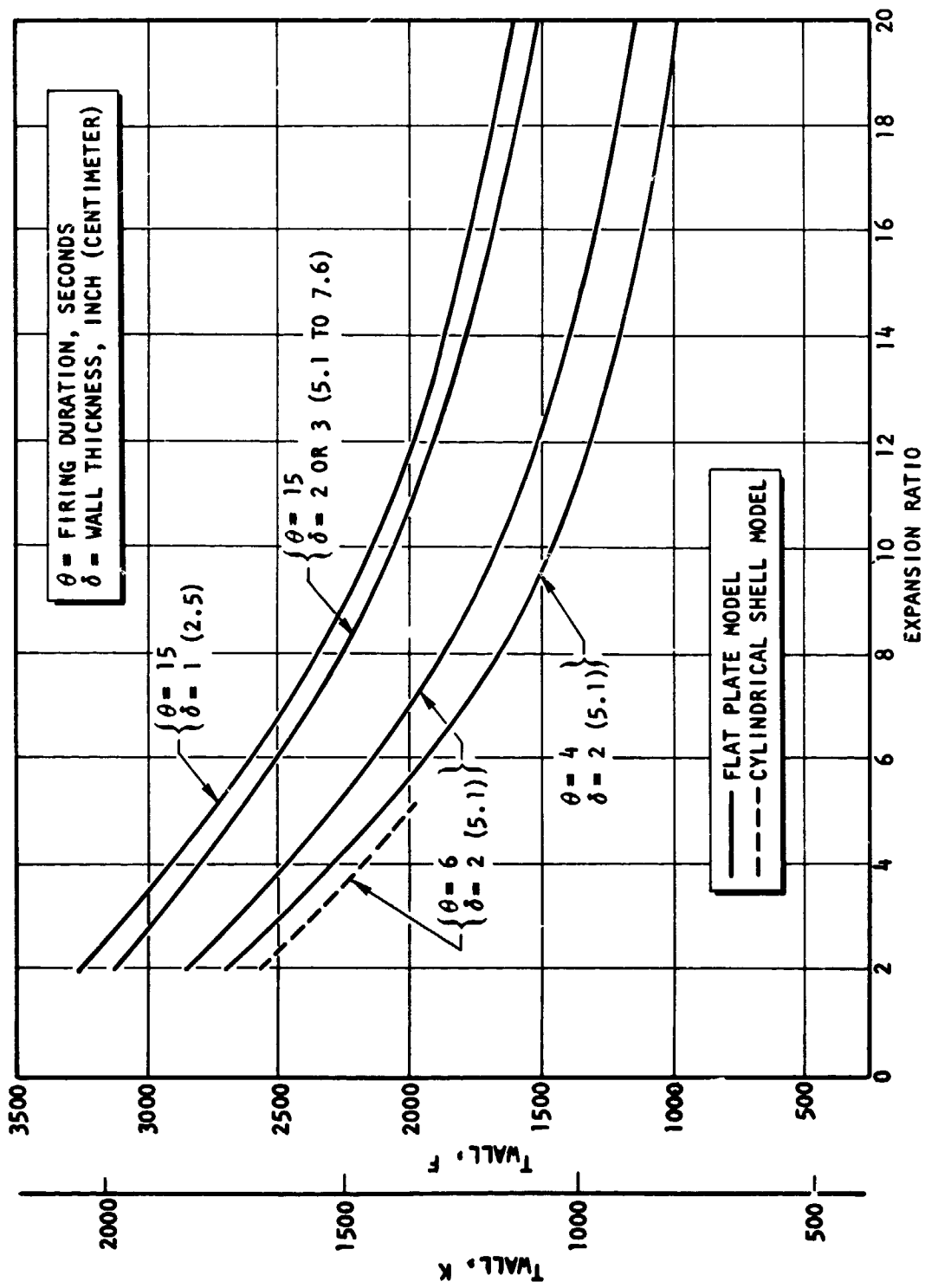


Figure 25. Thermal Response of Uncooled Graphite Nozzle. Li/F₂/H₂ at P_c = 750 psia (5.17 x 10⁶ N/m²), F₂/Li MR = 2.25, H₂ = 35 Percent. Axial Conduction Neglected

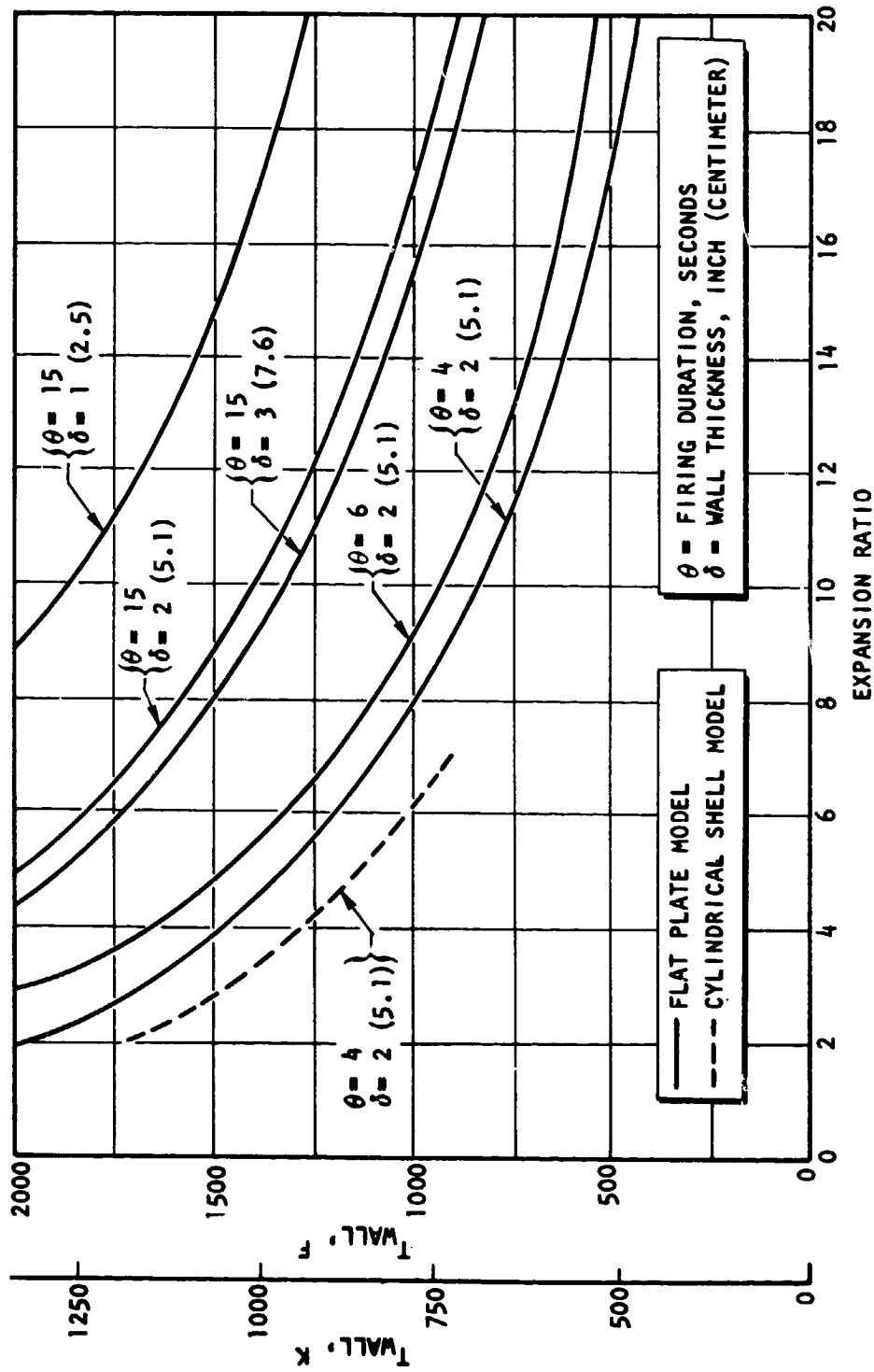


Figure 26. Thermal Response of Uncooled Copper Nozzle. $Li/F_2/H_2$ at $P_c = 750$ psia (5.17×10^6 N/m²), F_2/Li MR = 2.25, $H_2 = 35$ Percent. Axial Conduction Neglected

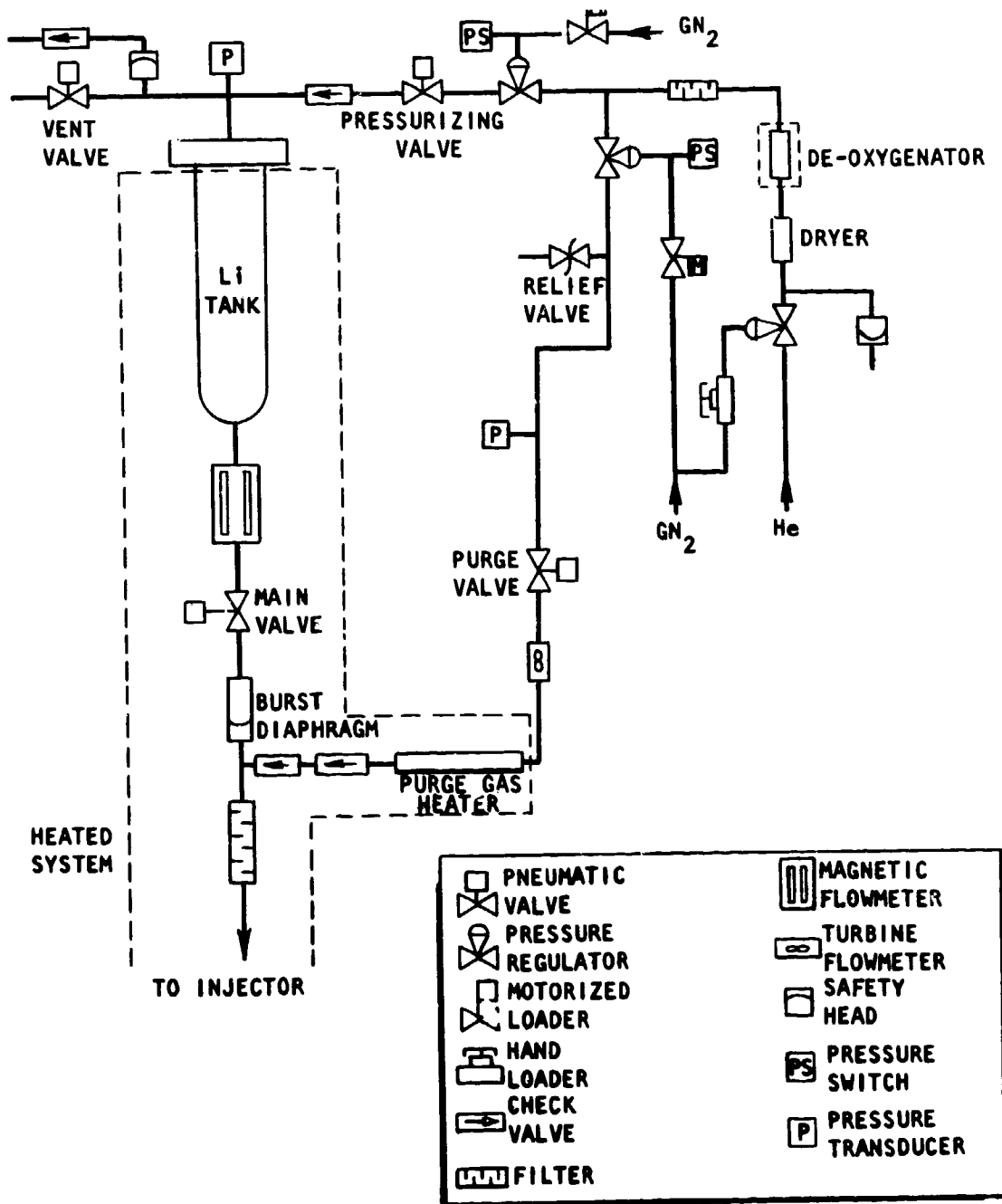
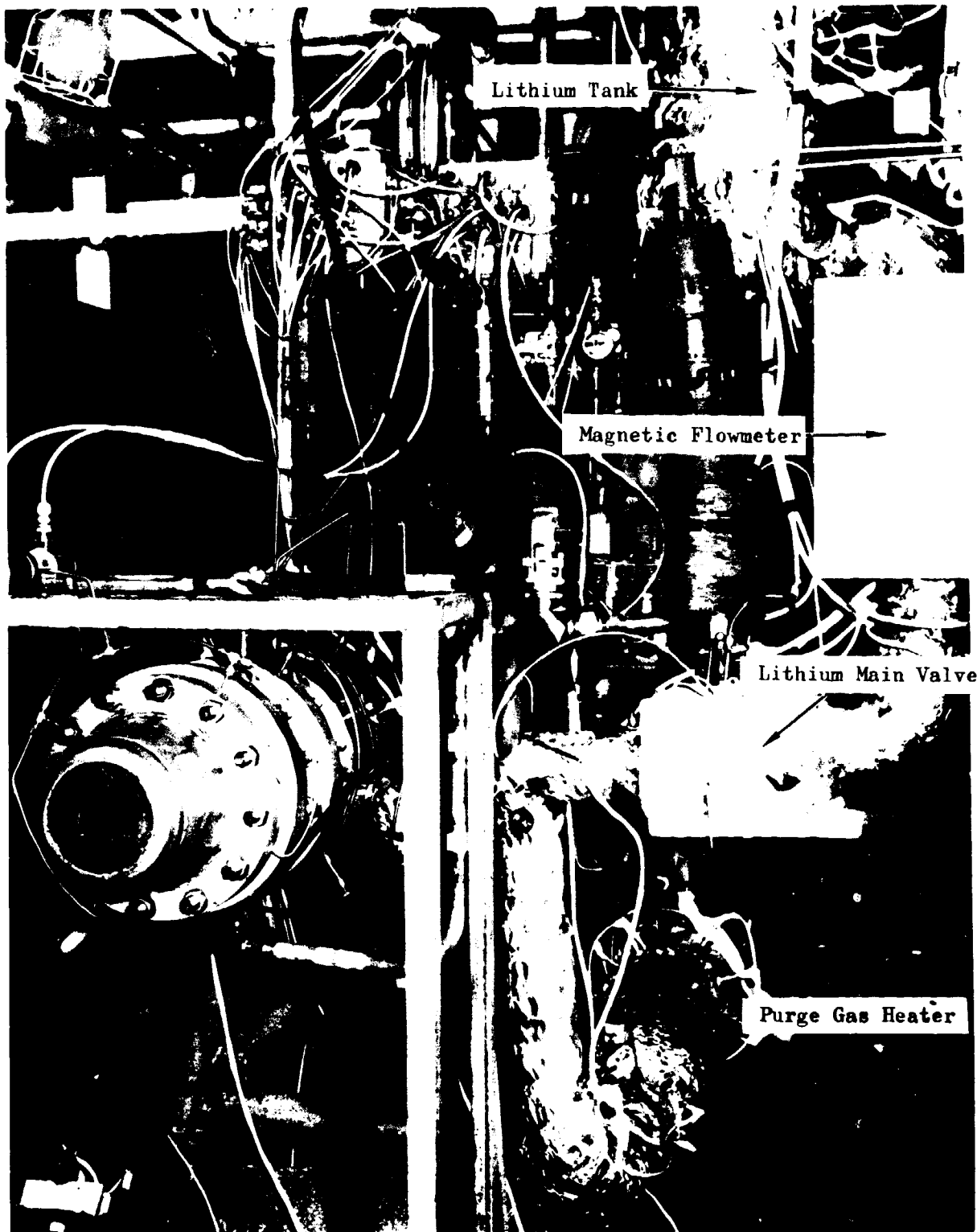


Figure 27. Schematic Flow Diagram of Liquid Lithium System



1HZ23-10/5/68-S1

Figure 28. Photograph of Lithium System on Test Stand, With Engine in Place

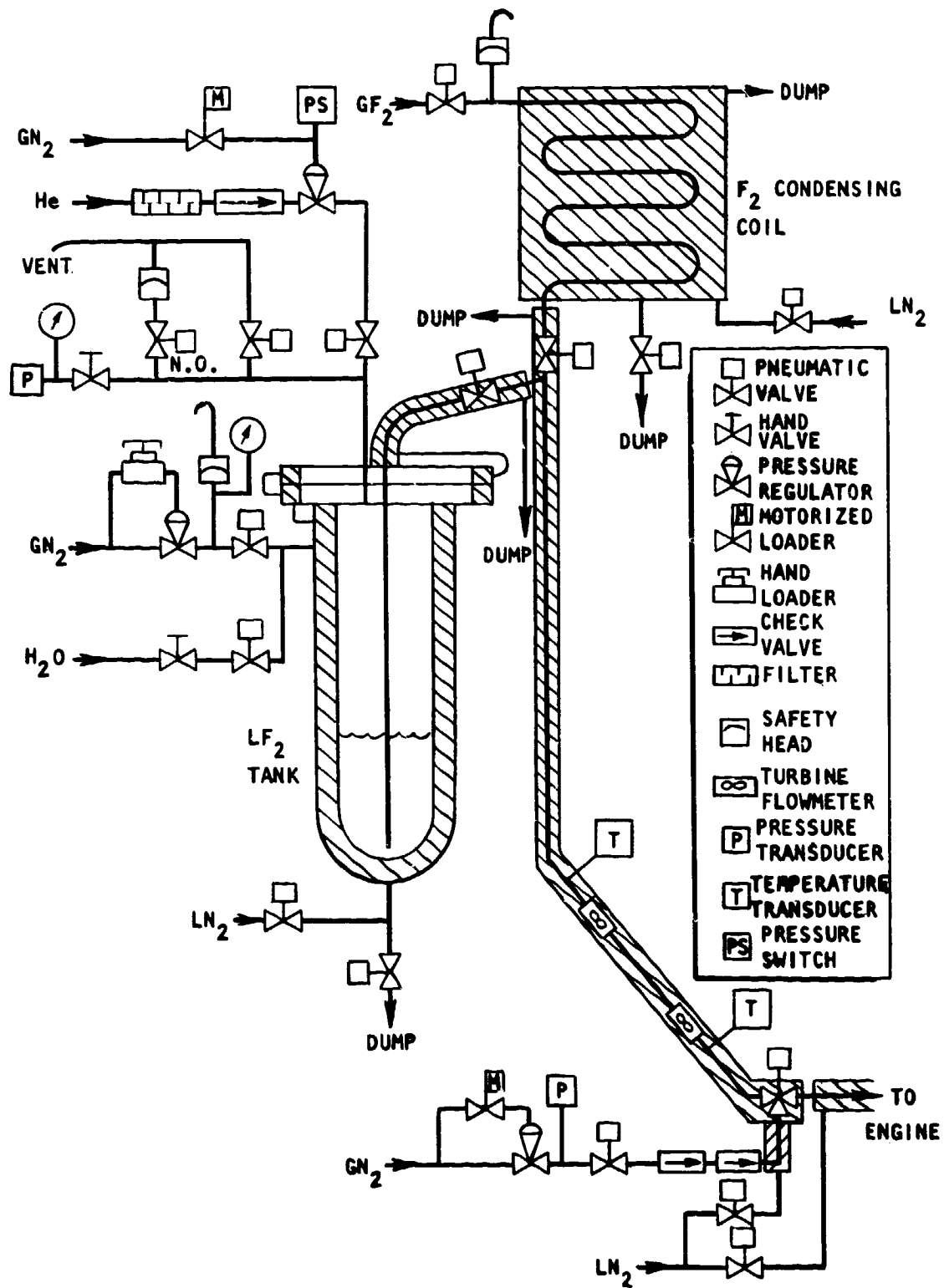


Figure 29. Schematic Flow Diagram of Fluorine System

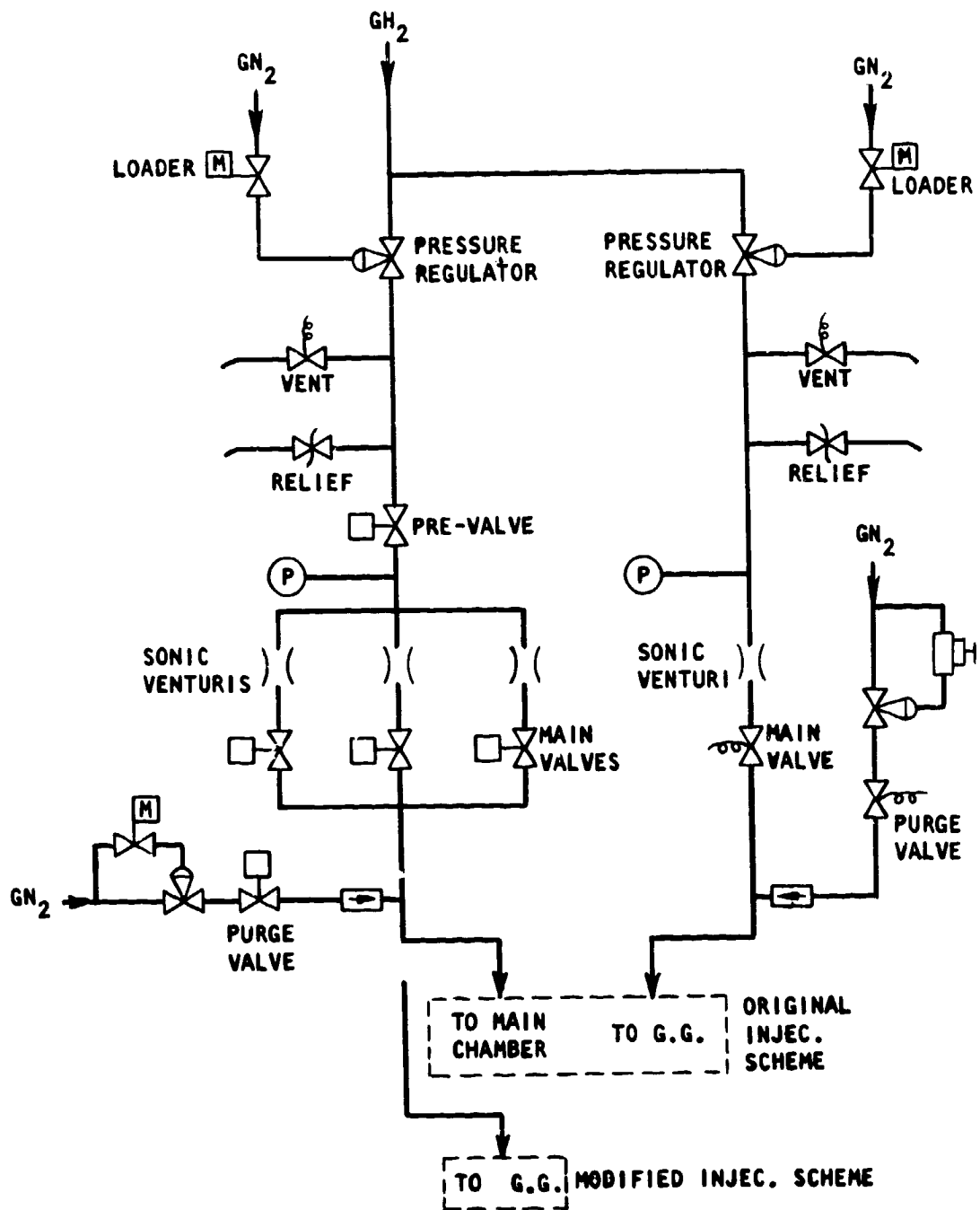


Figure 30. Schematic Flow Diagram of Hydrogen System

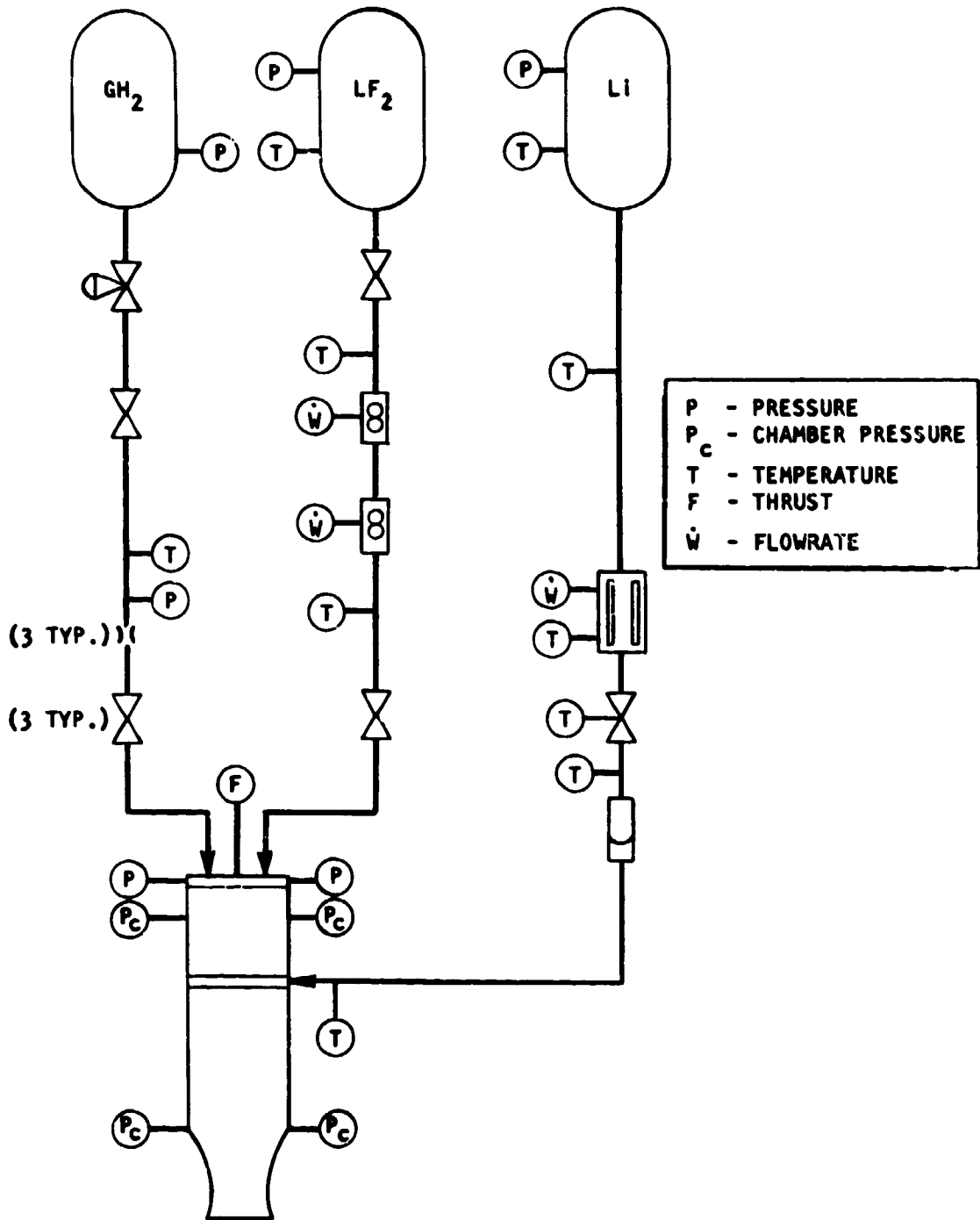


Figure 31. Schematic of Basic Instrumentation for the Li/F₂/H₂ Tripropellant Firings

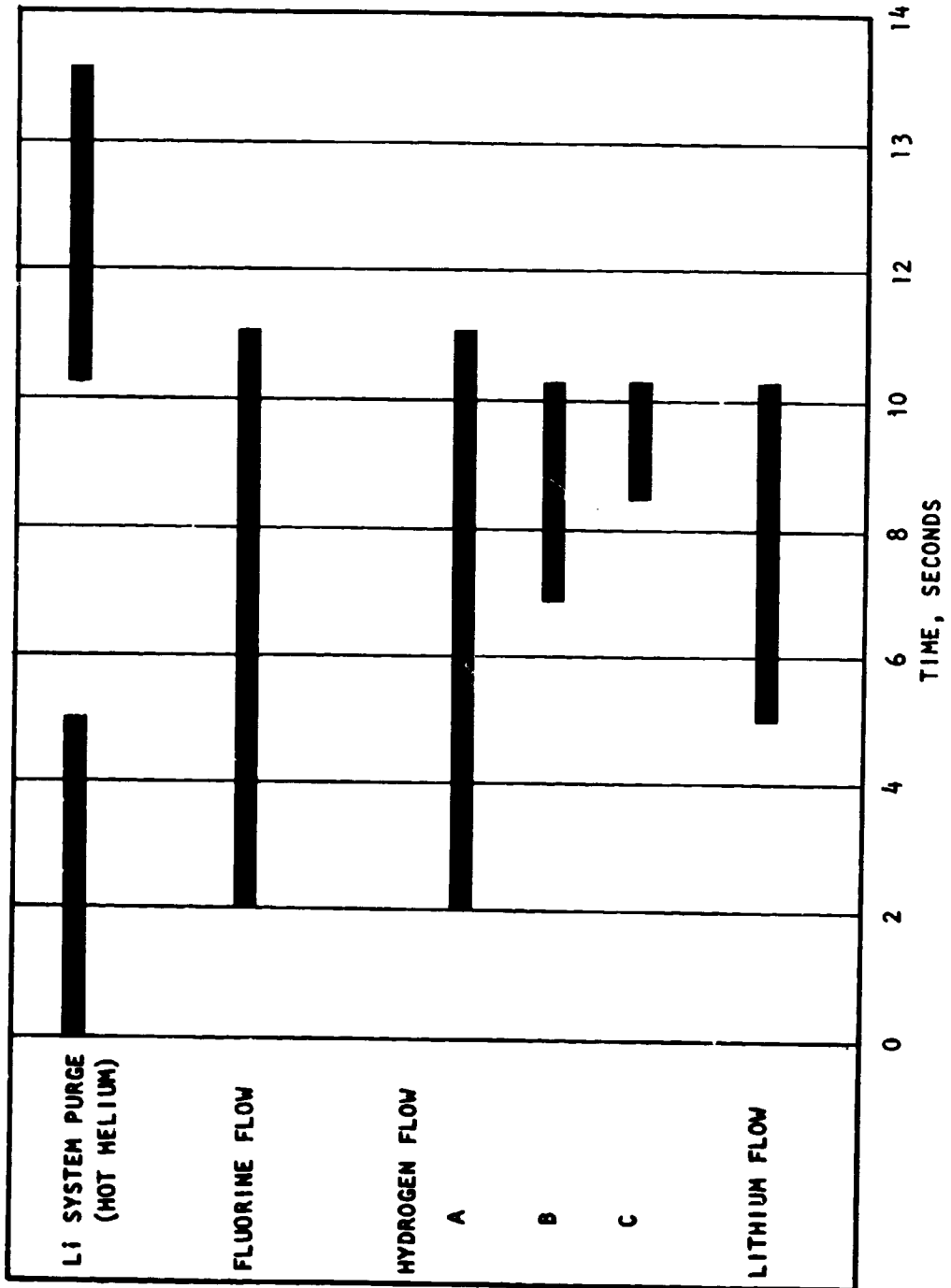
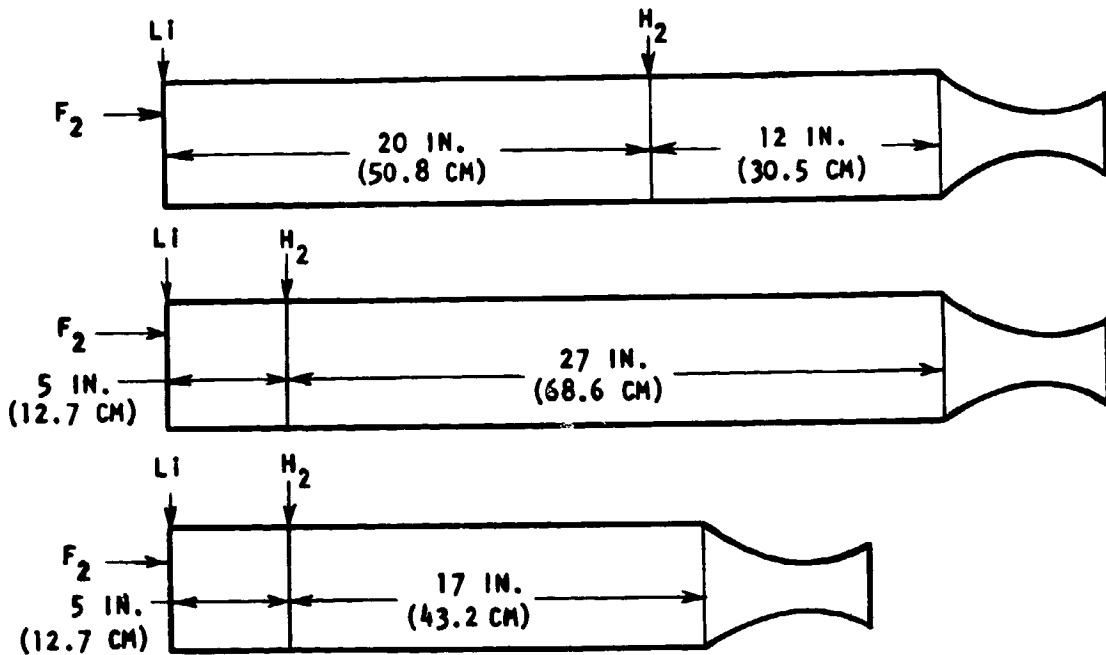
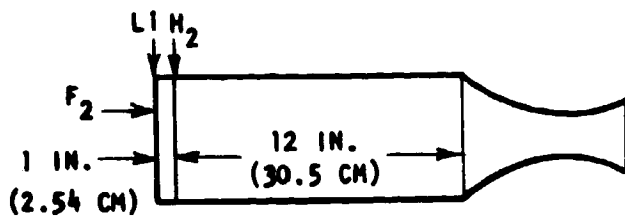
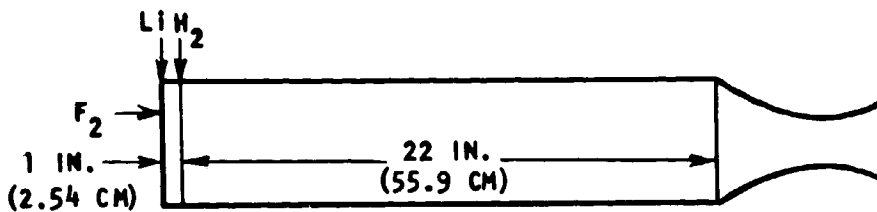


Figure 32. Programmed Firing Sequence, Showing Timing of Propellant and Lithium Purge Gas Flows



CHAMBER CONFIGURATIONS USED IN PREVIOUS $Li/F_2/H_2$ STUDY



CHAMBER CONFIGURATIONS USED IN PRESENT $Li/F_2/H_2$ INVESTIGATION

Figure 33. Chamber Configurations Employed With the Oxidizer-Rich Gas Generator Tripropellant Injection Method



5AA34-12/8/68-S1

Figure 34. Gas Generator Mounted on Test Stand

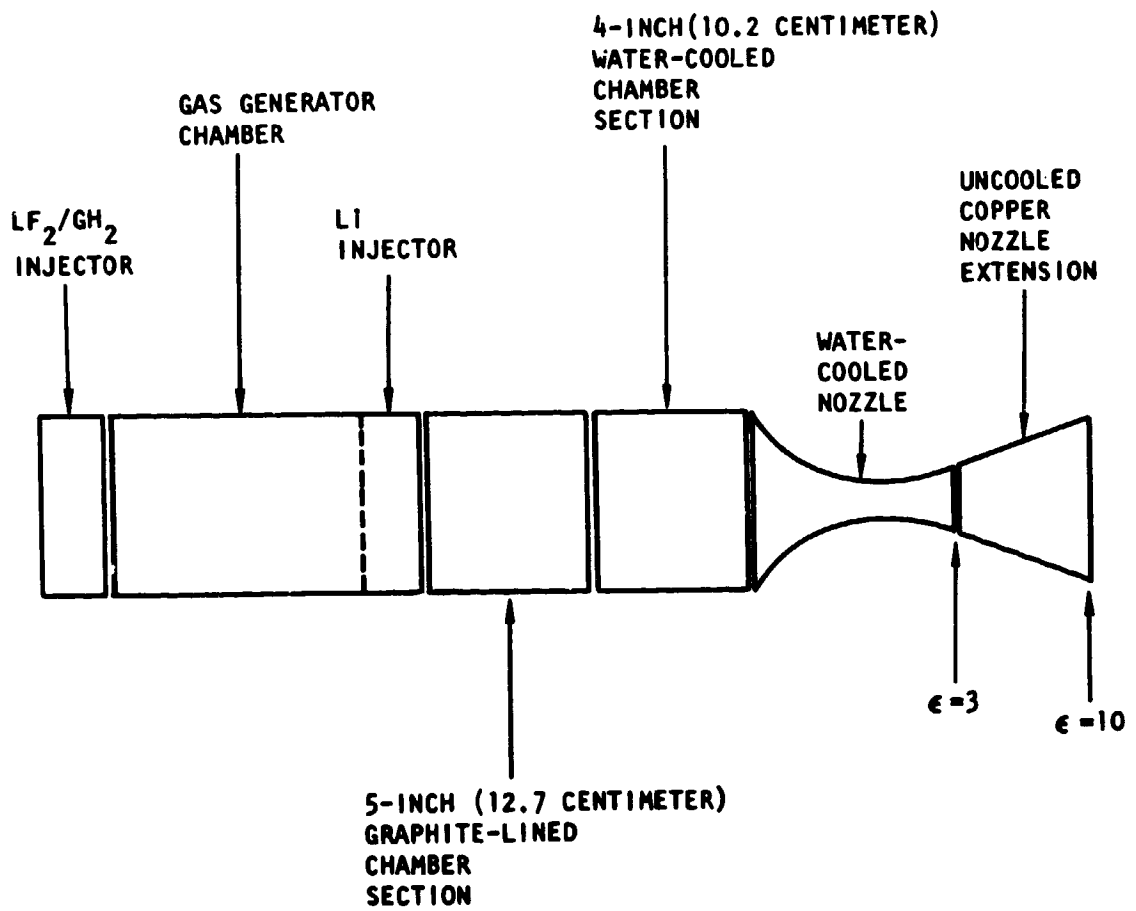
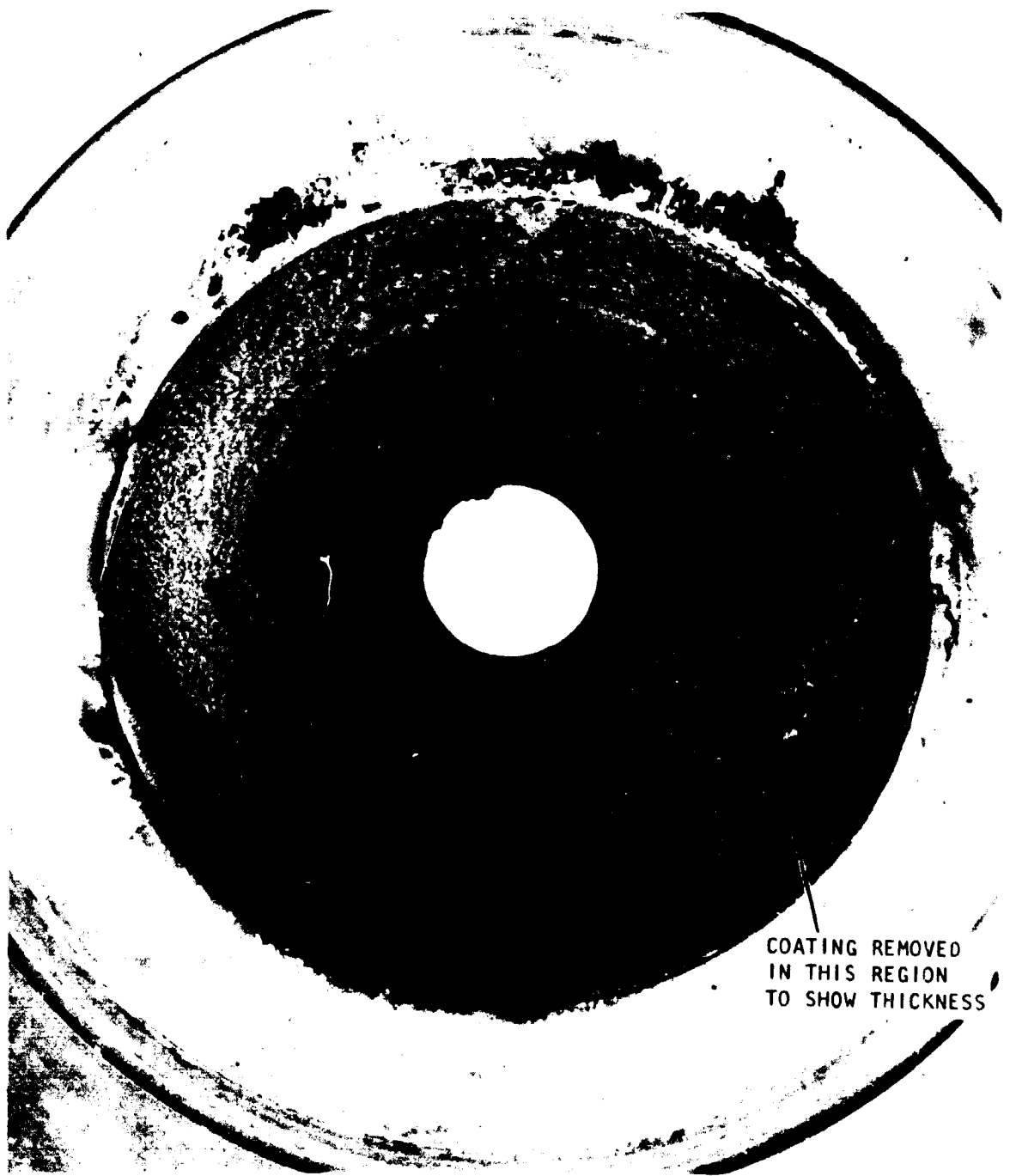


Figure 35. Schematic of Test Hardware Used for the Task II Firings



COATING REMOVED
IN THIS REGION
TO SHOW THICKNESS

Figure 36. Typical Posttest Appearance of Convergent Portion of Water-Cooled Nozzle, Showing Deposited Wall Coating

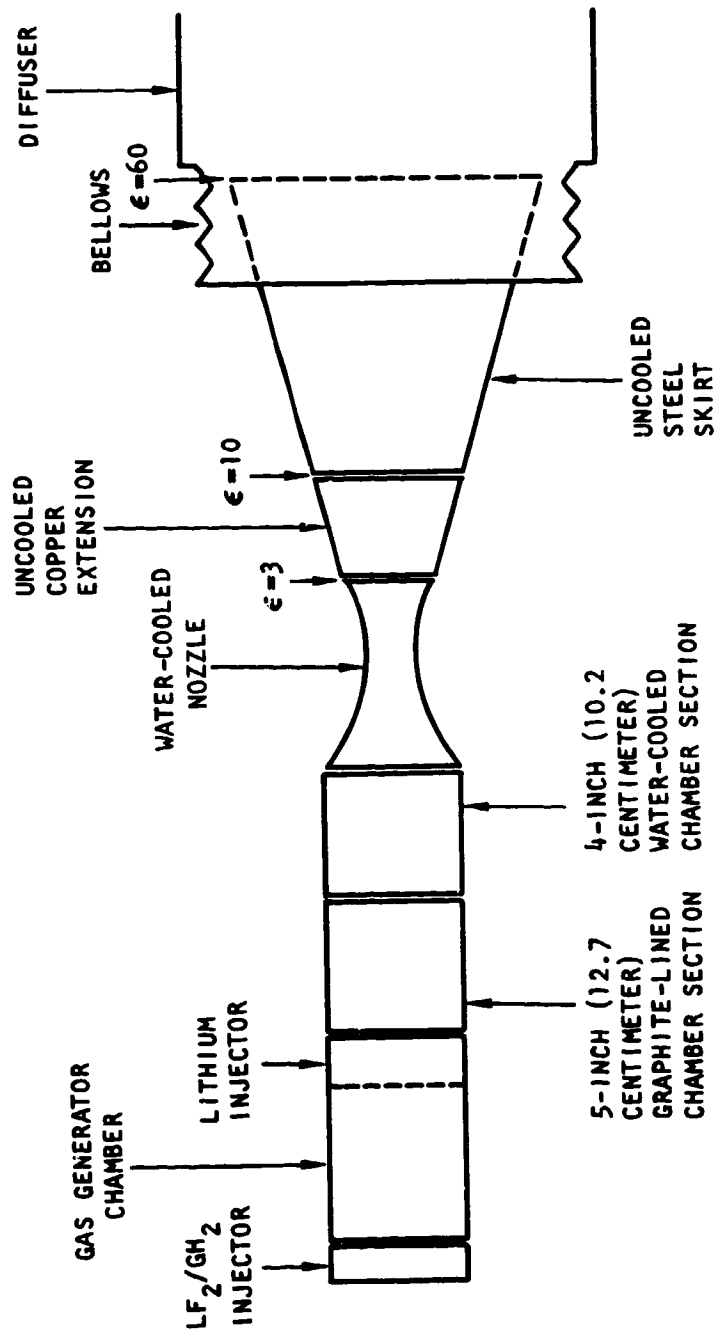


Figure 37. Schematic of Test Hardware Used in the Task III Altitude Simulation Firings

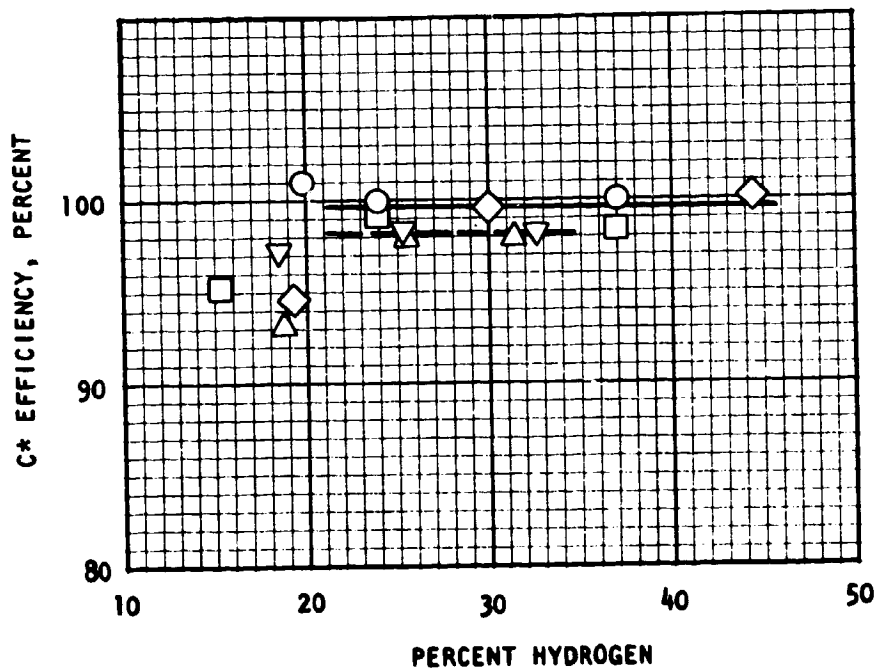


Figure 38. Photograph of Test Stand, Showing Engine and Diffuser in Place for Altitude Simulation Firing

	F_2/Li COMBUSTION CHAMBER LENGTH		H_2 MIXING CHAMBER LENGTH	
	IN.	CM	IN.	CM
○	20	50.8	12	30.5
□	5	12.7	27	68.6
◇	5	12.7	17	43.2
△	1	2.54	22	55.9
▽	1	2.54	12	30.5

	F_2/Li COMBUSTION CHAMBER LENGTH		H_2 MIXING CHAMBER LENGTH	
	IN.	CM	IN.	CM
○	20	50.8	12	30.5
□	5	12.7	27	68.6
◇	5	12.7	17	43.2
△	1	2.54	22	55.9
▽	1	2.54	12	30.5

———— COMBUSTION CHAMBER ≥ 5 IN. (12.7 CM)
 - - - - COMBUSTION CHAMBER = 1 IN. (2.54 CM)



Nominal $P_c = 500$ psia (3.45×10^6 N/m²)
 Nominal F_2/Li MR = 2.74

Figure 39. Corrected Characteristic Velocity Efficiency (Based on Chamber Pressure) of $Li/F_2/H_2$ With Oxidizer-Rich Gas Generator Injection Method, as Function of Percent Hydrogen

$P_c = 500 \text{ PSIA } (3.45 \times 10^6 \text{ N/m}^2)$

$F_2/LI \text{ MR} = 2.74$

$H_2 = 25\text{-}35\%$

OVERALL CHAMBER LENGTH: 13 TO 32 IN. (33 TO 81 CM)

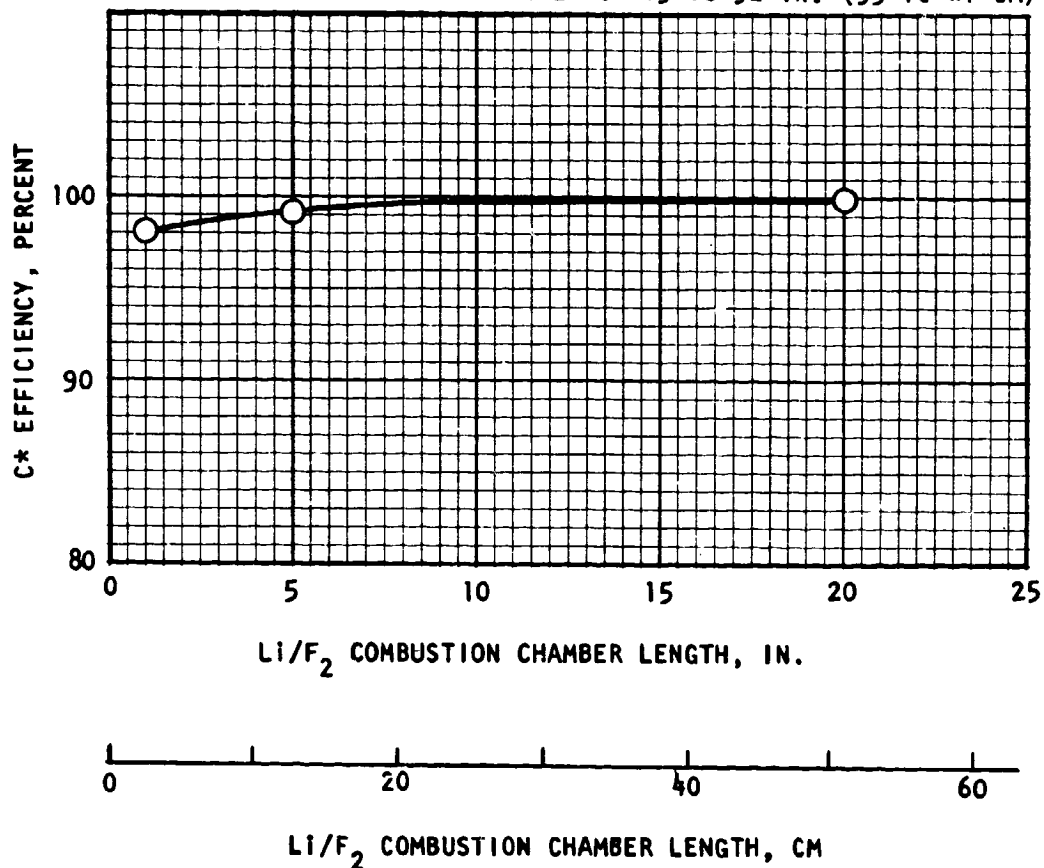


Figure 40. Corrected Characteristic Velocity Efficiency (Based on Chamber Pressure) of Li/F₂/H₂ With Oxidizer-Rich Gas Generator Injection Method, as Function of Length of Li/F₂ Combustion Chamber, at Indicated Nominal Test Conditions

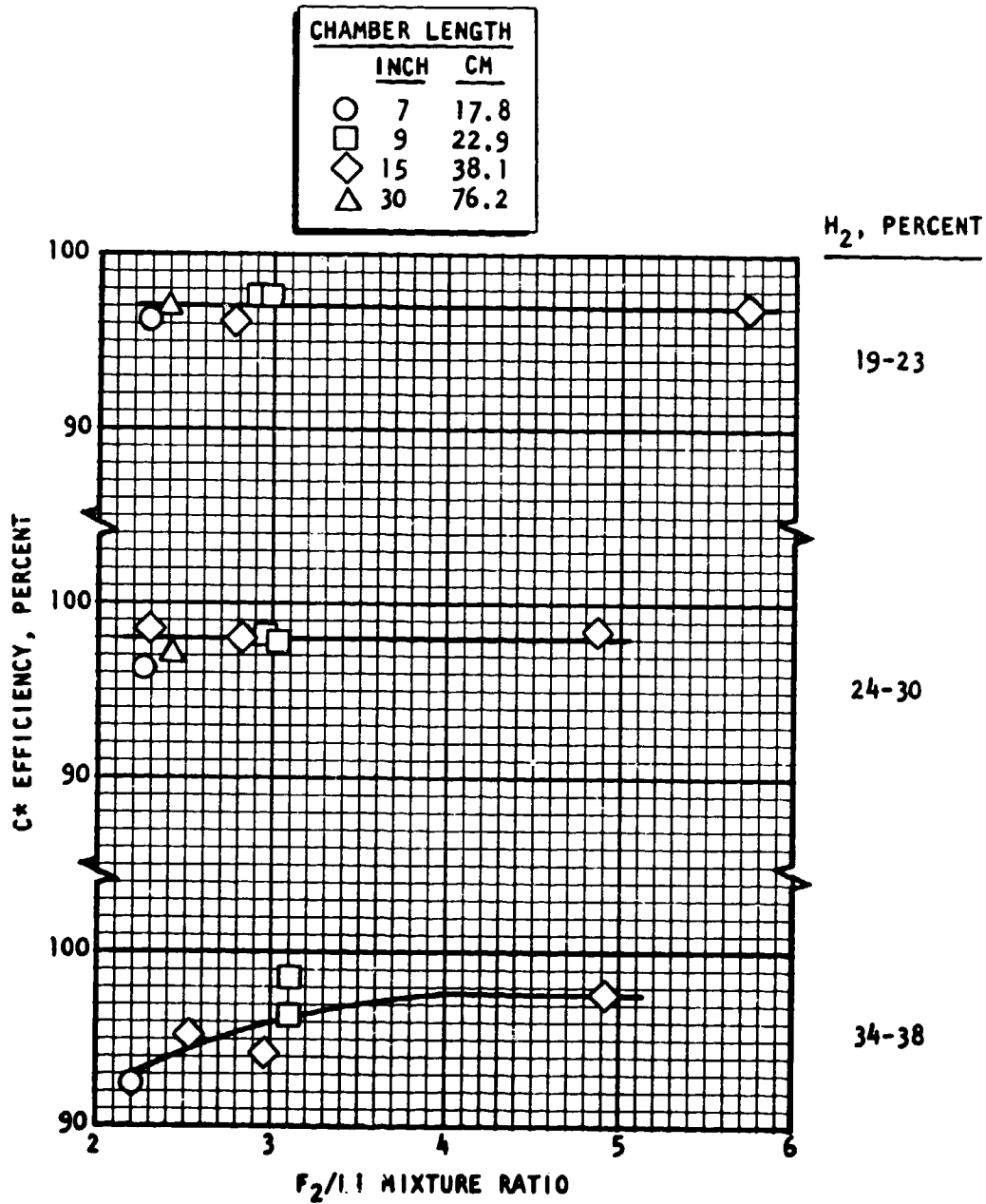


Figure 41. Corrected Characteristic Velocity Efficiency (Based on Chamber Pressure) of Li/F₂/H₂, With Fuel-Rich Gas Generator Injection Method, as Function of F₂/Li Mixture Ratio and Chamber Length at Indicated Percentages of Hydrogen

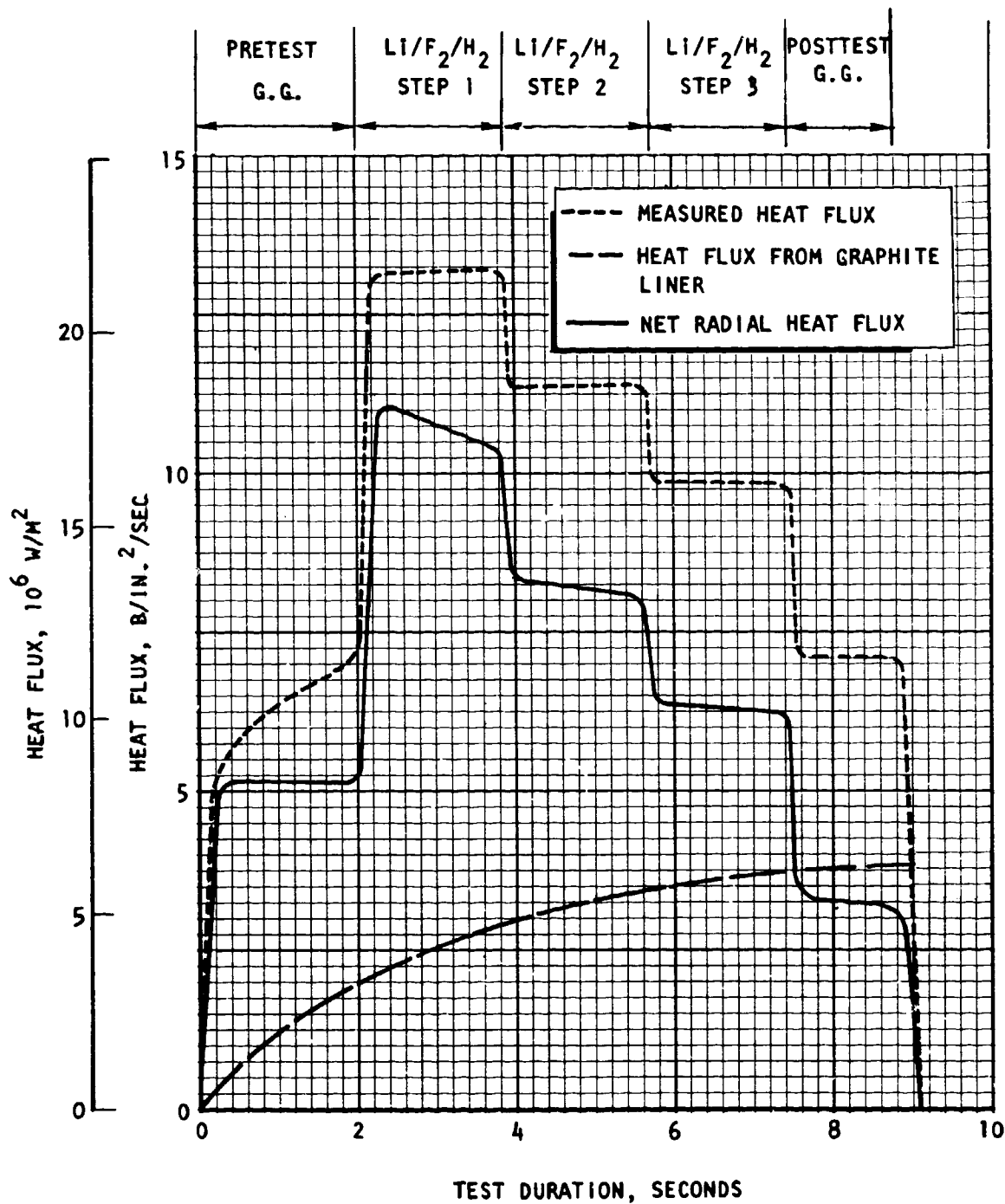


Figure 42. Typical Combustion Chamber Heat Fluxes Obtained in a Li/F₂/H₂ Test Firing, Showing Measured Values in Each Step, Estimated Heat Flux From Graphite Chamber Liner, and Net Radial Heat Flux. Faired Lines Used for Illustration

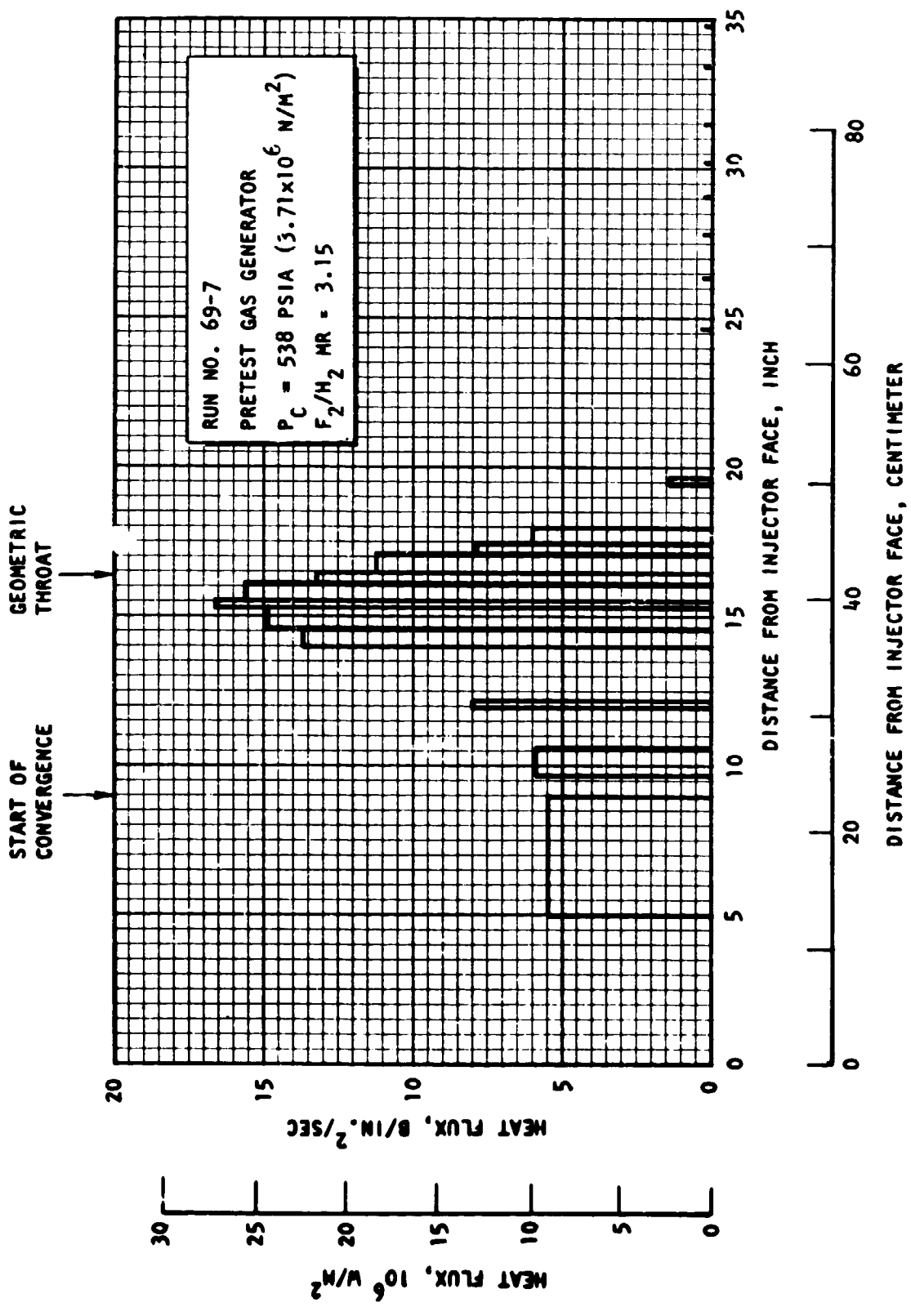


Figure 43. Experimental Heat Flux Data for Indicated Pretest Gas Generator Firing

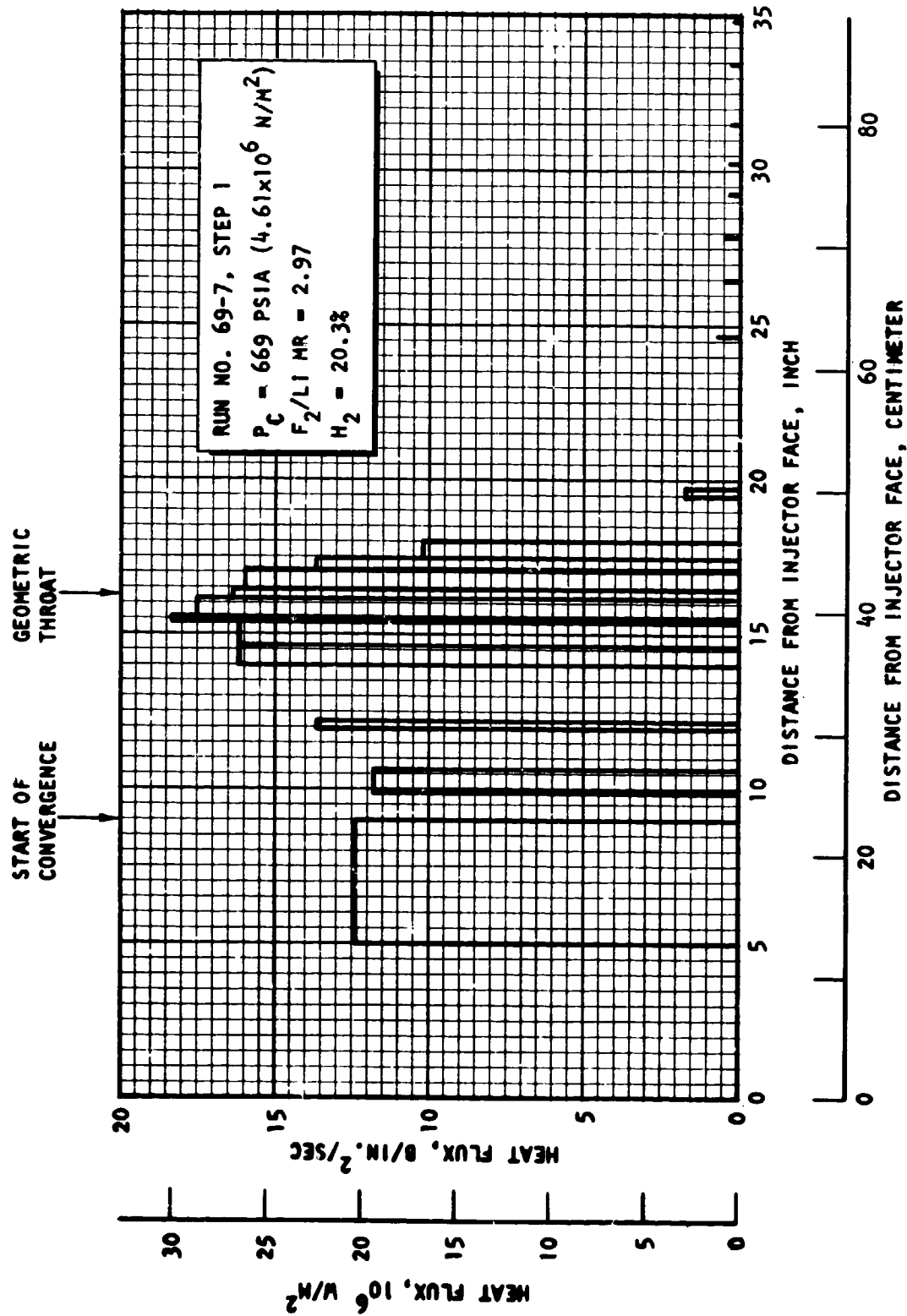


Figure 44. Experimental Heat Flux Data for Indicated Li/F₂/H₂ Firing

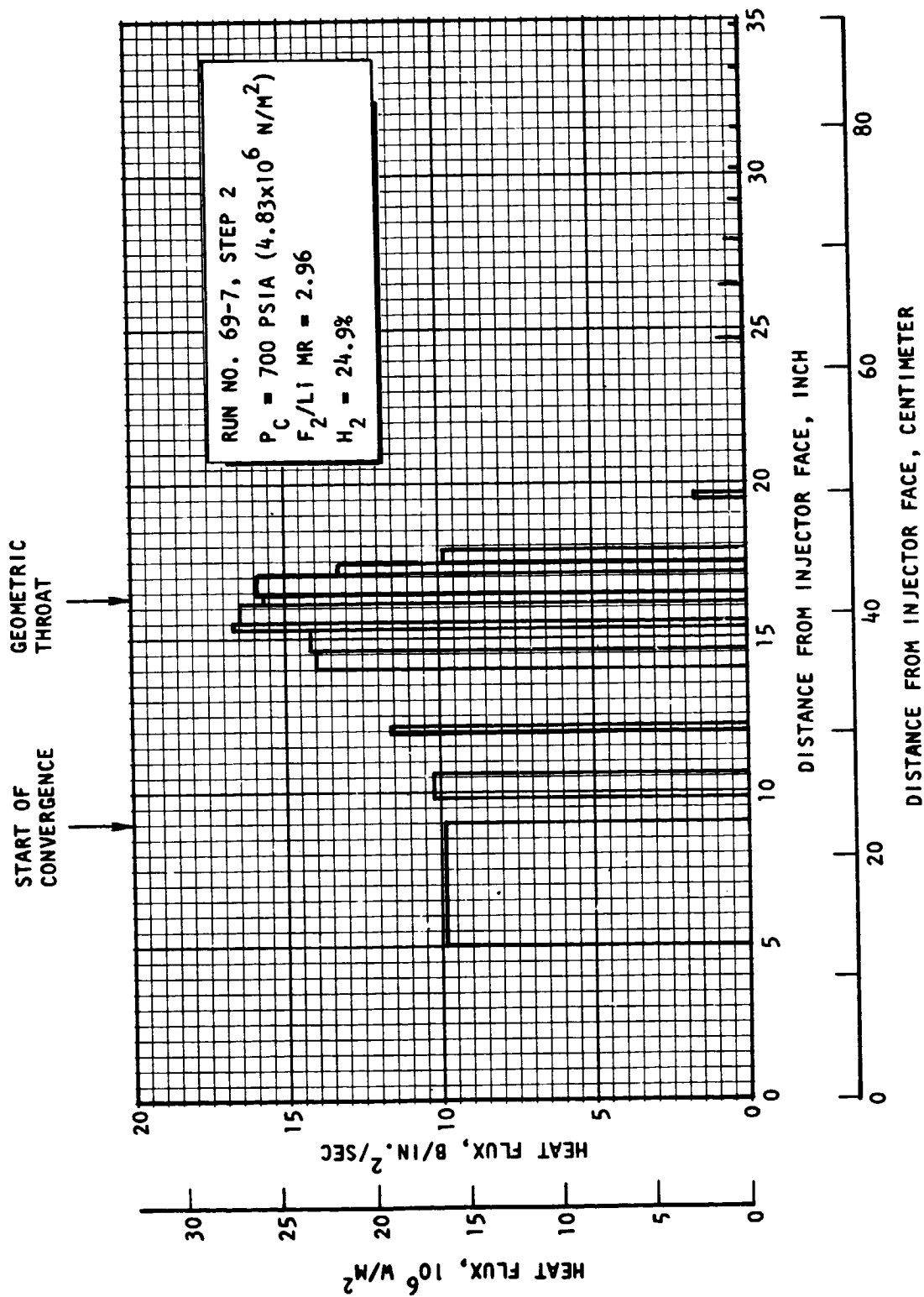


Figure 45. Experimental Heat Flux Data for Indicated Li/F₂/H₂ Firing

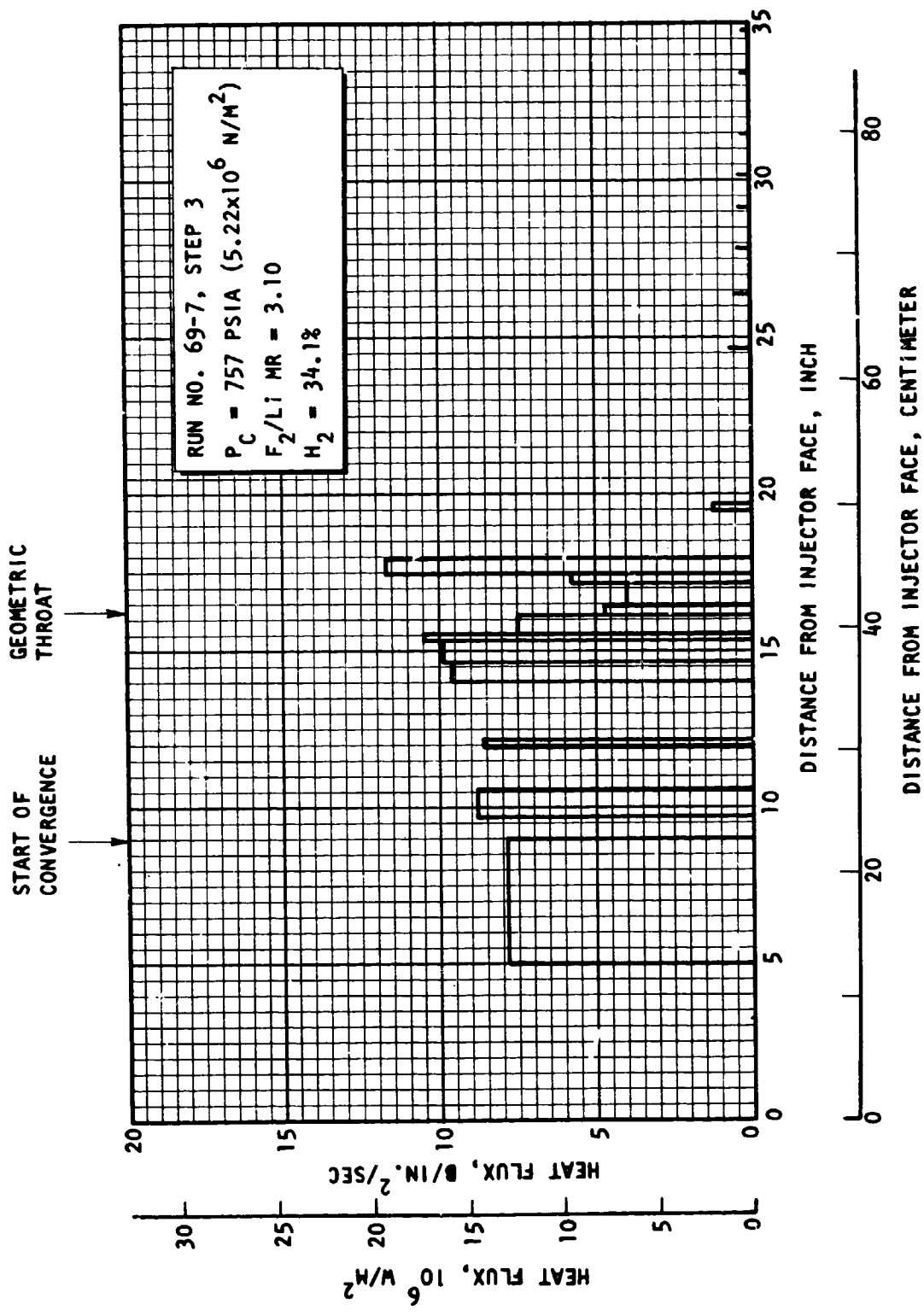


Figure 46. Experimental Heat Flux Data for Indicated Li/F₂/H₂ Firing

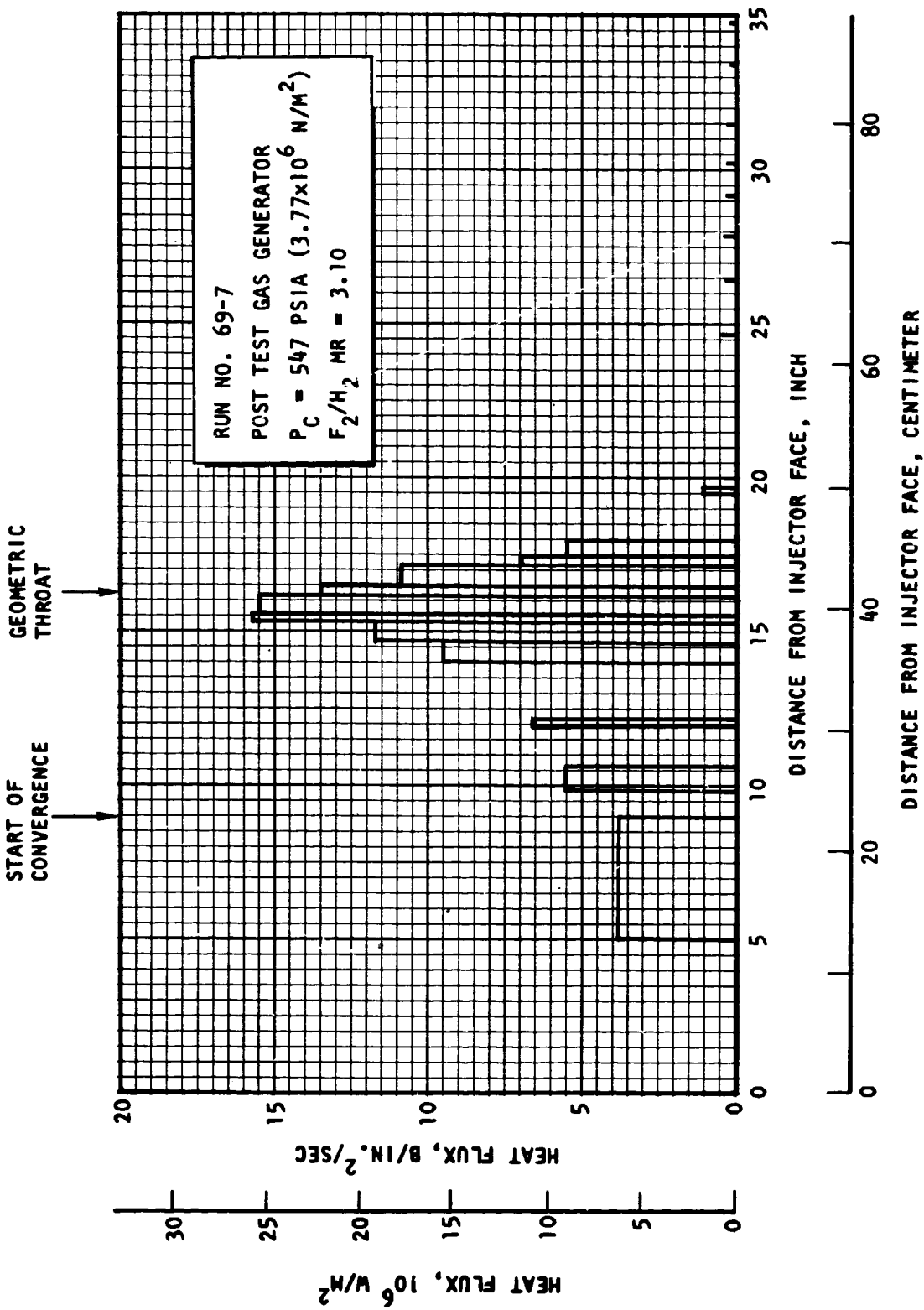


Figure 47. Experimental Heat Flux Data for Indicated Posttest Gas Generator Firing

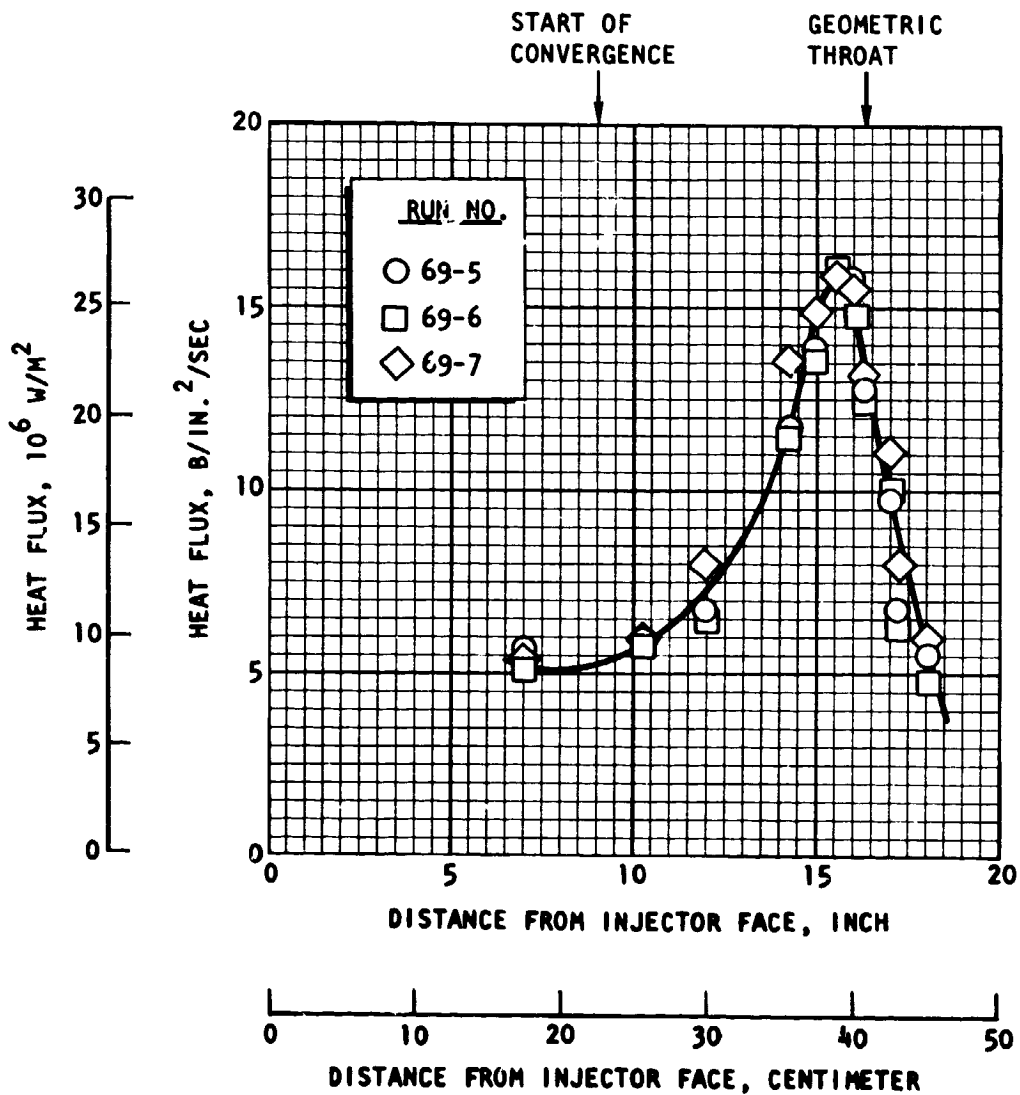


Figure 48. Measured Heat Fluxes During LF₂/GH₂ Gas Generator Portions of the Indicated Tripropellant Test Firings

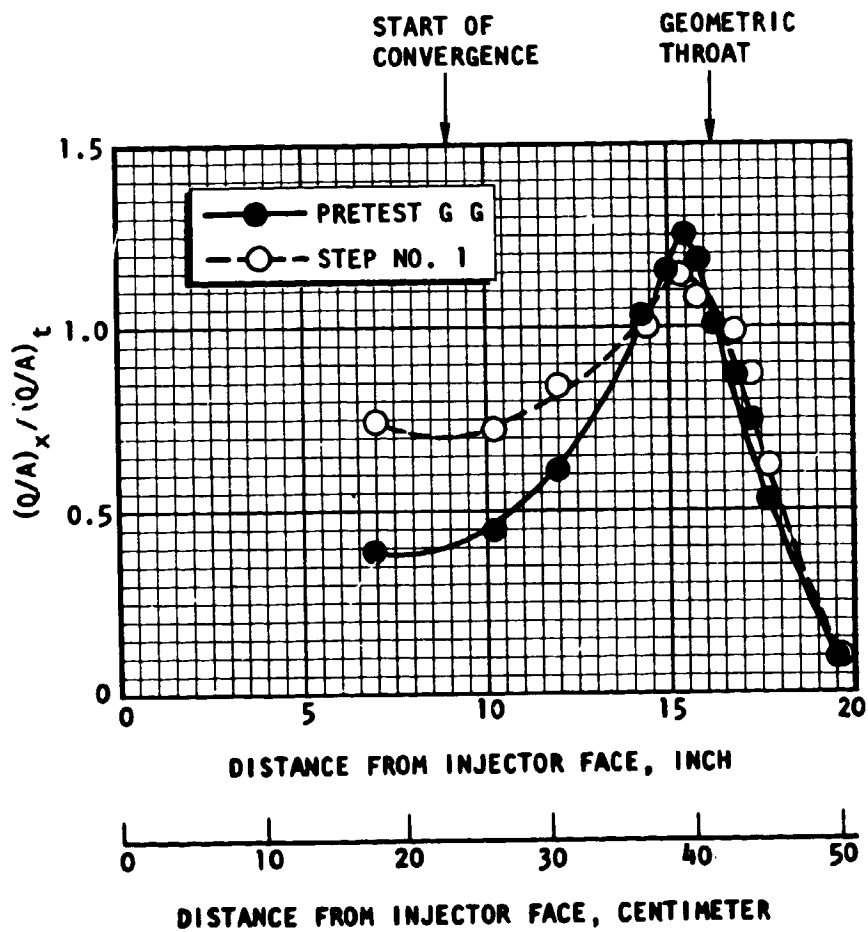


Figure 49. Heat Flux Profiles for Pretest Gas Generator Firing and for Step 1 of Li/F₂/H₂ Firing, Run No. 69-7

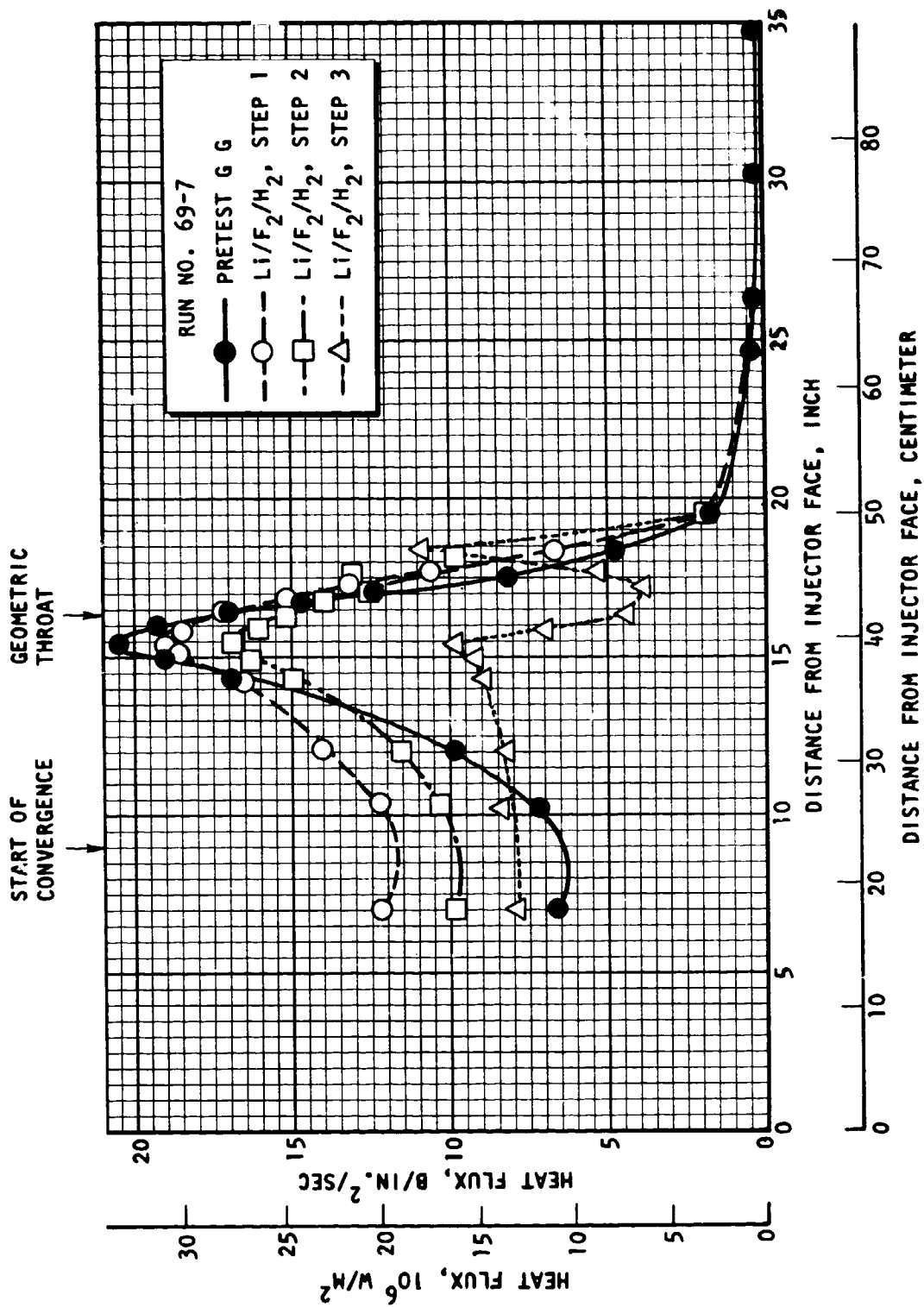


Figure 50. Thrust Chamber Heat Flux During Pretest LF₂/GH₂ Firing and Three Steps of Li/F₂/H₂ Firing (Run No. 69-7). Data are Normalized to Chamber Pressure of Step 2 (700 psia, 4.83 x 10⁶ N/m²)

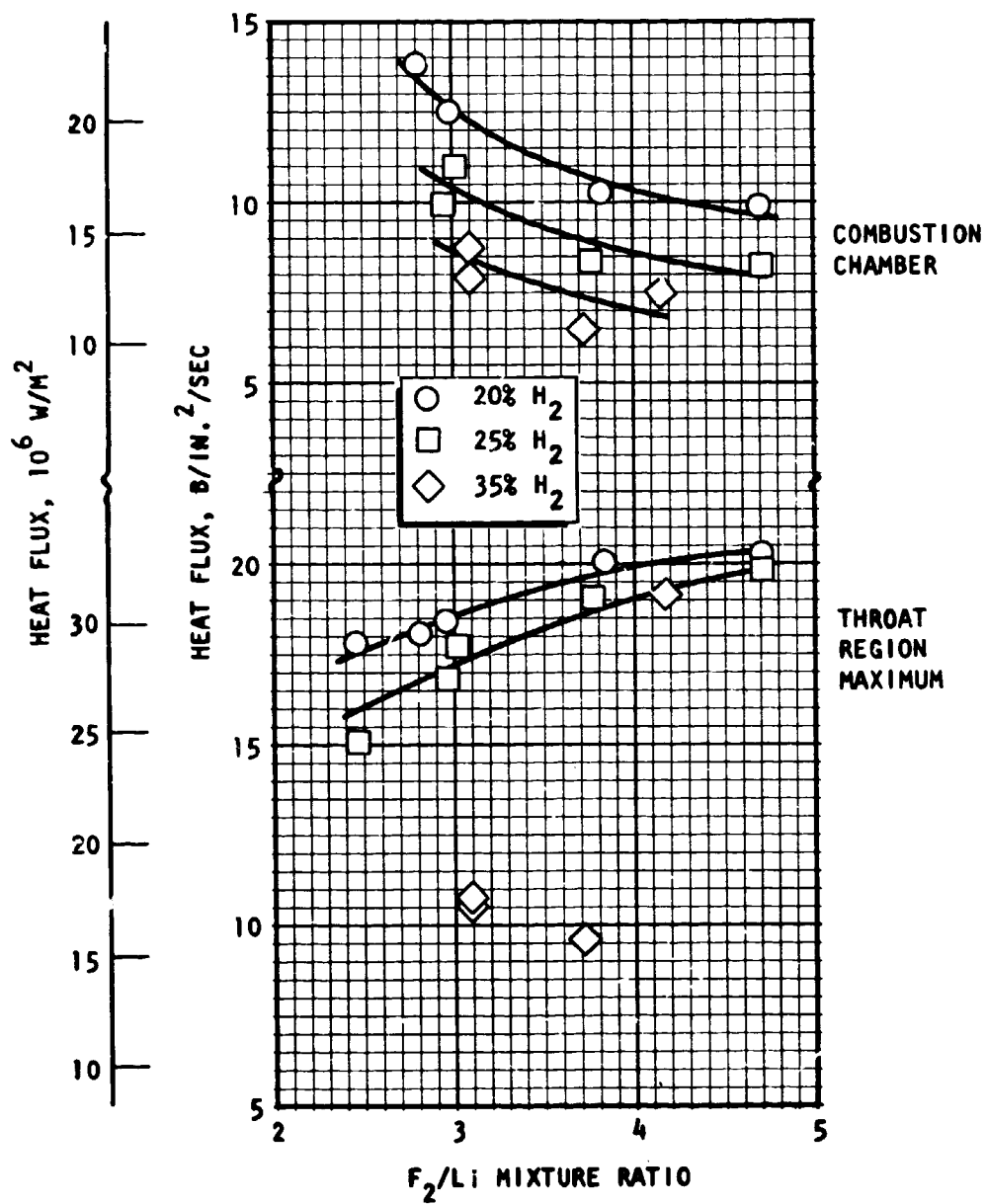


Figure 51. Combustion Chamber and Nozzle Throat Heat Flux for Li/F₂/H₂, as Functions of F₂/Li Mixture Ratio, at Indicated Percentages of Hydrogen

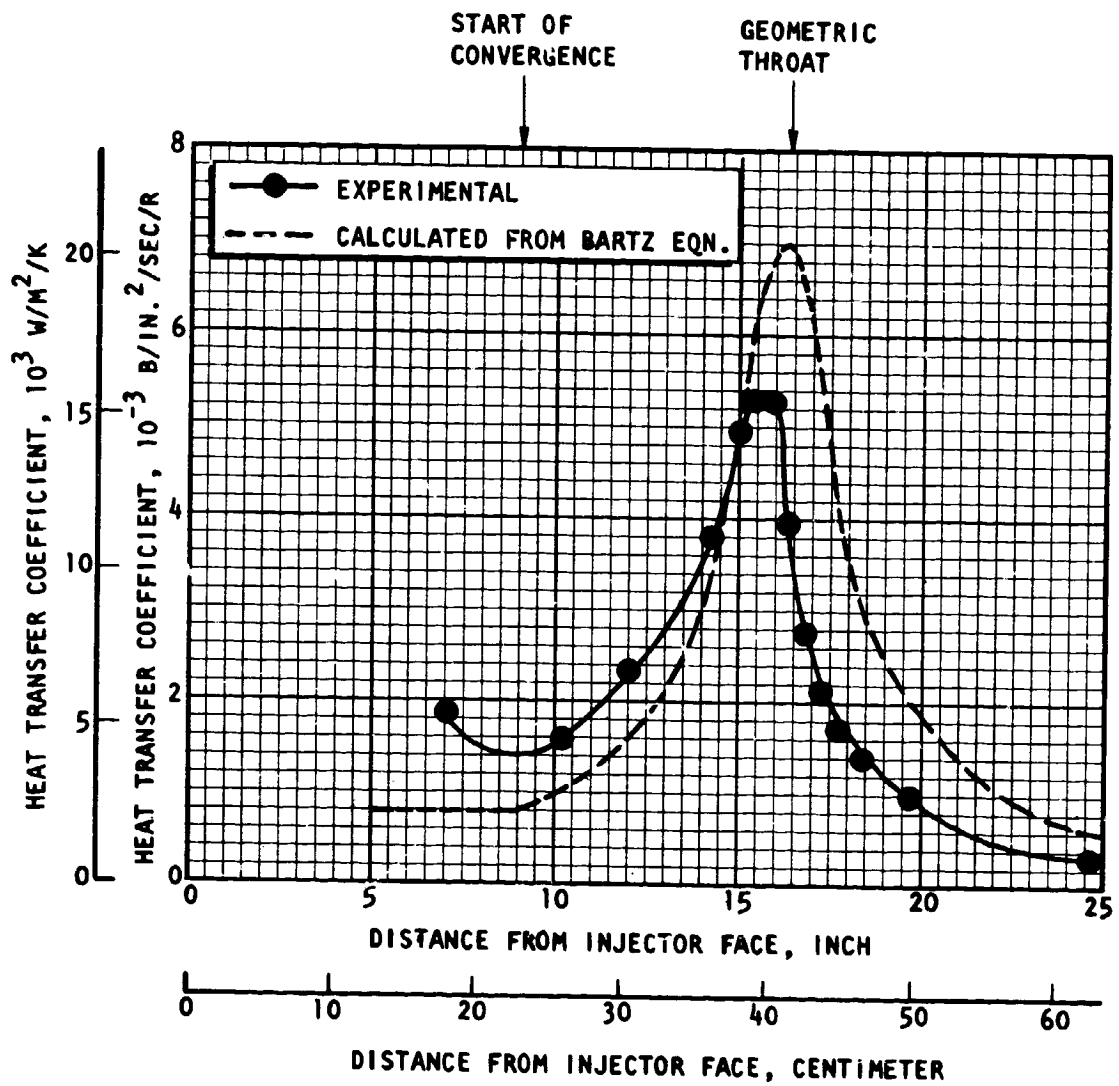


Figure 52. Experimental Heat Transfer Coefficients, Pretest LF₂/GH₂ Gas Generator Firing (Run No. 69-7), Compared With Values Calculated From Bartz Simplified Equation

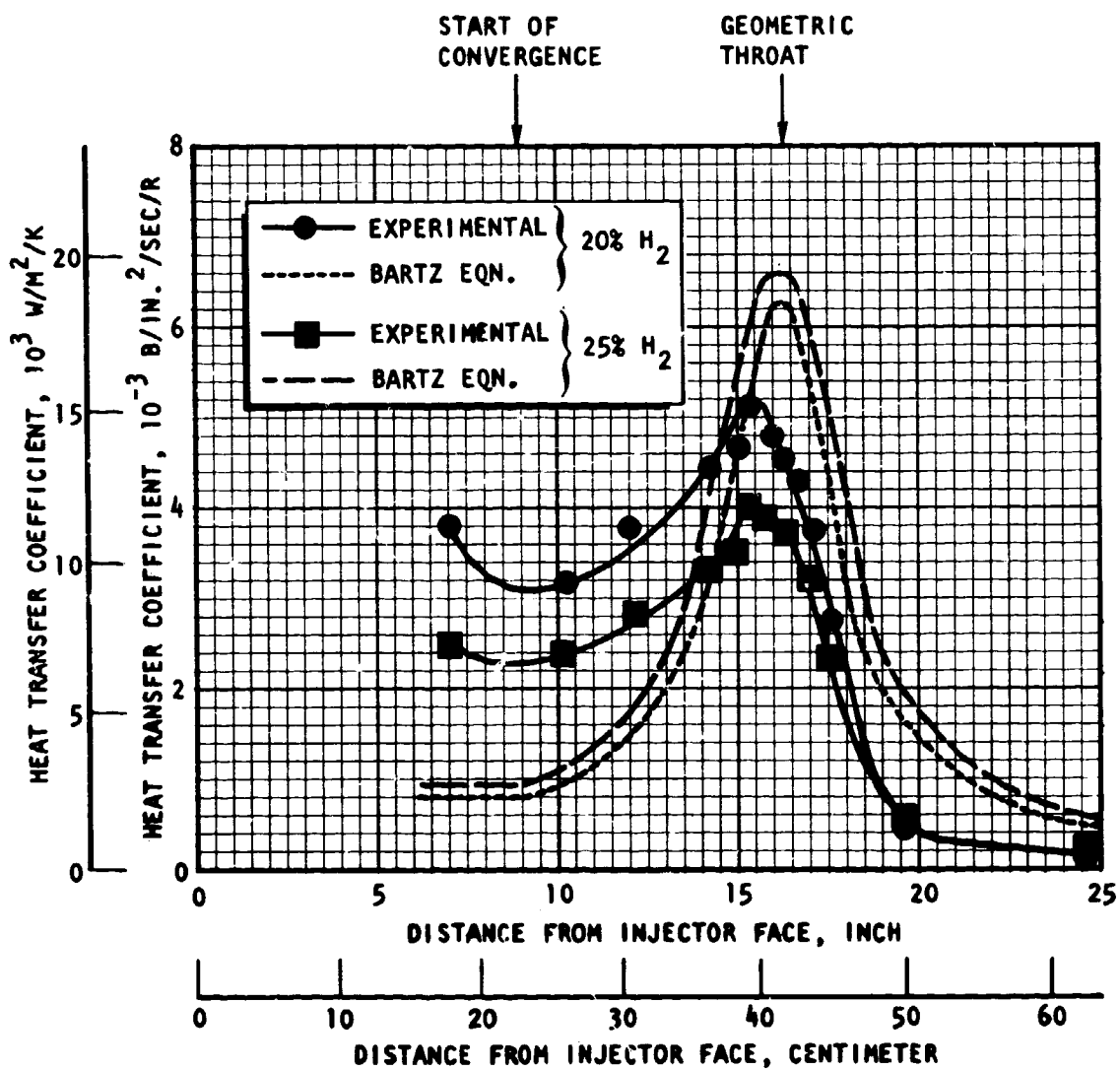


Figure 53. Experimental Heat Transfer Coefficients, Li/F₂/H₂ Tests at Indicated Percentages of Hydrogen (Run No. 69-7), Compared With Values Calculated From Bartz Simplified Equation

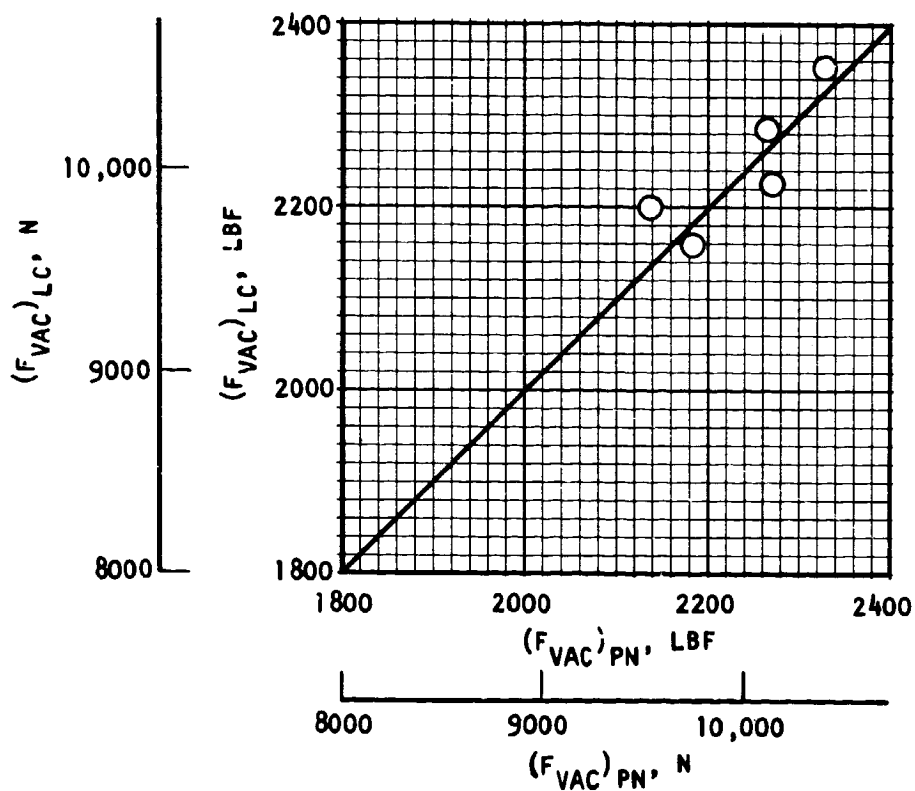


Figure 54. Comparison of Thrust Measurements Obtained Directly From Load Cell, $(F_{vac})_{LC}$, and by Integration of Nozzle Pressures, $(F_{vac})_{PN}$, in the Altitude Simulation Firings

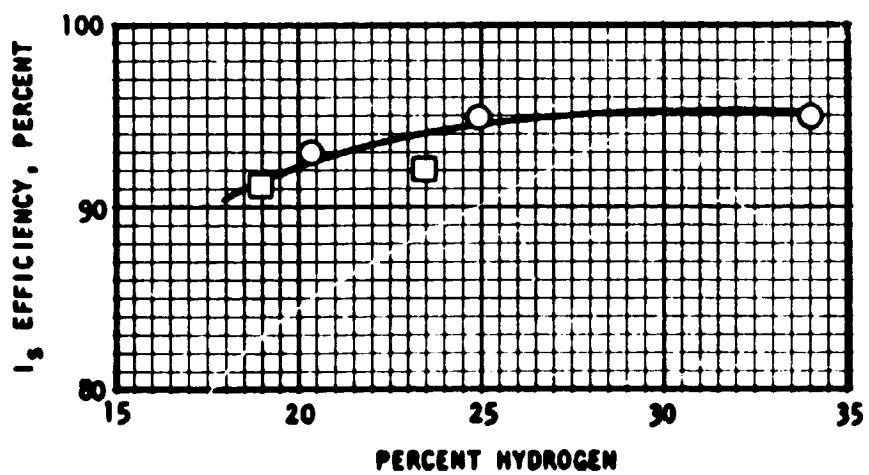
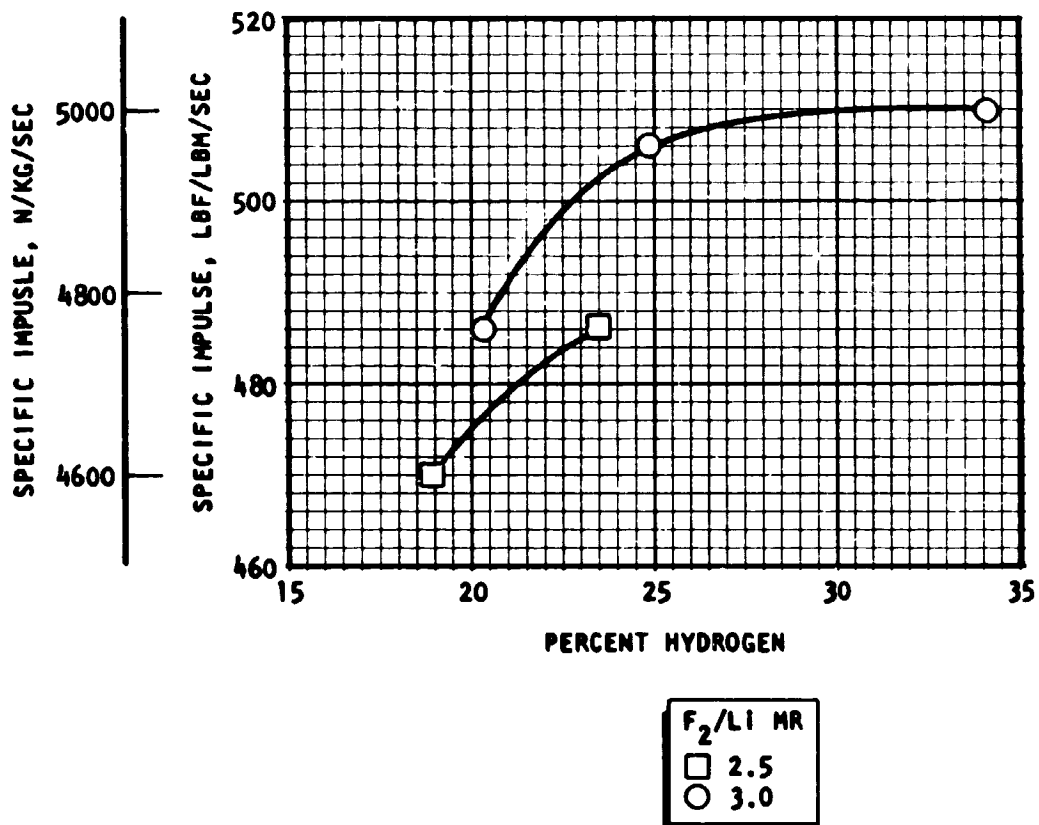


Figure 55. Measured, Uncorrected, Vacuum Specific Impulse and Specific Impulse Efficiency Obtained in the Li/F₂/H₂ Altitude Simulation Firings, $c = 60$

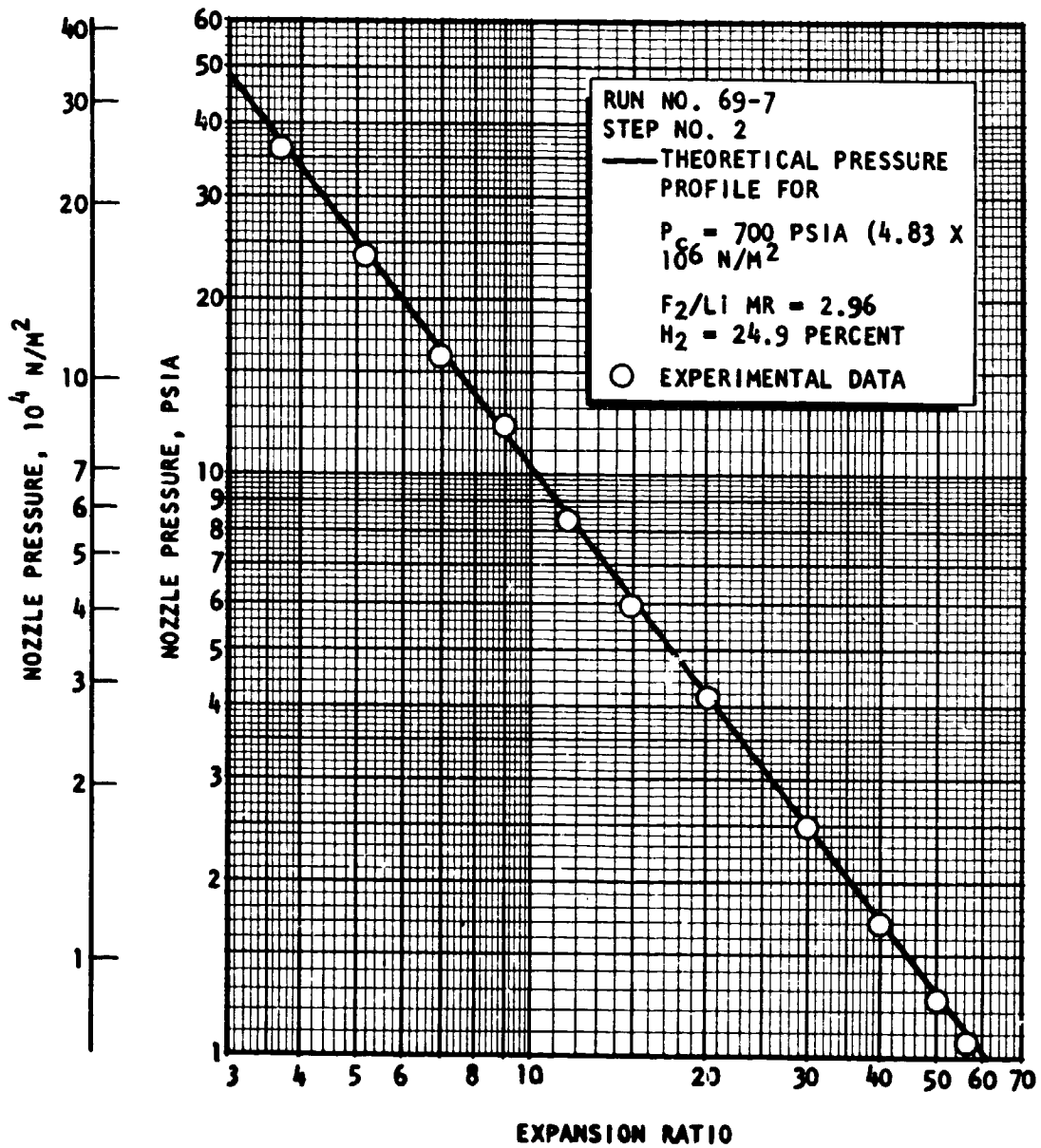


Figure 56. Comparison of Measured and Theoretical Nozzle Pressures for Typical Li/F₂/H₂ Altitude Simulation Test

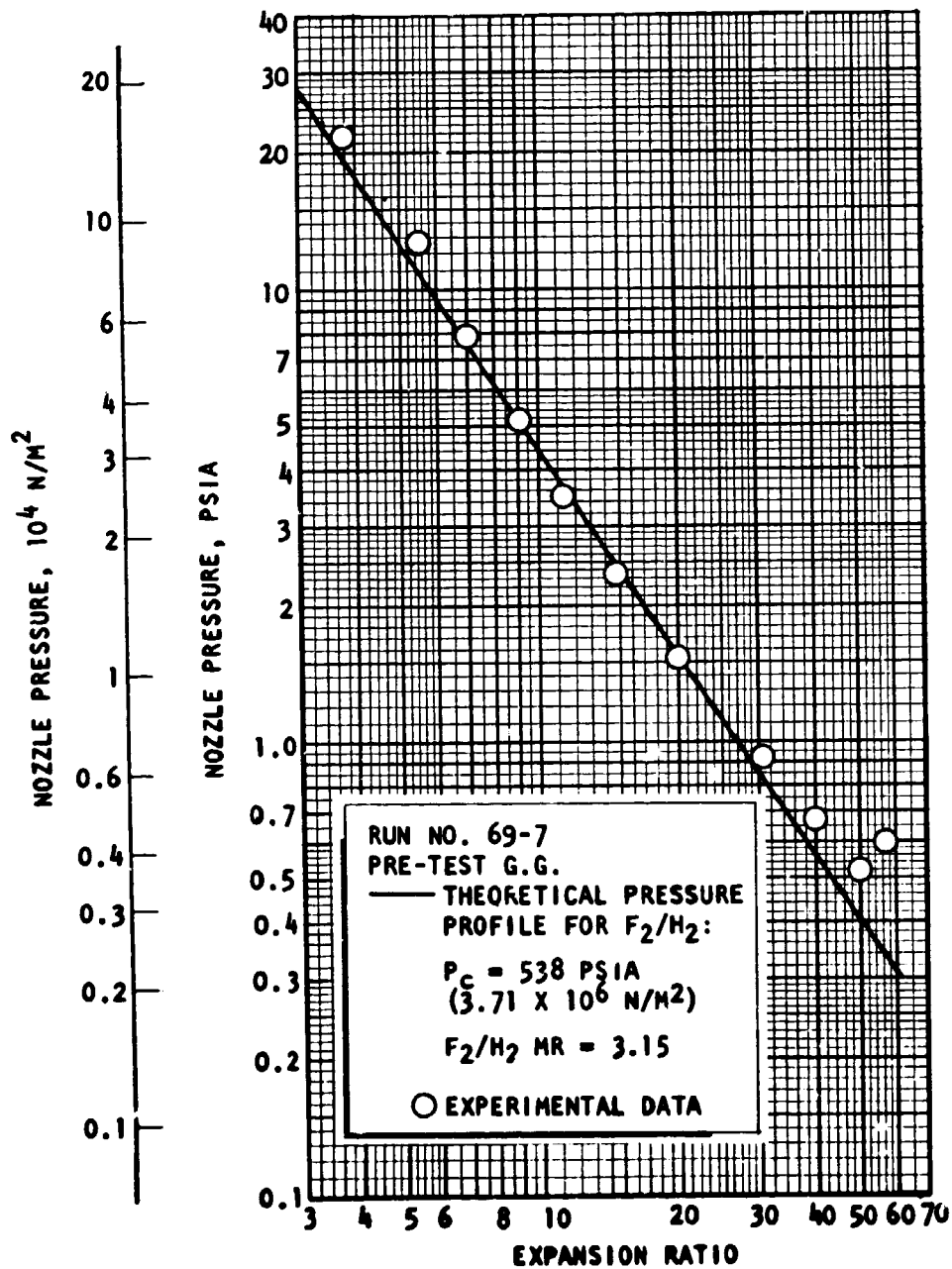


Figure 57. Comparison of Measured and Theoretical Nozzle Pressures for Typical LF₂/GH₂ Gas Generator Portion of Tripropellant Firing

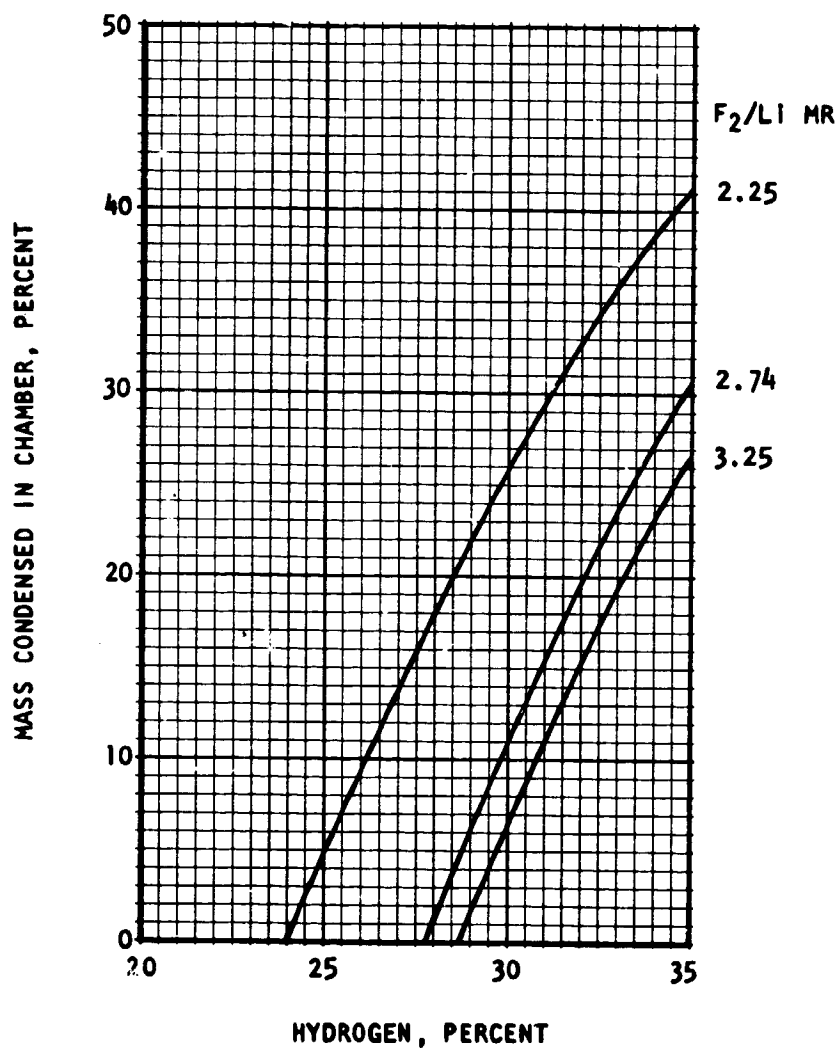


Figure 58. Weight Percent of Condensed Material (Liquid LiF) in Combustion Chamber. $Li/F_2/H_2$, $P_c = 750$ Psia (5.17×10^6 N/m²), at Indicated F_2/Li Mixture Ratios, as Function of Percent Hydrogen

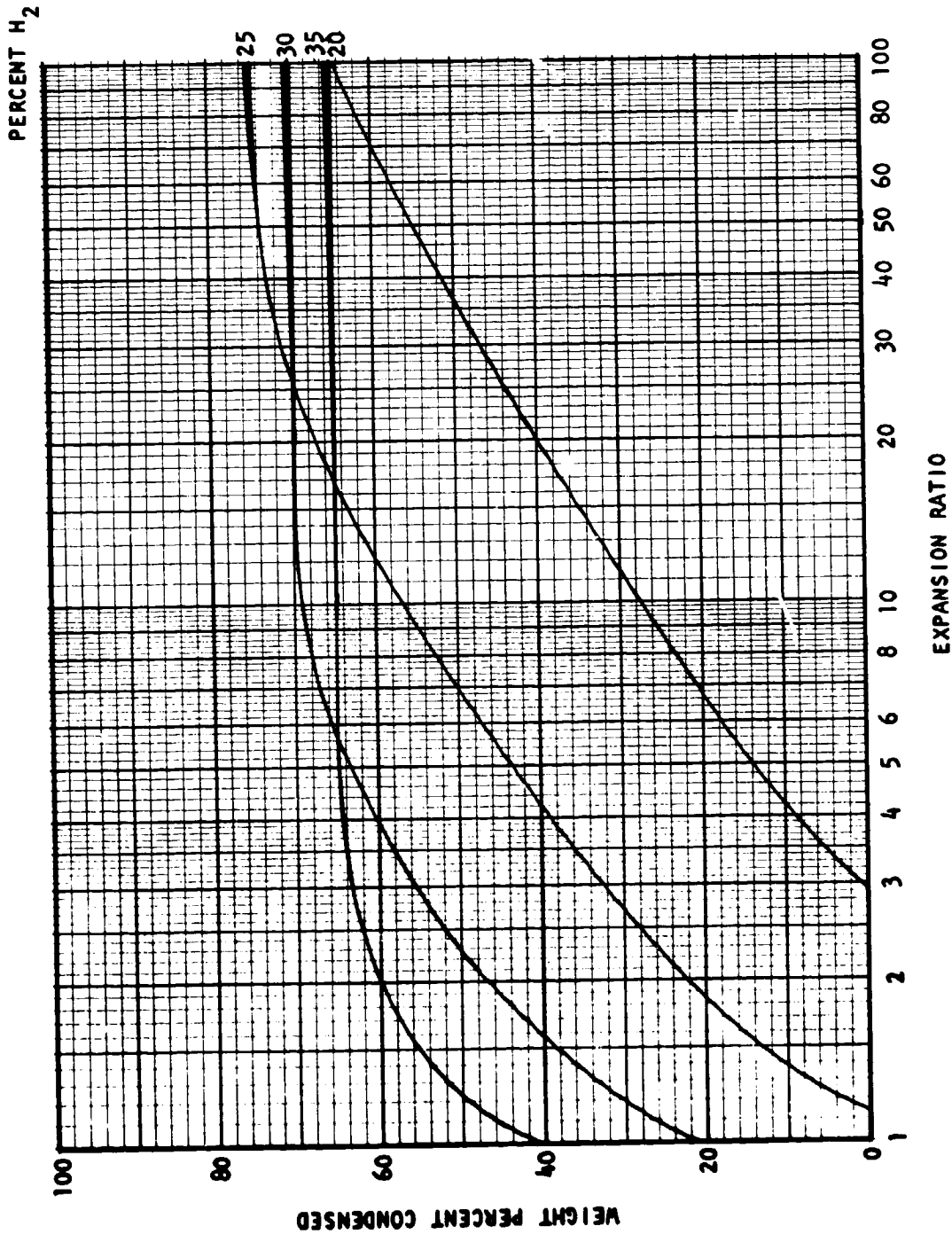


Figure 59. Weight Percent of Condensed Material in Divergent Nozzle. Thin Lines Represent Liquid LiF, Heavy Lines Represent Solid LiF. $\text{Li}/\text{F}_2/\text{H}_2$, $P_c = 750$ psia ($5.17 \times 10^6 \text{ N/m}^2$), F_2/Li MR = 2.74, at Indicated Percentages of Hydrogen

$P_c = 670 \text{ TO } 760 \text{ PSIA } (4.62 \times 10^6 \text{ TO } 5.24 \times 10^6 \text{ N/M}^2)$

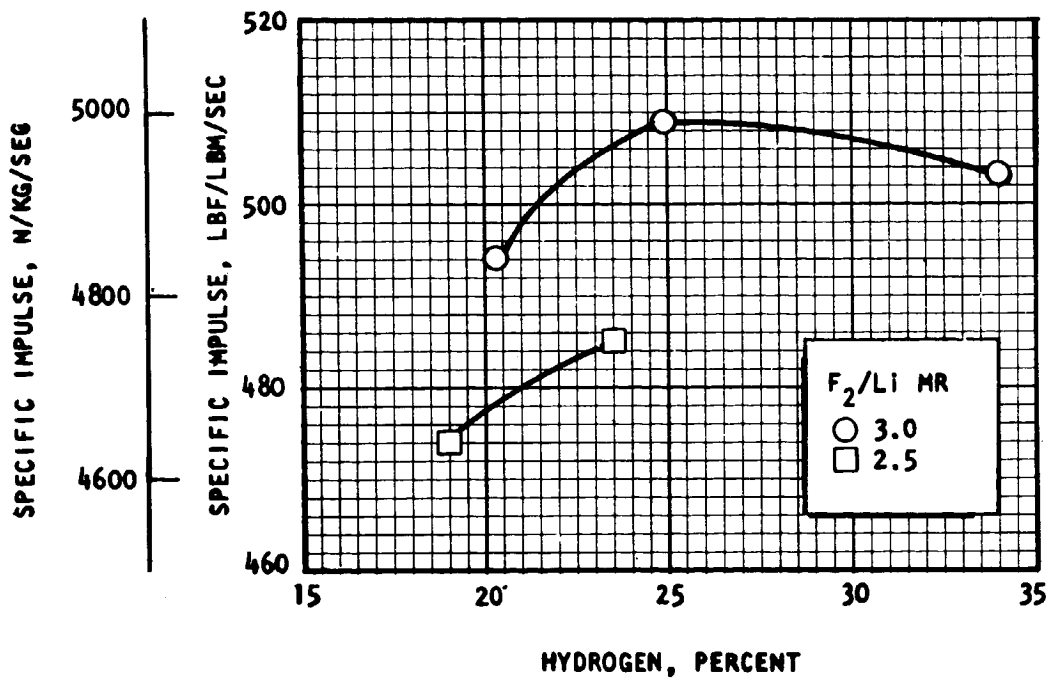


Figure 60. Vacuum Specific Impulse Deliverable by Li (533 K)/LF₂ (85 K)/LH₂ (20 K) Engine ($\epsilon = 60$) Cooled Regeneratively With Liquid Hydrogen, Based on Test Data, at Indicated Chamber Pressures and F₂/Li Mixture Ratios, as Function of Percent Hydrogen

APPENDIX A

PERFORMANCE CALCULATION METHODS

INTRODUCTION

The performance indices used in the present investigation were c^* and I_s efficiencies and deliverable vacuum specific impulse*. Corrected c^* efficiencies based on chamber pressure were determined for all the firings. Corrected c^* efficiencies based on thrust were determined only in the Task I firings, in which the nozzle expansion ratio was very low ($\epsilon = 2$), because the previous tripropellant study (Ref. A-1) had shown that the C_F efficiency of this short nozzle was essentially 100 percent. Specific impulse efficiencies were determined in the Task II and III firings, in which the nozzle expansion ratios were 10 and 60, respectively. Another performance parameter used in the altitude simulation tests of Task III was the vacuum specific impulse deliverable by an engine regeneratively cooled with liquid hydrogen. The calculated performance parameters are summarized below:

	<u>Task I</u>	<u>Task II</u>	<u>Task III</u>
$(\eta_{c^*})_{P_c}$	X	X	X
$(\eta_{c^*})_F$	X		
η_{I_s}		X	X
$(I_{s,vac})_{del}$			X

Details of the computational procedures and of the applicable corrections are given in this appendix.

*Thrust coefficient efficiency was not included as a performance index in this study because of the relatively high uncertainty level (± 2.2 percent) associated with its determination (Appendix B).

CHARACTERISTIC VELOCITY EFFICIENCY

Characteristic velocity (c^*) efficiency, or "energy release" efficiency, may be regarded as a measure of the ratio of the energy actually produced by propellant combustion to the energy theoretically available by conversion of the propellants from injection conditions to equilibrium conditions at the throat. Energy release occurs predominantly in the combustion chamber and, usually to a minor extent, within the subsonic portion of the nozzle. Energy release efficiency is one of the two factors which determine overall rocket engine performance, measured by delivered specific impulse; the other factor is the efficiency of the expansion process, or C_F efficiency. Energy release efficiency is experimentally determined by the application of suitable corrections to measured c^* efficiency.

Corrected c^* Efficiency Based on Chamber Pressure

Characteristic velocity efficiency based on chamber pressure is defined by the following equation:

$$[\eta_{c^*}]_{P_c} = \frac{(P_c)_o (A_t)_{\text{eff}} g_c}{(\dot{w}_T) (c^*)_{\text{theo}}} \quad (\text{A-1})^*$$

Values calculated from Eq. A-1 are referred to as "corrected" c^* efficiencies because the factors involved are not measured directly, but are obtained by application of suitable corrections to measured parameters. Thus, stagnation pressure at the throat is obtained from measured static pressure at the start of nozzle convergence by assumption of isentropic expansion, effective throat area is estimated from measured geometric area by allowing for radius changes during firing and for nonunity discharge coefficient, and chamber pressure is corrected to allow for energy losses from the combustion gases to the chamber wall by heat transfer and friction. Equation A-1 may therefore be written as follows:

$$[\eta_{c^*}]_{P_c} = \frac{P_c A_t g_c f_P f_{TR} f_{DIS} f_{FR} f_{HL}}{(\dot{w}_T) (c^*)_{\text{theo}}} \quad (\text{A-2})$$

*See Appendix I for nomenclature.

The methods used to estimate the correction factors in Eq. A-2 are described below.

Pressure Correction (f_p). Measured static pressure at the start of nozzle convergence was converted to stagnation pressure at the throat by assumption of no combustion in the nozzle (i.e., energy release completed in the combustion chamber) and application of the isentropic flow equations. For the firings using oxidizer-rich gas generator injection method ($\epsilon_c \approx 8$, $\gamma = 1.26$ to 1.29), $f_p = 1.003$; for those using the fuel-rich gas generator injection method ($\epsilon_c \approx 11$), $f_p = 1.002$.

Throat Radius Correction (f_{TR}). Temperature gradients produced in an uncooled nozzle wall by flow of hot combustion gases result in thermal stresses which may affect throat radius. Consequently, the geometric throat diameter measured in an ambient-temperature nozzle may not be the same as that which exists during firing. When firing begins, thermal penetration of the nozzle wall is small with respect to the wall thickness and the outer wall diameter is unchanged. The inner wall material will therefore expand toward the center, resulting in a decrease in throat diameter. As heat penetrates throughout the nozzle wall, the outer diameter will also increase, allowing outward expansion of the inner portion and consequent increase in throat diameter. Hence, throat diameter during firing is a function of time, as well as of the physical properties of the throat material and the temperature and pressure of the combustion gases.

A Rocketdyne computer program is available which estimates the change in throat radius as a function of firing time (Ref. A-2). The computation is based on numerical integration of the transient thermal stress equations for a hollow cylinder (Ref. A-3). A cubic temperature distribution is assumed in the wall, plastic as well as elastic strain in the wall material is considered, and allowance is made for stress caused by gas pressure. These calculations were carried out for the uncooled, graphite-lined nozzles used in the Task I firings. Convective film coefficients

at the throat were estimated from the Bartz equation (Ref. A-4) and calculations were made using both "with-grain" and "across-grain" properties of ATJ graphite. In both cases, over the range of test parameters and for the test durations employed, the throat radius change was less than 0.1 percent. Consequently, $f_{TR} = 1.000$.

Thermal stress throat diameter changes in the water-cooled nozzles used in the firings of Tasks II and III were assumed to be negligible; hence, in all the tests, $f_{TR} = 1.000$.

Throat Discharge Coefficient Correction (f_{DIS}). The discharge coefficient is defined as the ratio of actual mass flowrate through the throat to the theoretical maximum based on the geometric throat area and one-dimensional, inviscid flow. Values of the discharge coefficient may be estimated either analytically or from correlations of the results of experimental studies of gas flow through nozzles. In the present program, the ratio of the upstream wall radius at the throat to the throat radius was large (4:1), so that the discharge coefficient was very nearly unity and either of the two methods could be employed.

In a critical study of available theoretical analyses of nozzle flow (Ref. A-5), values of the throat discharge coefficient were calculated as functions of the nozzle wall/throat radius ratio and throat Reynolds number. The indicated value under the present test conditions was $f_{DIS} = 0.997$. This is in good agreement with the value (0.995) obtained by applying the correlations of experimental conical nozzle discharge coefficients obtained by various investigators (Ref. A-6) to the geometry of the present nozzle.

Frictional Drag Correction (f_{FR}). Calculations of c^* based on chamber pressure are concerned with chamber phenomena up to the nozzle throat. Drag forces to this point are generally small enough to be considered negligible, particularly when the contraction ratio is large, as in the present case. Hence, the factor f_{FR} was taken to be unity.

Heat Loss Correction (f_{HL}). Heat transfer from the combustion gases to the thrust chamber walls results in loss of enthalpy. This enthalpy loss is substantially reduced in an ablatively cooled chamber and is effectively recovered in a regeneratively cooled chamber. To obtain a realistic indication of energy release efficiency, measured c^* must be corrected by a factor which accounts for the heat lost to the chamber walls and injector face.

The heat loss correction factor may be calculated in two ways, both of which require an estimation of the total heat loss between the injector and throat. In the first method, the correction factor is obtained from the following equation (Ref. A-6):

$$f_{HL} = \left[1 + \left(\frac{c^*_{th}}{c^*_{obs}} \right) \left(\frac{Q_{total}}{\dot{w}_T C_p T} \right) \right]^{1/2} \quad (A-3)$$

In the second method, the heat loss correction factor is not calculated explicitly. Instead, the enthalpy of the injected propellants is reduced by an amount equivalent to the total heat lost, and the theoretical c^* is calculated on the basis of the reduced injection enthalpy. While this procedure lumps all the heat lost and confines it to the injection station instead of applying the loss gradually along the chamber length, the difference is not considered to be significant.

The second procedure was used in the previous Li/F₂/H₂ study (Ref. A-1) and was continued in the present investigation. Agreement between the two methods was good (± 0.2 percent). The required total heat loss was obtained by summation of the products of the heat fluxes in the various regions of the combustion chamber and convergent nozzle and the appropriate areas. For the water-cooled chamber sections, the heat fluxes were the actual measured values; for the uncooled sections, heat fluxes were estimated as discussed in Ref. A-1. Values of the heat loss correction factor were in the range 1.010 to 1.019 for the uncooled chambers and 1.015 to 1.029 for the water-cooled chambers.

Corrected c* Efficiency Based on Thrust

The alternate method of determining c* efficiency, which was used for the Task I tests, is based on the following defining equation:

$$[\eta_{c^*}]_F = \frac{F_{vac} g_c}{(C_F)_{vac} \dot{w}_T (c^*)_{theo}} \quad (A-4)$$

Corrected values of vacuum thrust were obtained by application of suitable corrections to measured thrust. With these corrections, and the assumption of 100-percent C_F efficiency, the expression for c* efficiency based on thrust becomes:

$$[\eta_{c^*}]_F = \frac{(F + P_a A_e) \phi_{FR} \phi_{DIV} \phi_{HL}}{(\dot{w}_T) (I_s)_{theo}} \quad (A-5)$$

Although they do not appear explicitly in Eq. A-5, corrections to the geometric throat area and to the measured static chamber pressure at start of nozzle convergence are implicit in the use of theoretical I_s values. Thus, the calculation of corrected c* efficiency from thrust includes all the corrections described above for calculation from chamber pressure plus an additional one to account for nonparallel nozzle exit flow. However, because $(I_s)_{vac}$ is essentially independent of the very small changes in chamber pressure and contraction ratio which are involved in corrections to P_c and A_t , these corrections are of no practical significance in the calculation of c* from thrust.

Correction for Frictional Drag (ϕ_{FR}). This factor corrects for the energy losses caused by drag forces resulting from the viscous action of the combustion gases on the thrust chamber wall. Its magnitude, which is the integral of the local friction forces over the chamber inside wall, was estimated by a boundary layer analysis utilizing the integral momentum equation for turbulent flow. This analysis accounts for boundary layer effects from the injector to the nozzle exit by suitable description of

the boundary layer profile and local skin friction coefficient. A computer program was used to carry out a numerical integration of the equation, including effects of pressure gradient and heat transfer. The program required a potential core solution of the nozzle flow which was obtained from the variable-property, axisymmetric method of characteristics calculation of the flow field outside the boundary layer; corresponding properties of the subsonic combustion chamber flow field were also calculated. This program considers only gas dynamics; no allowances were made for possible two-phase flow effects. Computed values of ϕ_{FR} ranged from 1.005 to 1.008 for the conditions of the Task I experimental firings.

Correction for Nozzle Divergence (ϕ_{DIV}). The one-dimensional theoretical performance calculations assume that flow at the nozzle exit is uniform and parallel to the nozzle axis. The correction factor, ϕ_{DIV} , allows for nozzle divergence (i.e., for nonaxial flow) and for nonuniformity across the nozzle exit plane. It was calculated from the standard equation (Ref. A-7):

$$\phi_{DIV} = [1/2 (1 + \cos \alpha)]^{-1} \quad (A-6)$$

This gave $\phi_{DIV} = 1.017$.

Correction for Heat Losses (ϕ_{HL}). The effect of heat loss to the chamber walls on measured I_s was determined by inclusion of the divergent nozzle heat flux in the total loss. In the calculations of theoretical specific impulse which included the effect of heat loss in the thrust chamber, the loss up to the throat was subtracted from the propellant injection enthalpy and the loss in the divergent portion of the nozzle (which was relatively small) was subtracted from the enthalpy of the combustion products at the throat. Values of ϕ_{HL} were in the range 1.018 to 1.034.

SPECIFIC IMPULSE EFFICIENCIES

The specific impulse efficiencies calculated in Tasks II and III were uncorrected values, taken directly from measured parameters:

$$\eta_{I_s} = \frac{F}{\dot{w}_T (I_s)_{\text{theo}}} \quad (\text{A-7})$$

DELIVERABLE VACUUM SPECIFIC IMPULSE

A regeneratively cooled engine would have all the performance losses of the water-cooled test hardware except the loss caused by heat flux to the chamber walls. Whereas this energy was not recoverable in the test hardware, it would be transmitted to the cooling propellant in the hypothetical regenerative engine and thus retained. Deliverable, regenerative-engine specific impulse might be calculated by subtracting the performance loss due to heat flux in the water-cooled thrust chamber from the total measured loss. However, the following more direct method was used to obtain deliverable vacuum specific impulse from the test data. Observed thrust under test conditions (determined by direct load cell measurement and by integration of nozzle pressures, Appendix C) was reduced to measured (uncorrected) specific impulse efficiency. Measured thrust chamber heat flux (including estimated flux in the uncooled portions of the chamber) was used to calculate the hydrogen injection temperature which would be obtained in a regeneratively cooled engine with LH₂ inlet temperature of 36 R (20 K). Theoretical Li/F₂/H₂ performance was computed with hydrogen at the calculated injection temperature and the deliverable specific impulse was then obtained from the observed I_s efficiency. This method assumes only that the measured, uncorrected I_s efficiency obtained with hydrogen injected at ambient temperature is the same as that with hydrogen injected at the temperature it would reach as a result of absorption of

heat from the thrust chamber. Both the c^* and C_F efficiencies are unchanged; the only difference is that instead of using the heat flux into the chamber wall to heat the coolant water, as in the experimental firings, it is used to heat hydrogen. These calculations are illustrated by the following example (Run No. 69-7, Step No. 2):

Measured I_s efficiency = 94.7 percent (Table 7)

Total heat loss to coolant hydrogen = 2519 B/sec (2.67×10^6 W)

Hydrogen injection temperature = 648 R (360 K)

Theoretical vacuum specific impulse for Li (533 K)/F₂ (85 K)/H₂ (360 K),
at $P_c = 700$ psia (4.83×10^6 N/m²), F₂/Li MR = 2.96, H₂ = 24.9 percent,
 $\epsilon = 60$, = 537.5 lbf/lbm/sec (5271 N/kg/sec)

Deliverable specific impulse = (0.947) (537.5)

= 509 lbf/lbm/sec (4991 N/kg/sec)

REFERENCES

- A-1. Arbit, H. A., R. A. Dickerson, S. D. Clapp, and C. K. Nagai, Lithium-Fluorine-Hydrogen Propellant Study, NASA CR-72325, Contract NAS3-7954, Prepared for National Aeronautics and Space Administration by Rocketdyne, a division of North American Rockwell Corporation, Canoga Park, California, 22 February 1968.
- A-2. Hauenstein, C. A., Alternate Throat Development Program for the Apollo Command Module Reaction Control Engines, Report No. R-5941, Rocketdyne, a division of North American Aviation, Inc., Canoga Park, California, 16 November 1964.
- A-3. Timoshenko, S. and J. N. Goodier, Theory of Elasticity, McGraw-Hill Book Company, New York, N. Y., 1951.
- A-4. Bartz, D. R., "A Simple Equation for Rapid Estimation of Rocket Nozzle Convective Heat Transfer Coefficients," Jet Propulsion, Vol. 27, 49-51, January 1957.
- A-5. Singer, H. A., Discharge Coefficients of Nozzles Having Sharp Throat Curvature, LAP 66-518, Rocketdyne, a division of North American Aviation, Inc., Canoga Park, California, 18 October 1966.
- A-6. Arbit, H. A. and S. D. Clapp, Fluorine-Hydrogen Performance Evaluation, Phase I, Part I: Analysis, Design, and Demonstration of High-Performance Injectors for the Liquid Fluorine-Gaseous Hydrogen Propellant Combination, NASA CR-54978, Contract NASw-1229, Prepared for NASA by Rocketdyne, a division of North American Aviation, Inc., Canoga Park, California, July 1966.
- A-7. Sutton, G. P., Rocket Propulsion Elements, Third Edition, John Wiley & Sons, Inc., New York, N. Y., p. 65, 1963.

APPENDIX B

MEASUREMENT ERROR ANALYSIS

INTRODUCTION

The true value of any physical property or parameter can never be known. Experimentally, it is possible only to determine that the true value probably falls within stated upper and lower limits, with the probability specified in a statistical sense. The limits define an uncertainty interval, or maximum error, which is associated with every experimental measurement and which necessarily constitutes an explicit or implicit part thereof. It is the purpose of this appendix to indicate the reliability of the experimental measurements made in the present program by estimation of the errors inherent in the data acquisition processes and in the calculation procedures. In turn, this permits estimates to be made of the range within which, at a given confidence level, the true values of the measured or calculated parameters may be expected to lie.

Measurement uncertainty has two components:

1. Systematic errors. These are associated with the particular system, with the experimental techniques employed, or with the calibration procedures. They cannot be estimated by purely statistical methods, and are minimized primarily by careful calibration with the best available standards, by requirements for consistency and traceability of the experimental and calibration techniques, and by critical examination of experimental data.
2. Random errors. These arise from unpredictable and unknown variations in the experimental situation and are generally assumed to follow a normal distribution to permit simple statistical analyses.

Error analysis is concerned only with random errors and implicitly assumes that systematic errors can be eliminated in a carefully conducted experimental program. Furthermore, such analysis does not include random variations in the parameters being measured; only uncertainties resulting from sources other than the variability of the parameter itself are considered. These sources are the ones included in the precision of the measurement process.

It is apparent that under some circumstances systematic errors (also referred to as constant error, or bias) may be orders of magnitude larger than random errors, for reasons which are avoidable, such as faulty systems or human errors, or unavoidable, such as inherent limitations of the particular experimental procedures being used. In the latter case, even if avoidable bias is eliminated, the presence of substantial unavoidable bias makes any elaborate analysis of random errors superfluous.

Methods of estimating measurement uncertainty in rocket engine systems have recently been systematized (Ref. B-1 and B-2), to provide a uniform basis for procedure standardization. These methods assume that the magnitude of any bias which may be present can be estimated, and are therefore concerned with the application of statistical techniques to analyses of random errors. The techniques are designed for both the calibration and test measurement processes, both of which are assumed to be random, to permit valid applications of population sampling methods.

As applied to the present program, the measurement analysis procedure consists of the following steps:

1. Estimation of the uncertainty intervals in the calibrations of the individual transducers, including the measuring and recording systems in which they are used.
2. Combination of the uncertainty intervals of duplicate or redundant sensors into an uncertainty interval for the measurement.

3. Combination of the uncertainty intervals of several measurements (e.g., pressure, temperature, and flowmeter frequency) into an uncertainty interval for the parameter they determine (e.g., flowrate).
4. Combination of the uncertainty intervals of the measurements entering into calculation of the value of the desired variable (e.g., characteristic velocity) to estimate the uncertainty interval of the calculated result.

SENSOR PRECISION

The precision of a measurement obtained as the output of a physical instrument or sensor is a quantitative estimate of the uncertainty associated with the random errors of that measurement. This estimate is made by statistical analysis of the outputs of the sensor when repeatedly acted upon by known inputs. By sensor is meant not only the transducer itself but the complete system which converts the transducer signal to a numerical value of its physical parameter analog. The known inputs, of course, have uncertainty limits of their own, but for practical purposes it is assumed that they are accurate (i.e., identical to true values) within the limits required by the experimental situation. Ultimately, these inputs must be directly traceable to established standards, such as those of the National Bureau of Standards.

When a sensor is calibrated against known inputs, the precision may be considered as delineating the limits of an uncertainty band within the calibration interval and within a given confidence level. Precision may be numerically expressed as the standard deviation of a measurement, which has the same units as the measurement itself, or as the coefficient of variation, which permits valid comparisons between measurements in different units. Coefficient of variation is the standard deviation expressed as a percentage of the mean, thus making it dimensionless:

$$C_v = 100 \frac{\sigma}{m} \quad (B-1)^*$$

*See Appendix I for nomenclature.

Measurement Analysis Program

A measurement analysis computer program was used in conjunction with the transducer calibration data. This program calculates calibration factors, a function which relates observed measurement system outputs to the corresponding system inputs, measurement precision, and other error estimates. In the general case, typical transducer output in the test range is linear, with an intercept that is not necessarily zero. Because of this intercept, or "offset," the input-output model is of the form

$$(\text{Input}) = K_1 + K_2 (\text{Output}) \quad (\text{B-2})$$

The measurement analysis program also computes a non-offset model of the type

$$(\text{Input}) = K_3 (\text{Output}) \quad (\text{B-3})$$

If neither (B-2) nor (B-3) satisfies a prespecified error limit, a quadratic model is used.

The computer program allows up to seven input-output pairs per calibration. Further, up to seven complete calibrations may be considered in obtaining a random measurement error, which is based on the assumption that the input-output ratio at a particular input level performs a random walk in time, with normal distribution and variance. On the basis of a sequence of periodic calibrations, the measurement analysis program provides all pertinent error estimates (including transducer precision, precision degradation, and offset variability), constants for the input-output models (B-2 and B-3), and the errors for each model. Also, on the basis of a prespecified imprecision requirement, one of three situations is recognized for further action:

1. The system can never meet required precision, and should be replaced.

2. The system will fail the requirement within the next 2 days and should be recalibrated immediately; or
3. The system will meet the requirement up to a certain date (30 days maximum), on or before which it should be recalibrated.

Transducer Uncertainty Intervals

The uncertainty interval, U , in a transducer measurement reported as $X \pm U$, indicates the reasonable limits of the measurement and should include both bias and precision error. Although precision error limits can be calculated from calibration data, bias can only be estimated, mainly on the basis of judgement and experience. To minimize such subjective estimates, one of two procedures may be followed:

1. Assume that the bias error is a specified fraction of the nominal value of the parameter.
2. Assume the absence of significant bias in the transducers and include only precision errors in the uncertainty intervals.

The second alternative was adopted in the present program because transducer bias was minimized by the establishment of calibration factors and input-output models traceable to NBS standards.

Pressure. The coefficients of variation of the pressure transducers were obtained by application of the measurement analysis program to the calibration data. The values obtained ranged from 0.09 to 0.5 percent, for static calibrations made on a pressure manifold mounted on the thrust stand.

Other errors in pressure measurements may arise, in addition to the random, statistical uncertainty limits. Thus, in the measurement of chamber pressure through a drilled wall tap, erroneous values of stream pressure may be indicated because of the effect of the tap upon the flow. The following

estimated magnitudes of this error, which is a function of stream velocity, are based on experimental data obtained with water and gas (Ref. B-3):

Mach No. \approx 0: 0.00 percent

Mach No. \approx 0.3: 0.05

Mach No. \approx 1.5: 1.30

Coupling errors, arising from effects of the tubing joining the pressure taps to the transducers, were not significant in the present series of firings because precise dynamic or transient response pressure measurements were not required (Ref. B-4) and tubing lengths were small.

Thrust. Values of the coefficient of variation obtained by application of the measurement analysis program to static thrust calibrations were in the range 0.1 to 0.5 percent for the sea level calibrations and 0.4 to 0.8 percent for the altitude simulation calibrations (Appendix C).

Throat Area. The geometric throat diameter was measured with an expansion micrometer by two observers before and after every firing. Maximum coefficient of variation of the calculated areas was 0.3 percent.

Volumetric Flowrate. The coefficients of variation of the turbine flowmeters used to measure LF_2 flowrate were determined from calibration data. Observed C_v values, which refer to flow bench water calibrations, were 0.1 percent for both meters. Corrections for thermal and viscosity effects in converting these calibrations to cryogenic LF_2 factors are discussed in the body of this report. In addition, there are unpredictable water-to-cryogenic calibration shifts (Ref. B-5) which introduce additional sources of error. The coefficient of variation arising from this source is approximately 0.5 percent (Ref. B-6).

Estimated C_v value for the magnetic flowmeter used for liquid lithium was 0.5 percent, based on several calibrations of the electromotive force output.

Temperature. Temperature measurements were made with resistance temperature sensors and with thermocouples.

Resistance Temperature Sensors. The platinum resistance thermometers were precision calibrated by the manufacturer. These calibrations were checked by taking several emf readings with the sensors immersed in LN₂ and in LO₂ at atmospheric pressure; these were correct within the limits of readability. Root-sum-square error limits of these sensors based on specifications for repeatability, insulation, time lag, friction heating, and interchangeability were 0.1 percent. Voltage readouts of the transducers were adjusted to calibration values by means of a standard decade resistance box, with error limits of 0.2 percent.

Thermocouples. Iron-constantan thermocouples were used to measure temperatures of GH₂ in the venturi plena, and chromel-alumel thermocouples were used to measure lithium system temperatures. Because the latter were not involved in performance measurements, they will not be considered in this section. Estimated error to be expected with new iron-constantan thermocouple wire at ambient temperature is 0.7 percent (Ref. B-3). Thermocouple calibrations were electrical only; i.e., the emf readouts were adjusted on the assumption that the thermocouple-generated electromotive forces corresponded to NBS standard values. Total estimated C_v was 1.0 percent.

COMBINED ERROR ESTIMATION

Redundant Measurements

Two independent transducers were used to measure some of the important test parameters to increase measurement reliability. The most probable value of a redundant measurement is a weighted average in which the weight (W_i) assigned to an individual determination is given by

$$W_i = \frac{1}{\sigma_i^2} \quad (B-4)$$

where σ_i is the standard deviation associated with the i^{th} measurement and σ_i^2 is the variance. The variance of the weighted mean, σ_m^2 , is given by

$$\frac{1}{\sigma_m^2} = \sum_i \frac{1}{\sigma_i^2} \quad (\text{B-5})$$

Combined Measurements

The standard deviation of a parameter which is a function of two or more independent measurements is the root-sum-square of the standard deviations of the independent measurements. Thus, LF_2 flowrate is a function of flowmeter frequency and fluorine temperature (assuming no significant error in conversion of fluorine temperature to equivalent density):

$$\dot{w}_O = \dot{w}_O(f, T) \quad (\text{B-6})$$

The standard deviation of the oxidizer flowrate is then:

$$\sigma_{\dot{w}_O} = \left[\sigma_f^2 + \sigma_T^2 \right]^{1/2} \quad (\text{B-7})$$

In the same way, the standard deviation of hydrogen flowrate, which is a function of measured pressure and temperature in the venturi plenum, is given by:

$$\sigma_{\dot{w}_{H_2}} = \left[\sigma_{P_{H_2}}^2 + \sigma_{T_{H_2}}^2 \right]^{1/2} \quad (\text{B-8})$$

Standard deviation is converted to coefficient of variation by Eq. B-1.

When several measured variables are combined algebraically to yield an experimental result, the standard deviation of the result, which takes into account the propagation of the individual errors, is given by

$$\sigma_R^2 = \left(\frac{\partial R}{\partial x_1} \sigma_1 \right)^2 + \left(\frac{\partial R}{\partial x_2} \sigma_2 \right)^2 + \dots + \left(\frac{\partial R}{\partial x_n} \sigma_n \right)^2 \quad (\text{B-9})$$

where

- σ_R^2 = variance of calculated result
 x_1, x_2, \dots, x_n = measured variables
 R = $R(x_1, x_2, \dots, x_n)$
 $\sigma_1, \sigma_2, \dots, \sigma_n$ = standard deviations of x_1, x_2, \dots, x_n , respectively

As an example, consider corrected c^* based on chamber pressure:

$$c^* = \frac{P_c A_t g_c (C.F.)}{\dot{w}_T} \quad (B-10)$$

where (C.F.) is the net correction factor. Application of Eq. B-9 gives the variance in corrected c^* as

$$\begin{aligned} \sigma_{c^*}^2 = & \left[\frac{A_t g_c (C.F.)}{\dot{w}_T} \sigma_{P_c} \right]^2 + \left[\frac{P_c g_c (C.F.)}{\dot{w}_T} \sigma_{A_t} \right]^2 + \\ & \left[\frac{P_c A_t g_c (C.F.)}{\dot{w}_T^2} \sigma_{\dot{w}_T} \right]^2 + \left[\frac{P_c A_t g_c}{\dot{w}_T} \sigma_{C.F.} \right]^2 \end{aligned} \quad (B-11)$$

The precision error estimate based on transducer calibrations is the square root of the variance calculated by Eq. B-9 (Ref. B-2):

$$S = \sigma_R \quad (B-12)$$

The uncertainty of a measured parameter is given by the following combination of bias limit and precision error (Ref. B-2):

$$U = \pm(B + t_{0.95} S) \quad (B-13)$$

For the large number of transducer calibrations reflected in the precision error, the recommended value of $t_{0.95}$ (which is the 95th percentile point of the two-tailed Student's "t" distribution) is 2. Assuming that bias is negligible, the uncertainty is therefore given by:

$$U = \pm 2 S \quad (B-14)$$

Numerically, of course, this is the same as the 2σ normal distribution error which is customarily used for a 95-percent confidence level.

DATA PRECISION

Performance

Examples of the application of this error analysis to three performance parameters (c^* , I_s , C_F) for a typical Li/F₂/H₂ test are given in Table B-1. The uncertainty intervals, or the limits beyond which no data would reasonably be expected to fall, are ± 1.3 percent for c^* , ± 1.6 percent for I_s , and ± 2.2 percent for C_F .

Heat Flux

The heat flux measurements in this program represent a case in which the systematic errors inherent in the experimental procedure may be as much as an order of magnitude greater than any possible precision errors. There is therefore no point in estimating the latter by elaborate error analyses. A rule-of-thumb estimate for the reliability of thrust chamber heat flux measurements is on the order of ± 5 to 10 percent.

Dynamic Precision

The estimates of precision calculated above are based on static calibrations of pressure and thrust sensors, and hence may not be strictly applicable to the dynamic system represented by a firing thrust motor. It is generally assumed, however, that such calibration data may be extended without significant change to dynamic systems oscillating at very low frequencies and amplitudes, and that steady-state stable combustion is such a system.

TABLE B-1

EXPERIMENTAL ERROR ANALYSIS
 RUN NO. 69-7 (STEP 2)
 (Bias Error Assumed Negligible)

Parameter	Nominal Value	Precision, Percent of Nominal	Uncertainty, Percent of Nominal
P_c	700 lbf/in. ² (4.83×10^6 N/m ²)	0.28	±0.56
F_{vac}	2276 lbf (10124 N)	0.67	±1.34
\dot{w}_T	4.49 lb/sec (2.04 kg/sec)	0.45	±0.90
A_t	1.680 in. ² (10.84 cm ²)	0.11	±0.22
C.F.	1.029	0.40	±0.80
c^* (uncorr)	8419 ft/sec (2566 m/sec)	0.55	±1.1
c^* (corr)	8663 ft/sec (2640 m/sec)	0.66	±1.3
I_{s-vac}	506 lbf/lbm/sec (4962 N/kg/sec)	0.80	±1.6
C_F	1.93	1.08	±2.2

REFERENCES

- B-1. Webb, S., M. Alexander, and C. Wildon, A Handbook for Estimating the Uncertainty in Measurements Made with Transducer Systems, Report No. 7086, Prepared for Dynamic Science, Inc., under NASA Contract NAS7-443 by Rocketdyne, a division of North American Rockwell Corporation, Canoga Park, California, 26 April 1968.
- B-2. ICRPG Handbook for Estimating the Uncertainty in Measurements Made with Liquid Propellant Rocket Engine Systems, CPIA Publication No. 180, 30 April 1969.
- B-3. Dean, R. C., Jr., Aerodynamic Measurements, Gas Turbine Laboratory, Massachusetts Institute of Technology, Cambridge, Massachusetts, 1953.
- B-4. Thomson, D. B., The Effect of Tubing on Dynamic Pressure Recording, TN-61-3, Rocketdyne, a division of North American Aviation, Inc., Canoga Park, California, 28 February 1961.
- B-5. Bucknell, R. L., "Calibration Systems and Turbine-Type Flow Transducers for Cryogenic Flow Measurements," Advances in Cryogenic Engineering, Vol. 8, Plenum Press, New York, 1963, 360-369.
- B-6. Alspach, W. J. and T. M. Flynn, "Considerations when Using Turbine-Type Flowmeters in Cryogenic Service," Advances in Cryogenic Engineering, Vol. 10, Plenum Press, New York, 1965, 246-252.

APPENDIX C

THRUST CALIBRATION AND MEASUREMENT PROCEDURES

THRUST CALIBRATION

End-to-end thrust calibrations, with readouts on the Beckman Data Acquisition System, were made immediately prior to every firing, at ambient temperature and with all propellant and transducer lines in place. The calibrations preceding the altitude simulation tests were made with the thrust chamber-diffuser system under vacuum (0.1 to 10 psia, 6.9×10^2 to 6.9×10^4 N/m²) to determine the effect of reduced pressure on the calibration factors.

Ideally, thrust calibrations should be made with all engine system conditions identical to those which exist during firing. (With all conditions identical, any inherent differences between static calibration and dynamic firing input/output factors are necessarily assumed to be negligible.) The effects on thrust measurement of variations in conditions which cannot be made identical during calibration and testing should be investigated and suitable corrections applied, if necessary. In the present program, the applicable nonidentical engine system conditions were propellant inlet line pressures and temperatures.

Inlet Line Pressure Effects

Propellant inlet line pressurization effects on thrust readings depend on the size and orientation of the propellant lines. Experimental determinations of these effects were made with the lines used in both the oxidizer-rich and the fuel-rich gas generator injection methods. With the former, applicable corrections to observed load cell output caused by pressurization of the propellant inlet lines were +0.85 to +1.1 percent, depending on the flowrate level. With the fuel-rich gas generator injection scheme,

the corrections were negligibly small within the experimental range of propellant flowrates. The observed differences in the effects of propellant line pressurization between the two injection methods were due primarily to differences in the hydrogen supply lines to the thrust chambers.

Inlet Line Temperature Effects

During a test firing, the fluorine inlet line was chilled, the lithium inlet line was heated, and the hydrogen inlet line remained at ambient temperature. Calibration tests showed that while propellant delivery line temperature changes usually alter the thrust zero point readings, they do not significantly affect net load cell output over the ranges used in the present investigation. That is, if zero readings are taken with the propellant inlet lines at run temperatures, no corrections are required for this factor.

At one critical point in the LF_2 delivery system, however, the temperature changed throughout the firing and so the corresponding change in the thrust zero reading had to be considered. This temperature change occurred at the uncooled fitting joining the chilled LF_2 inlet line to the chilled LF_2/GH_2 injector in the fuel-rich gas generator injection scheme. The fitting, which was exactly at the chamber axis, was cooled only by conduction before the test, when zero readings were taken. As soon as flow of LF_2 began, its temperature dropped at a substantial rate (approximately 16 F/sec, 9 K/sec). There was a corresponding significant effect on the thrust readings, ranging from 8 lbf (35.6 N) for a temperature change of the inlet fitting of 20 F (11 K) to 35 lbf (155.6 N) for a change of 150 F (83 K). Temperature of the fitting was monitored during each firing so that proper corrections could be applied for this factor.

In the oxidizer-rich gas generator injection method, the LF_2 was injected perpendicularly to the chamber axis, through a yoke mechanism. Temperature changes of the inlet fittings in this case had no significant effect on thrust zero readings.

Altitude Simulation Tests

Thrust calibrations for the altitude simulation firings were made with the complete thrust chamber-diffuser system (Appendix G) in place. Calibrations were made over a range of system pressures, so that the input/output factor corresponding to actual test diffuser pressure could be used in data reduction. The effect of diffuser pressure on the calibration factor was small, but real and reproducible (approximately 0.2 percent change in the calibration factor per psi change in diffuser pressure, 0.2 percent per $7 \times 10^3 \text{ N/m}^2$). Use of calibration factors obtained at ambient pressure for the altitude simulation test data would have resulted in a systematic error of about -2.5 percent in measured thrust.

THRUST MEASUREMENT

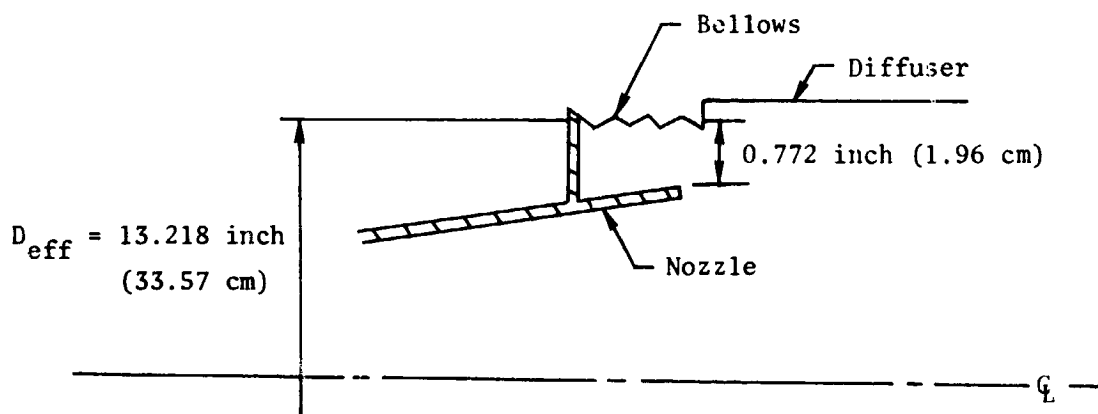
Sea-Level Tests

Measured thrust in the sea-level firings was obtained directly from the load cell readings, with suitable corrections for LF_2 inlet fitting temperature and line pressurization, as required.

Altitude Simulation Tests

Because of the critical importance of thrust measurements in the altitude simulation firings and the frequently encountered difficulty of obtaining reliable thrust measurements with attached diffusers, two methods were employed to determine thrust in this series of firings. The first was the value based directly on the load cell reading and the second was based on the integration of measured nozzle pressures together with the specific impulse efficiency measured in earlier sea-level tests.

Load Cell Measurements. The nozzle exit-bellows-diffuser junction (Appendix G) is sketched below:



The diffuser was fixed, so that the axial engine movement reflected in the load cell readings was taken up at the bellows. The following step-wise procedure was used to convert load cell readings to vacuum thrust:

1. The net unbalanced area of the system over which atmospheric pressure acted (in a direction opposing thrust) was the "effective" cross-sectional area of the bellows joining the nozzle and diffuser. To determine this area, the engine-diffuser system was evacuated to various pressures from 0.1 to 10 psia (6.9×10^2 to 6.9×10^4 N/m²) and the resulting negative thrust was measured on the load cell. The bellows dimensions thus obtained were:

$$\begin{aligned}
 A_{\text{eff}} &= 137.2 \text{ in.}^2 \text{ (885.2 cm}^2\text{)} \\
 D_{\text{eff}} &= 13.218 \text{ inches (33.57 cm)} \\
 \text{Bellows ID} &= 12.5 \text{ inches (31.75 cm)} \\
 \text{Bellows OD} &= 13.7 \text{ inches (34.80 cm)}
 \end{aligned}$$

2. The distance between the outer edge of the nozzle and the bellows was 0.772 inch (1.96 cm) and the corresponding annular area (over which diffuser pressure acts in the thrust direction) was 30.2 in.² (194.8 cm²).

3. Vacuum thrust was then given by:

$$F_{vac} = F_{lc} + F_{atm} - F_{diff} \quad (C-1)^*$$

$$= F_{lc} + (137.2 \times P_{atm}) - (30.2 \times P_{diff}) \quad (C-2)$$

4. To convert the load cell reading, F_{lc} , to thrust at any desired altitude, the pressure at that altitude is substituted for P_{atm} in Eq. C-2.

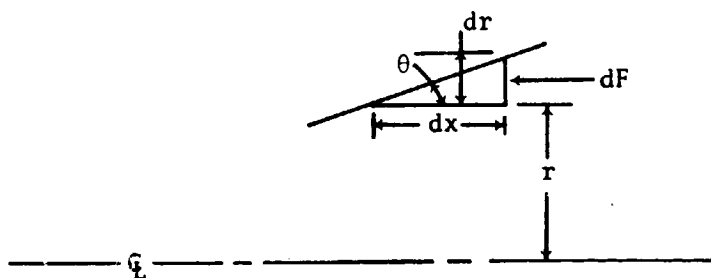
5. This procedure is consistent with the customary method of converting F_{lc} to F_{vac} in sea-level firings:

$$F_{vac} = F_{lc} + (A_{exit} \times P_{atm}) \quad (C-3)$$

where A_{exit} is the effective area over which atmospheric pressure acts in a direction opposing engine thrust.

Integration of Nozzle Pressures. The second method of determining thrust in the altitude simulation tests with the 60:1 area ratio nozzle was as follows:

1. The thrust increment between area ratio 10 and area ratio 60 was determined from the measured nozzle pressures in this region, as shown:



$$dA = 2 \pi r dr$$

$$r = x \tan \theta$$

$$dr = dx \tan \theta$$

*See Appendix I for nomenclature

$$\therefore dA = 2\pi x \tan^2 \theta \, dx$$

$$dF = PdA$$

$$\therefore F_{10-60} = \int_{x(\epsilon=10)}^{x(\epsilon=60)} 2\pi x P \tan^2 \theta \, dx \quad (C-4)$$

Equation C-4 was evaluated by numerical integration. The nozzle pressure thrust contribution between area ratios 10 and 60 was in the range 220 to 240 lbf (979 to 1068 N).

2. The thrust to area ratio 10 was obtained from the specific impulse efficiency measured in sea level tests under similar conditions with a 10:1 nozzle.
3. Vacuum thrust for the 60:1 nozzle was the sum of the two contributions:

$$F_{vac} = (F_{vac})_{\epsilon=10} + (F_{vac})_{\epsilon=10 \rightarrow 60} \quad (C-5)$$

APPENDIX D

HEAT TRANSFER MEASUREMENT AND DATA REDUCTION PROCEDURES

INTRODUCTION

Three different measurement techniques were employed in the determination of thrust chamber heat flux: calorimetric measurement (in the water-cooled chamber sections), use of heat flux transducers (in the nozzle segment between area ratio 3 and area ratio 10), and use of externally welded thermocouples (in the nozzle section between area ratio 10 and area ratio 60).

CALORIMETRIC MEASUREMENTS

The water-cooled thrust chamber segments included a 4-inch (10.16-cm) combustion chamber section and a convergent-divergent nozzle section extending to area ratio 3. Both are described in detail in the design section of this report. Heat flux into an axial or circumferential coolant passage (used in the combustion chamber and nozzle segments, respectively) was determined calorimetrically from the water flowrate and temperature rise:

$$\frac{Q}{A} = \frac{\dot{w} C_p \Delta T_b}{A} \quad (D-1)*$$

The coolant passages in the combustion chamber segment had common inlet and outlet manifolds; the measured overall water flowrate through the segment was assumed to be divided equally among the passages. The bulk temperature rise across a given passage was measured from the inlet manifold to the passage exit, where a 4-unit thermopile was located (immediately upstream of the junction of the passage and the exit manifold). In the

*See Appendix I for nomenclature

nozzle section, the coolant temperature rise between the inlet and outlet of a given passage was measured directly with a differential thermocouple. The applicable heat transfer area in Eq. D-1 is the product of the length of the coolant passage and the distance between the two points midway between the given passage and its neighboring passages.

The coolant-side heat transfer coefficient was computed from the following correlation for forced convection heat transfer at high heat fluxes (Ref. D-1):

$$h_c = 0.005 \frac{k}{D} (Re)^{0.95} (Pr)^{0.4} \quad (D-2)$$

Water properties in Eq. D-2 were evaluated at the average bulk temperature.

The coolant-side wall temperature was calculated from the one-dimensional convection equation:

$$T_{wc} = \frac{Q/A}{h_c} + (T_{avg})_{H_2O} \quad (D-3)$$

In the few cases in which the value of the coolant-side wall temperature calculated from Eq. D-3 exceeded the coolant saturation temperature, the coolant was assumed to be in the nucleate boiling regime and the coolant-side wall temperature was taken as 50 F (28 K) higher than the coolant saturation temperature. This is a generally used approximation of the wall temperature in the presence of nuclear boiling (Ref. D-2).

The gas-side heat transfer coefficient is based on a driving temperature which is the difference between the gas-side wall temperature and the adiabatic wall temperature. The latter was calculated from the combustion gas properties and the recovery factor:

$$T_{aw} = T_o \left[\frac{1 + R_T \left(\frac{\gamma-1}{2} \right) M_\infty^2}{1 + \left(\frac{\gamma-1}{2} \right) M_\infty^2} \right] \quad (D-4)$$

The recovery factor was approximated from the Prandtl number:

$$R_T \approx (\text{Pr})^{1/3} \quad (\text{D-5})$$

Combustion gas stagnation temperature was obtained by correcting the theoretical stagnation temperature for performance loss:

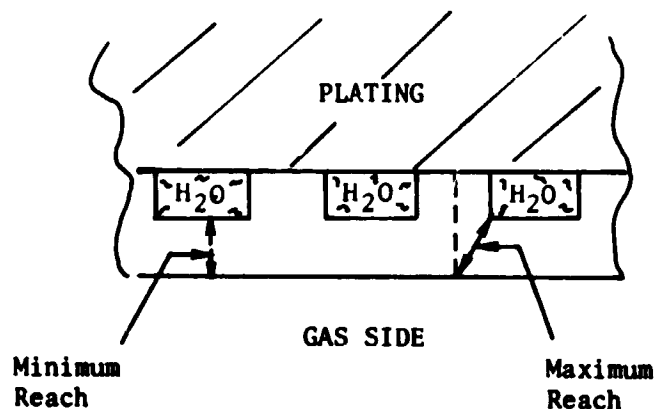
$$T_o = \eta_{c^*}^2 T_{\text{theo}} \quad (\text{D-6})$$

The observed, uncorrected c^* efficiency is used in Eq. D-6.

The gas-side wall temperature was calculated from the coolant-side wall temperature:

$$T_{wg} = T_{wc} + \frac{x}{k} \frac{Q}{A} \quad (\text{D-7})$$

The wall thickness, x , used in Eq. D-7 is the average of the minimum and maximum "reaches" sketched below. This give results in agreement with those obtained from a two-dimensional conduction analysis of the wall geometry (Ref. D-3):



The gas-side heat transfer coefficient was then calculated from:

$$h_g = \frac{Q/A}{T_{aw} - T_{wg}} \quad (\text{D-8})$$

HEAT FLUX METERS*

Design

A convenient method of measuring heat flux in the uncooled, thick-walled copper nozzle section between area ratios 3 and 10 was by means of simple heat flux meters. The transducer used consisted essentially of two sheathed chromel/alumel thermocouples within a 0.125-inch (3.17-mm) copper rod. The thermocouples were positioned, one above the other, in a 0.032 by 0.062 inch (0.81 by 1.57 mm) slot milled into the copper rod (Fig. D-1). A copper filler strip was placed in the slot between the first thermocouple and the end of the copper rod. The remaining slot volume was filled with "Silvalloy 301" silver solder, whose thermal conductivity is about 80 percent that of copper. Finally, a 0.188-inch (4.76-mm) copper tube was brazed to the aft end of the copper rod. A photograph of the finished heat flux meter is shown in Fig. D-2. The meter was swaged in place, with a 0.002-inch (0.05-mm) gap between the copper rod and the nozzle wall. Transducer output is the differential emf between the two thermocouples, which is a measure of their instantaneous temperature difference and hence of the heat flux along the copper rod.

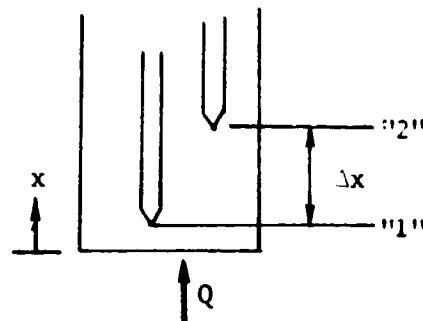
Calibration

The heat flux transducers were calibrated against a thermal transfer standard, consisting of a constantan cylinder with copper plates at each end, with known thermal response. The calibration system (Fig. D-3) included a heat source, the heat flux transducer, the thermal transfer standard, and a heat sink, connected in series. The interface connections were made with soft solder and copper adapters. The steady-state heat flux calibrations of the two transducers used in the present program are shown in Fig. D-4.

*These meters were designed, built, and calibrated by P. A. Kinzie, Measurements and Instruments Group, Research Division, Rocketdyne.

Heat Flux Measurement

The following analysis relates the steady-state calibrations shown in Fig. D-4 to the nonsteady heat flux measured in the thrust chamber. Heat flow into the surface of the heat flux meter results in a temperature difference between stations "1" and "2." Because station 1 is only 0.015 inch (0.38 mm) from the heated surface, the heat flux at this point may be taken as the surface heat flux, even under transient conditions.



The heat flux at station 1 is given by

$$\left(\frac{Q}{A}\right)_1 = -k \left(\frac{\partial T}{\partial x}\right)_1 \quad (D-9)$$

To evaluate the partial derivative in Eq. D-9, T_2 was expanded as a Taylor series in terms of T_1 :

$$T_2 = T_1 + \left(\frac{\partial T}{\partial x}\right)_1 \Delta x + \left(\frac{\partial^2 T}{\partial x^2}\right)_1 \frac{(\Delta x)^2}{2} + \left(\frac{\partial^3 T}{\partial x^3}\right)_1 \frac{(\Delta x)^3}{6} + \dots \quad (D-10)$$

The second derivative in Eq. D-10 was evaluated from the transient heat conduction equation:

$$\left(\frac{\partial^2 T}{\partial x^2}\right)_1 = \frac{\rho C_p}{k} \left(\frac{\partial T}{\partial t}\right)_1 \quad (D-11)$$

Because station 2 was only 0.05 inch (1.27 mm) from station 1, the third derivative in Eq. D-10 could be obtained from the following approximation:

$$\left(\frac{\partial^3 T}{\partial x^3}\right)_1 \approx \frac{\left(\frac{\partial^2 T}{\partial x^2}\right)_2 - \left(\frac{\partial^2 T}{\partial x^2}\right)_1}{\Delta x} \quad (D-12)$$

Substitution of Eq. D-11 and D-12 into D-10 gives:

$$\left(\frac{\partial T}{\partial x}\right)_1 = \frac{\Delta T}{\Delta x} - \frac{\rho C_p}{k} \left(\frac{\partial T}{\partial t}\right)_1 \frac{\Delta x}{2} - \frac{\rho C_p}{k} \left[\left(\frac{\partial T}{\partial t}\right)_2 - \left(\frac{\partial T}{\partial t}\right)_1 \right] \frac{\Delta x}{6} \quad (D-13)$$

The heat flux meter calibrations gave curves of steady-state transducer millivolt output as functions of heat flux into the meter surface, according to the following relation:

$$\frac{Q}{A} = -k \frac{T_2 - T_1}{x_2 - x_1} = -k \frac{\Delta T}{\Delta x} \quad (D-14)$$

In using the heat flux meters, temperature data were taken after the initial transient portion of each step of a firing had passed. Because the time derivatives were then zero, only the first term of Eq. D-13 remained and the steady-state calibrations could therefore be directly used to determine heat flux into the meter.

EXTERNAL TEMPERATURE MEASUREMENTS

Heat flux to the steel nozzle skirt (from area ratio 10 to area ratio 60) was determined by means of iron/constantan thermocouples spot-welded externally along the length of the nozzle. Measured wall temperatures were used in conjunction with an existing Rocketdyne Thermal Analyzer Program (Ref. D-4) to compute the heat flux at each station.

The Thermal Analyzer Program applies a lumped parameter representation and numerical difference methods to a continuous physical system governed by a set of diffusion equations. The program uses a Numerical Differencing Analyzer of the network type, for which a thermal analog network is constructed by a lumping process. In this lumped-geometry approximation, the total thermal capacity of the continuous physical system is apportioned among a set of nodes. Each node is connected to one or more adjacent nodes by conducting paths, to each of which an admittance (the reciprocal of the thermal resistance) is assigned. The temperature associated with each node represents that at the centroid of the corresponding element of the physical system.

The nozzle skirt was divided into 37 nodes. The seven thermocouples along the nozzle surface corresponded to seven boundary nodes. Assumed values of the gas side heat transfer coefficient were used as initial program input to calculate temperatures at the seven boundary nodes. These were compared with the measured temperatures and the procedure was iterated until the calculated and measured temperatures agreed to within 2 F (1.1 K). The final values of the heat transfer coefficients were then used to compute local heat flux.

REFERENCES

- D-1. Hines, W. S., Turbulent Forced Convection Heat Transfer to Liquids at Very High Heat Fluxes and Flowrates, RR 61-14, Rocketdyne, a division of North American Aviation, Inc., Canoga Park, California, 30 November 1961.
- D-2. Jens, W. and P. Lorres, Report No. ANL-4627, Argonne National Laboratory, Argonne, Illinois, May 1951.
- D-3. Landis, R. B., Computer Program for Reduction of Calorimetric Water-Cooled Segment Heat Transfer Data, Report LAP 67-379 (RC), Rocketdyne, a division of North American Aviation, Inc., Canoga Park, California, 13 September 1967.
- D-4. Finkelstein, T., Manual for the Thermal Analyzer Program (TAP), SE ARP 8889-5000, Rocketdyne, a division of North American Rockwell, Inc., Canoga Park, California, January 1968.

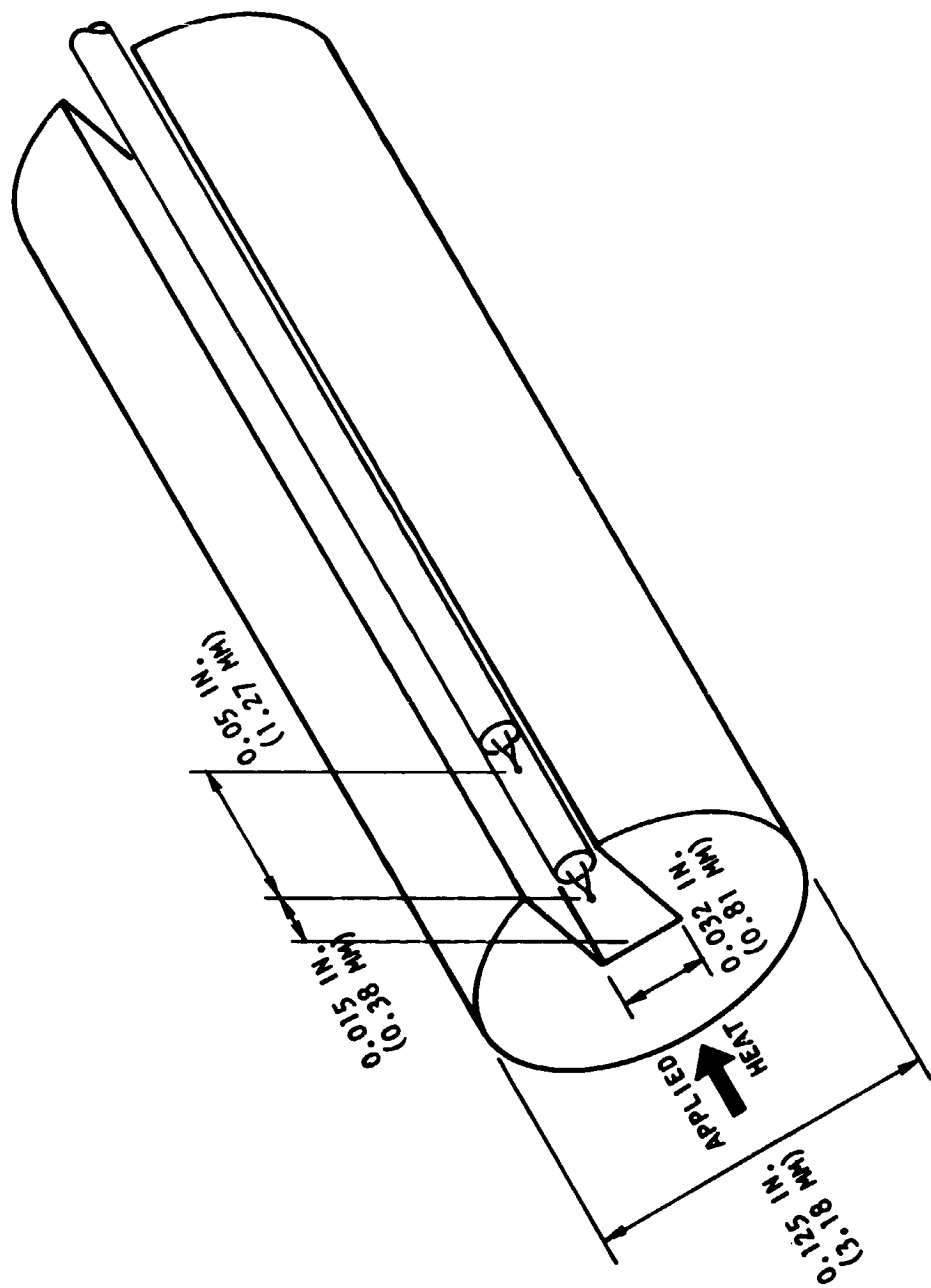


Figure D-1. Sketch of Heat Flux Transducer Used in Uncooled Section of Nozzle

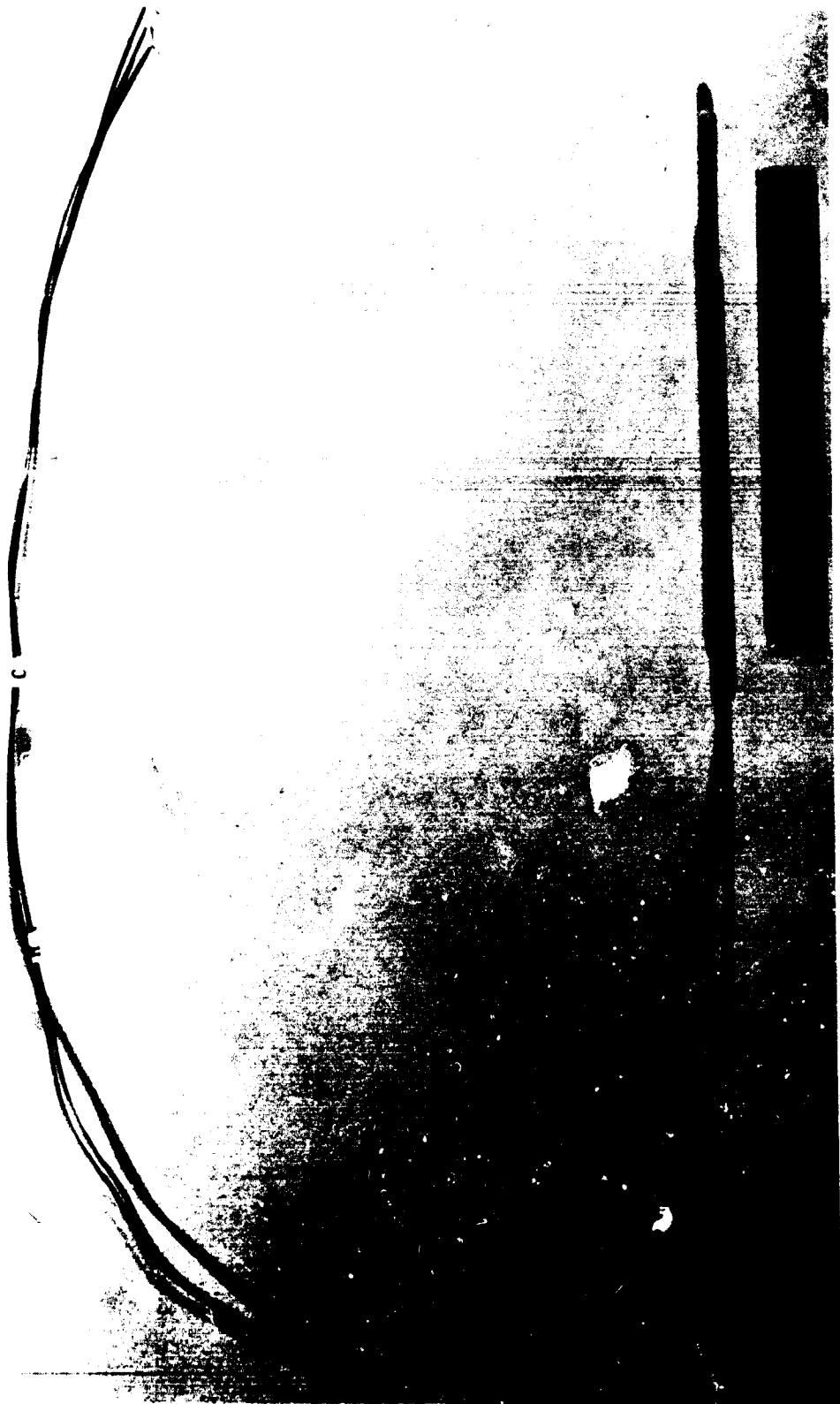


Figure D-2. Heat Flux Meter

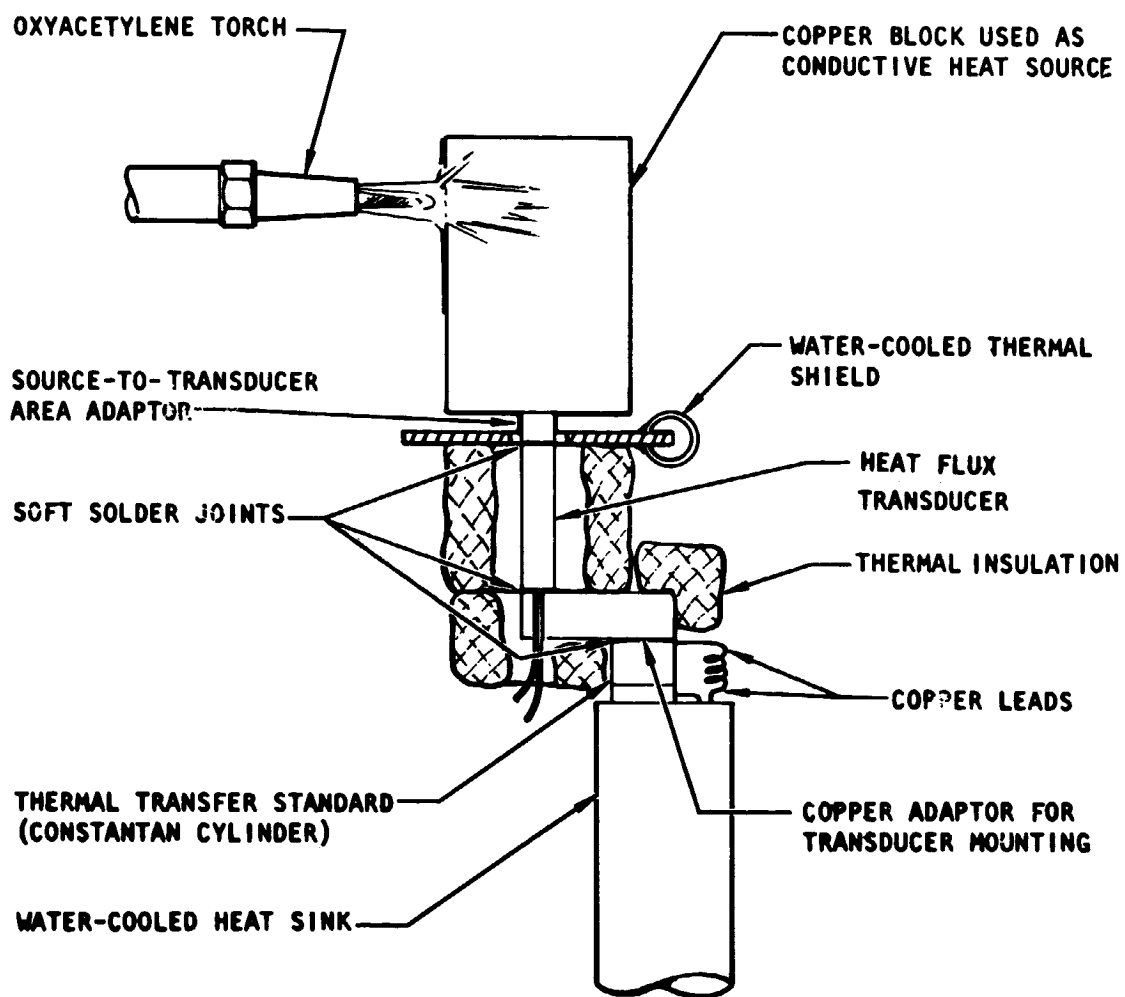


Figure D-3. Schematic of Heat Flux Comparison Calibration Apparatus

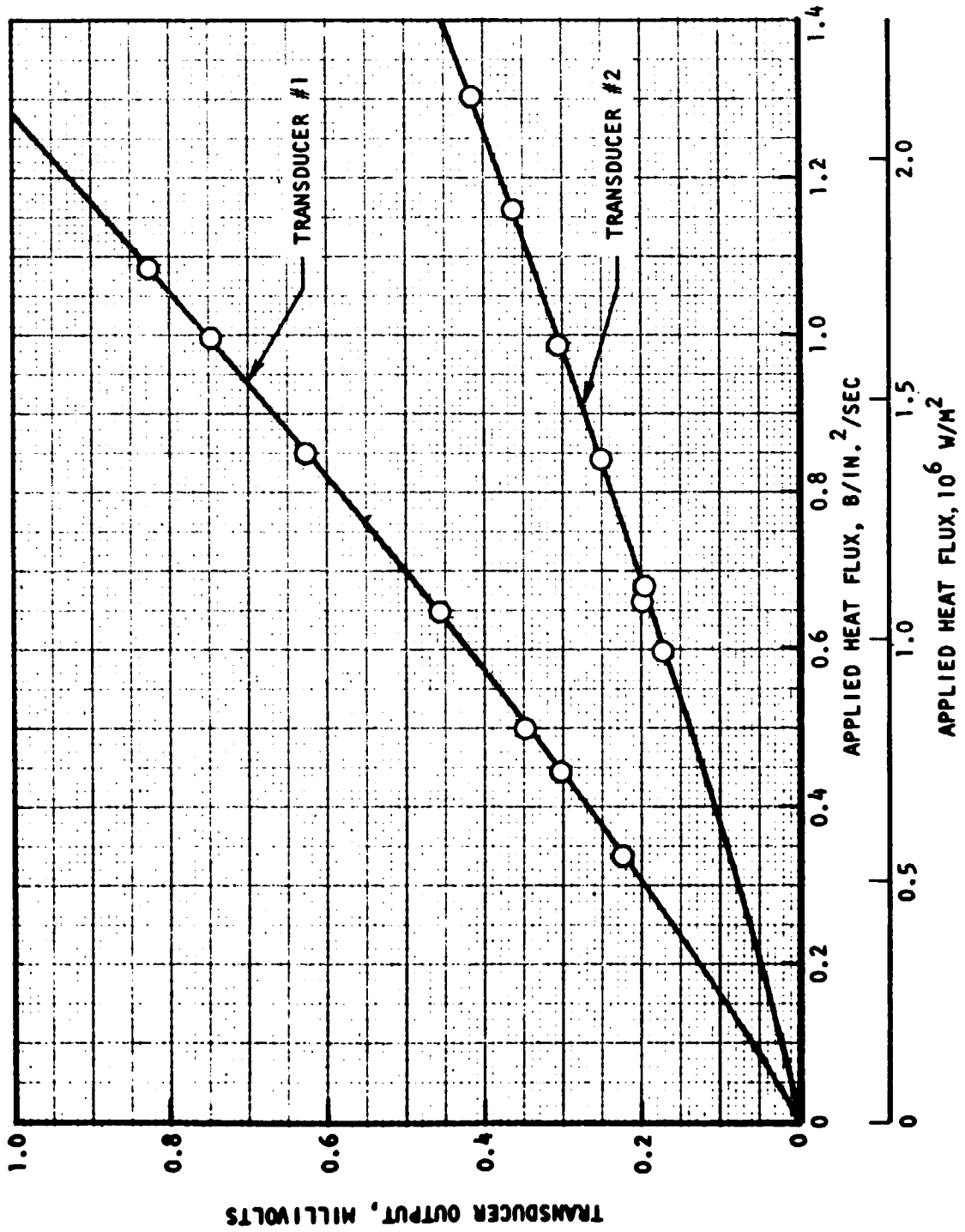


Figure D-4. Heat Flux Transducer Calibration Curves

APPENDIX E

COLD-FLOW STUDIES OF SINGLE-ELEMENT LITHIUM INJECTOR

INTRODUCTION

Lithium-fluorine-hydrogen firings carried out with the fuel-rich gas generator injection method resulted in some erosion of the graphite liner of the combustion chamber. The erosion occurred about 1.5 to 4 inches (3.8 to 10.2 cm) from the lithium injector face, in a scalloped pattern corresponding to injector element orientation. Since this indicated that the erosion may have resulted from localized lithium-graphite reaction, a short series of cold-flow tests was conducted with a single-element lithium injector to determine the gas and liquid distributions which it produced. Schlieren photography was used to obtain qualitative indications of the gas flow patterns and a multitube collector (Ref. E-1) was used to measure liquid distribution characteristics.

SIMILARITY PARAMETERS

The lithium injector propellants are gas generator product gas and liquid lithium. For the schlieren photographs, water was used as lithium simulant and helium as the combustion gas ($\text{HF} + \text{H}_2$) simulant; for the liquid distribution tests, nitrogen replaced helium as the combustion gas simulant. The test firing parameters which were matched in the cold-flow tests were the degree of penetration of the liquid stream into the gas jet (i.e., the momentum ratio) and the gas/liquid orifice diameter ratio.

RESULTS

The biplanar lithium injector pattern, which was described in the design section of this report, consisted of a single lithium stream intersecting a gas jet, with four auxiliary gas jets intersecting the central reacting mixture at a downstream point. Cold-flow tests were first made with the central gas/liquid orifice pair, to study the initial distribution, and then on the complete element, to study the overall distribution.

A schlieren photograph of the flowing, central, gas/liquid unlike doublet is shown in Fig. E-1 and a side view of the same flow is shown in Fig. E-2. The penetration of the water stream into the helium jet was 80 percent. The liquid was uniformly dispersed in the gas jet, indicating that the design penetration distance (80 percent) was sufficient to provide good mixing.

The liquid distribution produced by the gas/liquid unlike doublet was determined at a distance of 3 inches (7.6 cm) from the injector face. A CRT plot of the results is shown in Fig. E-3. Each small square in the plot represents a sample tube which had measurable liquid in it at the end of the test. The number of lines in each square is proportional to the mass of liquid in the corresponding collection tube; the number in each square, with the given identification, represents the mass fraction in the tube as percent of total collected mass. The dashed line shows the location of the chamber wall relative to the injector. Essentially all of the liquid was collected within the chamber area and the distribution is reasonably uniform. The gas jet was located at the indicated center of mass.

A schlieren photograph of the spray field formed by the entire injection element, including the four auxiliary gas jets, is shown in Fig. E-4 and the corresponding side view in Fig. E-5. The indicated distribution was less uniform than that observed with the simple gas/liquid doublet. The liquid distribution obtained with the complete element is shown in Fig. E-6, which verifies the qualitative schlieren results. A considerable fraction of the collected liquid mass was outside the chamber boundary. Hence, the graphite liner erosion in the $\text{Li}/\text{F}_2/\text{H}_2$ firings may indeed have resulted from contact of unreacted lithium with the chamber wall. Geometric consideration of the physical boundaries of the gas jets and the liquid stream at various points downstream of the injector face indicated that, because of jet spreading, the two auxiliary gas jets closest to the lithium stream may have stripped liquid from the latter and carried it downstream along the chamber wall.

REFERENCES

- E-1. Dickerson, R., K. Tate, and N. Barsic, Correlation of Spray Injector Parameters with Rocket Engine Performance, Report AFRPL-TR-68-147, Contract F04611-67-C-0081, Prepared for Air Force Rocket Propulsion Laboratory by Rocketdyne, a division of North American Rockwell Corporation, Canoga Park, California, June 1968.



Figure E-1. Schlieren Photograph of Flowing Gas/Liquid Unlike Doublet Injection Element ($\text{He}/\text{H}_2\text{O}$), $x_p/D_G = 80$ Percent. Front View

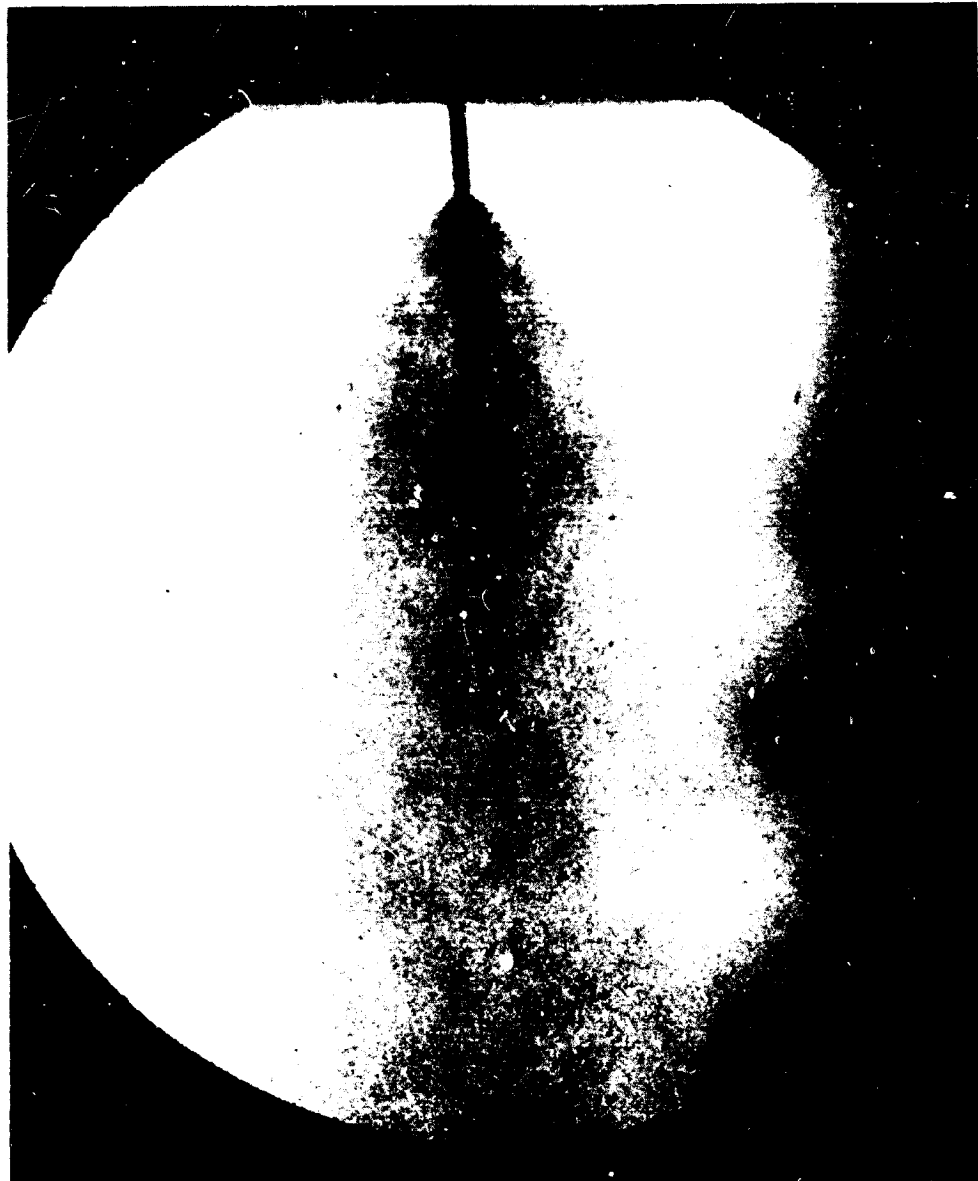
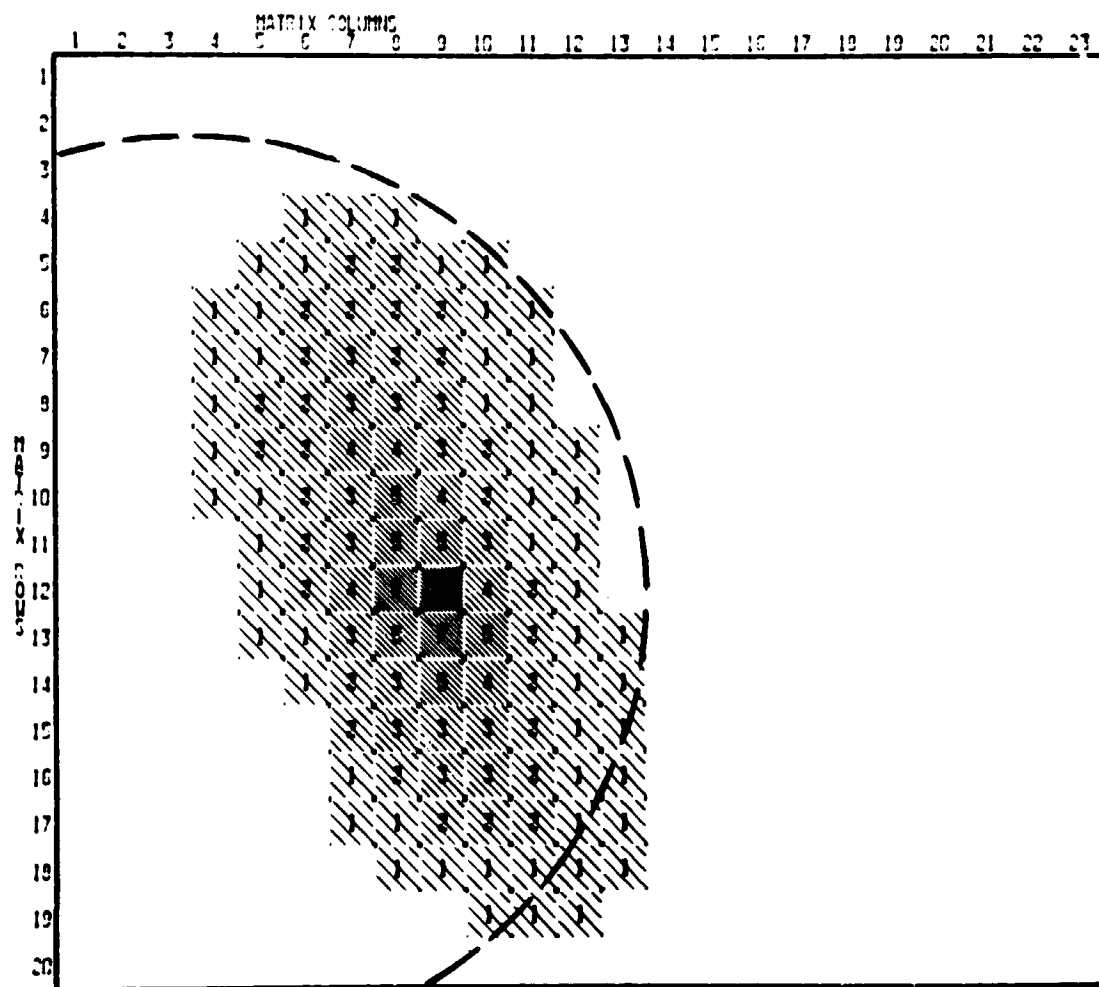


Figure E-2. Schlieren Photograph of Flowing Gas/Liquid Unlike Doublet Injection Element (He/H₂O), $x_p/D_G = 80$ Percent. Side View

LOCAL MASS FRACTION

INJECTOR NO. 11

627746
0711



IDENTIFICATION

1	0.100
2	0.200
3	1.000
4	1.000
5	2.000
6	3.000
7	4.000
8	3.000
9	2.000
10	1.000

INLET

Ox 1	0
Ox 2	0.000
Fu 1	0.000
Fu 2	0.000

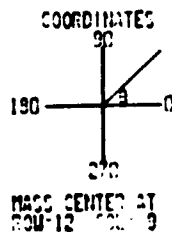


Figure E-3. CRT Plot of Liquid Distribution Obtained With Gas/Liquid Unlike Doublet Injection Element. Dashed Line Shows Location of Combustion Chamber Wall Relative to the Injector



Figure E-4. Schlieren Photograph of Flowing Biplanar Gas/Liquid Element Identical to Those in Lithium Injector. Front View (Large Specks are Mirror Imperfections)



Figure E-5. Schlieren Photograph of Flowing Biplanar Gas/Liquid Element
Identical to Those in Lithium Injector. Side View (Large Specks are
Mirror Imperfections)

LOCAL MASS FRACTION

RUN 9
INJECTOR NO 4 HOLE

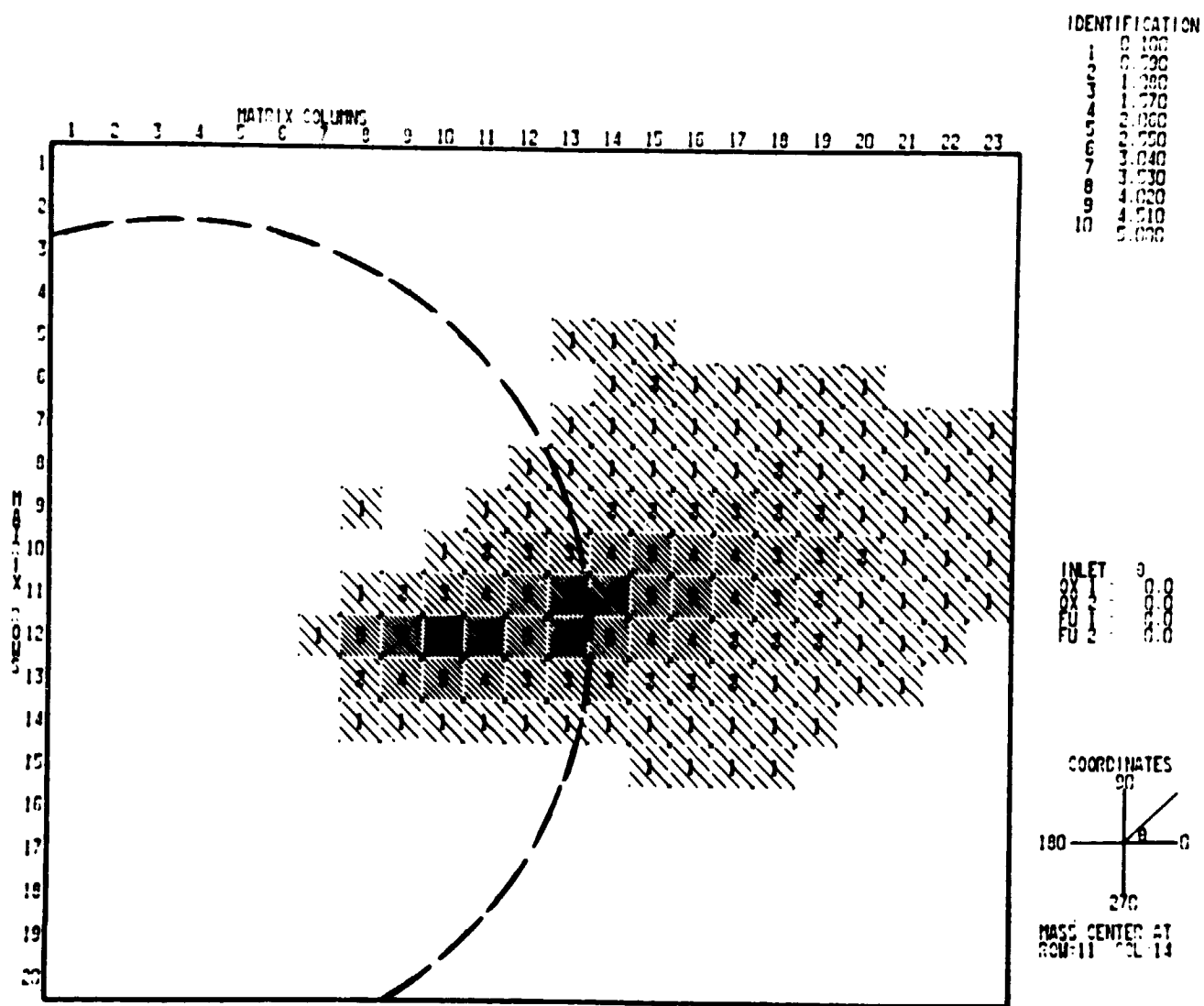


Figure E-6. CRT Plot of Liquid Distribution Produced by Biplanar Gas/Liquid Injection Element, Dashed Line Shows Location of Combustion Chamber Wall Relative to the Injector

APPENDIX F

EFFECT OF PARTICLE SIZE ON $\text{Li}/\text{F}_2/\text{H}_2$ PERFORMANCE

The study* presented in this appendix was carried out to determine the effect on nozzle performance of the presence of particulate matter in the $\text{Li}/\text{F}_2/\text{H}_2$ combustion products. A number of methods have been developed for the analysis of two-phase flow in rocket nozzles (Ref. F-1 to F-13) and a computer program for the calculation of one-dimensional, two-phase, reacting gas, nonequilibrium performance has recently become available (Ref. F-5). However, because this program does not include provision for the consideration of lithium compounds, it could not be applied to the $\text{Li}/\text{F}_2/\text{H}_2$ nozzle.

The method used was that of Rannie (Ref. F-1) and Marble (Ref. F-14 and F-15), which appears to be as good as any available and which offers the best combination of simplicity and reliability of results. This is a linearized analysis based on a perturbation technique and is limited to small particle sizes. It appeared to be applicable to $\text{Li}/\text{F}_2/\text{H}_2$ combustion because the earlier c^* efficiency data (Ref. F-16) had indicated that the particles in the combustion products were indeed quite small.

COMPUTATIONAL METHOD

The assumptions utilized in the development of this method were as follows:

1. The flow is steady, one-dimensional and heterogeneous.
2. Interactions between particles and wall are neglected.
3. Interactions between particles are neglected.
4. Particle heat conductivity is much greater than gas heat conductivity.

*This study was carried out by Dr. G. A. Hosack, Heat and Fluid Physics Section, Research Division, Rocketdyne.

5. Radiative heat transfer between particles is neglected.
6. A modified Stokes' drag law applies.
7. A semiempirical heat transfer law applies.
8. The particles are small and can be approximated by small spheres so that a perturbation solution can be obtained.
9. The gas viscosity is a function of temperature and can be represented by a power law.
10. The Prandtl number of the gas is constant over a wide temperature range.
11. There is no mass transfer between the particles and the gas (no burning) and the particle size remains constant.
12. Although distributed particle sizes may be included in Rannie's method, this option has not been included in the computer program developed in the present study.

The equations describing this model (Ref. F-1) are solved by a perturbation method in which pressure is the independent variable. A computer program was written to carry out the calculations*. The final result was given as the ratio of the specific impulse that would be obtained with the computed particle lags to that which would be produced if there were continuous particle-gas equilibrium throughout the flow.

APPLICATION TO Li/F₂/H₂ ENGINE

The computer program was used to determine the effect of particle size variations on Li/F₂/H₂ performance at the following nominal conditions: chamber pressure of 700 psia (4.83×10^6 N/m²), F₂/Li mixture ratio of 2.74, and 25-percent hydrogen. The nozzle geometry is shown in Fig. F-1.

*This program was written by P. L. Bailey, Advanced Technology Group, Rocketdyne.

Conventional, one-dimensional, isentropic performance calculations were first made for the following two cases:

1. Full shifting equilibrium
2. No condensation of particles

The full shifting equilibrium calculations indicated that LiF condensation begins downstream of the throat, at an expansion ratio of about 2.

The effect of particle formation on performance for each of the two cases is shown in Fig. F-2. The upper curve represents the theoretical performance obtainable if the particles condense out and maintain thermal and velocity equilibrium with the gas. The difference between the curves, approximately 16 lbf/lbm/sec (157 N/kg/sec) at expansion ratio 60, represents the theoretical loss in specific impulse if the particles do not condense.

Actual nozzle performance is obtained by correcting the full shifting theoretical specific impulse (upper curve of Fig. F-2) for the effects of losses due to c^* efficiency, nozzle divergence, boundary layer effects, chemical kinetics, and finite particle/gas temperature and velocity lags.

A Bray freezing criterion analysis was carried out to estimate losses resulting from chemical kinetics. It was found that the chemical composition of the flow freezes at an expansion ratio of about 30. The resulting change in nozzle performance from the theoretical shifting equilibrium value at expansion ratio of 60 is negligibly small. The nozzle divergence loss was determined from a method-of-characteristics analysis using full shifting flow. A transonic flow analysis program was utilized to determine a starting characteristic line in the vicinity of the nozzle throat. The divergence loss was found to be 0.015. The wall drag loss was calculated to be 0.013.

The net nozzle vacuum thrust efficiency was then:

$$\eta_{C_F} = 1 - \delta_{\text{div}} - \delta_{\text{drag}} - \delta_{\text{particles}} \quad (\text{F-1})^*$$

$$= 0.967 - \delta_{\text{particles}} \quad (\text{F-2})$$

where $\delta_{\text{particles}}$ is the two-phase flow performance loss:

$$\delta_{\text{particles}} = 1 - \frac{I_s}{(I_s)_{\text{ideal}}} \quad (\text{F-3})$$

The overall vacuum specific impulse was then computed from:

$$I_s = \frac{1}{g_c} \eta_{c^*} (c^*)_{\text{ideal}} \eta_{C_F} (C_F)_{\text{ideal}} \quad (\text{F-4})$$

Parametric calculations were carried out to determine the two-phase flow performance loss as a function of particle size and mass fraction of particles in the flow. The initial gas properties were chosen as the values for full shifting flow at the nozzle throat. Particle size was varied from 0.5 to 10 microns, with the results shown in Fig. F-3. By the nature of the analytical method, the values of the perturbation parameters should remain small to render meaningful results. The computations indicated that for particle sizes greater than approximately 2 microns, the accuracy of the program declines.

A curve of vacuum specific impulse including all the above-mentioned losses versus particle size is presented in Fig. F-4, which shows that even for high particle loading (mass ratio up to 40 percent) the deliverable specific impulse is in excess of 500 lbf/lbm/sec (4900 N/kg/sec) for particles 1 micron or less in diameter, at the nominal test conditions.

*See Appendix I for nomenclature

The full shifting equilibrium performance calculations indicate that at these conditions the mass fraction of LiF (liquid) particles is on the order of 5 percent just downstream of the throat and increases to approximately 75 percent at an area ratio of 60. Thus, even though a large particle/gas mass ratio exists near the nozzle exit, a much lower mass ratio exists in the region immediately downstream of the throat, where particle acceleration effects are most important (Ref. F-2). Therefore, a value of 0.25 was chosen as an average loading factor, weighted more heavily on the mass ratio present in the flow immediately downstream of the throat. The experimentally determined vacuum specific impulse at the nominal test conditions was 509 lbf/lbm/sec (4991 N/kg/sec). From Fig. F-4, this corresponds to a particle size of 0.5 to 1.0 microns, depending on the average loading factor. With such small particles, the effect of loading factor variation between 10 and 40 percent is minor. These results tend to confirm the earlier assumption that the mass median diameter of the particles resulting from Li/F₂/H₂ combustion is on the order of 1 micron or less.

REFERENCES

- F-1. Rannie, W. D. "Perturbation Analysis of One-Dimensional Heterogeneous Flow in Rocket Nozzles," Progress in Astronautics and Rocketry: Detonation and Two-Phase Flow, Vol. 6, pp. 117-144, Academic Press, New York (1962).
- F-2. Marble, F., "Nozzle Contours for Minimum Particle Lag Loss," AIAA Journal, Vol. 1, No. 12, pp. 2793-2801 (December 1963).
- F-3. Bailey, W. S., E. N. Nilson, R. A. Serra, and T. F. Zupnik, "Gas-Particle Flow in an Axisymmetric Nozzle," ARS Journal, Vol. 31, No. 6, pp. 793-798 (June 1961).
- F-4. "Axisymmetric Two-Phase Perfect Gas Performance Program," TRW Systems Report, Contract NAS9-4358 (1967).
- F-5. "One-Dimensional Two-Phase Reacting Gas Nonequilibrium Performance Program," TRW Systems Report, Contract NAS9-4358 (1967).
- F-6. Netzer, D. W., "Calculations of Flow Characteristics for Two-Phase Flow in Annular Converging-Diverging Nozzles," Report No. TM-6203, Jet Propulsion Center, Purdue University (1962).
- F-7. Starkman, E. S., V. E. Schrock, K. F. Neusen, D. J. Maneely, and R. A. Brown, "Two-Phase Flow in Convergent-Divergent Nozzles," Series No. 160, Issue No. 2, University of California, Berkeley (1962).
- F-8. Chiu, H., One-Dimensional Heterogeneous Two-Phase Flow in Rocket Nozzles, Ph.D. Thesis, Princeton University (1962).
- F-9. Hoffman, J. D., "An Analysis of the Effects of Gas-Particle Mixtures on the Performance of Rocket Nozzles," Report No. TM-63-1, Jet Propulsion Center, Purdue University, Lafayette, Indiana (January 1963).
- F-10. Hoffman, J. D., A General Method for Determining Optimum Thrust Nozzle Contours for Gas-Particle Flows, AIAA Paper No. 66-538, Presented at AIAA Second Propulsion Joint Specialist Conference, Colorado Springs, Colorado (1966).

- F-11. Hoffman, J. D. and S. A. Lorenc, "A Parametric Study of Gas-Particle Flows in Conical Nozzles," AIAA Journal, Vol. 3, No. 1, pp. 103-106 (1965).
- F-12. Kliegel, J. R., "Gas-Particle Nozzle Flows," Ninth Symposium (International) on Combustion, Academic Press, New York, N. Y. (1963), pp. 811-826.
- F-13. Kliegel, J. R. and G. R. Nickerson, "Flow of Gas-Particle Mixtures in Axially Symmetric Nozzles," Progress in Astronautics and Rocketry: Detonation and Two-Phase Flow, Vol. 6, Academic Press, New York, New York (1962).
- F-14. Marble, F. E., "Dynamics of a Gas Containing Small Solid Particles," Proceedings of the 5th AGARD Colloquium, 1963, pp. 175-213, Pergamon Press, Oxford (1963).
- F-15. Marble, F. E., "The Role of Approximate Analytical Results in the Study of Two-Phase Flow in Nozzles (U)," Proceedings of the Air Force Rocket Propulsion Laboratory Two-Phase Flow Conference, AFRPL-TR-67-223, Vol. II, pp. 407-426, August 1967, CONFIDENTIAL.
- F-16. Arbit, H. A., R. A. Dickerson, S. D. Clapp, and C. K. Nagai, Lithium-Fluorine-Hydrogen Propellant Study, CR-72325, Contract NAS3-7954, Prepared for NASA by Rocketdyne, a division of North American Rockwell Corporation, Canoga Park, California, February 1968.

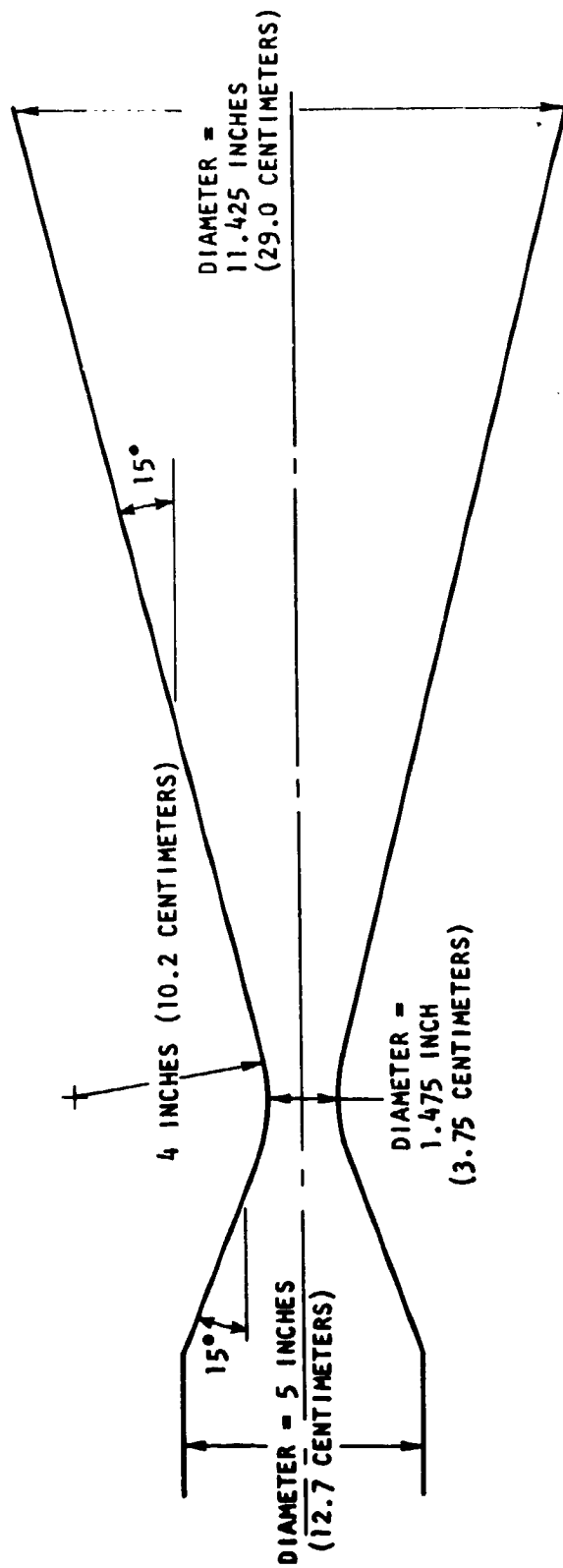


Figure F-1. Nozzle Geometry Used for Particle Effect Computations. This is Identical to Test Chamber Geometry Employed in the Experimental Altitude Simulation Firings

$P_c = 700 \text{ PSIA } (4.83 \times 10^6 \text{ N/M}^2)$
 $F_2/\text{Li MR} = 2.74$
 $H_2 = 25 \text{ PERCENT}$

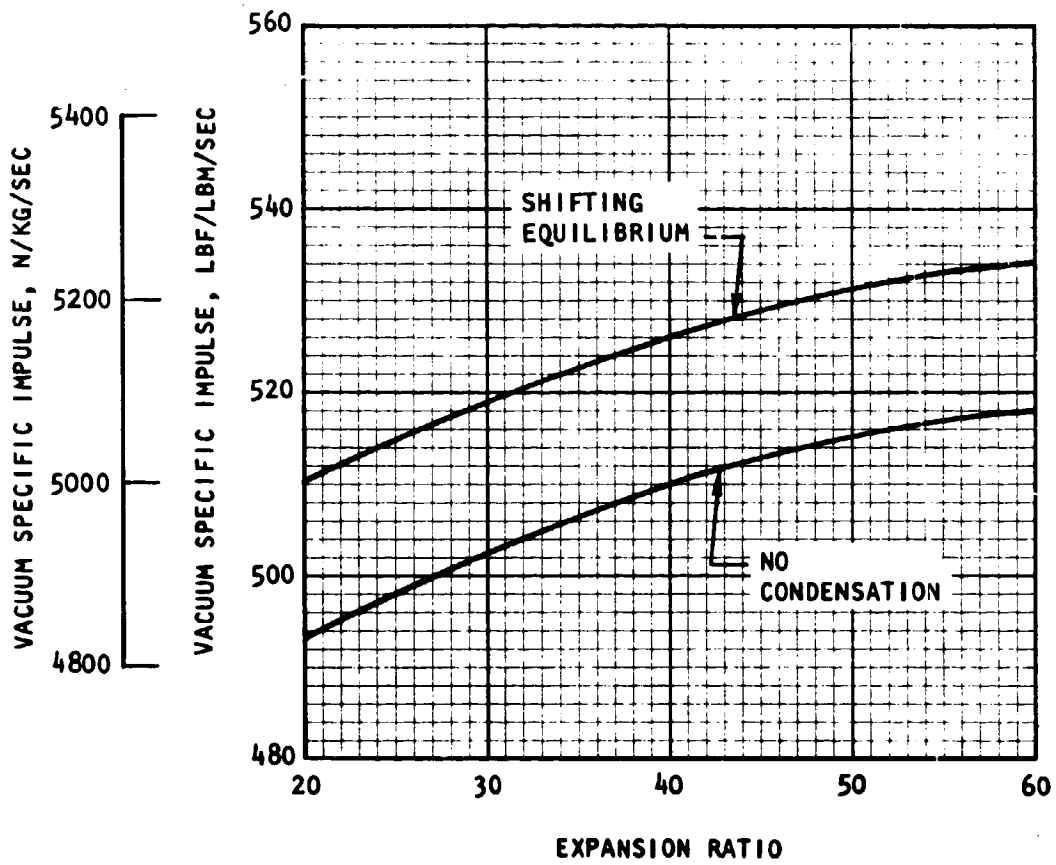


Figure F-2. Effect of Noncondensation of LiF on Theoretical Performance of Li/F₂/H₂ at Indicated Conditions

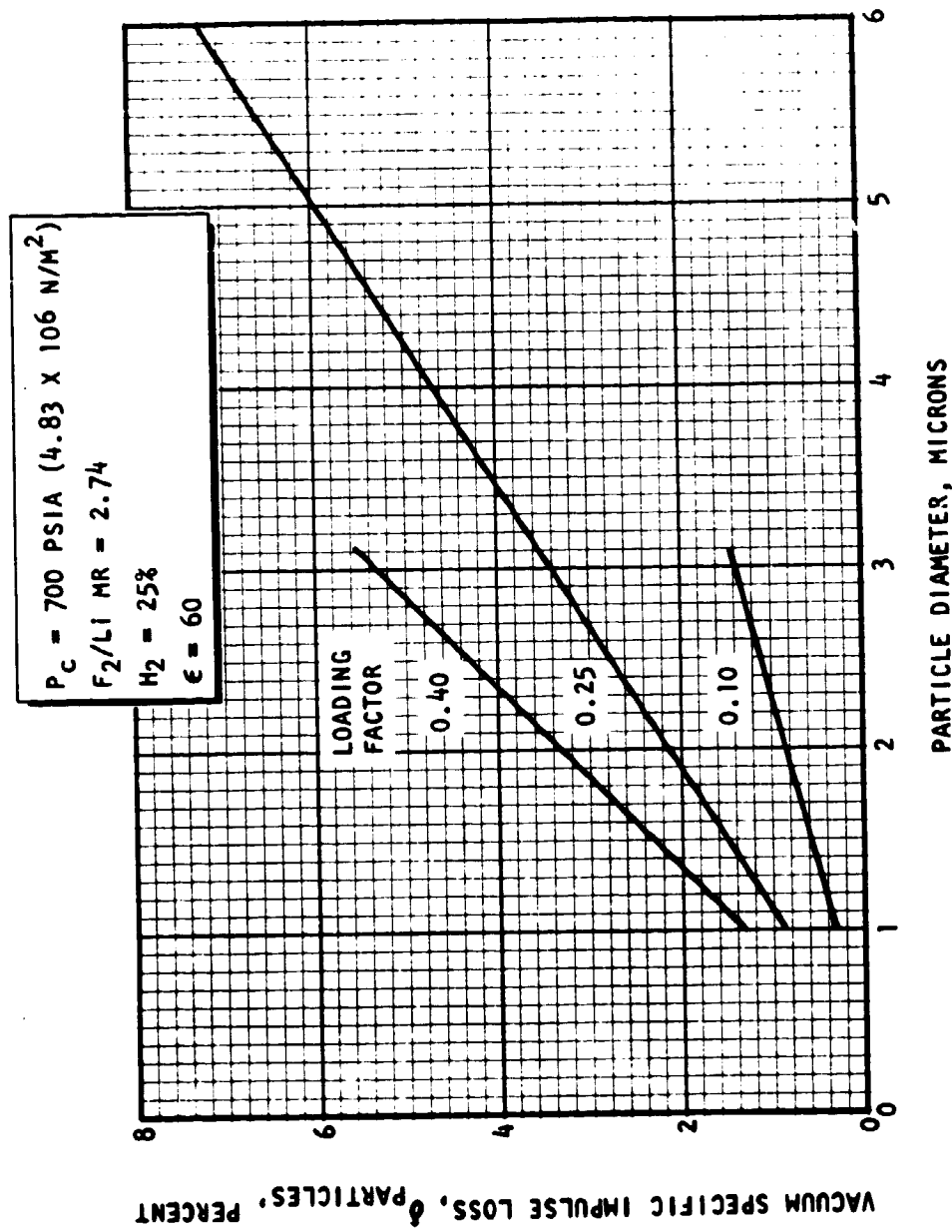


Figure F-3. Effect of Particle Size on Two-Phase Flow Performance Loss at Indicated Loading Factors (Weight Fraction of Condensed Phase) for $\text{Li}/\text{F}_2/\text{H}_2$ at Indicated Test Conditions

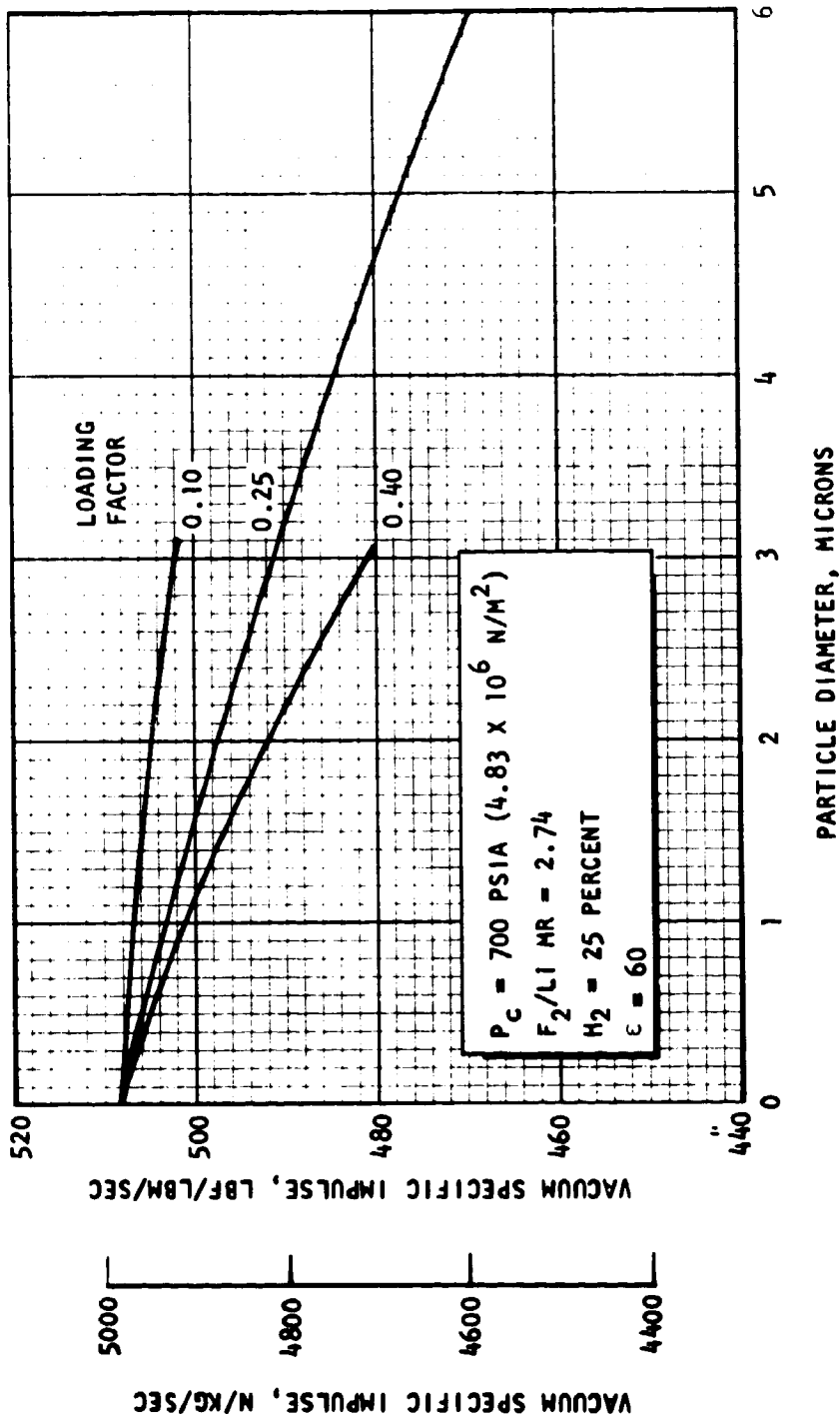


Figure F-4. Net Vacuum Specific Impulse, Including all Losses, for $Li/F_2/H_2$ at Indicated Test Conditions, Calculated as Function of Particle Diameter at Indicated Loading Factors (Weight Fraction of Condensed Phase)

APPENDIX G

DESIGN AND INSTALLATION OF EXHAUST DIFFUSER

INTRODUCTION

Experimental evaluation of engine performance with the 60:1 area ratio nozzle required a means of reducing nozzle back pressure by an amount sufficient to prevent flow separation within the nozzle. This was accomplished by use of an exhaust diffuser, which utilizes the momentum of the engine exhaust products for this purpose. Note that the only requirement in this connection is that the nozzle flow full, because if it does, vacuum thrust may be calculated whatever the actual nozzle back pressure may be. The simplest exhaust diffuser is a constant-diameter duct attached to the nozzle exit; however, diffuser performance is usually improved by incorporation of a minimum cross-sectional area ("second throat") in the duct. Static pressure recovery in the diffuser is accomplished by a progressive shock wave system, with accompanying gas deceleration to subsonic velocity. Although the actual flow process in a supersonic diffuser departs greatly from a simple normal-shock model, the latter may be used for approximate prediction of diffuser performance.

The two factors to be considered in the design of an exhaust diffuser are the conditions required for start (i.e., for the shock system to be established in the diffuser) and the conditions for continued diffuser operation after start. Generally, conditions for starting are more stringent than those for steady-state operation, so that once the diffuser is started it will continue to operate. The maximum nozzle expansion ratio which can be accommodated by a given diffuser is a function of the pressure ratio (chamber to ambient) and of the specific heat ratio (γ) of the exhaust gas. The higher the pressure ratio (at constant γ) the larger the expansion ratio that may be used, and the lower the γ (at constant pressure ratio) the larger the usable expansion ratio.

With a diffuser consisting of a constant-area duct ($L/D > 8$), the experimental data in Ref. G-1 may be combined with normal shock calculations to provide an indication of the maximum expansion ratio that may be accommodated. This is shown for $\text{Li}/\text{F}_2/\text{H}_2$ in Fig. G-1 as a function of chamber pressure and percent H_2 . For a constant-area diffuser, minimum starting and operating pressure ratios are the same.

A second-throat diffuser theoretically requires the same starting pressure ratio as a constant-area diffuser of the same diameter, but has a lower operating pressure ratio. However, substantial experimental evidence (e.g., Ref. G-1) indicates that not only is the starting pressure ratio of a second-throat diffuser generally lower than that of a corresponding constant-area duct, but also that the starting and operating conditions of the former may be nearly equal to each other. The operational characteristics of a second-throat diffuser are more difficult to predict than those of a constant-area duct, and are sensitive to seemingly minor design changes. Figure G-2 shows the estimated maximum expansion ratios that could be accommodated by a "standard" second-throat diffuser (Ref. G-1) at the indicated $\text{Li}/\text{F}_2/\text{H}_2$ test conditions. For conservative design, allowance should be made for higher starting than operating pressure ratios, as shown.

DIFFUSER DESIGN

The tripropellant test conditions under which the exhaust diffuser would be operated required that it start at the 20-percent H_2 level, with minimum chamber pressure of 650 psia ($4.48 \times 10^6 \text{ N/m}^2$), then continue to operate through the 25- and 35-percent H_2 levels. The curves in Fig. G-2 show that this is well within the capability of a second-throat diffuser.

Given the general type of diffuser to be used (such as a second-throat system), the required specific dimensions of the unit are derived not only from available experimental data (e.g., Ref. G-1 and G-2) but also

from operating experience obtained with similar systems under comparable test conditions. The diffuser design specified for the altitude simulation firings is shown in Fig. G-3. It differed from more conventional second-throat diffusers in that no divergent cone was used at the exit and the length of the throat was 7 diameters instead of the customary 10 diameters. Also, the diameters of the plenum section (upstream of the convergence) and of the throat were slightly larger than usual, to permit more rapid pump-down of the plenum and to "loosen" the geometric restriction near the nozzle exit. Diffuser material was type 1020 carbon steel; its wall thickness was 0.375 inch (9.5 mm) along the entire length.

Estimated inside wall temperatures of the diffuser at the end of a 6-second tripropellant firing were 400 F (480 K) at the entrance, 520 F (540 K) at the start of the cylindrical throat, and 1020 F (820 K) near the exit, where wall pressure rises to ambient values. No specific design provision was made for diffuser cooling. In actual use, water from two perforated circumferential pipes around the diffuser was sprayed over the exit region.

DIFFUSER INSTALLATION

Mounting and Support

For reliable and reproducible thrust calibrations and measurements in the altitude simulation tests, it was essential that the diffuser be fixed. Further, in addition to a support structure which prevented diffuser movement, provision had to be made for thermal expansion of the diffuser during testing. A schematic of the diffuser mounting and support structure is shown in Fig. G-4. The structural base consisted of three 15-inch (38-cm) I-beams buried to floor level in 24 inches (61 cm) of concrete. The eight channel supports of the diffuser were joined to 4-inch (10-cm) angles welded to the underlying I-beams. Lateral

solidity was provided by an additional side channel near the diffuser inlet, as shown in Fig. G-4. Thermal growth of the diffuser was permitted by supporting the exit end in a clevis mount, as sketched.

Nozzle-Diffuser Junction

A stainless-steel bellows* was used to join the nozzle to the diffuser. One end of the bellows was welded to the flange on the nozzle skirt and the other end was bolted to the diffuser inlet. A thin, stainless-steel liner inside the bellows protected the convolutions from recirculating exhaust gases. The diffuser was positioned in such a way that the 5-inch (12.7 cm) bellows was compressed to 4.7 inches (11.9 cm) when the engine/diffuser system was assembled. In this way, the bellows was in compression throughout the calibration and test procedures. The bellows spring rate (35 lb/in., 61 N/cm) was low enough so that the compressive force change during firing was completely negligible.

DIFFUSER FUNCTIONING

No diffuser operational problems or difficulties were encountered in the altitude simulation firings. When the gas generator alone was firing, before and after lithium flow, at chamber pressure of approximately 500 psia ($3.45 \times 10^6 \text{ N/m}^2$), the nozzle did not quite flow full. This marginal situation is indicated by the nozzle pressure curves in Fig. G-2. As soon as lithium flow began, however, and the chamber pressure increased, there was immediate full flow in the nozzle.

External wall temperatures of the diffuser were monitored at three points along its length during every firing. As predicted, the highest temperature was near the exit, reaching approximately 700 F (650 K) at the end of the test when water was sprayed over this region and about 850 F (730 K) without the water spray.

*Type T-9321, Gardner Bellows Corp., Van Nuys, California, 91405

REFERENCES

- G-1. Roschke, E. J., P. F. Massier, and H. L. Gier, Experimental Investigation of Exhaust Diffusers for Rocket Engines, Techn. Report No. 32-210, Jet Propulsion Laboratory, Pasadena, California, 15 March 1962.
- G-2. Goodsell, N. I., Propulsion System Diffusers for Space Flight Simulation, AIAA Space Simulation Testing Conference, Pasadena, California, 16-18 November 1964, AIAA Publication CP-11, pp. 202-212.

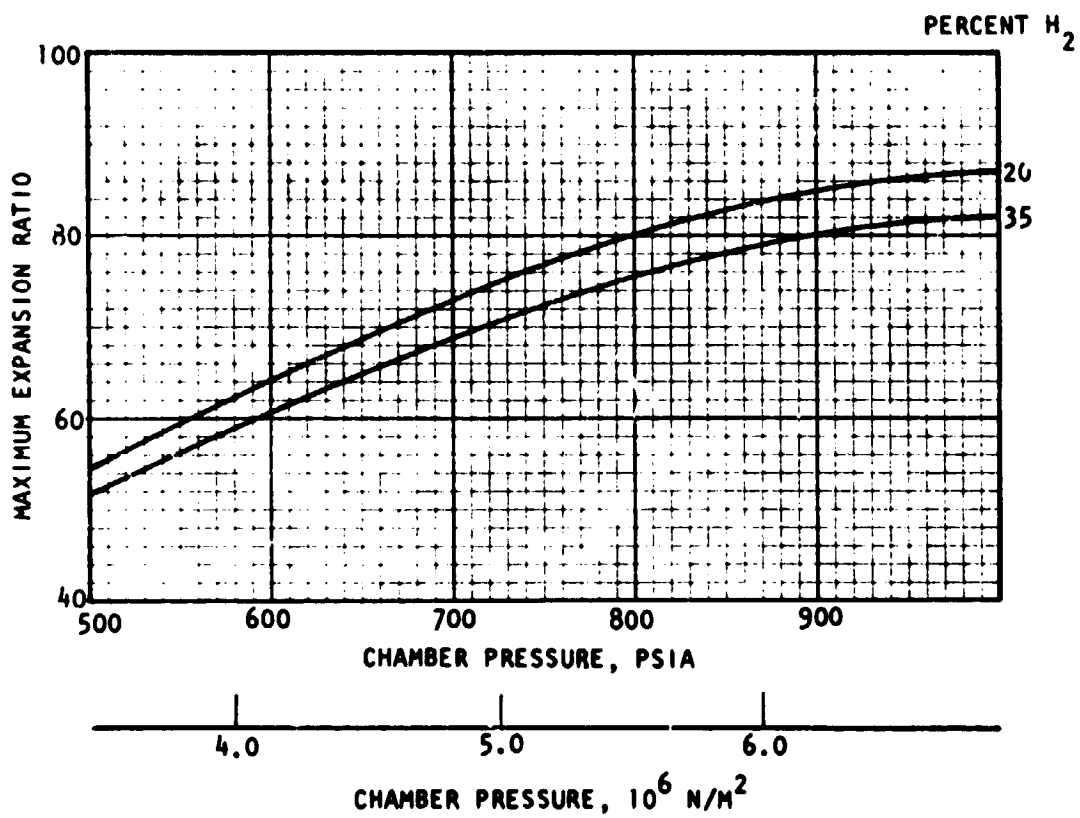


Figure G-1. Maximum Expansion Ratio Which can be Accommodated by Constant-Area Duct Diffuser as Function of Chamber Pressure, for Li/F₂/H₂ Firings With F₂/Li·MR = 2.74 and Indicated Percentages of Hydrogen

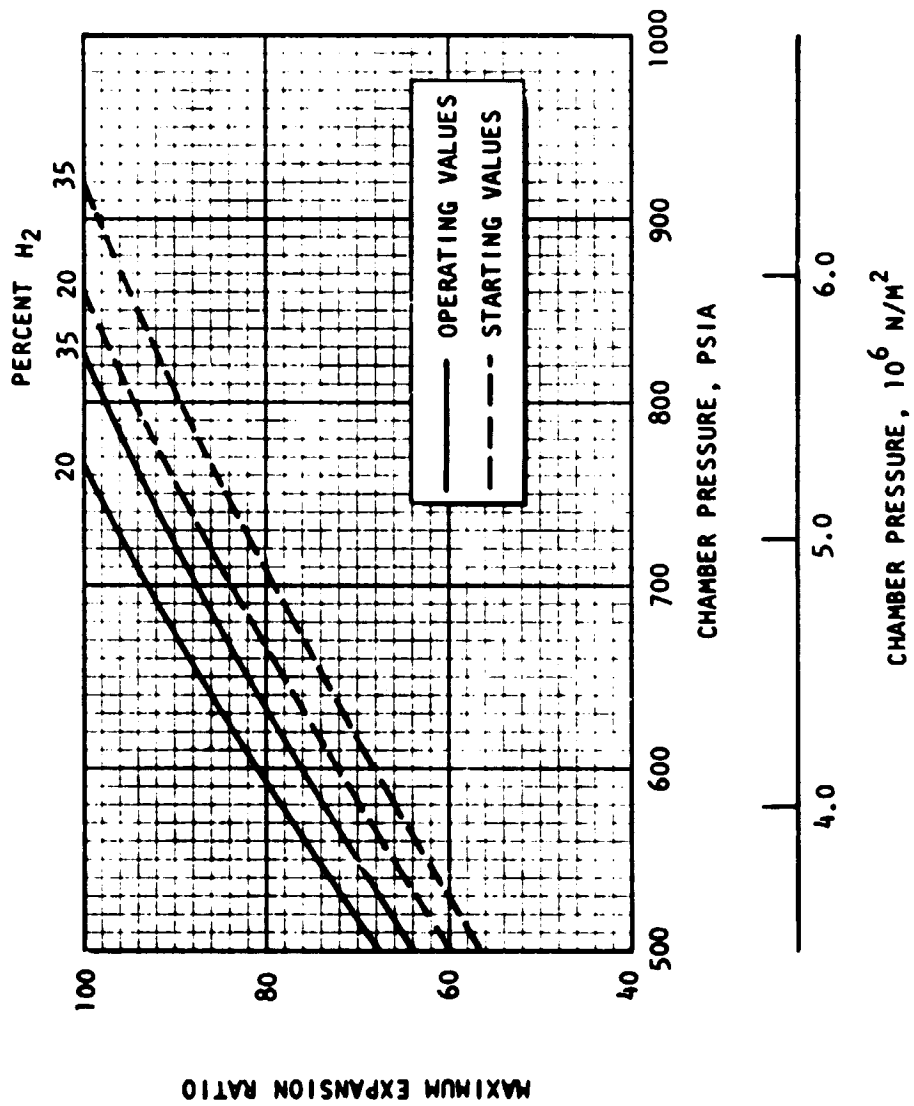
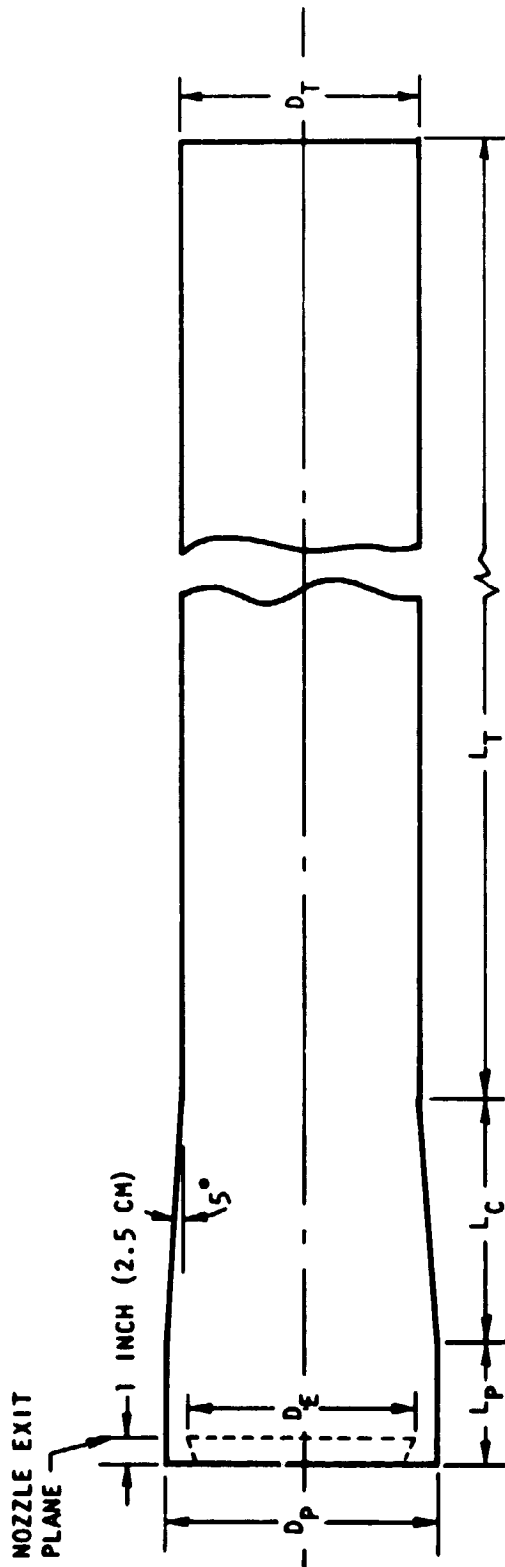


Figure G-2. Maximum Expansion Ratio Which can be Accommodated by Second-Throat Diffuser as Function of Chamber Pressure, for Li/F₂/H₂ Firings With F₂/Li MR = 2.74 and Indicated Percentages of Hydrogen



- D_E = NOZZLE EXIT DIAMETER = 11.425 INCH (29.02 CM)
- D_P = DIFFUSER PLENUM DIAMETER = 13.20 INCH (33.5 CM)
- D_T = DIFFUSER THROAT DIAMETER = 10.40 INCH (26.4 CM)
- L_P = DIFFUSER PLENUM LENGTH = 7.60 INCH (19.3 CM)
- L_C = CONVERGENT SECTION LENGTH = 15.70 INCH (39.9 CM)
- L_T = DIFFUSER THROAT LENGTH = 72.0 INCH (183 CM)

Figure G-3. Design of Self-Starting Exhaust Diffuser for $Li/F_2/H_2$ Altitude Simulation Firings

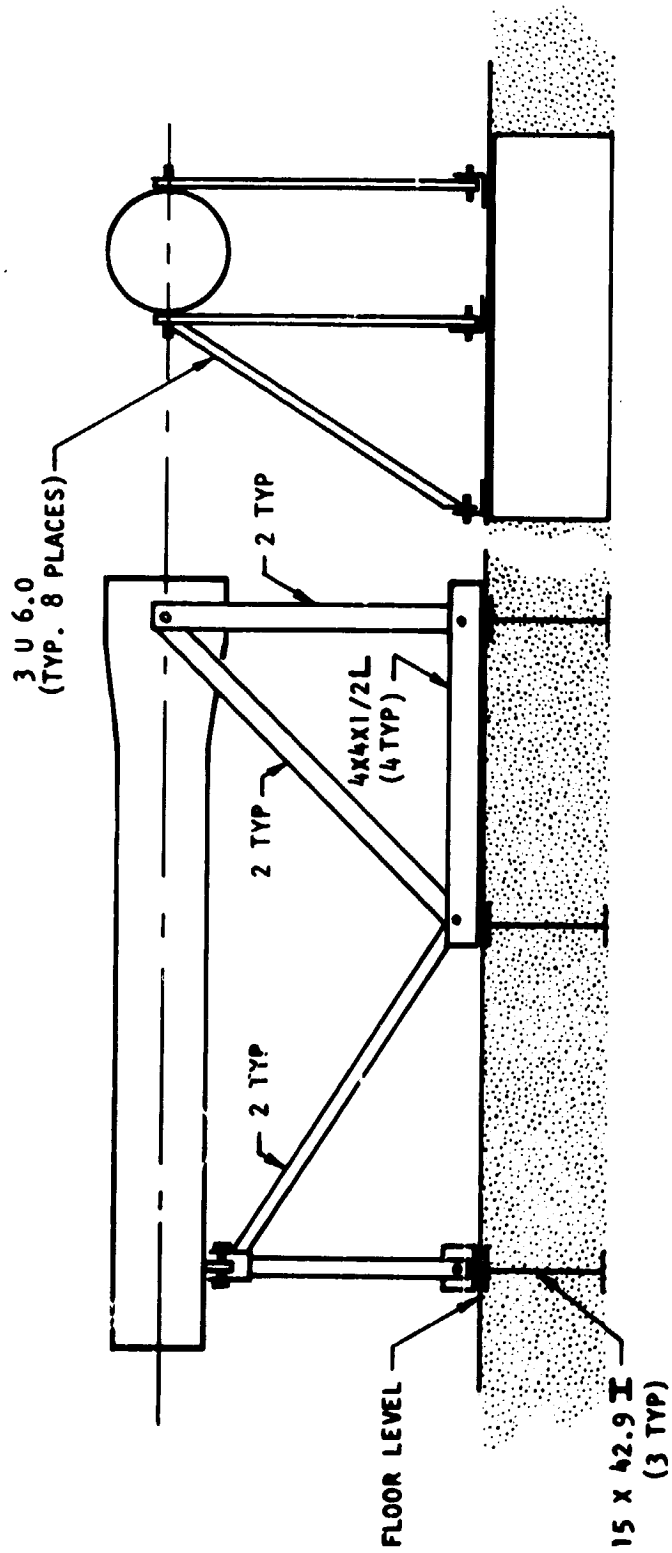


Figure G-4. Schematic of Mounting and Support Structure of Exhaust Diffuser

APPENDIX H

SPECIFIC IMPULSE EFFICIENCIES OF TASK II TEST FIRINGS

The primary objective of the test firings carried out in Task II was the measurement of chamber and nozzle heat flux. However, I_s efficiencies for the 10:1 expansion ratio nozzle (Fig. 35) were also determined in these tests, for use in the calculation of thrust based on nozzle pressure profiles in the Task III altitude simulation firings (Appendix C) and for comparison with data obtained with the 60:1 nozzle. For convenience, these results are summarized in Table H-1. As pointed out in the body of this report, chamber pressures in two of the firings were estimated from measurements of gas generator pressures, because of plugging of the chamber pressure taps by condensed solids. These values are enclosed in parentheses in Table H-1.

TABLE H-1

DATA SUMMARY, TASK II

Chamber Length = 9 inches (22.9 cm)

 $\epsilon = 10$

Run No.	69-4			69-5			69-6		
	1	2	3	1	2	3	1	2	3
\dot{w}_{LF} , lb/sec	2.74	2.60	2.34	2.72	2.58	2.33	2.65	2.53	2.30
\dot{w}_{L_2} , kg/sec	1.24	1.18	1.06	1.23	1.17	1.06	1.20	1.15	1.04
\dot{w}_{Li} , lb/sec	0.71	0.69	0.63	0.94	0.85	0.75	0.56	0.54	0.55
\dot{w}_{Li} , kg/sec	0.32	0.31	0.29	0.42	0.39	0.34	0.26	0.24	0.25
\dot{w}_{GH_2} , lb/sec	0.89	1.11	1.54	0.90	1.12	1.56	0.90	1.11	1.55
\dot{w}_{GH_2} , kg/sec	0.40	0.50	0.70	0.41	0.51	0.71	0.41	0.50	0.70
\dot{w}_T , lb/sec	4.34	4.40	4.52	4.56	4.55	4.64	4.11	4.18	4.41
\dot{w}_T , kg/sec	1.97	1.99	2.05	2.07	2.07	2.10	1.86	1.89	2.00
H ₂ , percent	20.5	25.2	34.1	19.8	24.6	33.7	21.8	26.7	35.2
F ₂ /Li MR	3.84	3.77	3.72	2.91	3.02	3.10	4.70	4.71	4.16
P _C , psia	(664)	(674)	(739)	680	696	730	(624)	(654)	(715)
$10^6 N/m^2$	(4.58)	(4.65)	(5.10)	4.69	4.80	5.03	(4.30)	(4.51)	(4.93)
η_{I_s} (uncorr), percent	92.4	93.9	94.7	92.6	93.8	93.9	90.2	91.2	91.7

APPENDIX I

NOMENCLATURE

A	=	local cross-sectional area of flow, in. ² (cm ²) (Eq. 4)
A	=	applicable area for heat flux, in. ² (cm ²)
A _e	=	area of nozzle exit, in. ² (cm ²)
A _t	=	measured geometric throat area, in. ² (cm ²)
(A _t) _{eff}	=	effective thermodynamic throat area, in. ² (cm ²)
B	=	bias error estimate (Appendix B)
c*	=	characteristic velocity, ft/sec (m/sec)
(c*) _{theo}	=	theoretical c* based on shifting equilibrium, ft/sec (m/sec)
(c*) _{obs}	=	observed, uncorrected characteristic velocity, ft/sec (m/sec)
C	=	constant (Eq. 1)
C _F	=	thrust coefficient
C _L	=	specific heat of liquid phase, B/lbm/R (J/kg/K) (Eq. 6)
C _p	=	specific heat at constant pressure, B/lbm/R (J/kg/K)
C _v	=	coefficient of variation
D	=	diameter of passage or orifice, in. (cm)
D _G	=	diameter of gas jet, in. (cm)
D _L	=	diameter of liquid stream, in. (cm)
\bar{D}_L	=	diameter of liquid stream, in. (only) (Eq. 1)
D _t	=	diameter of nozzle throat, in. (cm)
D ₃₀	=	volume mean diameter of liquid droplets in a spray field, microns
f _p	=	factor correcting observed static pressure to throat stagnation pressure
f _{TR}	=	factor correcting for change in throat radius

- f_{DIS} = factor correcting throat area for effective discharge coefficient
 f_{FR} = factor correcting measured chamber pressure for frictional drag of combustion gases at chamber wall
 f_{HL} = factor correcting measured chamber pressure for heat losses from combustion gases to chamber wall
 f_{TOTAL} = total correction applicable to measured characteristic velocity
 F = thrust, lbf (N)
 F_{atm} = thrust due to atmospheric pressure, lbf (N)
 F_{diff} = thrust due to diffuser pressure, lbf (N)
 F_{lc} = thrust measured on load cell, lbf (N)
 F_{vac} = measured thrust corrected to vacuum conditions, lbf (N)
 g = local acceleration, ft/sec² (m/sec²) (Used in Eq. 6)
 g_c = conversion factor (32.174 lbf-ft/lbf-sec², 1.00 kg-m/N-sec²)
 h = heat transfer coefficient, B/in.²/sec/R (W/m²/K)
 h_c = coolant-side heat transfer coefficient, B/in.²/sec/R (W/m²/K)
 h_g = gas-side heat transfer coefficient, B/in.²/sec/R (W/m²/K)
 I_s = specific impulse, lbf/lbm/sec (N/kg/sec)
 $(I_s)_{del}$ = deliverable specific impulse, lbf/lbm/sec (N/kg/sec)
 $(I_s)_{theo}$ = theoretical specific impulse based on shifting equilibrium lbf/lbm/sec (N/kg/sec)
 k = thermal conductivity, B/in./sec/R (J/m/sec/K)
 k_L = thermal conductivity of liquid, B/in./sec/R (J/m/sec/K)
 K = venturi meter calibration factor (Eq. 7)
 K_1, K_2, K_3 = constants (Appendix B)
 m = mean value of a set of measurements (Appendix B)
 M_∞ = free-stream Mach number
 MR = mixture ratio
 Nu = Nusselt number
 P = pressure, lbf/in.² (N/m²)

P_a	= ambient pressure, lbf/in. ² (N/m ²)
P_{atm}	= atmospheric pressure, lbf/in. ² (N/m ²)
P_c	= chamber pressure, lbf/in. ² (N/m ²)
$(P_c)_o$	= stagnation pressure at nozzle throat, lbf/in. ² (N/m ²)
P_{diff}	= diffuser pressure, lbf/in. ² (N/m ²)
Pr	= Prandtl number
Q	= rate of heat flow, B/sec (W)
Q/A	= heat flux, B/in. ² /sec (W/m ²)
Q_{total}	= total rate of heat loss, B/sec (W)
r_c	= throat radius of curvature, in. (cm)
Re	= Reynolds number
R_T	= recovery factor
S	= precision error estimate (Appendix B)
t	= time, sec
T	= temperature, R (K)
T_{avg}	= average temperature, R (K)
T_{aw}	= adiabatic wall temperature, R (K)
T_b	= inlet bulk temperature, R (K)
T_o	= stagnation temperature, R (K)
T_s	= saturation temperature, R (K)
T_{theo}	= theoretical temperature, R (K)
T_w	= wall temperature, R (K)
T_{wc}	= coolant-side wall temperature, R (K)
T_{wg}	= gas-side wall temperature, R (K)
ΔT_b	= change in bulk temperature, R (K)
U	= uncertainty estimate (Appendix B)
V_G	= velocity of gas jet, ft/sec (m/sec)

\bar{V}_G	= velocity of gas jet, ft/sec (only) (Eq. 1)
V_L	= velocity of liquid stream, ft/sec (m/sec)
\bar{V}_L	= velocity of liquid stream, ft/sec (only) (Eq. 1)
ΔV	= relative gas-liquid velocity, ft/sec (m/sec)
\dot{w}	= mass flowrate, lbm/sec (kg/sec)
\dot{w}_G	= flowrate of gas, lbm/sec (kg/sec)
\dot{w}_L	= flowrate of liquid, lbm/sec (kg/sec)
\dot{w}_T	= total propellant flowrate, lbm/sec (kg/sec)
x	= length, in. (cm)
x_p	= penetration of liquid stream into gas jet, in. (cm)
α	= nozzle divergence half angle, degrees
γ	= ratio of specific heats
δ_{div}	= divergence loss, percent (Appendix F)
δ_{drag}	= drag loss, percent (Appendix F)
$\delta_{particles}$	= two-phase flow performance loss, percent (Appendix F)
ϵ	= expansion ratio
ϵ_c	= contraction ratio
$[\eta_{c^*}]_{P_c}$	= c^* efficiency based on chamber pressure, percent
$[\eta_{c^*}]_F$	= c^* efficiency based on thrust, percent
$\bar{\eta}_{C_F}$	= thrust coefficient efficiency, percent
η_{I_s}	= specific impulse efficiency, percent
θ	= angle between liquid stream and injector face, degrees
λ	= heat of vaporization, B/lbm (J/kg)
μ	= viscosity, lbm/ft/sec (kg/m/sec)
ν_L	= liquid viscosity, lbm/ft/sec (kg/m/sec)

- ρ = density, lbm/ft³ (kg/m³)
 ρ_G = gas density, lbm/ft³ (kg/m³)
 ρ_L = liquid density, lbm/ft³ (kg/m³)
 ρ_V = vapor density, lbm/ft³ (kg/m³)
 σ = standard deviation
 σ_B = dimensionless factor accounting for property variations across boundary layer (Eq. 4)
 σ_L = liquid surface tension, lbf/ft (N/m)
 ϕ = $\left[\frac{3 (\dot{w}_L/\dot{w}_G)}{1 - [1 + (\dot{w}_L/\dot{w}_G)]^{-3}} \right]^{1/3}$ (Used in Eq. 2)
 ϕ_{FR} = correction for frictional losses
 ϕ_{DIV} = correction for nozzle divergence
 ϕ_{HL} = correction for heat losses to chamber and nozzle walls
 ϕ_{TOTAL} = total correction applicable to measured thrust